TAMPEREEN TEKNILLINEN YLIOPISTO
TAMPERE UNIVERSITY OF TECHNOLOGY

Sanna Turunen

Direct Laser Writing of Proteins and Synthetic Photoresists for Neuronal Cell Growth Guidance

Julkaisu 1486 • Publication 1486

Tampere 2017

Tampereen teknillinen yliopisto. Julkaisu 1486
Tampere University of Technology. Publication 1486

Sanna Turunen

Direct Laser Writing of Proteins and Synthetic Photoresists for Neuronal Cell Growth Guidance

Thesis for the degree of Doctor of Science in Technology to be presented with due permission for public examination and criticism in Tietotalo Building, Auditorium TB109, at Tampere University of Technology, on the 13th of October 2017, at 12 noon.

Tampereen teknillinen yliopisto - Tampere University of Technology
Tampere 2017

Doctoral candidate: Sanna Turunen
Biomaterials and Tissue Engineering Group
Faculty of Biomedical Sciences and Engineering
Tampere University of Technology
Finland

Supervisor: Minna Kellomäki, Prof., Dr. Tech.
Biomaterials and Tissue Engineering Group
Faculty of Biomedical Sciences and Engineering
Tampere University of Technology
Finland

Pre-examiners: Boris Chichkov, Prof., Dr.
Nanotechnology Department
Laser Zentrum Hannover e.V.
Germany

Frederik Claeyssens, Dr., Ph.D.
Department of Materials Science and Engineering
University of Sheffield
United Kingdom

Opponent: Sami Franssila, Prof., Ph.D.
Department of Chemistry and Materials Science
Aalto University
Finland

ISBN 978-952-15-3985-5 (printed)
ISBN 978-952-15-4001-1 (PDF)
ISSN 1459-2045

Abstract

In vitro cell culture platforms are important tools for the study of neural functions in health and disease. The formation of controlled neuronal networks increases the robustness of the results, which facilitates the transition of the results to *in vivo*. Controlled cell growth on predefined axes can be achieved via chemical or topographical cues, such as the microscale patterns of cell-adhesive peptides or physically confining 3D microstructures. Computer-assisted laser-based fabrication techniques such as direct laser writing by two-photon polymerization (2PP-DLW) offer a versatile tool to fabricate such controlled cell culture platforms with highly ordered geometries in the size scale of natural 3D cell environments. 2PP-DLW is a sequential fabrication technique based on the phenomenon of two-photon absorption (2PA) by photoinitiator molecules, which initiates radical chain-growth polymerization that converts small, unsaturated monomer molecules from a liquid state to solid macromolecules. The 2PP-DLW technique allows the fabrication of complex features including internal walls, overhangs, or tortuous channels with feature sizes in the µm and sub-µm range.

In this thesis, 2PP-DLW was used to fabricate microscale chemical and topographical guidance cues for neuronal cells. The main goal was to find appropriate photosensitive materials for the microstructures, to optimize the 2PP-DLW processing parameters for different material-photoinitiator combinations, and to design and fabricate several novel microstructures to be tested with human pluripotent stem cell (hPSC)-derived neuronal cells. As hPSCs can be differentiated into several cell types, such as neurons, astrocytes, and oligodendrocytes, they offer a promising cell source for cell culture models. Overall, four different custom-built 2PP-DLW fabrication setups based on either Nd:YAG or Ti:sapphire lasers were used for the polymerization experiments. First, the processability of photosensitive custom-synthetized methacrylated poly(caprolactone) oligomer (PCL-o) and commercial poly(ethylene glycol)diacrylate (PEGda) were studied together with Irgacure®127 photoinitiator. Although both PCL-o and PEGda could be successfully fabricated into simple microstructures with a picosecond Nd:YAG laser, the PCL-o required the use of very slow scanning speed in order to achieve complete polymerization. Thus, it was concluded that the fabrication of larger or more complex structures from PCL-o was not feasible. The inability of PEGda and PCL-o to support the migration or functionality of neuronal cells make them therefore poor candidates for cell culture purposes.

Next, avidin and biotinylated bovine serum albumin (bBSA) proteins together with flavin mononucleotide (FMN) photosensitizer were fabricated into surface patterns using several protein concentrations in combination with different average laser power and scanning speed values to determine the range of fabrication conditions suitable for protein crosslinking. It was demonstrated that the bioactivity of proteins is retained during the exposure to the high laser intensities required for photocrosslinking with the Nd:YAG laser. Avidin and bBSA together with Irgacure® 2959 photoinitiator were also photocrosslinked into 2D single neuron guidance patterns, functionalized

with extracellular matrix-derived peptides, and used for the study of cell growth guidance with hPSC-derived neuronal cells for 14 days. As several difficulties were encountered during the fabrication of the protein patterns and cell culture experiment, proteins were excluded from any further studies and replaced with the commercially available hybrid polymer-ceramic Ormocomp® that possesses superior photocrosslinking properties.

Ormocomp® combined with Irgacure®127 was fabricated into 3D confinement microstructures and 3D tubular microtowers with or without intraluminal guidance cues. The applicability of the confinement structures to control the location of neurons and to direct the growth of neurites on predefined axes was evaluated during the cell culture experiments. The functionality of three different microtower designs for the long-term 3D culturing of human neuronal cells and their ability to orient neurites was assessed with a four-week cell culture study. The observations achieved in this thesis support the use of the microtower-based platform for long-term cell culture as the microtowers were proven to facilitate neurite orientation and 3D network formation via suspended neurite bridges. Thus, the proposed microstructure-based culturing concept could in future be used as a substitute for the hydrogel matrices commonly used to mechanically support the formation of 3D cell networks.

Acknowledgements

The research work presented in this thesis was carried out during 2009-2017 in the Biomaterials and Tissue Engineering Group, at the Faculty of Biomedical Sciences and Engineering, Tampere University of Technology.

I wish to express my gratitude to my supervisor, Prof. Minna Kellomäki, for giving me the opportunity to work on this challenging subject and for her guidance throughout the years. I am also grateful to the official pre-examiners, Prof. Boris Chichkov from the Laser Zentrum Hannover e.V. and Dr. Frederik Claeyssens from the University of Sheffield, for the thorough evaluation of this thesis.

I would like to thank all my co-authors, Elli Käpylä, Jenni Koskela, Minna Lähteenmäki, Maiju Hiltunen, Jouko Viitanen, Tiina Joki, Laura Ylä-Outinen, Teemu Ihalainen, Susanna Narkilahti, Konstantina Terzaki, Maria Farsari, and Costas Fotakis, for their contributions to this research and for the fruitful collaboration. Special thanks go to Jouko for providing me with access to his Machine Vision lab at the VTT Technical Research Centre of Finland and for his expertise and endless encouragement during the years of our collaboration. I would like to express my deepest gratitude to Elli for her valuable help, friendship, and the inspiring conversations throughout this research work. I would also like to acknowledge all my colleagues and the staff in the Biomaterials and Tissue Engineering group for all their support and help. Anne-Marie Haaparanta and Suvi Heinämäki, especially, deserve my special thanks for being such pleasant lunch companions and helping me to find the silver lining from every cloud at the times of desperation. I am also grateful to Peter Heath for all his help and encouraging comments while language editing this thesis.

This research was made possible by the financial support from the Finnish Foundation for Technology (TES), the Finnish Cultural Foundation (SKR), and the Finnish Funding Agency for Innovation (TEKES).

I want to thank my parents, Sirpa Lampinen and Esko Peltola, for always believing in me and for encouraging me to continue down the academic path. I also appreciate the support from my closest relatives and dear friends.

Finally, I want to thank my beloved husband Markku and our dearest children Emmi and Nuutti for all your love and patience during this thesis project. Thank you for completing my life!

Akaa, August 2017

Sanna Turunen

Table of contents

List of original publications

This thesis is based on the following original publications that are referred to as Publications I–IV in the text. The publications are reprinted with permissions from the publishers.

I. Koskela, J., Turunen, S., Ylä-Outinen, L., Narkilahti, S. & Kellomäki, M. Two-photon microfabrication of poly(ethylene glycol) diacrylate and a novel biodegradable photopolymer – comparison of processability for biomedical applications. Polymers for Advanced Technologies 23(2012)6, pp. 992-1001.

II. Turunen, S., Käpylä, E., Terzaki, K., Viitanen, J., Fotakis, C., Kellomäki, M. & Farsari, M. Pico- and femtosecond-laser induced crosslinking of protein microstructures: Evaluation of processability and bioactivity. Biofabrication 3(2011)4, pp. 045002.

III. Turunen, S., Käpylä, E., Lähteenmäki, M., Ylä-Outinen, L., Narkilahti, S. & Kellomäki, M. Direct laser writing of microstructures for growth guidance of human pluripotent stem cell derived neuronal cells. Journal of Optics and Lasers in Engineering 55(2014)April, pp. 197-204.

IV. Turunen, S., Joki, T., Hiltunen, M. L., Ihalainen, T. O., Narkilahti, S. & Kellomäki, M. Direct laser writing of tubular microtowers for 3D culture of human pluripotent stem cell-derived neuronal cells. ACS Applied Materials & Interfaces 9(2017)31, pp. 25717-25730.

Author's contribution

I. The author co-designed the 2PP-DLW experiments and supervised the work of Jenni Koskela, who performed the actual polymerization tests. The author assisted with the analysis and interpretation of the data, and co-wrote the manuscript as the second author.

II. The author designed the entire experimental part and performed the 2PP-DLW experiments with the Nd:YAG laser; experiments with the Ti:sapphire laser were carried out in collaboration with Elli Käpylä and Konstantina Terzaki. The author analyzed and interpreted the data and wrote the manuscript as the first author.

III. The author co-designed and performed the 2PP-DLW experiments together with Elli Käpylä. The author also co-designed the cell culture experiments and participated in analyzing and interpreting the data. The author wrote the manuscript as the first author.

IV. The author designed and performed all the 2PP-DLW experiments and co-designed the cell culture experiments. The author analyzed and interpreted the data from the 2PP-DLW experiments, and participated in analyzing and interpreting the data from the cell culture experiment. The author wrote the manuscript as the co-first author.

Abbreviations

1PA	Single-photon absorption
1PP	Single-photon polymerization
2D	Two-dimensional
2PP	Two-photon polymerization
2PP, TPA	Two-photon absorption
3D	Three-dimensional
4-MU	4-methylumbelliferone
AFM	Atomic force microscopy
AP	Alkaline phosphatase
APTES	(3-aminopropyl) triethoxysilane
B35	Rat neuroblastoma cell line
bBSA	Biotinylated bovine serum albumin
BSA	Bovine serum albumin
CAD	Computer-aided design
CCD	Charge-coupled device
CHO	Chinese hamster ovary
CNS	Central nervous system
CT	Computed tomography
cyt c	Bovine heart cytochrome c
DAPI	4',6-diamidino-2-phenylindole fluorescent stain
DLW	Direct laser writing
DRG	Dorsal root ganglion
ECM	Extracellular matrix
FAD	Flavin adenine dinucleotide
FDA	Food and Drug Administration
FESEM	Field emission scanning electron microscope
FGF	Fibroblast growth factor
FMN	Flavin mononucleotide

fs	Femtosecond
GFAP	Glial fibrillary acidic protein antibody
GFSHR-17	Immortalized rat steroidogenic granulosa cell line
GM-7373	Bovine aortic endothelial cell line
HA	Hyaluronic acid
HEMA	2-hydroxyethyl methacrylate
hESC	Human embryonic stem cell
HMDS	Hexamethyldisilazane
hPSC	Human pluripotent stem cell
IKVAV	Isoleucine-lysine-valine-alanine-valine peptide sequence
IR	Infrared
MAP-2	Microtubule-associated protein
MAPLE DW	Matrix-assisted pulsed-laser evaporation direct writing
MAPTMS	3-(trimethoxysilyl) propyl methacrylate
MRI	Magnetic resonance imaging
NA	Numerical aperture
NDS	Normal donkey serum
Nd:YAG	Neodymium-doped yttrium aluminum garnet
NG108-15	Neuroblastoma-glioma cell line
NHS	N-hydroxysuccinimide
NIR	Near-infrared
NPC	Neural progenitor cells
ORMOCER®	Organically modified ceramic
ORMOSIL	Organically modified silicate
PBS	Phosphate buffered saline
PC12	Rat pheochromocytoma cell line
PCL	Polycaprolactone
PDMS	Polydimethylsiloxane
PEG	Poly(ethylene glycol)
PEGda	Poly(ethylene glycol) diacrylate

PEO	Poly(ethylene oxide)
PETA	Pentaerythritol triacrylate
PLA	Polylactide
PNS	Peripheral nervous system
ps	Picosecond
RGD	Tripeptide of L-arginine, glycine and L-aspartic acid
SEM	Scanning electron microscopy
SH-SY5Y	Human neuroblastoma cell line
SI	International System of Units
SLS	Selective laser sintering
TDE	2,2'-thiodiethanol based embedding media
TEM_{00}	Fundamental transverse electromagnetic mode of the laser
UV	Ultraviolet
v.-%	Volume percent
YIGSR	Tyrosine-isoleucine-glycine-serine-arginine peptide sequence
β-tub	β-tubulin isotype III
μSL	Microstereolithography

Symbols

[hv]	Number density (or concentration) of excitation photons
$[N_0]$	Number density (or concentration) of ground-state molecules
$[N_1]$	Number density (or concentration) of excited-state molecules
ΔP	Pressure difference
A	Aspect ratio of the exposure volume
A	Cross-sectional area of the laser beam
C	Molar concentration
c	Speed of light
d_{axial}	Axial resolution
$d_{lateral}$	Lateral resolution
d_s	Lateral resolution according to Sparrow criterion
E	Photon energy
f	Laser pulse repetition frequency
F	Photon flux
GM	10^{-50} cm^4 s $photon^{-1}$ $molecule^{-1}$
h	Planck's constant
I	Laser beam intensity
k	Reaction rate coefficient
l	Absorption path length
N_0	Molecule in a ground state
N_1	Molecule in an excited state
N_A	Avogadro's number
P	Laser power

P_{ave}	Average laser power
P_{peak}	Peak laser power
R_{TPE}	Rate of two-photon excitation
v	Scanning speed
δ	Two-photon absorption cross-section
θ	Contact angle
λ	Wavelength
ν	Frequency
σ	Surface tension
τ	Laser pulse width

1 INTRODUCTION

The precise control of the cellular architecture is vital for creating engineered tissue constructs. For example, functional nerves and blood vessels can only form when the cells are highly organized in a specific manner (Wang & Ho 2004). Cellular adhesion, proliferation and differentiation *in vitro* can be guided by microscale topographical and chemical cues. These *in vitro* cell culture platforms are also invaluable tools for the study of neural functions in health and disease (Puschmann *et al.* 2014). However, the planar culture of neuronal cells represents an oversimplification of the structure of the *in vivo* neural system. Moreover, two-dimensional (2D) cultures may lead to uncharacteristic cell-cell and cell-matrix interactions and alter cell behavior. (LaPlaca *et al.* 2010) Hence, one of the major strategies in the field of neuroscience and neural tissue engineering is to develop three-dimensional (3D) cell culture models that more closely mimic the complexity of the cellular microenvironment found *in vivo* (Cullen *et al.* 2011). Along with three-dimensionality, axonal alignment is also an important goal for neural tissue engineering in central nervous system (CNS) and peripheral nervous system (PNS) injuries and deficits.

Computer-aided design (CAD)-based direct laser writing techniques (DLW) offer a powerful tool for fabricating microstructure-based cell culture platforms for tissue engineering and regenerative medicine applications. Although traditional DLW techniques, such as UV laser stereolithography and selective laser sintering, are able to fabricate complex 3D structures, they cannot produce submicron features. In contrast, two-photon polymerization (2PP), a pulsed laser light-based rapid prototyping process, enables true 3D direct writing of predesigned structures with resolution beyond the diffraction limit of light (Raimondi *et al.* 2012; Gittard *et al.* 2013). 2PP-DLW is based on the optical phenomenon of two-photon absorption (2PA), where the simultaneous absorption of two photons by photoinitiator molecules initiates the polymerization and solidification of a photosensitive resin. Due to the nonlinear intensity dependence of 2PA, the polymerization is localized within the focal volume of the laser beam, which makes 2PP an intrinsically 3D fabrication technique (Lee *et al.* 2007; Juodkazis *et al.* 2009).

Very high peak intensity but low average power is required to launch 2PA and to minimize thermal damage to the photopolymerizable material. Commonly, this requirement for photon density is met by utilizing Ti:sapphire lasers as light sources for 2PP-DLW. These lasers emit at infrared wavelengths and are capable of producing pulses with widths of several tens of femtoseconds (fs) (Lee *et al.* 2008). These lasers cannot, however, be directly diode-pumped, and therefore the need for additional pump lasers makes Ti:sapphire lasers too expensive and cumbersome to be widely used for research purposes in materials science and biomedical engineering laboratories. Consequently, a more affordable visible wavelength picosecond laser was tested in the three research studies included in this thesis and its performance was compared with that of the Ti:sapphire laser.

2PP-DLW enables experimentation with different structure designs because it does not require the use of unalterable mask masters as is the case in conventional photolithographic techniques. The technique is also a less laborious and time-consuming process than photolithography as there are fewer manual work phases involved. In this thesis, the advantages offered by the possibility of easily testing numerous structure designs with 2PP-DLW was taken to the greatest possible extent. Several different design and material combinations were explored to find the most efficient microscale topographical or chemical guidance structure to control the attachment, growth and orientation of individual neurons *in vitro*. The literature review of this thesis provides an overview of the fundamentals of the 2PP-DLW process, the role of the processing parameters on achievable resolution, and presents the properties of the selected photosensitive materials including methacrylated poly(caprolactone), poly(ethylene glycol) diacrylate, avidin, BSA, and the polymer-ceramic hybrid material Ormocomp®. In addition, the applications of 2PP-DLW fabricated structures for the growth guidance of neuronal cells are reviewed. The experimental part of this thesis sums up the details of the used materials, 2PP-DLW processing, and the characterization methods of the four original research studies. As most of the published neural cell culture experiments involving 2PP-DLW fabricated microstructures have been performed with rodent tumor cell lines, there seems to be an obvious need for studies conducted with human neuronal cells of nonmalignant origin. Thus, in this thesis, human pluripotent stem cell (hPSC)-derived neuronal cells were selected as the cell type for the cell culture experiments with the fabricated structures. The main results are divided into subsections that describe the comparison and selection of photosensitive materials for 2PP-DLW, the fabrication and applicability of bioactive protein surface patterns, 3D confinement microstructures, and 3D tubular microtowers with and without intraluminal guidance cues for supporting neuronal cell migration and orientation.

2 LITERATURE REVIEW AND THEORETICAL BACKGROUND

2.1 Fundamentals of direct laser writing

Direct laser writing (DLW) is a sequential fabrication technique in which structures are created by translating either the focal spot of a tightly focused laser beam, or the target according to a predefined computer-aided design (CAD) model (Juodkazis *et al.* 2008). The main advantage of direct laser writing techniques over other manufacturing techniques, such as molding, is its ability to fabricate devices with complex interior geometries. Even patient-specific medical devices and prostheses can be fabricated using CAD models based on patient data, for example, computed tomography (CT) scans or magnetic resonance imaging (MRI) (Gittard & Narayan 2010). DLW by two-photon polymerization (2PP-DLW) is a unique fabrication technique because it enables the fabrication of computer-designed, truly three-dimensional structures with resolution below one micrometer. The other classic laser-based direct writing techniques, such as UV laser microstereolithography (μSLA) (Farsari *et al.* 2000), selective laser sintering (SLS) (Antonov *et al.* 2005) or matrix-assisted pulsed-laser evaporation direct writing (MAPLE DW) (Wu *et al.* 2003) do not provide resolution beyond a few microns (Malinauskas *et al.* 2013). The field of direct laser writing by two-photon polymerization originated from the demonstration of localized excitation in two-photon fluorescence microscopy by Denk *et al.* more than two decades ago (Denk *et al.* 1990). A year later, the same group also presented the concept of three-dimensional optical data storage inside a photoresist using two-photon excitation (Strickler & Webb 1991). In 1997, Kawata and his group demonstrated the feasibility of this method as a true 3D direct laser writing technique by fabricating a spiral coil with a diameter of seven μm inside a photosensitive resin (Maruo *et al.* 1997). Over the past decade, 2PP-DLW has matured from a laboratory curiosity to a versatile tool for the fabrication of three-dimensional micro- and nanostructures. Due to the variability of 2PP-DLW, several applications have emerged in the fields of photonics (Serbin *et al.* 2004; Rill *et al.* 2008), micro-optics (Guo *et al.* 2006; Malinauskas *et al.* 2010a; Sun *et al.* 2014), microfluidics (Maruo *et al.* 2009b; Liu *et al.* 2014), biomedical devices (Gittard *et al.* 2009; Doraiswamy *et al.* 2010; Gittard *et al.* 2011a), and tissue engineering (Hidai *et al.* 2009; Bakar *et al.* 2012; Terzaki *et al.* 2013; Greiner *et al.* 2014; Kufelt *et al.* 2014).

2.1.1 Mechanisms of initiation

Classically, the two-photon absorption (2PA, TPA) of photoinitiator molecules and subsequent generation of initiating radicals has been considered to be the workhorse of DLW. Recently, however, several other proposals for the underlying initiation mechanism have been suggested. For example, Malinauskas *et al.* have proposed that the avalanche multiplication of electrons via direct bond cleavage and ionization (Figure 1) is the dominant mechanism in creating initiating radicals, although two-photon absorption is still required for seeding the avalanche (Malinauskas *et al.* 2010e; Buividas *et al.* 2013; Rekštytė *et al.* 2014). In their studies, the hybrid sol-gel-based photoresist SZ2080 and polydimethylsiloxane (PDMS) were polymerized with 30 to 300 fs-pulses at low repetition rate (1 kHz to 200 kHz) (Malinauskas *et al.* 2010e; Buividas *et al.* 2013; Rekštytė *et al.* 2014), and SZ2080

with 16 to 25 ps-pulses at high repetition rate (0.5 MHz to 1 MHz) (Malinauskas *et al.* 2011). The avalanche chain-reaction is created when the free electrons oscillate in the electromagnetic field of the laser pulse and gain energy by multiple collisions with other atoms of the medium, thereby ionizing them. Additional electrons are thus released and accelerated and, as they collide with further atoms, even more electrons are released. Furthermore, it has been suggested that heat diffusion and accumulation at the focal spot play a major role in the polymerization when the repetition rate is larger than the cooling time of the focal volume (Malinauskas *et al.* 2011; Baldacchini *et al.* 2012). Heat is capable of affecting the polymerization process either directly by decomposing the photoinitiator into radicals, or indirectly by increasing the rate constants of the polymerization reaction according to the Arrhenius equation (Baldacchini *et al.* 2012).

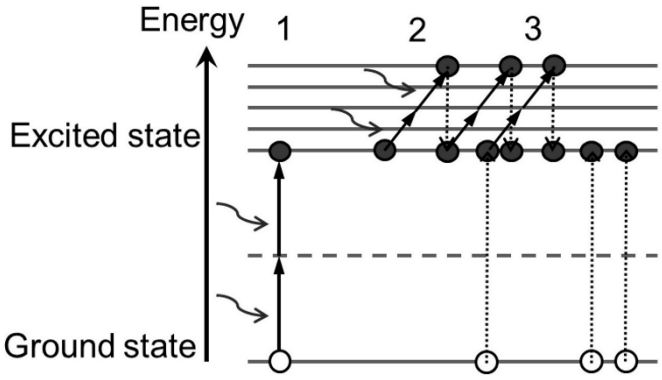

Figure 1. Schematic illustration of different light-matter interactions: (1) two-photon absorption by an electron, (2) multiplication of electrons by impact ionization: electron absorbs photons and gains enough energy to raise another electron to the excited state; (3) the process is repeated creating avalanche ionization. Adapted from (Rekštytė et al. 2014).

According to the assumption about localized heat accumulation, the initiation mechanism for low repetition rates (~few kHz) and high repetition rates (~MHz) would be fundamentally different. With a low repetition rate, the focal spot has time to cool down before the next pulse arrives, but with a high repetition rate the temperature could accumulate over consecutive laser pulses. (Fischer *et al.* 2013) Although some authors have suggested that the heat accumulation is of high importance when working with high-repetition-rate laser systems (Malinauskas *et al.* 2011; Baldacchini *et al.* 2012), recent *in-situ* local temperature measurements during the three-dimensional direct laser writing of a common pentaerythritol triacrylate photoresist (PETA) have revealed only a few degrees temperature increase under normal writing conditions (P < 9 mW, v = 10 μm/s) (Mueller *et al.* 2013). However, on the contrary, as the laser power exceeds the breakdown threshold of the monomer, the temperature change becomes prominent and extends up to 300 K. This step-like behavior of the temperature change indicates that the mechanism for the laser-induced breakdown is distinctly different from the photo-induced polymerization. One explanation for this highly nonlinear process could be photoionization and subsequent plasma formation. (Mueller *et al.* 2013)

Fischer *et al.* have studied the effects of different laser repetition rates (150 fs pulses) on initiation mechanisms for PETA photoresist and found that in photoresists sensitized with Irgacure

photoinitiators, the polymerization is clearly induced by two-photon absorption at repetition rates above 100 kHz. With repetition rates below 10 kHz, the process appears to be more non-linear indicating the dominance of the photoionization of the photoinitiator molecules over the two-photon absorption mechanism. Fischer *et al.* did not find, however, any region where the polymerization threshold energy would have shown linear dependence on the laser repetition rate, which could have been interpreted as a sign of avalanche ionization dominating over other processes. (Fischer *et al.* 2013) Obviously, the mechanism leading to the generation of photoinitiator radicals upon excitation with focused laser beam is more complex than initially predicted, and due to the variety of photosensitive material formulations and experimental conditions, it might even be impossible to agree on a universal mechanism for DLW.

2.1.2 Two-photon absorption mechanism

Two-photon absorption is a radiation-matter interaction where an atom or a molecule is excited from a lower quantum state to an excited state due to the sequential or simultaneous absorption of two photons. The theory of the two-photon absorption process was introduced already in 1931 by Göppert-Mayer in her PhD thesis (Göppert-Mayer 1931), but it was not experimentally verified until the advent of the ruby laser in 1961 because of the high photon intensities required (Kaiser & Garrett 1961). In the sequential absorption process, a real intermediate state with a lifetime of 10^{-4}–10^{-9} s is populated by the first absorbed photon, which is further pumped to a higher energy level via the absorption of the second photon. In simultaneous 2PA, generally referred to as 2PA, a virtual intermediate state is created when the first photon is absorbed. The second photon can only be absorbed if it arrives within the lifetime of the virtual state, i.e., approximately 10^{-15} s. (Lee *et al.* 2006) The combined energy of the two photons enables access to the excited state of the molecule. If the energy of the two photons is identical, the process is referred to as degenerate 2PA, otherwise the process is a non-degenerate one. (Belfield *et al.* 2008) Most 2PA applications concentrate on the degenerate process.

A comprehensive theoretical derivation of the expression for the two-photon transition probability (Göppert-Mayer 1931; Bischel *et al.* 1976) is based on quantum mechanics, but for practical reasons it is also possible to explain the nonlinear behavior of 2PA by modelling the excitation as the rate-limiting step in a chemical reaction. The interaction of radiation with matter is commonly modeled using a second-order kinetic rate equation (Fisher *et al.* 1997a). For single-photon absorption (1PA), the photochemical reaction can be described as follows:

$$N_0 + h\nu \rightarrow N_1, \tag{1}$$

where N_0 is a molecule in the ground state, being promoted to an excited state, N_1, after interacting with one photon having energy of $h\nu$. The rate equation describing the probability of formation of the excited state of a molecule by 1PA can be written as follows:

$$\frac{d[N_1]}{dt} = k[N_0][h\nu], \tag{2}$$

where k is the reaction rate coefficient and $[N_0]$, $[N_1]$ and $[h\nu]$ are the number densities (or concentrations) of ground-state molecules, excited-state molecules and excitation photons, respectively. According to Equation 2, the rate of excitation of a molecule by 1PA is linearly related to the concentration of photons, $[h\nu]$, in the incident radiation (which can also be expressed as the photon flux, F, divided by the speed of light, $[h\nu]=F/c$). The photon flux is related to the beam intensity (Rumi & Perry 2010), I (power per unit area) by the photon energy, $E= h\nu$:

$$F = \frac{I}{E} = \frac{I}{h\nu}. \tag{3}$$

Thus, the rate equation can also be expressed in terms of the beam intensity, which further emphasizes the linear dependence of the rate of 1PA on the incident light intensity. For two-photon absorption (2PA), the photochemical reaction can be described as follows:

$$N_0 + 2h\nu \rightarrow N_1. \tag{4}$$

The rate law for the absorption of two photons of light by a molecule (Fisher *et al.* 1997a) will then be of the following form:

$$\frac{d[N_1]}{dt} = k[N_0][h\nu]^2. \tag{5}$$

Since this rate is proportional to the square of the photon concentration, 2PA is referred to as a nonlinear process. Equation 5 can be rearranged to give an expression for the rate of two-photon excitation, R_{TPE}. One simply has to define an interaction volume for the absorption with the path length of l multiplied by the cross-sectional area of the laser beam, A; defining a two-photon cross-section $\delta=2k/c^2$; changing from number density to molar concentrations, $C=N_0/N_A$, where N_A is Avogadro's number; converting photon density to laser power, P; and finally dividing by 2, because two photons are absorbed for each excitation.

$$R_{TPE} = \frac{\delta}{2}\frac{l}{A}CP^2 \tag{6}$$

According to Equation 6, R_{TPE} is proportional to the square of the instantaneous power of the laser beam. For a continuous wave laser, average and peak powers are equal to P, and thus the instantaneous power can be expressed as a product of $P_{ave} \times P_{ave}$. For a pulsed laser, it is convenient to express P^2 in terms of $P_{peak} \times P_{ave}$, in which P_{ave} can also be expressed as follows:

$$P_{ave} = P_{peak} \times \tau \times f, \tag{7}$$

where τ is the pulse width of the laser, and f is the pulse repetition frequency. Thus, the rate equation may also be described as follows:

$$R_{TPE} = \frac{\delta}{2}\frac{l}{A} C P_{peak} P_{ave} = \frac{\delta}{2}\frac{l}{A} C \tau f P_{peak}^2. \tag{8}$$

Although this formula is an approximation, it can still be used to illustrate the nature of the two-photon excitation process and the differences between 1PA and 2PA. However, more detailed expressions for describing the nonlinear nature of 2PA can be derived by modelling the energy transfer from the electromagnetic light field to matter as a series development of material polarization in terms of optical susceptibility (Fisher *et al.* 1997b). According to Equation 8, it is obvious that the rate of 2PA depends primarily on the peak power of the laser source, but it also depends on the pulse width and repetition frequency of the laser, the cross-sectional area of the beam, and on the concentration and two-photon absorption cross-section of the absorbing molecule.

Since both a temporal and spatial overlap of two photons at the virtual state are required for 2PA, the probability of a nonlinear absorption process can be improved by increasing the density of photons by spatial compression using objectives with high numerical apertures (Figure 2) and by temporal compression using ultrafast pulse lasers (Spangenberg *et al.* 2013).

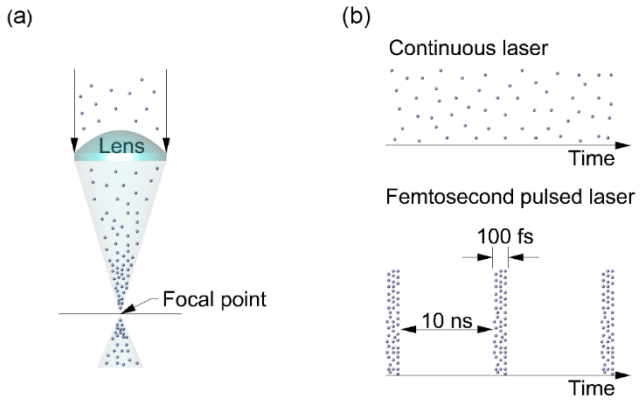

Figure 2. Increasing the probability of the 2PA process by (a) the spatial compression of photons with a high numerical aperture objective lens, which restricts two-photon excitation to the focal spot, and (b) the temporal compression of photons into short packets with ultrafast pulsed laser. Although continuous and pulsed lasers can have the same average

power (mean number of photons per second), titanium-sapphire pulsed lasers are able to concentrate photons into ~100 fs long bursts having greater peak power. Adapted from (Spangenberg et al. 2013).

2.1.3 Photoinitiation and photopolymerization

DLW via photopolymerization triggered by the absorption of two photons is a series of photochemical reactions that has been widely used for the fabrication of variety of nano- and microstructures (Juodkazis *et al.* 2009). Photopolymerization refers to the chain-growth polymerization that employs light to initiate the polymerization reaction that converts small unsaturated molecules in the liquid state to solid macromolecules. In radical photopolymerization, a mixture of photoinitiators and monomers or oligomers is irradiated by ultraviolet, visible, or infrared region light. During the first step, the photoinitiators absorb either one (single photon polymerization) or two (two-photon polymerization) photons and are excited to an intermediate state, after which they decompose into radicals. The photogenerated radicals are reactive species that will further react with monomers and oligomers and produce monomer radicals, which further combine with new monomers in a chain reaction during the chain propagation step, until two radicals meet each other in termination phase. (Sun & Kawata 2004; Park *et al.* 2008; Kim & Lee 2010) In addition to photoinitiator, a light absorbing molecule called a photosensitizer can be added into the reaction mixture to enhance the two-photon activation. The photosensitizer is excited by the simultaneous absorption of two photons and thereupon emits fluorescence light in the UV-visible regime. The fluorescent light is absorbed by photoinitiators, which then generate radicals. (Lee *et al.* 2007)

Most research thus far has been performed with commercially available UV-photoinitiators that have been optimized only for linear absorption. Their two-photon absorption activity, which can be expressed as 2PA cross-section (δ), is generally very low, i.e., $< 10\times10^{-50}$ cm^4 s $photon^{-1}$ $molecule^{-1}$. The units for δ are named Göppert-Mayer (GM), after the Nobel-laureate physicist, and are defined in SI units as 1 GM = 10^{-50} cm^4 s $photon^{-1}$ $molecule^{-1}$. (Zhou *et al.* 2002) Because of low δ, laser power near the damage threshold of the material and long exposure times are required to induce 2PP. The development of two-photon photoinitiators with large 2PA cross-sections has enabled the use of inexpensive continuous wave lasers (Thiel *et al.* 2010) and nanosecond pulsed lasers (Boiko 2008; Wang *et al.* 2010) instead of the more sophisticated femtosecond lasers.

The efficiency of a radical photoinitiator for 2PP-DLW depends not only on the 2PA cross-section, but also on the quantum yield of the radical generation as well as the initiation efficiency of the generated radicals. In addition, the concentration of initiators should be chosen carefully, as too high a concentration of initiators can lead to inefficient energy transfer if the initiator has a high extinction coefficient. Solubility is also an important factor when choosing the ideal initiator for a particular monomer. The initiator should disperse uniformly in the monomer solution before polymerization. (Wu *et al.* 2006; LaFratta *et al.* 2007) Generally, the maximum absorption wavelength of the utilized photoinitiator should be around half the wavelength of the fabrication laser beam. In other words, initiators designed to work at UV or visible wavelengths, ca. λ, can be used for polymerization under 2λ irradiation. (Wu *et al.* 2006)

Utilization of a two-photon initiator can lower the polymerization threshold, i.e., the laser intensity below which the fabrication is not possible. Thus, the fabrication window becomes broader and the possibility of damaging the structure due to high laser intensity and long exposure time is reduced. (Wu *et al.* 2006; Fischer *et al.* 2013) The development of highly active organic two-photon photoinitiators has already extended 2PA cross-section values from ~10 GM to the order of ~10^4 GM (Lee *et al.* 2006). However, although significant progress has been achieved in the area of engineering efficient initiators, a detailed understanding of the relationship between the molecular structure and two-photon properties of such molecules still remain to be explored.

2.1.4 Experimental setup for 2PP-DLW

The most typical laser source utilized for 2PP-DLW is a titanium:sapphire laser operating at an approximately 800 nm wavelength and capable of emitting femtosecond pulses with an 80 MHz repetition rate (Raimondi *et al.* 2012). Recently, low cost picosecond microlasers, such as Nd:YAG emitting at 532 nm, have also been shown to be applicable for launching 2PA in synthetic and protein-based materials (Wang *et al.* 2002; Kaehr *et al.* 2006; Jariwala *et al.* 2010; Malinauskas *et al.* 2011; Käpylä *et al.* 2011). Generally, the repetition rate of the laser used for 2PP-DLW can vary between 1 kHz to 80 MHz, the average laser power from 200 mW to 6 W, the pulse length between 20 fs to 10 ps, and the wavelength from 515 nm to 1030 nm (Malinauskas *et al.* 2013). An example of a typical fabrication setup used for 2PP-DLW is illustrated in Figure 3. A half-wave plate and a polarizer are positioned right after the laser source and used for the attenuation of the laser power to the suitable polymerization power level. The beam is expanded with a telescopic lens to match or overfill the back aperture of an oil immersion objective lens. The position of the focus inside the photopolymerizable material is adjusted with a piezoelectric stage along the z-direction. The planar direction (x, y) of the beam is controlled with a set of Galvano-mirrors. The laser beam is closely focused into a volume of photocurable material with an objective lens that has a high numerical aperture. A fast mechanical shutter is employed to control the exposure of the sample. A highly sensitive CCD camera is mounted behind a dichroic mirror to provide online process monitoring. Since the refractive index of the photoresist changes upon polymerization, the polymerized patterns become visible and any failures in the process can be detected and corrected in real time. However, any fine details of the 3D microstructures cannot be observed, hence a careful investigation of the structures has to be performed by scanning electron microscopy to check the geometry and surface roughness of the objects. (Ovsianikov & Chichkov 2008; Kim & Lee 2010)

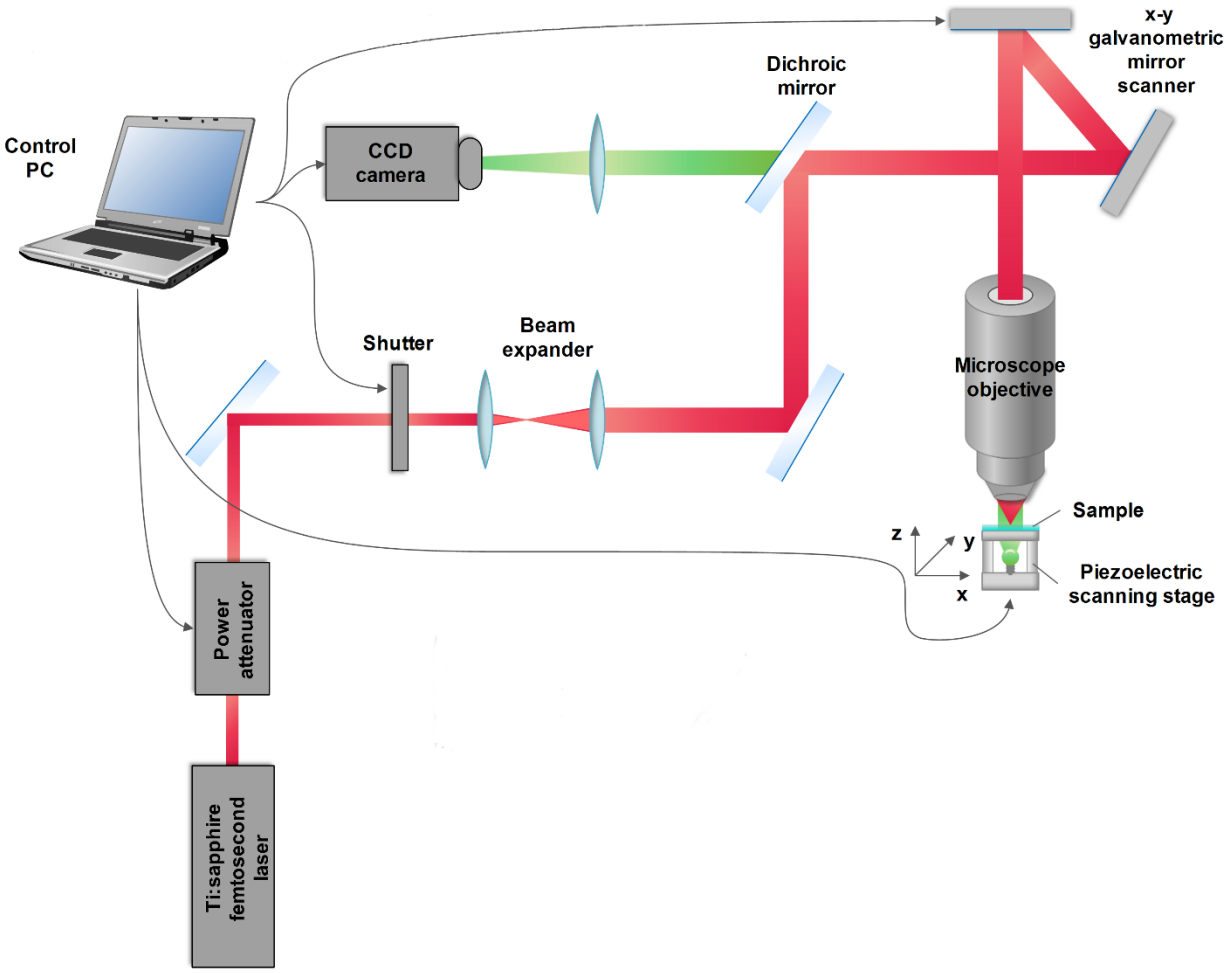

Figure 3. A schematic diagram of the fabrication setup for 2PP-DLW.

The material is polymerized along the trace of the moving laser focus during the laser scanning step, which converts the predesigned CAD pattern into a solidified structure. The designed CAD model is sliced into planes with a constant or varying slice thickness to create scanning paths in the xy-plane. Another layer is fabricated and incorporated to the previous solidified layers after translating the laser focus along the z-axis using the piezoelectric stage. The entire 3D structure is fabricated by repeating these stages. (Lee *et al.* 2006) Two different approaches for direct laser scanning can be used, i.e., raster scanning or contour scanning (also known as surface profile scanning). In the raster scanning method, the entire volume of the structure is scanned, but in the contour scanning approach only the contour profile of the structure is solidified. The contour scanning method requires less processing time and thus increases the fabrication efficiency. (Kawata *et al.* 2001; Tanaka *et al.* 2002)

Depending on the phase of the photopolymerizable material, two different sample configurations are used: liquids are sandwiched between two coverslips separated by a spacer enabling sample uniformity; solid materials can be simply placed on a coverslip and processed upside down (Raimondi *et al.* 2012). With this bottom up approach, distortion of the focused laser beam by the already fabricated parts of the structures can be avoided. In contrast to the sandwich format where the first

fabricated layer is attached to the bottom glass slide, in the bottom up approach it is the last layer of the structure that is attached to the glass coverslip. (Farsari *et al.* 2010) Immersion oil is used between the objective lens and the coverslip to reduce the refractive index difference. In a subsequent development phase, the freestanding structures are isolated by removing the unpolymerized resin with organic solvents. (Kim & Lee 2010)

2.1.5 Advantages and challenges of 2PP-DLW

Direct laser writing by 2PP is distinguished from other currently available micro- and nanofabrication technologies such as conventional UV photolithography or stereolithography because it has an intrinsic ability to produce 3D structures. For example, in single-photon polymerization (1PP) with UV light, the light is absorbed by the photosensitive material within the first few micrometers (Figure 4(a)). This restricts the process to the surface of the resin, and thus 3D structures can only be fabricated by working 2.5-dimensionally, i.e., by using a layer-by-layer approach. Moreover, this also limits the resolution along the z-axis to the range of several micrometers as the minimum achievable feature size is mainly determined by the layer thickness, which in turn depends on the viscosity and surface tension of the resin. In the 2PP-DLW process, however, the polymerization can be initialized anywhere in the volume of the resin, which needs to be transparent in the range of the utilized laser wavelength. Any desired 3D pattern can thus be recorded into the volume of the photosensitive material (Figure 4(b)). (Serbin *et al.* 2003; Wu *et al.* 2006; Narayan *et al.* 2010)

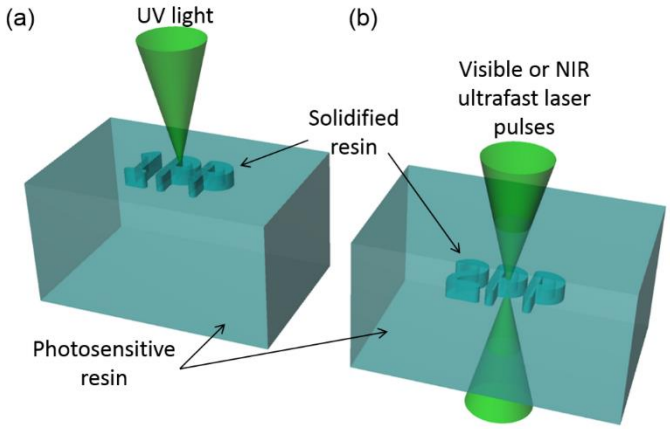

Figure 4. Processing of photosensitive material by (a) single-photon absorption with UV light, which is absorbed at the surface of the material; (b) two-photon absorption with visible or near-infrared pulsed laser, which can be used for true 3D structuring when focused into the volume of UV-sensitive resin.

High-resolution 1PP fabrication has to be performed in an inert gas atmosphere as contact with oxygen quenches the radicalized initiator molecules at the surface of the photosensitive material and hence only the first layer of the photoresist is polymerized. In contrast with 1PP fabrication, a 2PP-DLW setup does not need to be operated in an expensive and energy consuming high-vacuum environment as the fabrication is done in the volume of the resin instead of on the surface. (Sun & Kawata 2004; Wu *et al.* 2006) The 2PP-DLW technique is a particularly appealing production method for medical devices because it does not utilize harsh chemicals or extreme temperatures (Gittard *et*

al. 2011b). As a 2PP-DLW fabrication setup does not require any cleanroom facilities, it can be situated in a conventional clinical environment, such as an operating theater, which greatly reduces costs and allows medical devices to be produced on demand in-house (Ovsianikov *et al.* 2007a). Microfabrication by 2PP-DLW also offers the unique possibility to achieve feature sizes well beyond the diffraction limit of the laser light by employing laser intensities just above the polymerization threshold (Wu *et al.* 2006). The most appealing property of 2PP-DLW is its ability to fabricate complex 3D devices with moving parts and overhangs without using additional supporting structures (Kaehr & Shear 2008; Wu *et al.* 2009; Schizas *et al.* 2010; Ikegami *et al.* 2012; Spivey *et al.* 2013).

Because 2PP-DLW is a CAD-based fabrication method, no masks, molds or stamps are utilized during the process. This also enables the rapid modification and iteration of the designs. (Sun & Kawata 2004) Two-photon polymerization is compatible with various commercially available photosensitive materials, such as acrylate-based polymers, organically modified ceramic materials, and zirconium sol-gels (Narayan *et al.* 2010). From an economic and environmental perspective, it is also beneficial that with 2PP-DLW the fabrication of 3D structures requires only a minimal amount of photosensitive material and produces little waist (Juodkazis *et al.* 2009).

Unfortunately, a major drawback exists that prevents 2PP-DLW technology from spreading from laboratory settings to a wider industrial level: as a serial process by nature, 2PP-DLW is capable of producing only one sample at a time. In addition, the single beam scanning lowers fabrication efficiency and increases costs (Zhang *et al.* 2010). However, there has been some research towards parallel processing by utilizing microlens arrays for multibeam fabrication (Kato *et al.* 2005), which together with commercial highly efficient photoinitiators and resins could ultimately offer a solution to the issue of low fabrication rate. From the material research perspective, a major challenge delaying the development of 2PP-DLW as a universal microfabrication tool is the lack of commercial photoinitiators with high 2PA cross-sections. The advent of such initiators would further boost the use of inexpensive microlasers instead of ultrafast Ti:sapphire systems. (LaFratta *et al.* 2007)

Another essential drawback of the 2PP-DLW technique is the shrinkage of the polymerized structures during the development stage. The shrinkage of the fabricated structure is a common problem related to the processing of negative tone photosensitive materials. If the structuring is performed slightly above the 2PP threshold intensity, the polymerization yield is not 100%. Hence, after the removal of the unpolymerized material, a sponge-like material is left behind. The collapse of this material at the molecular level leads to distortions and deviations from the original CAD model. (Ovsianikov *et al.* 2007d; Ovsianikov *et al.* 2009) As the ratio of the cross-linked material to non-cross-linked material in the sample depends on the exposure dose, less shrinkage is observed when using higher average laser power (Sun *et al.* 2010a). The shrinkage of the structure is anisotropic because the bottom part of the structure is tethered to the substrate and thus cannot shrink, while the top part has more freedom to shrink. At a certain distance from the substrate, the shrinkage reaches a saturation point and the subsequent layers shrink identically. (Ovsianikov *et al.* 2007d) Due to the anisotropic shrinkage, cubical structures typically take the form of trapezoidal (Li *et al.* 2008). To solve this problem, several approaches, such as numerical pre-compensation of the CAD model for deformation (Sun *et al.* 2004;

Ovsianikov *et al.* 2007d) and single (Maruo *et al.* 2009a) or multi-anchor (Ovsianikov *et al.* 2009) supporting methods to eliminate the non-uniform shrinkage caused by attachment to the substrate, have been successfully tested.

In addition, it has been shown that due to the capillary pressure difference sustained across the interface between the rinse material and air during the drying stage, the fabricated structures are prone to distortion and collapse (Sun *et al.* 2012). The receding level of the rinse material produces a concave meniscus between the fabricated walls and thus generates a pulling force on the walls, which causes a bowing of the walls (Tanaka *et al.* 1993). The pressure difference is generated by the evaporation of the rinse material (Namatsu *et al.* 1995). The driving force for the collapse can be described by Young-Laplace equation:

$$\Delta P = 2\sigma \cos\theta \left(\frac{1}{a} + \frac{1}{b}\right), \tag{9}$$

where σ is the surface tension of the rinse material. The radii of the curvature of the meniscus have been substituted with distance between structure walls (a and b) and a contact angle (θ) between the rinse liquid and the solidified microstructure. Thus, the effect of the collapse force can be reduced by using a rinse liquid with a low surface tension. However, the overall success of the fabrication also depends on the dimensions and design of the microstructure as a greater number of voids and higher aspect ratios tend to lead to more severe pattern collapse. (Kondo *et al.* 2005; Park *et al.* 2008) The strength of the patterns against deformation can be enhanced by utilizing the multipath scanning method in which multiple contours are scanned with an appropriate offsetting. The method enables the fabrication of reinforced 3D microstructures without loss of precision as only the wall thickness becomes thicker without increasing the voxel height. (Yang *et al.* 2007)

2.2 Resolution

Linewidth and resolution on the scale of few tens of nanometers and even below would be very advantageous in several applications in nanotechnology; after all, the shaping of matter from the atomic scale to the macroscopic scale in three dimensions is the ultimate dream of nanoscience. The biggest challenge in 2PP-DLW is not to achieve subdiffraction-sized features, but to create subdiffraction-sized gaps between features. For example, if an attempt is made to polymerize two features at a subdiffraction distance from each other, the polymerization threshold is also exceeded in the interstice between the features due to the diffraction-limited widths of the illumination intensity profiles. (Sakellari *et al.* 2012) Indeed, it is important not to confuse the dimensions of isolated structures (i.e., linewidth) with the term resolution, which is defined by the minimal spacing between two adjacent yet separated structures and can only be determined by creating a grating within a certain period (Wollhofen *et al.* 2013). Thus far, the smallest reported linewidths for structures fabricated with 2PP-DLW have been 90 nm (Burmeister *et al.* 2012), 80 nm (Xing *et al.* 2007; Paz *et al.* 2012), and 65 nm (Haske *et al.* 2007) when using wavelengths of 1030, 800, and 520 nm. However, the

smallest axial resolution achieved so far with regular 2PP-DLW is 510 nm, which is still higher than the axial diffraction-limit of 506 nm (Fischer & Wegener 2011).

2.2.1 Focusing Gaussian laser beams

In general, the beam emitted from a single-mode (TEM_{00}) laser can be assumed to have an ideal Gaussian intensity profile. However, as the beam is focused using lenses, the Gaussian shape is truncated at some diameter by the aperture of the objective lens. Beams that are smaller than the pupil diameter of the lens form a spot with a Gaussian shape. As the intensity profile of a Gaussian beam never falls to zero, the diameter of the focal spot is commonly defined either at the 50% intensity level or at the $1/e^2$ (13.5%) intensity level (Figure 5(b)). If the beam is larger than the pupil diameter, the truncation plays an important role and the spot's shape approaches that of the classic Airy disc. It is the circular bright core in the middle of the Airy diffraction pattern with alternating bright and dark zones. In the case of the Airy disc, the intensity falls to zero at the point $d_{zero}=1.22\lambda/NA$, defining the diameter of the focal spot (Figure 5(a)). (Byatt 2003)

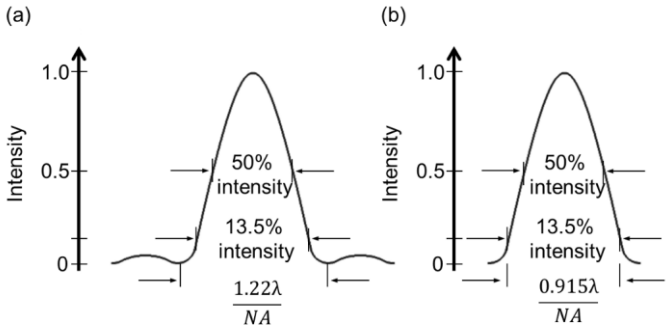

Figure 5. (a) Airy disc intensity profile and (b) Gaussian intensity profile at the focal spot. Adapted from (Byatt 2003).

2.2.2 Polymerization threshold

An important aspect in many applications of 2PP-DLW is the size and shape of the voxels (volumetric pixels), which are the basic unit structures or building blocks polymerized in the focal spot of the laser. Voxels are generally considered to take the form of a spinning ellipsoid with the two minor axes perpendicular to the optical axis and being about 3 to 5 times smaller than the major axis. (Sun *et al.* 2002; LaFratta *et al.* 2007) The ellipsoidal contour of the voxels is a consequence of the nature of diffraction and thus cannot be pronouncedly modified by adjusting the optics of the polymerization setup (Sun *et al.* 2002).

During the initial exposure, voxels take the shape of the focal spot. This process is called focal spot duplication. The formed voxel comprises a highly polymerized solid phase with high-weight polymers surrounded by a more liquid-like phase with a lower degree of polymerization comprising monomers, radicals, and oligomers. As the exposure time is prolonged, the voxel continues to grow as the radicals diffuse either towards or away from the focal spot, depending on their location. This radical diffusion-dominated process is called the voxel growth. (Sun *et al.* 2003b)

The ability to fabricate structures with subdiffraction-limited size using 2PP-DLW results from the existence of an intensity threshold for the photochemical processes. For all photosensitive materials, this threshold or a level of light intensity exists, below which no polymerization occurs. Only when the light is concentrated at the focal point is the threshold light intensity exceeded, and a minimum density of radicals is formed at the focal spot. Then the resin can undergo a phase transformation from liquid to solid resulting in the formation of structures with enough structural integrity to survive the developing step. (Tanaka *et al.* 2002; Ovsianikov *et al.* 2007d)

As long as the photoresist exhibits a threshold behavior, the diffraction limit becomes just a measure of focal spot size, but does not actually restrain the voxel sizes. In the case where the photoresist has no memory for previous sub-threshold exposures (i.e., the resist regions are able to regenerate due to diffusion), lines could be polymerized directly next to the previous ones and the center-to-center distance would only be limited by the linewidth. However, as long as the photoresist remembers previous below-threshold exposures, the lateral and axial resolutions are still limited by Abbe's diffraction law. (Fischer & Wegener 2011; Fischer & Wegener 2013) Ernst Abbe found that in optical microscopy the lateral resolution is as follows:

$$d_{lateral} = \frac{\lambda}{2NA}, \tag{10}$$

where λ is the laser wavelength and *NA* is the numerical aperture of the objective (Abbe 1873). Thus, two simultaneously emitting point sources separated by a smaller distance than $d_{lateral}$ cannot be distinguished. The two-photon modified Abbe formula states that the smallest possible lateral center-to-center distance ($d_{lateral}$) is the following:

$$d_{lateral} = \frac{\lambda}{2\sqrt{2}NA}. \tag{11}$$

This two-photon-modified Abbe criterion corresponds well with the Sparrow criterion, which states that two slightly separated spectral line pairs broadened by diffraction are resolvable if the sum of the intensity profiles has a local minimum (Figure 6) (Sparrow 1916). The axial minimum distances in 2PP-DLW are at least 2.5 times larger than the lateral ones, thus a further modified Abbe formula has been suggested to approximate the axial resolution (d_{axial}):

$$d_{axial} = \frac{\lambda A}{2\sqrt{2}NA}, \tag{12}$$

where $A = 2.5$ is the aspect ratio of the exposure volume for an objective lens with $NA = 1.4$ and a photoresist with a refractive index around 1.5 (Fischer & Wegener 2011).

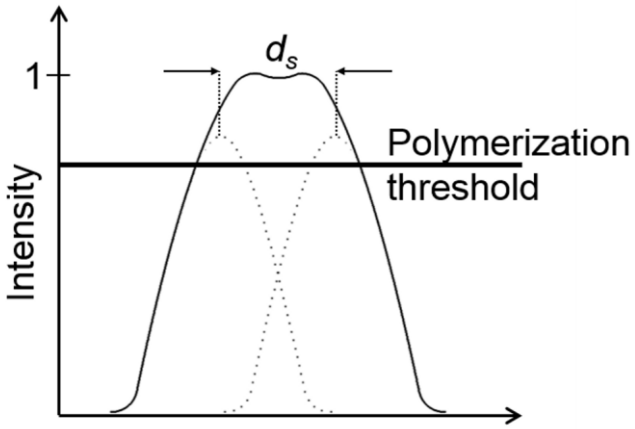

Figure 6. Schematic representation of lateral resolution (d_s) of 2PP-DLW according to Sparrow criterion. The dashed line plots represent the exposure profile of the single exposures and the solid line plot shows the sum of the intensity profiles with a local minimum. The horizontal line denotes the polymerization threshold intensity, above which the monomer is solidified sufficiently to withstand development. Adapted from (Wollhofen et al. 2013; Fischer & Wegener 2013).

The voxel dimensions can be tuned by controlling the irradiation time and the radiation intensity. However, the polymerization threshold and the laser-induced breakdown threshold define the tuning range or the process window. The polymerization threshold is determined by the quantum yield of the photoinitiator, i.e., the ratio between the number of initiating species produced and the number of photons absorbed. In addition, no attempt is made in 2PP-DLW to eliminate molecular oxygen from the photoresist, and thus this greatly contributes to the formation of an intensity threshold. Besides, quenching the triplet state of the photoinitiator, oxygen interacts with propagating radicals producing much fewer active peroxyl radicals. (Sun & Kawata 2004) If the laser intensity is carefully controlled, the polymerization threshold can be exceeded in only a small fraction of the focal volume. For example, a laser beam with a 400 nm diffraction limited focal spot can exceed the threshold in a region as small as 100 nm in width at the center of the spot. (LaFratta *et al.* 2007) At the threshold intensity, the theoretical size of the voxel should be infinitely small, but in practice the minimum voxel size is always limited by the power fluctuations of the laser, the limited pointing stability of the laser, and the positioning system performance (Serbin *et al.* 2003).

If the laser irradiation exceeds a particular value, damage is induced in the material. This laser-induced breakdown is dominated by a thermal process for laser pulse lengths longer than 10 ps and by plasma generation for pulse lengths below 1 ps. The breakdown causes ablation at the sample surface and micro-explosions or microbubbles inside the bulk, both which lead to the vaporization and atomization of the material. The breakdown-induced material bubbling damages existing structures and prevents further polymerization reaction from taking place. (Sun & Kawata 2004)

2.2.3 Truncation effect

In order to accurately obtain and measure isolated, complete voxels, the truncation effect caused by the partial submerge of the laser focal spot in the substrate has to be taken into account. For voxels to

withstand the development phase without being flushed away, they must be in contact with the substrate. However, in that case only a partial voxel is formed. In fact, if more than half of the focal spot is below the substrate, the observed voxel is only the tip of the iceberg. (LaFratta *et al.* 2007)

To solve the problem of the accurate representation of voxels, an ascending scan method has been developed (Figure 7). In this method, a series of voxels are polymerized under the same irradiation conditions by increasing the height of the focal spot after every voxel. In this way, identical voxels can be generated ranging from submerged to suspended ones. Somewhere between, loosely bound voxels are formed, which will therefore topple over during washing but remain tethered to the substrate. The width and height of these individuals represent the true lateral and longitudinal feature size. (Sun *et al.* 2002)

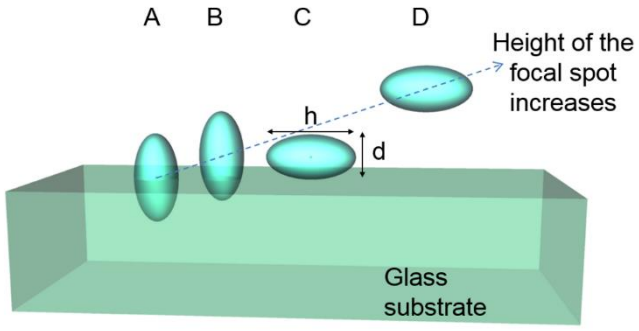

Figure 7. In the ascending scan method, the focal spot is translated to a new position and elevated slightly for the fabrication of each subsequent voxel. In the case of A and B voxels, the laser focus has been partially submerged inside the glass substrate, and thus the formed voxels only reveal their lateral size. In the case of D, the focal spot height is too far from the glass, and the voxel floats away during the development phase. The voxel C is ideal for height and diameter measurements, as it was only weakly attached to the substrate surface and has toppled over during development.

2.2.4 Role of different parameters on resolution

The ultimate dimensions of voxels depend on fabrication conditions and system parameters, such as laser power, exposure time, the truncation amount of a voxel, the numerical aperture (N.A.) of the objective lens, and the sensitivity of the photoinitiator (Lee *et al.* 2007). The effect of different parameters on resolution can be described by a schematic of interaction volumes influencing the achievable voxel sizes (Figure 8). The technical interaction volume (red) is mainly determined by the employed optics, the stability of the laser, and the accuracy of the positioning system. Thus, it can be optimized by utilizing specially adapted optics (Fuchs *et al.* 2006), stabilizing the laser source, and by using very accurate positioning stages. The chemical interaction volume (green) depends on several factors, such as the reaction kinetics of the photosensitive material, which in turn depends on the diffusion of initiators and oxygen molecules in the liquid resin and the process efficiency of the photosensitive material and the photoinitiator. The third interaction volume is determined by the threshold behavior of the reaction (blue) (Tanaka *et al.* 2002). In addition to the laser dose, which is determined by a combination of laser power and exposure time, the threshold behavior also depends on the minimum initiator concentration necessary to start the chemical reaction. However, the lowest

density of radicals required for polymerization can only be roughly estimated, and thus the effect of initiator threshold on resolution is not as well defined as the role of laser parameters. (Houbertz *et al.* 2010)

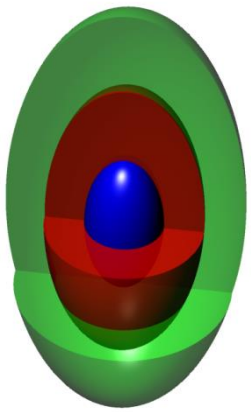

Figure 8. Graphical illustration of different interaction volumes and their influence on the achievable voxel sizes with 2PP-DLW: green represents the chemical interaction volume, red represents the technical volume, and blue illustrates the effect of threshold behavior. Adapted from (Houbertz et al. 2010).

Theoretically, the voxel dimensions are still predominantly determined by the laser dose, i.e., by the combination of laser power and exposure time (Lee *et al.* 2007). Voxel length is more sensitive to laser power than to exposure time, and thus by polymerizing with near-threshold power it is possible to achieve smaller, nearly spherical voxels (Sun *et al.* 2003b). The numerical aperture of the objective lens is also one of the most important parameters influencing the achievable aspect ratio. Hence, in order to achieve high fabrication resolution, high-N.A. objectives are essential. (Sun *et al.* 2003a) In high-N.A. objectives, the convergence angle of the beam is larger, and energy is thus more concentrated in the center of the focal spot, which causes polymerization at smaller volume (Sun & Kawata 2004). The aspect ratio of the voxels, i.e., the ratio of the lateral and longitudinal dimensions, can be varied from 1:3 (for N.A. = 1.4) to 1:50 (for N.A. = 0.1) by merely changing the objective lens (Malinauskas *et al.* 2010c; Danilevičius *et al.* 2013). However, high-N.A. objective lenses usually also have short working distances, i.e., the distance between the focal plane and the surface of the objective. This limits the ability to fabricate 3D microstructures deep inside the material volume. Thus, there always exists a trade-off between the achievable fabrication resolution and the working distance for each application. (Koji & Ya 2012)

2.3 Materials for 2PP-DLW

The material formulations for 2PP-DLW are composed of a prepolymer (monomer) resin and a photoinitiator. The photoinitiator is a photosensitive molecule that absorbs the laser light and generates an active species (radical or ion), which initiates the polymerization of the monomers. Monomers are the polymerizable material that will form the polymeric structure backbone. The monomer is chosen according to the final application whereas the photoinitiator is chosen to match the irradiation wavelength and the nature of the monomer. (Spangenberg *et al.* 2013; Malinauskas *et*

al. 2013) The essential requirement for the both the photoinitiator and the monomer is that they need to be transparent at the employed laser wavelength to allow the laser beam transmission and focusing inside the material volume. To avoid thermal damage, the monomer should also be transparent at the 2PA wavelength ($\lambda/2$). An ideal photoinitiator should be easily synthesized, low-priced, non-toxic, have a high thermal stability and stability in darkness, have a good solubility in the monomer, and of course have a high two-photon cross-section and a high quantum yield in the generation of active moieties. (Lee *et al.* 2008; Malinauskas *et al.* 2013) The monomer should have a suitable viscosity to keep the early-polymerized structures in place, but at the same time to allow the removal of unsolidified resin from intervals. In addition, the monomer should have a high polymerization efficiency, low post-polymerization shrinkage, and post-irradiation dark polymerization (Sun & Kawata 2004)

There exists two classes of photosensitive materials that can be polymerized via 2PP-DLW: negative-tone and positive-tone photoresists (Ovsianikov *et al.* 2007d). In negative-tone photoresists, laser exposure results in the crosslinking of polymer chains by changing the exposed volume insoluble in the development solvent. Thus, the structure is written directly inside the photosensitive material. In positive-tone materials, on the contrary, 2PA introduces breakage of the polymer chains, which in turn become soluble to the development solvent. In positive-tone photoresists, the reverse structure is written inside the material. (Farsari & Chichkov 2009)

Two-photon polymerization is compatible with several materials originally developed for single-photon stereolithography decades before the advent of tabletop femtosecond lasers. The first and one of the most common negative-tone material classes used for two-photon polymerization is acrylate photopolymers (Maruo *et al.* 1997). The wide variety of commercially available acrylate monomers and their transparency to visible and near-IR wavelengths makes them an attractive choice for 2PP-DLW. In addition, acrylates can be polymerized rapidly with low shrinkage and developed with non-aggressive solvents, such as isopropanol. (Malinauskas *et al.* 2013) The suitability of the epoxy-based negative-tone photoresist SU-8 for 2PP-DLW was first demonstrated by Witzgall *et al.* as they fabricated 3D cylindrical structures with a series of single laser shots (Witzgall *et al.* 1998). Since then, SU-8 has been employed for the fabrication of photonic (Deubel *et al.* 2004; Mizeikis *et al.* 2004) and microfluidic (Stoneman *et al.* 2009; Kumi *et al.* 2010) structures by several research teams. However, SU-8 requires the use of spin coating and post-baking steps, which adds complexity to the whole fabrication procedure (Raimondi *et al.* 2012).

Recently, silicate-based hybrid composite materials have been adapted to 2PP-DLW by utilizing suitable photoinitiators. The most widely used silicate material is the photopolymer ORMOCER® that has been used to fabricate a variety of photonic (Ovsianikov *et al.* 2008a; Grossmann *et al.* 2011) and medical devices such as microneedles (Ovsianikov *et al.* 2007b) and tissue engineering scaffolds (Weiß *et al.* 2009). ORMOCER®s combine the properties of organic polymers (low-temperature processing and functionality) with those of inorganic glasses (hardness, thermal and chemical stability, and optical transparency) (Raimondi *et al.* 2012). As ORMOCER®s, however, do not allow fine tuning of the material's properties, another group of hybrid sol-gel materials has been developed

in collaboration with Laser Zentrum Hannover and the Foundation for Research and Technology Hellas (FORTH). These materials include highly transparent, biocompatible non-shrinkable photoresists, and materials with tailored activity for the fabrication of nonlinear photonic devices (Farsari & Chichkov 2009).

Although these biocompatible hybrid materials have been successfully used as inert medical devices and topological cell matrixes, their lack of biodegradability has led to the development of photocurable oligomers based on bioresorbable polymers such as polylactide (PLA) (Melissinaki *et al.* 2011) and polycaprolactone (PCL) (Claeyssens *et al.* 2009). These biodegradable materials have been successfully formed into scaffold-like structures (Claeyssens *et al.* 2009) and cell delivery vehicles (Melissinaki *et al.* 2011). The biocompatibility and nonfouling properties of polyethylene glycol diacrylate (PEGda) has made it an appealing material for tissue engineering scaffolds and microneedles for transdermal drug delivery fabricated by means of 2PP-DLW (Gittard *et al.* 2010; Ovsianikov *et al.* 2011). The ability to crosslink natural, bioactive, macromolecules such as native proteins has also been demonstrated. Proteins, such as bovine serum albumin (BSA) (Pins *et al.* 2006), avidin (Kaehr *et al.* 2004), and laminin (Chen *et al.* 2009; Su *et al.* 2012), have been crosslinked into 2D and 3D structures and used for cell guidance purposes.

2.3.1 ORMOCER®s

Organically modified ceramics (ORMOCER®s) are inorganic-organic hybrid materials developed by Fraunhofer Gesellschaft zur Förderung der Angewandten Forschung e.V., Germany (Haas 2000). The material was first called organically modified silicate (ORMOSIL) since silicon was always present in the material (Schmidt 1985). However, the name was later changed to ORMOCER® to emphasize its ceramic nature (Aura *et al.* 2008). ORMOCER®s are molecular composite materials that cannot be prepared by conventional composite processing, such as via the physical mixing of components. As molecular composites, ORMOCER®s combine the properties of organic polymers (functionalization, processing at low temperatures, toughness) with the properties of glass-like materials (hardness, chemical and thermal stability, transparency) that are not otherwise accessible by mixtures of macroscopic phases, such as glass-fiber reinforced polymers. (Haas & Wolter 1999; Haas 2000) ORMOCER®s belong to the so-called class II hybrid materials, where the inorganic and organic components are covalently bonded to each other (Sanchez *et al.* 1999).

In order to combine different components on a molecular scale, homogenous systems, such as miscible liquids, have to be utilized. Due to the low thermal stability of polymers, they cannot usually be mixed with glass melts. Instead, low thermal processing based on sol-gel type reactions is used. (Haas 2000) The sol-gel reactions start by mixing the metal alkoxysilanes with water. The catalytic hydrolysis and condensation of the sol-gel precursor results in the formation of a porous interconnected cluster structure (Figure 9). (Farsari *et al.* 2010)

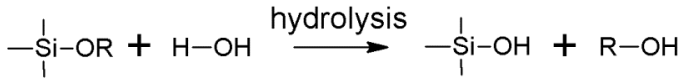

Figure 9. Hydrolysis reaction of the sol-gel precursors.

In the second step, the solvent is removed and the gel is formed by heating at low temperature (Figure 10).

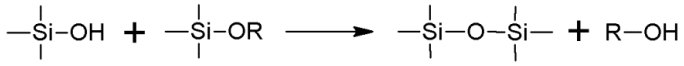

Figure 10. Gelation reaction to form a macromolecular hybrid network structure.

Next, either UV or thermal initiators are added to the resulting resin, and the organic crosslinking is initiated either photochemically or thermally, which leads to the formation of an inorganic-organic network (Houbertz *et al.* 2010). Instead of simple alkoxides (SiO_2, ZrO, TiO_2), the precursors of ORMOCER® materials are organically modified silicon alkoxides. They are composed of four functional parts: -Si-O- groups to form the inorganic network, spacer/connecting groups, organic polymerizable units, and non-reactive groups for modifying the material properties, such as acryl groups to increase the refractive index or alkyl groups to lower the refractive index (Obi 2006). The organic polymerizable groups are chosen with respect to the final curing method. For UV or laser patterning, methacrylate, acrylate, or styryl moieties are favored. Epoxy groups are preferred for thermal curing at 120 °C to 200 °C. (Haas & Wolter 1999; Houbertz *et al.* 2010)

A commercially available ORMOCER® material with the trade name Ormocomp® (also known as US-S4) was chosen as photopolymerizable material for our studies with the 2PP-DLW system. The commercial supplier of Ormocomp® is Micro Resist Technology GmbH, Germany. The detailed chemical structure and composition of the material is a proprietary trade secret, but according to the manufacturer, the resin contains 20% to 35% of trimethylolpropane triacrylate as a trifunctional organic polymerizable unit (Figure 11). The material is sold as a highly viscous transparent resin containing 1% of Darocur® TPO (2,4,6-trimethylbenzoyldiphenyl phosphine oxide) by Ciba Specialty Chemicals (Switzerland) as photoinitiator. Ormocomp® was originally designed for use as material for the fabrication of various optical components (Obi 2006).

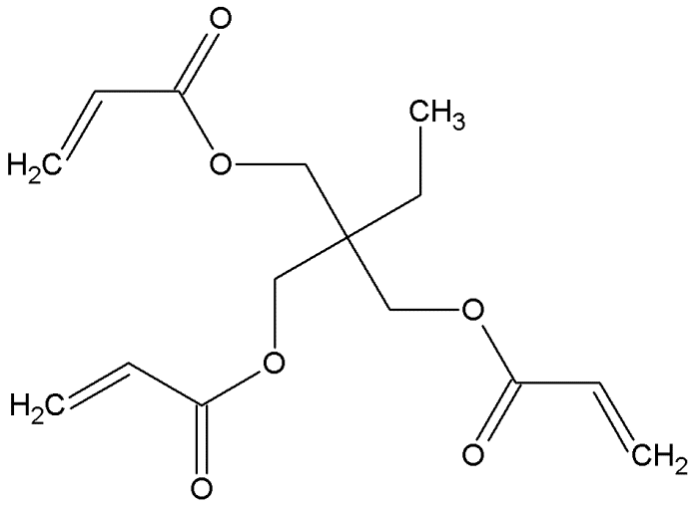

Figure 11. Chemical structure of trimethylolpropane triacrylate.

Due to the three-dimensional network of organic and inorganic components, ORMOCER®s exhibit no detectable phase separation and are thus materials with exceptional chemical and thermal stability (Doraiswamy *et al.* 2006). Their thermal stability is limited by the organic parts of the network. For most ORMOCER®s, the temperatures for permanent service are below 200 °C. However, by attaching a phenyl or cyclophosphazane unit to the inorganic network thermal stability even above 400 °C can be achieved. (Haas 2000) ORMOCER® materials are colorless materials showing no absorption in the visible spectrum. Their refractive index especially depends on the heteroatoms (Ti, Zr) used in the composition and can be varied from 1.42 up to 1.65. (Haas & Wolter 1999; Haas 2000)

Several materials prepared by sol-gel processing exhibit high volume shrinkage (> 50%) during solvent removal, curing, and network densifying. This shrinkage can lead to significant cracks, mechanical stresses, and reduced mechanical stability. Due to the preformation of the inorganic Si-O-Si network before the actual crosslinking of the organic parts, ORMOCER® materials shrink much less. For example, in acrylate alkoxysilane-based ORMOCER®, shrinkage upon polymerization is reduced into 2–8 v.-% as compared with the pure organic polymerized acrylates, which usually shrink more than 20 v.-%. (Haas & Wolter 1999) The inorganic parts of ORMOCER®s are responsible for their high stiffness and hardness compared with organic polymers. The Young's modulus can vary between 70 MPa and 4 GPa. (Haas 2000)

ORMOCER®s have also received significant interest from the medical device community as they have been shown to be nontoxic and biologically inert in several biological studies, including the ISO 10933-5 cytotoxicity assay (Al-Hiyasat *et al.* 2005). For example, Ormocomp® containing 1.8% of photoinitiator Irgacure 369 (Ciba Specialty Chemicals, Switzerland) has been proven as biocompatible material with CHO cells, GFSHR-17 granulosa cells, GM-7373 endothelial cells, and SH-SY5Y neuroblastoma cells. The cells were counted after a different period of cultivation, and their proliferation rates were statistically compared with the cells cultivated on control samples. In addition, the DNA strand breaks were analyzed with a comet assay. The performed tests demonstrated that Ormocomp® did not affect the cell growth rate or cause DNA damage. (Schlie *et al.* 2007)

2.3.2 Poly(ethylene glycol) diacrylate

Poly(ethylene glycol) (PEG) is a highly hydrophilic and biocompatible material used in several tissue engineering applications and medical devices (Figure 12) (Nguyen & West 2002). Chains with molecular weight over 10 000 g/mol are usually known as poly(ethylene oxide) (PEO) due to the negligible number of end groups (Slaughter *et al.* 2009). PEG is intrinsically resistant to protein adsorption and cell adhesion due to the lack of protein binding sites on the polymer chain (West & Hubbell 1995; Slaughter *et al.* 2009). PEG chains can be modified with either acrylate or methacrylate moieties to form photopolymerizable PEG precursors. In the presence of photoinitiators and upon exposure to UV light, these macromers undergo rapid polymerization into hydrogels. The free radicals of photoinitiators attack carbon-carbon double bonds of the acrylate groups initiating the formation of a hydrogel network. (Nguyen *et al.* 2012) When exposed to aqueous solvent, the hydrogel swells until it reaches equilibrium with its surroundings. At this equilibrium, the two opposing forces, the thermodynamic force of mixing of the fluid molecules with the polymer chains and the retractive force of the polymer chains, are equal. (Peppas *et al.* 2000)

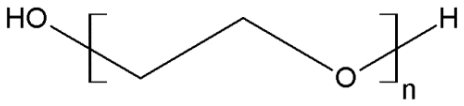

Figure 12. Chemical structure of poly(ethylene glycol)(PEG).

The size of the poly(ethylene glycol) diacrylate (PEGda) macromers generally used varies from 500 g/mol (Lanasa *et al.* 2011) to 10 000 g/mol (Temenoff *et al.* 2002) (Figure 13). The structure and swelling properties of PEGda hydrogels depend on the molecular weight and concentration of the precursors (Temenoff *et al.* 2002; Bryant & Anseth 2002; Hou *et al.* 2010; Lanasa *et al.* 2011). Mesh size, the average distance between adjacent crosslinks, increases with molecular weight, for example, from 7.6 nm to 16 nm as the molecular weight of PEG increases from 860 g/mol to 10 000 g/mol (Temenoff *et al.* 2002). In addition, the mechanical properties of PEGda hydrogels are modulated by the molecular weight and concentration of the precursors. Hydrogels with higher concentration have higher compressive modulus (Bryant *et al.* 2004) and higher tensile modulus (Hou *et al.* 2010). At similar precursor concentrations, hydrogels with low molecular weight are more brittle than gels with higher molecular weight (Temenoff *et al.* 2002; Bryant *et al.* 2004; Hou *et al.* 2010).

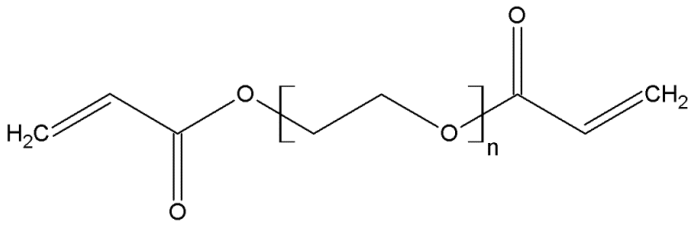

Figure 13. Chemical structure of poly(ethylene glycol) diacrylate (PEGda).

PEG hydrogels have been the most successful synthetic gels used for tissue engineering applications thus far because they function as biological “blank slates” into which the desired bioactivity can be

tailored to match need. The term “blank slate” means that the material is free of any biochemical signals that natural polymers, such as collagen, have. Thus, PEG scaffolds can be specifically modified with bioactive peptides, such as the integrin-binding Arg-Gly-Asp (RGD) sequence found in cell-binding domains of extracellular matrix proteins, to induce cellular adhesion. (Slaughter *et al.* 2009) Typically, the bioactive moiety is tethered to the PEG network via an N-hydroxysuccinimide (NHS) coupling reaction that couples any primary amine with NHS functionalized PEG (Burdick & Anseth 2002).

2.3.3 Photocurable poly(caprolactone)

As most commonly used UV curable resins are non-bioresorbable, there has been a need for the development of new biodegradable and photocurable materials for tissue engineering applications. During the resorbable-polymer-boom of the 1970s and 1980s, poly(caprolactone) (PCL) was used in several drug-delivery devices. Its popularity was soon overwhelmed by faster resorbable polymers, such as polylactides and polyglycolides, that had fewer disadvantages associated with long-term degradation and could be resorbed intracellularly. Thus, PCL was almost forgotten for almost two decades. (Woodruff & Hutmacher 2010) The interest in PCL re-emerged along with the rise of the tissue engineering field during the 1990s and 2000s as it was realized that when compared with other commercially available bioresorbable polymers, PCL is one of the most flexible and easy processed materials and can therefore be straightforwardly manufactured into a wide range of scaffolds (Zein *et al.* 2002).

Polymers based on caprolactone monomers are now in common clinical use and extensive *in vitro* and *in vivo* biocompatibility studies have resulted in FDA approval of a number of medical and drug delivery devices composed of PCL (Figure 14) (Bezwada *et al.* 1995; Chuenjitkuntaworn *et al.* 2010). PCL is a hydrophobic, semi-crystalline polymer having an unusually low glass transition temperature of −62 °C and a high decomposition temperature of 350 °C. It exists in a rubbery state at room temperature, as its melting temperature is around 60 °C (Suggs *et al.* 2007). PCL homopolymer degrades by random hydrolytic chain scission of the ester linkages in around 2 years. (Middleton & Tipton 2000) It undergoes a two-stage degradation process. In the first phase, the molecular weight is diminished due to the non-enzymatic hydrolytic cleavage of the ester groups. In the second stage, the more crystalline polymer undergoes intracellular degradation as the PCL fragments are uptaken by macrophages and fibroblasts. (Woodward *et al.* 1985)

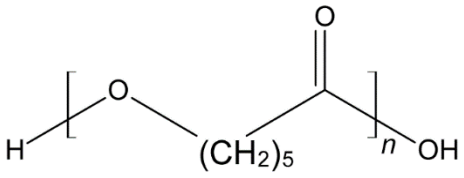

Figure 14. Chemical structure of poly(caprolactone) (PCL).

In order to fabricate bioresorbable scaffolds by 2PP-DLW, branched oligomers based on bioresorbable PCL have been synthetized by using multifunctional alcohol as an initiator. These

oligomers have hydroxyl-terminated chains that are then functionalized with photocrosslinkable methacrylate groups. For example, a star-shaped methacrylated PCL oligomer (PCL-o) (Figure 15) has been synthetized via ring-opening polymerization of the prepolymer with stannous octoate as initiator and pentaerythritol as co-initiator followed by functionalization with methacrylic anhydride (Helminen *et al.* 2002; Rich *et al.* 2009). The four-armed highly viscous transparent liquid oligomer had a molecular weight of around 1 000 g/mol. After the functionalization, the oligomers were cured by the photoinduced polymerization of the methacrylic end groups in the presence of camphorquinone as a photoinitiator. The degradation of this photocured material was evaluated with a hydrolysis study in phosphate buffer solution (pH 7.4) at 37 °C for 21 days. The pure PCL oligomer matrix absorbed only 2.6% water in 3 weeks, and mass loss was 1%. (Rich *et al.* 2009) Similar results were also obtained with a PCL oligomer having a molecular weight of 11 550 g/mol thermally crosslinked in the presence of dibenzoyl peroxide as radical initiator. Samples showed water absorption of less than 2% and mass loss of 1% after immersion in phosphate buffer solution (pH 7.0) at 37 °C for 12 weeks. The slow degradation behavior of the PCL oligomer originates from its partial crystallinity and high hydrophobicity. (Helminen *et al.* 2002)

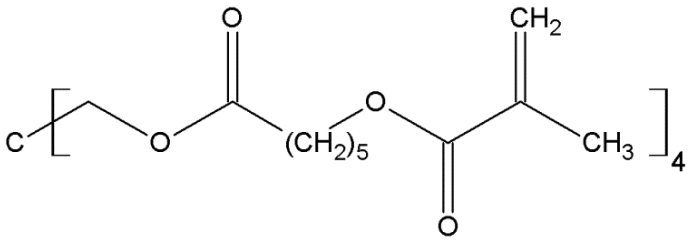

Figure 15. Chemical structure of four-armed methacrylated poly(caprolactone).

2.3.4 Proteins

Many proteins found in solutions and in cells can form inter- and intramolecular covalent crosslinks when irradiated in the presence of a suitable photosensitizer (Van Steveninck & Dubbelman 1984; Webster *et al.* 1989). The capability of a protein to be photocrosslinked may be affected by changing its conformation; this implies that the amino acids involved in crosslinking have to be at or near the protein surface and have proper orientation (Spikes *et al.* 1999). Although the mechanisms involved in the photocrosslinking of proteins are not well understood, the crosslinking is believed to proceed either via free radical formation (Type I) (Webster *et al.* 1989; Balasubramanian *et al.* 1990) or via singlet oxygen generation (Type II) (Shen *et al.* 1996a; Shen *et al.* 1996b) depending on the sensitizer, the reaction conditions, and the wavelength and intensity of the exciting light. The singlet oxygen or the radicals interact with photooxidizable amino acid residues containing olefins, dienes, aromatics, and heterocyclic groups, such as tyrosine, cysteine, histidine and tryptophan, in one protein molecule to form products that react with residues in another protein molecule to promote crosslinking (Dubbelman *et al.* 1978; Verweij *et al.* 1981). A derivate of Fluorescein, Rose Bengal (4,5,6,7-tetrachloro-2',4',5',7'-tetraiodofluorescein), is a stain that can be used as a photosensitizer. It sensitizes the protein crosslinking primarily through a singlet oxygen pathway (Basu & Campagnola 2004). Rose Bengal transfers its energy of excitation to triplet ground state oxygen to produce singlet

oxygen, the first excited electronic state of molecular oxygen. The singlet oxygen is electrophilic, and thus it reacts readily with electron-rich molecules, such as amino acids with double bonds or sulfur-containing moieties (Cló *et al.* 2007). The reaction between singlet oxygen and an amino acid residue of a protein leads to the formation of an electron deficient protein that may react with another protein's amino acid residue to form a covalent bond (Basu *et al.* 2004).

Naturally occurring flavin mononucleotide (FMN) has been shown to sensitize crosslinking by both Type I and Type II mechanisms depending on the pH conditions. The FMN-sensitized photo-oxidation at pH < 8 is probably mediated by mechanisms that do not involve singlet oxygen. Instead, the reaction involves the formation of a long-lived triplet state FMN, which in turn can abstract an electron (or an H atom) from the protein to generate radicals of the sensitizer and the protein (e.g., tyrosyl radicals). The resulted tyrosyl radical is isomerization-stabilized and can recombine with another tyrosyl radical to create intermolecular crosslinks between proteins (Figure 16). (Spikes *et al.* 1999; Shen *et al.* 2000) The excitation of FMN to triplet state can also be achieved via absorption of the combined energy of two or multiple photons, as in the case of 2PA-induced photocrosslinking. In fact, another flavin cofactor, flavin adenine dinucleotide (FAD), has previously been successfully utilized as a photosensitizer for the 2PP-DLW of bovine serum albumin (BSA) and bovine heart cytochrome c (cyt c) induced by picosecond lasers (Kaehr *et al.* 2006; Ritschdorff & Shear 2010).

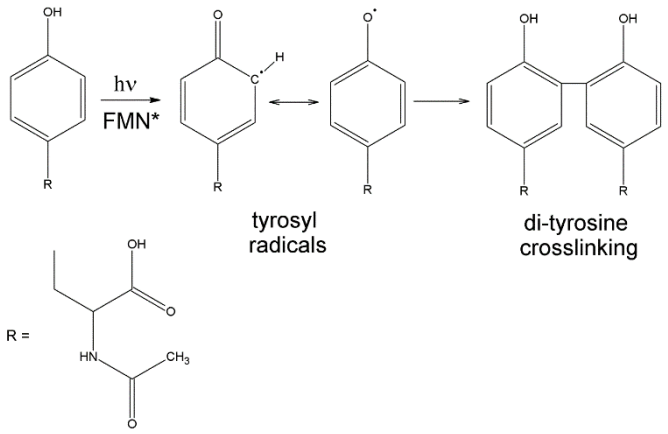

Figure 16. Mechanism of flavin mononucleotide (FMN) sensitized photocrosslinking between tyrosine residues of native proteins.

As synthetic polymers, such as PLA and PCL, generally lack bioactivity and are mechanically rather stiff, hydrogels crosslinked from natural proteins have become an appealing material for various biomedical applications. The mechanical properties, especially the stiffness, of natural hydrogels are comparable to many biological soft tissues. In addition, their ability to contain a high content of water and open network structure facilitates the diffusion of nutrients and dissolved gases to the cell suspended inside the gels. (Stampfl & Liska 2011) Different native proteins contain different cell adhesive ligands capable of interacting with cells. In a natural extracellular matrix (ECM), cell attachment is regulated by the interaction between integrin receptors on cell membranes and integrin binding motifs, such as RGD peptides. These cell adhesive ligands are found from several naturally derived proteins, such as collagen, gelatin, and fibrinogen, or the hydrogel matrices can be

subsequently functionalized, for example, with laminin-derived peptides using avidin-biotin linkage. (Torgersen *et al.* 2013)

Avidin-biotin complex is an excellent example of binding molecule pairs. Avidin is a glycoprotein found in egg white and possesses four binding sites for biotin (vitamin H). The avidin-biotin system has the largest affinity constant known for a ligand-protein interaction. (Bayer & Wilchek 1992) It has been shown that avidin retains its substantial biotin-binding capacity after it has been crosslinked into microstructures and patterns by 2PP-DLW. Thus, avidin microstructures can be decorated with a variety of biotinylated molecules, including enzymes or bioactive peptides, and used to enhance cell adhesion and proliferation. (Kaehr *et al.* 2004; Allen *et al.* 2005; Kaehr *et al.* 2006) However, as commercially available avidin is relatively expensive and because high concentrations (> 100 mg/ml) are required for photofabrication, it is more feasible to exploit avidin-biotin interactions by using biotinylated BSA (bBSA) instead of avidin (Seidlits *et al.* 2009). BSA is similar to human serum albumin being a monomeric protein with high solubility in water and a lack of carbohydrate chains. It is the most abundant plasma protein, and it is synthetized in the liver and exported as a non-glycosylated protein into the plasma. BSA is a multifunctional protein with extraordinary ligand binding capacity and serves as a transporter molecule for a variety of metabolites, drugs, nutrients, and metals. (Majorek *et al.* 2012)

2.4 Applications of 2PP-DLW for neuronal cell growth guidance

The ability to culture cells *in vitro* has become a standard methodology in cell and molecular biology as well as in drug screening and toxicology assays. The traditional cell culture procedure, consisting of the immersion of a large cell population on a 2D cell culture surface (e.g. petri dish, slide or a well) in a homogenous fluid medium, has remained unchanged for almost a century. This approach is fundamentally quite limiting, as the cells *in vivo* are actually surrounded by a complex spatiotemporal microenvironment. Cellular processes, such as adhesion, migration, and growth, are influenced by local time-varying concentrations of molecules that may be dissolved in extracellular medium (e.g., enzymes, nutrients, ions), be present on the underlying surface (e.g., ECM proteins), or on the surface of neighboring cells (e.g., membrane receptors). (Li *et al.* 2003) About 20 years ago, microfabrication techniques started to attract the interest of biologists because these techniques enabled scientists to design cell culture platforms with well-defined geometries to control the behavior of cells on a micrometer scale (Dow *et al.* 1987; Voldman *et al.* 1999). Cell culture substrates were patterned with surface chemistries (Kane *et al.* 1999; Ito 1999) and/or topographical features (Flemming *et al.* 1999) to study the response of living cells on such changes.

Due to the location and immense complexity of neural networks, studying these networks *in vivo* is very laborious (Horner & Gage 2000; Wyart *et al.* 2005). As the complex cytoarchitecture of nervous tissue is lost during the dissociation procedures used to create primary cell cultures, it is obvious that neuronal cells were among the first cell types to be plated onto patterned substrates to study cell attachment, outgrowth, and motility. Indeed, it would be convenient to be able to construct 2D *in vitro* models mimicking the architecture of the neural networks found *in vivo*. These culture models

would enable the study of the developmental and computational properties of neural systems in a simplified, controlled environment. (Kleinfeld *et al.* 1988) Without a doubt, there exists an obvious need for new efficient methods to study and treat neurodegenerative disorders, such as Alzheimer's and Parkinson's disease, as they affect about 30 million individuals worldwide leading to either disability or death (Chong *et al.* 2012). Several different approaches have been demonstrated to have an influence on the morphology of neurons, such as simple geometrical cues (Rajnicek *et al.* 1997; Withers *et al.* 2006), biologically-active protein patterns (Kam *et al.* 2001; Oliva *et al.* 2003), and combinations of topographical and chemical cues (Britland *et al.* 1996; Miller *et al.* 2002).

Contact guidance, the phenomenon of cell alignment due to the physical shape of the substratum, was recognized already at the dawn of tissue culture (Harrison 1914). Clearly, the substratum topography affects the ability of cells to orient, migrate, and produce organized cytoskeletal arrangements (Flemming *et al.* 1999). Despite the recognition of the importance of topographical features, surprisingly little is known about the details of the cellular events of contact sensing and their transduction into directional growth, and especially about the mechanism for neuronal growth cone contact guidance (Rajnicek & McCaig 1997). Moreover, although neural networks have been engineered for many years now using micro- and nanofabrication techniques, networks with predesigned functionality have nevertheless remained very difficult to achieve. The main challenge is to organize individual cells so that one can control the polarity of neurons (differentiation of neurites into axons and dendrites) at distinct predefined locations. (Greene *et al.* 2011)

Nevertheless, 2D neuronal cell cultures represent an oversimplification of the neural system anatomy found *in vivo* (Kleinfeld *et al.* 1988; Limongi *et al.* 2013). Thus, one of the major strategies in the field of neuroscience and neural engineering is to develop 3D neuronal culture models that more closely mimic the organization of neural networks into segregated neuronal nuclei connected by discrete axonal tracts (Cullen *et al.* 2011). Three-dimensionality can be introduced to a neuronal cell culture by using various approaches, such as synthetic polymer scaffolds (Lai *et al.* 2012), hydrogel matrices (McKinnon *et al.* 2013; Koutsopoulos & Zhang 2013), microscale tubular guidance conduits (Cullen *et al.* 2012) or arrays of nano- and microscale structures, e.g., pillars (Limongi *et al.* 2013) or towers (Cullen *et al.* 2011).

Nowadays, computer-assisted laser-based fabrication techniques, such as 2PP-DLW, offer a powerful tool to produce cell culture substrates with highly ordered geometries that recapitulate the structure and length scale of natural 3D cell environments (Greiner *et al.* 2012). The published literature on 2PP-fabricated surface topographies, the 2.5D and 3D architectures for growth guidance of neuronal cells, is collated in Table 1. Fabricated geometries can be classified into structures with isotropic or anisotropic architecture. Structures used for contact guidance of neuronal cells are often composed of pores, ridges, pillars, cylinders, or lines, but may also be more complicated free-shaped scaffolds.

The non-biodegradable organically modified ceramic, Ormocomp®, has been structured into various geometrical shapes, such as Lego-like blocks (Doraiswamy *et al.* 2006), pillars (Schlie *et al.* 2007; Ovsianikov *et al.* 2007c), and microridges (Marino *et al.* 2013), that have been successfully used for

contact guidance of neuroblastoma cells of rat or human origin. Yet another hybrid material, Zr-Si, has been fabricated into scaffolds comprising two layers of hollow cylinders. The scaffolds were able to promote mouse hippocampal neurons to form 3D neuronal networks. (Timashev *et al.* 2016) Due to the Food and Drug Administration (FDA) approval of PEG for various medical applications, the acrylated form, PEGda, has been used as a key component in microstructures for neuronal cell growth guidance studies either on its own (Sherborne *et al.* 2012) or as a mixture with 2-hydroxyethyl methacrylate (HEMA) (Jhaveri *et al.* 2006). Proof-of-concept studies with line structures have shown promising results that these types of simple geometries could be used as topographical features inside peripheral neural guidance channels (Sherborne *et al.* 2012).

Biodegradable microstructures, such as honeycomb-like scaffolds made of methacrylated polylactide (PLA), have been shown to support the growth of rat Schwann cells through the channeled structure (Koroleva *et al.* 2012). Although so far tested only *in vitro*, these scaffolds could potentially be used as implantable nerve guidance conduits if clinical trials turn out to be successful. Effective orientation of neuroblastoma-glioma (NG108-15) cells with PLA-based photopolymer has also been achieved by using suspended guidelines between rectangular blocks, as well as linear struts (Melissinaki *et al.* 2011). Natural biopolymers, such as BSA (Kaehr *et al.* 2006; Seidlits *et al.* 2009), avidin (Allen *et al.* 2005) and laminin (Kaehr *et al.* 2004), have also been crosslinked into simple neuronal cell growth guidance structures *in situ*, i.e., in the presence of live cells, without compromising the viability of neurons. Although these biopolymer structures adequately mimic the native cellular microenvironment from the chemical perspective, they often lack the necessary mechanical stability. However, by combining the advantages of natural biopolymers with the mechanical stability of a synthetic polymer, such as PEG, a hydrogel system providing good interaction with neuronal cells can be created (Livnat *et al.* 2007).

Table 1. Summary of the published literature on direct laser written microstructures for growth guidance of neuronal cells.

Material	Photoinitiator	Laser setup	Feature geometry	Cell type	Culture time	Cell response	Reference
Ormocomp®	Irgacure® 369	Ti:sapphire laser 780 nm 94 MHz 60 fs	Lego-like interlocking scaffolds with arrays of pillars on both sides of a flat chip	Rat neuroblastoma (B35) cells	2 days	Orientation along the pillar walls and proliferation over time	(Doraiswamy *et al.* 2006)
Ormocomp®	Irgacure® 369	Ti:sapphire laser 780 nm 94 MHz 80 fs	Cylindrical structure (3D pillars)	Human neuroblastoma (SH-SY5Y) cells	3–4 days	Adherence and proliferation along the vertical surfaces of 3D structures	(Schlie *et al.* 2007; Ovsianikov *et al.* 2007c)
Ormocomp®	n.a.	Fiber laser 790 mn 80 MHz 120 fs	Microridges	Rat pheochromocytoma (PC12) and human neuroblastoma (SH-SY5Y) cells	5 days	Strong neurite outgrowth and orientation along the ridges	(Marino *et al.* 2013)
Zr-Si hybrid	4,4′-bis(diethylamino) benzophenone	Ti:sapphire laser 780 nm 80 MHz 150 fs	Scaffolds composed of hollow cylinders	Mouse hippocampal neuronal cells	14 days	Adhesion of cells, formation of functional 3D networks	(Timashev *et al.* 2016)
HEMA[1] + PEGda[2]	Irgacure® 651 + AF-240[3]	Ti:sapphire laser 780 nm ~80 MHz ~100 fs	Neurotrophin-releasing cubic structures	Rat pheochromocytoma (PC12) cells	3 days	Stimulation of neurite outgrowth towards neural prosthetic device	(Jhaveri *et al.* 2006)
PEGda, methacrylated PCL and methacrylated PLA	n.a.	Nd:YAG laser 532 nm ~0.5 ns	Line structures	Rat Schwann cells, rat DRG cells and neuroblastoma-glioma (NG108-15) cells	10 days	Oriented growth	(Sherborne *et al.* 2012)
Methacrylated PLA[4] oligomer	4,4-bis(diethylamino) benzophenone	Ti:sapphire laser 800 nm 75 MHz < 20 fs	Suspended guidelines between rectangular blocks, linear struts, porous microscaffolds sea-shell structures	Rat pheochromocytoma (PC12) and neuroblastoma-glioma (NG108-15) cells	7 days	Adhesion, proliferation and alignment, formation of 3D networks	(Melissinaki *et al.* 2011)

Methacrylated PLA oligomer	Irgacure® 369	Ti:sapphire laser 780 nm 80 MHz 120 fs	Scaffolds composed of hollow cylinders	Rat Schwann cells	7 days	Adhesion and growth along the scaffold channels	(Koroleva *et al.* 2012)
PEGylated collagen and fibrinogen	Irgacure® 2959	Ti:sapphire laser 700-920 nm ~100 fs	Nerve guidance conduits	Chick dorsal root ganglion (DRG) cells	5 days	Outgrowth of sprouting neurites, unidirectional guidance of the neurites and glial cells	(Livnat *et al.* 2007)
bBSA[5] functionalized with biotinylated peptides inside methacrylated HA[6] gel	Methylene blue	Ti:sapphire laser 740 nm 76 MHz	Lines, concentric squares, helices	Rat primary DRG cells and embryonic neural progenitor cells (NPC)	3–7 days	Differentiation into mature neurons, neurite outgrowth and orientation along micropatterns	(Seidlits *et al.* 2009)
BSA and laminin	FAD[7]	Ti:sapphire laser 740–790 nm	Low-profile barriers	Neuroblastoma-glioma (NG108-15) cells and rat brain cortical cells	*In situ* photofabrication, 240 min	Confinement and redirection of neurites	(Kaehr *et al.* 2004)
BSA	No additional photoinitiator	Nd:YAG laser 532 nm 7.65 kHz ~600 ps	Low-profile barriers	Rat brain cortical cells	*In situ* photofabrication, 95 min	Confinement of neurite outgrowth	(Kaehr *et al.* 2006)
Avidin	FAD	Ti:sapphire laser ~750 nm ~80 MHz ~150 fs	Scaffold functionalized with biotin-AP[8]	Neuroblastoma-glioma (NG108-15) cells	n.a.	Exposure of cells to real-time chemical gradient of fluorescent 4-MU[9]	(Allen *et al.* 2005)

[1] 2-Hydroxyethyl methacrylate, [2] Poly(ethylene glycol) diacrylate, [3] (7-Benzothiazol-2-yl-9,9-diethylfluoren-2-yl) diphenylamine, [4] Polylactide, [5] Biotinylated bovine serum albumin, [6] Hyaluronic acid, [7] Flavin adenine dinucleotide, [8] Biotinylated calf intestinal alkaline phosphatase, [9] 4-methylumbelliferone

3 AIMS OF THE STUDY

The overall aim of this thesis was to optimize 2PP-DLW processing with respect to material choice, structure design, and processing parameters in order to feasibly fabricate microstructures from photosensitive biomaterials for neuronal cell growth guidance purposes and to determine the most efficient microscale topographical or chemical guidance cue to control the attachment, growth, and orientation of individual neurons *in vitro*.

In order to accomplish the overall goal, the following specific steps were defined:

1. Comparison and selection of photosensitive materials for 2PP-DLW. Assessment of the suitability of several photosensitive materials for the fabrication of microstructured cell culture platforms in terms of optimal processing parameters, overall processability, achievable feature size, retention of bioactivity after processing, and possible cytotoxicity of the used material-photoinitiator combinations. The investigated material options were methacrylated poly(ε-caprolactone)-based oligomer, poly(ethylene glycol) diacrylate, polymer-ceramic hybrid material Ormocomp®, avidin and bovine serum albumin. (Publications I & II)

2. Design and 2PP-DLW fabrication of bioactive protein surface patterns. Evaluation of the ability of the peptide functionalized avidin and BSA micropatterns to guide the growth of hPSC-derived neurons. (Publication II & Unpublished data)

3. Design and 2PP-DLW fabrication of 3D confinement microstructures from Ormocomp®. Evaluation of the applicability of the confinement structures to control the location of neurons and direct the growth of neurites on predefined axes. (Publication III)

4. Optimization of the design and 2PP-DLW fabrication of 3D tubular microtowers with or without intraluminal guidance cues from Ormocomp®. Evaluation of the different microtower designs for long-term 3D culturing of human neuronal cells and their ability to orient neurites. (Publication IV)

4 MATERIALS AND METHODS

4.1 2PP-DLW fabrication setups

Three different custom-built 2PP-DLW fabrication setups at the VTT Technical Research Centre of Finland and one setup at the Institute of Electronic Structure and Laser of the Foundation for Research and Technology-Hellas (IESL-FORTH) were used for polymerization experiments in this Doctor of Science (Technology) degree project. The first generation fabrication setup was used in Publication I. The setup (Figure 17) was based on a diode-pumped passively Q-switched frequency doubled Nd:YAG microchip laser (PULSELAS-P-1064-300-FC, Alphalas GmbH, Germany) emitting at 532 nm with a pulse duration of 800 ps, maximum repetition rate of 15 kHz and maximum average output power of 100 mW. The setup was assembled over an upright microscope frame (Nikon ECLIPSE ME 600, Nikon, Japan) and the beam was directed into a 50× oil immersion objective (N.A. = 0.90, Meiji Techno, Japan). In order to achieve diffraction limited focal spot with the size of the Airy disk, the incident laser beam was expanded 10× to overfill the back aperture of the objective lens. The expansion of the beam resulted in a measured average transmittance of 56% for the 50× objective. The laser exposure was controlled with a mechanical shutter (SH05 Beam Shutter, Thorlabs, Germany) connected to its controller (TSC001 T-Cube Shutter Controller, Thorlabs, Germany). The minimum shutter open time was 27 ms. A motorized xyz-stage (SCAN 130 × 85, Märzhäuser Wetzlar, Germany) with an accuracy of ± 3 μm and repeatability below 1 μm was employed to move the sample with respect to the stationary laser focal spot.

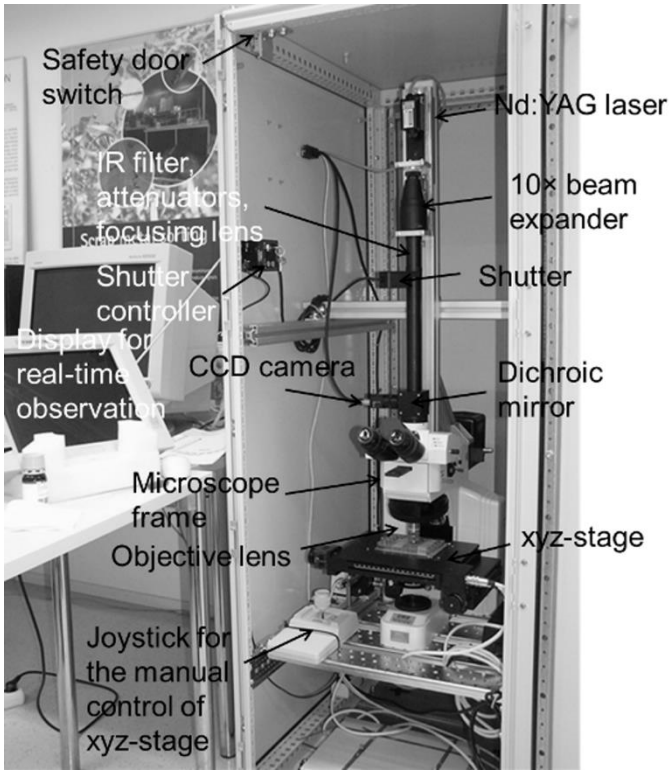

Figure 17. First generation 2PP-DLW fabrication setup.

The xyz-stage and the shutter were controlled either by the commercial software WinPos (ITK Dr. Kassen, Germany), or by the custom-designed CorvusControl software (Figure 18). The WinPos software was used for rudimentary fabrication of simple structures, such as voxels and lines, and the CorvusControl software for all 3D fabrication. The real-time monitoring of the polymerization process was enabled by a charge-coupled device (CCD) camera (CV-M10RS, JAI Corporation, Japan) mounted behind a dichroic mirror and used in combination with commercial visualization software (Ulead DVD MovieFactory 4.0, Ulead Systems, Inc., Taiwan).

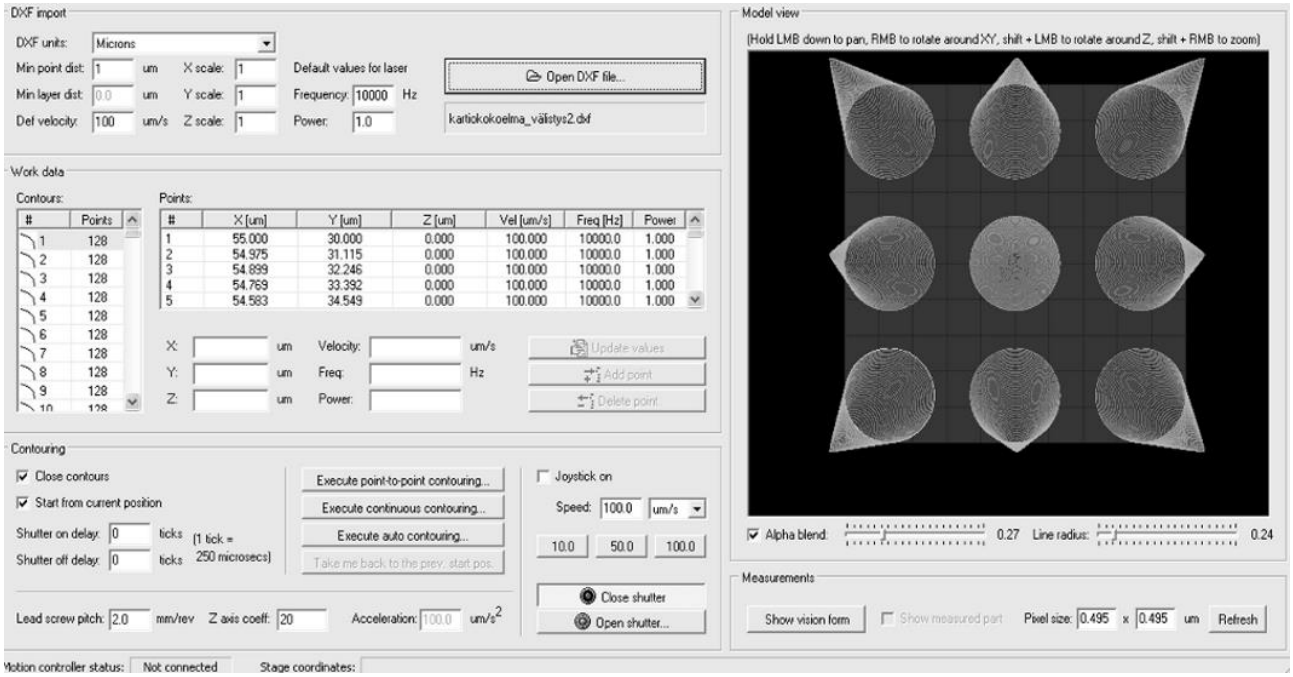

Figure 18. The graphical user interface of the custom-designed CorvusControl software.

The second-generation fabrication setup was used in Publications II and III. It also utilized the Nd:YAG picosecond laser as an irradiation source and was built over the Nikon microscope frame (Figure 19). In addition to the 10× expander, another adjustable 1–3× beam expander was added to the optical path. Consequently, the average transmittance of the 50× objective was measured to be 30%. The slow mechanical shutter was replaced with a fast electronic shutter (Oriel 76992, Newport Corporation, USA) having an exposure time of 2 ms at the shortest. The xyz-stage was used only for the initial sample positioning, whereas the beam was scanned in the xy-direction with a fast mirror scanner (FSM-300, Newport Corporation, USA) and in the z-direction with a piezoelectric objective lens positioning system (Mipos 250 SGEX, Piezosystem Jena GmbH, Germany).

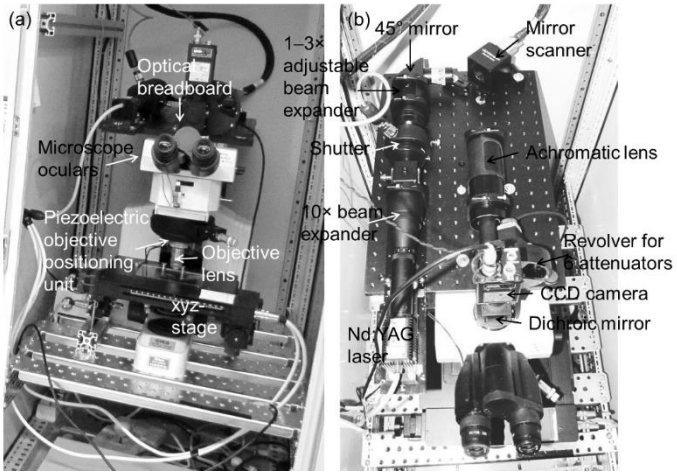

Figure 19. Second-generation 2PP-DLW fabrication setup: (a) side-view of the upright microscope and (b) top view of the optical breadboard.

The six motion axes, the shutter, and the real-time video image were controlled by a completely new version of the operating software called the LaserControlSystem (Figure 20). The main reason for updating the control software was the inability of the previous system to run synchronously, and at high speed, the multiple axes and the shutter.

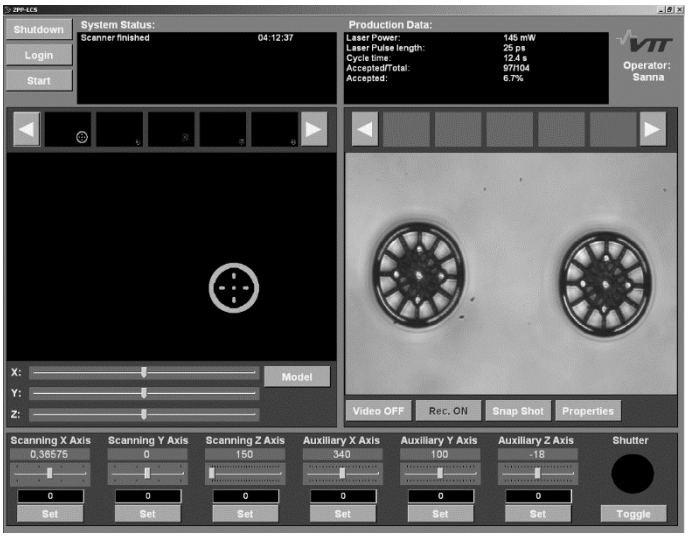

Figure 20. The graphical user interface of the custom-designed LaserControlSystem software.

In the first and second-generation fabrication setups, the laser output power was attenuated to a suitable polymerization level with optical absorptive filters after the beam expander. In Publication I, an attenuator with a 25% transmittance of the incident light was used, and an attenuator with 50% transmittance in Publication II, and an attenuator with 10% transmittance in Publication III. During the polymerization, the laser power could be further fine-tuned by adjusting the pump diode current from 1.70 A to 2.52 A. However, the adjustment of the diode current also affected the pulse frequency within a range from 5 kHz to 15 kHz. In Publications I–III, the average power values were measured

at the back aperture of the objective with a hand-held laser power meter (LaserCheck, Coherent Inc., USA).

The third generation fabrication setup was used in Publication IV and in unpublished data concerning the fabrication of protein patterns from bBSA and avidin with Irgacure® 2959. It was an updated version of the second-generation setup. The Nd:YAG laser was replaced with a frequency doubled femtosecond fiber laser (FP-532-0.2-FS-01, Fianium Ltd., United Kingdom) operating at 532 nm with a pulse duration of 200 fs, repetition rate of 40 MHz, and average output power of 200 mW. The average laser power was adjusted to a suitable polymerization level with a motorized attenuator (Watt Pilot, UAB Altechna, Lithuania). The laser power was measured at the back aperture of the objective with a power meter console (PM100USB, Thorlabs Inc., USA) coupled with a S310C thermal sensor. With this optical setup, the 50× objective had an average transmittance of 48%. All the other components in the third generation fabrication setup were the same as in the second-generation setup.

The 2PP-DLW fabrication setup located at IESL-FORTH was used in Publication II as a reference system. The fabrication setup was based on the Ti:sapphire femtosecond laser (FEMTOSOURCE™ FUSION™ 20, FEMTOLASERS Produktions GmbH, Austria) operating at 800 nm. The laser generated sub-20 fs pulses with a repetition rate of 75 MHz and maximum output power of 450 mW. The beam movement was achieved with an x-y galvanometric mirror digital scanner (hurrySCAN® II, SCANLAB AG, Germany) and on the z-axis with a three-axis linear encoder stage (Physik Instrumente GmbH & Co. KG, Germany). The beam was controlled using a mechanical shutter (Uniblitz, USA) and the laser power was adjusted with a motorized attenuator (UAB Altechna, Lithuania). A high numerical aperture 100× objective lens (N.A. = 1.40, Carl Zeiss Microscopy GmbH, Germany) was used to focus the laser beam into a focal spot. The overall transmittance of the laser beam measured after the objective was approximately 17% of the initial laser output power.

4.2 Materials

The photosensitive materials and photoinitiators used in this work are listed in Table 2 along with the suppliers and concentrations. The molecular structure of the custom-synthetized PCL-o with a molecular weight of slightly over 1000 g/mol is presented in Figure 15 in section 2.3.3. The chemical structure of PEGda with a molecular weight of 575 g/mol is shown in Figure 13 in section 2.3.2. Both of these materials were used in combination with Irgacure® 127 photoinitiator, the chemical structure of which is shown in Figure 21.

Table 2. Photosensitive materials and photoinitiators used in this thesis work.

Material	Supplier	Photoinitiator	Supplier	Concentration	Publication
PCL-o[1]	Laboratory of Polymer Technology at Aalto University, Finland	Irgacure® 127	Ciba Specialty Chemicals, Switzerland	2 wt%, 3 wt%, or 5 wt%	I
PEGda[2]	Sigma-Aldrich Finland Oy, Finland	Irgacure® 127	Ciba Specialty Chemicals, Switzerland	0.5 wt%, 1 wt%, or 1.5 wt%	I
BSA[3]	Sigma-Aldrich Finland Oy, Finland	FMN[4]	Sigma-Aldrich Finland Oy, Finland	4 mM	II
bBSA[5]	Protein Dynamics, BioMediTech, University of Tampere	FMN	Sigma-Aldrich Finland Oy, Finland	0 mM, 1 mM, 2 mM, or 4 mM	II
		Irgacure® 2959	BTC Europe GmbH, Denmark	0.6 wt%	Unpublished data
Avidin	Belovo Chemicals, Belgium	FMN	Sigma-Aldrich Finland Oy, Finland	0 mM, 1 mM, 2 mM, or 4 mM	II
		Irgacure® 2959	BTC Europe GmbH, Denmark	0.6 wt%	Unpublished data
Ormocomp®	Micro Resist Technology GmbH, Germany	Darocur® TPO and Irgacure® 127	Ciba Specialty Chemicals, Switzerland	1% and 2 wt%	III, IV

[1] Star-shaped methacrylated poly(caprolactone) oligomer, [2] Poly(ethylene glycol) diacrylate, [3] Bovine serum albumin, [4] Flavin mononucleotide, [5] Biotinylated bovine serum albumin

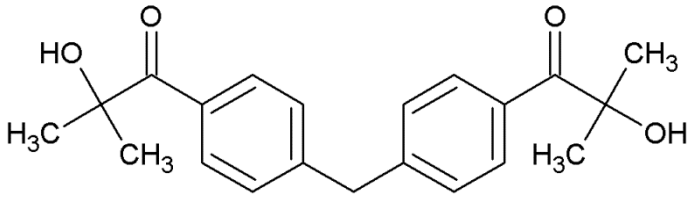

Figure 21. Chemical structure of Irgacure® 127.

BSA, bBSA, and avidin proteins were photosensitized with FMN or Irgacure® 2959. Their molecular structures are presented in Figure 22.

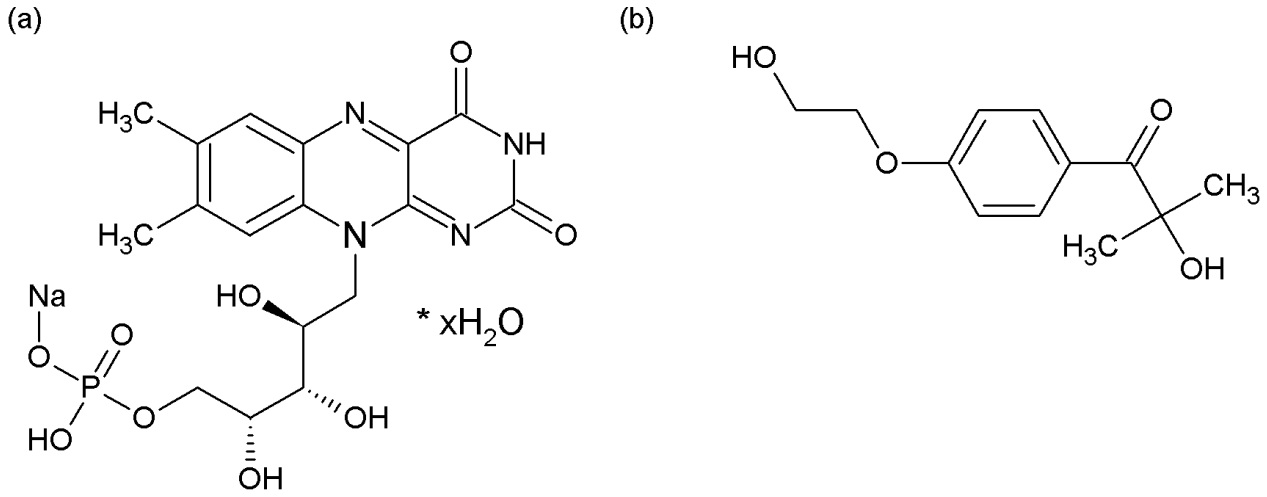

Figure 22. Chemical structures of (a) flavin mononucleotide and (b) Irgacure® 2959.

Ormocomp® hybrid material was purchased as a resin containing 1% of Darocur® TPO as a photoinitiator (Figure 23), but was further sensitized by adding 2 wt% (w/w) of Irgacure® 127 into the resin.

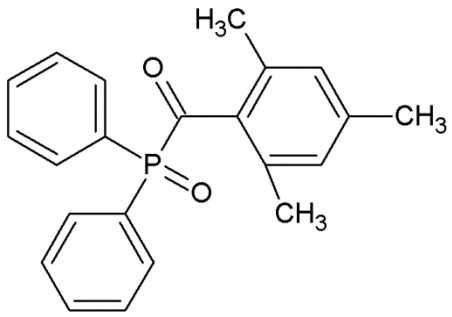

Figure 23. Chemical structure of Darocur® TPO.

4.3 Verification of the absorption spectra

To verify the compatibility of the photosensitive PCL-o and PEGda resins (Publication I) and the FMN photosensitizer (Publication II) with the utilized laser wavelength of 532 nm, UV-visible absorption spectra were measured. The spectra were obtained with a Unicam UV 540 spectrophotometer (Thermo Spectronic, United Kingdom) in the range of 190 nm to 700 nm for PCL-o diluted in dichloromethane and PEGda diluted in ion-exchanged water with and without the Irgacure® 127 photoinitiator, and in the range of 190 nm to 900 nm for FMN dissolved in ion-exchanged water to a concentration of 0.1 mM.

4.4 Sample preparation for 2PP-DLW

Photosensitive resins of PCL-o and PEGda were prepared by dissolving Irgacure® 127 at different concentrations into them. Henceforth, these resins are referred to as PCL-o-α and PEGda-β, in which α and β denote the weight percentage of the photoinitiator for each resin. PCL-o resins of α = 2, 3, and 5, and PEGda resins of β = 0.5, 1, and 1.5 were used for polymerization tests in Publication I. In Publication II, the reagent solution of BSA was prepared by dissolving the protein at a concentration of 200 mg/ml into phosphate buffered saline (PBS, pH ~7.4) containing 4 mM of FMN. bBSA was used as a solution containing 100 mg/ml of protein and from 0 mM to 4 mM of FMN, or together with BSA as a solution of 100 mg/ml of bBSA and 100 mg/ml of BSA using 0 mM to 4 mM of FMN. BSA was added to the solution to provide higher photo-crosslinkability and better mechanical stability. Avidin was studied as solutions containing 50 mg/ml, 100 mg/ml, 200 mg/ml, or 400 mg/ml of protein and from 0 mM to 4 mM of FMN in PBS. In addition, bBSA was tested as a solution of 400 mg/ml of protein with 0.6 wt% (w/w) of Irgacure® 2959 and avidin as a solution of 400 mg/ml of protein with 0.6 wt% (w/w) of Irgacure® 2959 (unpublished data). Ormocomp® was used as a solution together with 2 wt% (w/w) of Irgacure® 127 (Publications III & IV).

For 2PP-DLW, all the samples for polymerization were prepared by drop casting without any pre- or post-baking procedures. A drop of photosensitive material was sandwiched between a microscope slide and a coverslip separated by a 150 μm (Publications I–III, Figure 24) or a 250 μm (Publication IV) thick stainless steel spacer, or by a ~300 μm thick PDMS spacer (unpublished data). In Publications I and IV, the microscope glass slides were pre-treated with a coupling agent 3-(trimethoxysilyl) propyl methacrylate (MAPTMS, Sigma-Aldrich Finland Oy, Finland) to ensure the adequate attachment of the microstructures to the substrate. The slides or coverslips were first cleaned with a strong soap solution, rinsed with water, and allowed to air dry. The slides were then immersed in a MAPTMS solution (1:200 of MAPTMS in 99.5% ethanol with 3:100 of dilute acetic acid (1:10 glacial acetic acid: water)) for 3 min. Afterwards, the slides were rinsed with 99.5% ethanol and allowed to air dry. In order to enhance the adherence of the protein structures on glass, (3-aminopropyl) triethoxysilane (APTES) treated microscope slides (Electron Microscopy Sciences, USA) were used on some occasions with the Nd:YAG laser setup in Publication II to provide a hydrophobic substrate for the proteins.

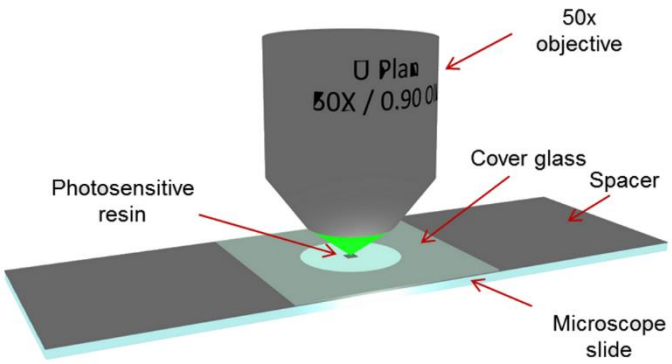

Figure 24. Sample configuration used in Publications I–III: liquid resin is sandwiched between a microscope glass and a coverslip separated by a steel spacer.

Due to the crystallization tendency of the PCL-o solution, samples of PCL-o had to be heated to approximately 30 °C before polymerization. After the polymerization, PCL-o samples were developed with dichloromethane (Sigma-Aldrich Finland Oy, Finland) or with Ormodev® (Micro Resist Technology GmbH, Germany), which is a 50:50 mixture of 4-methyl-2-pentanone and 2-propanol. Afterwards, the PCL-o samples were rinsed with 2-propanol (99.8%, Labscan Ltd., Ireland). PEGda and protein samples, on the other hand, were developed with ion-exchanged water. The non-illuminated Ormocomp® was removed by immersing the samples in Ormodev® and by rinsing with either 2-propanol or hexamethyldisilazane (HMDS, Sigma-Aldrich Finland Oy, Finland).

4.5 Fabrication of UV-cured thin films

For preliminary neuronal cell viability and migration tests (Publication I), Ormocomp®, PEGda, and PCL-o prepolymer solutions containing 2 wt%, 1.5 wt%, and 3 wt% of photoinitiator, respectively, were UV-cured into thin films. A drop of the prepolymer solution was placed between a microscope slide and a coverslip separated by a 150 µm thick spacer and exposed to UV light for 10 s using a BlueWave® 50 UV curing spot lamp (DYMAX Corporation, USA) with a 300 nm to 450 nm wavelength and ~540 mW/cm^2 intensity. Afterwards, the films were placed in Ormodev® (Ormocomp® and PCL-o) or in water (PEGda) for 20 min to remove any unreacted monomer. The Ormocomp® and PCL-o samples were subsequently rinsed thoroughly with 2-propanol. The films were die cut into 6-mm-diameter samples to fit inside a 96-well plate.

For the investigation of the mechanical properties of UV-cured Ormocomp® samples in Publication IV, photoresist with 2 wt% of the photoinitiator Irgacure® 127 was polymerized into thin films. A similar curing protocol as in Publication I was used, but the development with Ormodev® and rinsing with 2-propanol was omitted. Instead, the cured films (three pieces) were left attached to the coverslips for easy access with the AFM probe.

4.6 Computer-aided design and fabrication of microstructures

In Publication I, simple 2D microstructures, such as voxels, lines, and lattices, were fabricated using the WinPos software, which converted the entered data of coordinates into xyz-stage movements and simultaneously controlled the shutter as programmed. 2D protein patterns as well as all of the 3D structures were designed with Rhinoceros® CAD (Robert McNeel & Associates, USA). The designed models were laterally sliced into closed contours having appropriate layer spacing depending on the structure geometry, and the contour data was exported either to the CorvusControl software (Publication I) or to the LaserControlSystem software (Publications II–IV). The software translated the contour information into movement coordinates and shutter commands.

4.6.1 Fabrication of voxels, lines and lattices from PCL-o and PEGda

To estimate the achievable feature size of the PCL-o and PEGda resins, arrays of voxels were polymerized with the 50× objective (N.A. = 0.90) by varying the average laser power (Publication I). Individual voxels were fabricated with an ascending scan method by programming the shutter to open and close periodically while the laser focus position was increased by 1 µm after every voxel to find the optimal focus position for creating isolated, complete voxels. Each row of voxels was polymerized with a constant laser power and the power was increased between every row from 0.8 mW to 7.5 mW (measured before the objective). In order to evaluate the effect of photoinitiator concentration on the achievable feature size, comparable voxel arrays were fabricated from PCL-o-α resins of $\alpha = 2$, 3, and 5, and PEGda-β resins of $\beta = 0.5$ and 1.5.

In addition to voxels, 2D lines and lattices were fabricated from each resin. By varying the scanning speed from 1 µm/s to 150 µm/s while keeping the laser power as a constant, or by increasing the average laser power from 1.2 mW to 7.6 mW while keeping the constant scanning speed the dependence of the line width and robustness on scanning speed and laser power could be studied. The overall size of the simple lattices was either 60 µm × 60 µm or 150 µm × 150 µm, while the distance between individual lines was 15 µm.

4.6.2 Fabrication of 3D microstructures from PCL-o and PEGda

After optimizing the polymerization processing parameters for each resin, microstructures that are more complex were fabricated according to CAD models using the CorvusControl software in Publication I. 3D fabrication capabilities were tested, for example, by polymerizing hollow bonfire-type structures. With PCL-o, contour spacing of 0.5 µm, 1 µm, 2 µm, and 4 µm was used, whereas PEGda structures were fabricated with layer spacing varying from 0.35 µm to 2 µm. PCL-o microstructures were scanned using a speed from 5 µm/s to 25 µm/s combined with an average laser power of approximately 2 mW to 3 mW. PEGda structures, however, could be fabricated with a scanning speed ranging from 30 µm/s to100 µm/s together with an average laser power of 2 mW to 3 mW.

4.6.3 Fabrication of 2D and 3D microstructures from proteins

In Publication II, simple 2D patterns, such as the arrays of seven concentric squares spaced 2 µm apart with the outer square having a side length of 25 µm, were fabricated from each of the protein solution using either the 50× objective (N.A. = 0.90) or the 100× objective lens (N.A. = 1.40). With the Nd:YAG laser setup, the concentric squares were crosslinked with scanning speeds of 5 µm/s, 10 µm/s, 20 µm/s, and 40 µm/s and varying the average laser power from 0.7 mW to 6.1 mW (measured at the back aperture of the objective). The average laser power for the Ti:sapphire laser setup was varied from 38 mW to 123 mW and the samples were scanned with speeds of 10 µm/s, 20 µm/s, 30 µm/s, 40 µm/s, and 50 µm/s.

With the Nd:YAG laser setup, the 3D fabrication ability was demonstrated by fabricating simple woodpile microstructures from BSA. The overall size of the CAD model of the woodpile was 40 µm × 40 µm × 10 µm. Fabrication of the rods of the woodpile was executed by single line scans with a 5 µm spacing between the scanning paths in the xy-direction and 1 µm between the scanning paths in the z-direction. The scanning speed used for the woodpile fabrication was 10 µm/s and the average laser power was 5.7 mW.

Avidin and bBSA combined with Irgacure® 2959 were also photocrosslinked into 2D single neuron guidance patterns (Figure 25) comprising a 25 µm wide round node area to promote the attachment of a cell soma, and a continuous line departing from the node to promote the differentiation of rapidly extending neurites into axons (unpublished data). Five interrupted lines radiating from the node were intended to encourage the formation of dendrites by slowing down the neurite growth. In addition, the continuous line was capped with a 10 µm diameter node intended to allow the growth cone of a neurite to spread out after reaching the end of the path. The continuous line was designed to be 45 µm long and have a width of 4 µm. Discontinuous lines comprised 5 µm long and 4 µm wide cues separated by a distance of 5 µm. These neuron guidance patterns were fabricated with a 20× oil immersion objective (N.A. = 0.75, Nikon) by multipath scanning method, in which each feature was formed by scanning adjacent or concentric contours separated by a distance of 0.5 µm. A 4 × 4 array of protein guidance patterns was fabricated on each coverslip.

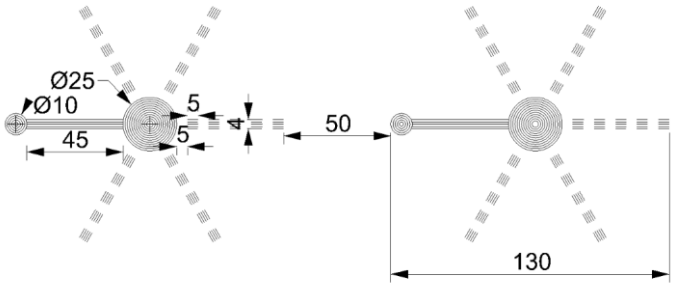

Figure 25. The design of the 2D single neuron guidance patterns. The dimensions are given in micrometers.

In order to avoid damaging the crosslinked protein patterns via laser-induced material breakdown and micro-bubbling during fabrication, the damage threshold values were determined for both protein solutions for the chosen scanning speeds. For the determination of damage threshold value, the laser focus was positioned inside the protein solution volume to exclude any interaction with the glass surface, and the laser power value was gradually increased while polymerizing simple square patterns at a constant scanning speed. The damage threshold was defined as the average laser power value where the microexplosions first started to emerge. For bBSA, the damage threshold was determined as 8.9 mW while scanning the laser beam at a speed of 50 µm/s. The damage threshold for avidin was measured as 9.6 mW for the scanning speed of 14 µm/s. bBSA patterns were fabricated with a laser power of 8.0 mW corresponding to 90% of the damage threshold and avidin patterns with a power value of 6.7 mW corresponding to 70% of the damage threshold.

4.6.4 Determination of polymerization window and feature size for Ormocomp®

Implementation of the motorized attenuator in the third generation fabrication setup enabled the accurate determination of the window of practical operation for the fabrication of Ormocomp® microtowers with good quality (Publication IV). The polymerization windows (P_w) were determined for scanning speeds 150 µm/s, 350 µm/s, and 550 µm/s. The polymerization window was calculated as the power range between the polymerization (P_{th}) and the damage thresholds (P_D). For the threshold value determination, the laser focus was positioned inside the resist volume and the laser power value was gradually increased while polymerizing square patterns with the chosen scanning speed. The polymerization threshold was defined as the lowest average laser power that yielded to a barely visible polymerized pattern and the damage threshold as the power value where the microbubbling first emerged. The average threshold values were calculated from the measurements made from four separate samples. To ensure a large enough margin for the damage-free fabrication without the appearance of microexplosions due to the laser power fluctuation or the inhomogeneity of the resin, microtowers were chosen to be fabricated with power values corresponding to 70% of the polymerization window according to the formula $P = P_w \times x + P_{th}$, where P_w is the polymerization window, P_{th} is the polymerization threshold and $x = 0.7$ is the power factor.

In order to determine the achievable feature size for the chosen scanning speeds and the optimal slicing distance for the contours, suspended lines were polymerized between supporting wall structures with scanning speeds of 150 µm/s, 350 µm/s, and 550 µm/s. All of the suspended lines were fabricated with the average laser power values corresponding to 70% of the polymerization window determined previously for each scanning speed.

4.6.5 Fabrication of 3D microstructures from Ormocomp®

In order to control the location of neurons and direct the growth of neurites on predefined axes, three novel prototypes of 3D confinement microstructures (Figure 26), called neurocages, were designed and fabricated from Ormocomp® in Publication III. The neurocages comprised so-called nodes and channels. The node diameter was chosen to be 40 µm, and the channel width was set to 5 µm in order

to ensure that neurites could easily fit inside the channels. The cage wall height was set to 25 µm. For 2PP-DLW, the neurocage models were sliced in the z-direction into contours having 1µm spacing. The neurocages were polymerized using the 50× objective, average laser power from 1.0 mW to 1.4 mW, and scanning speed of 120 µm/s. The cages were produced using the multipath scanning method, i.e., the cage walls were formed by two sets of contours separated by a distance of 1 µm.

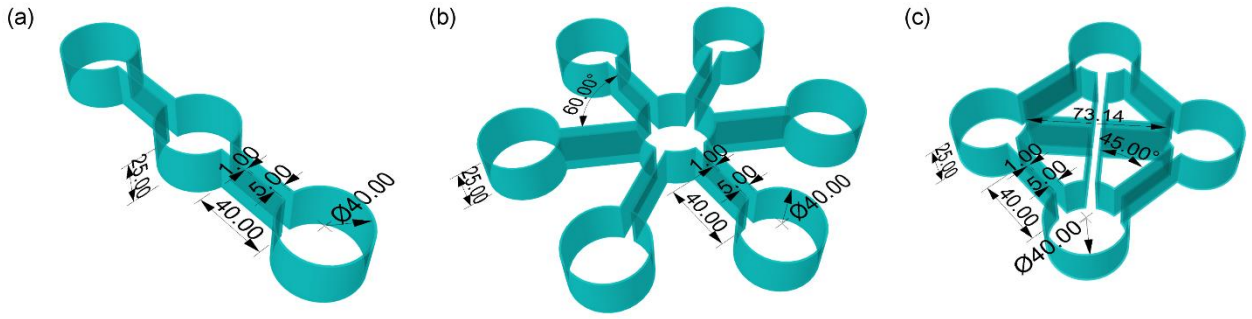

Figure 26. Neurocage designs: (a) type I, (b) type II and (c) type III. The dimensions are given in micrometers.

In Publication IV, tubular microtowers with structural intraluminal guidance cues were designed to study their ability to support the adhesion, migration, and orientation of neuronal cells. The outer shell of the towers was a 150 µm high cylinder with an outer diameter of 77 µm and an inner diameter of 75 µm. The cylinder was designed to have openings at the foot of the tower for cells to enter, and in the upper part of the tower to allow an efficient flow of medium also in the lumen of the tower. Two different shapes for the openings, i.e., elliptical and rectangular, were tested to find the one that best retained its shape and size after polymerization. A set of five longitudinal micropillars inspired by the axonal tracts present *in vivo* were placed inside the tower to offer oriented topography for neurites to migrate along the channel. The diameter of the pillars was set to 5 µm to achieve thin but robust enough structures. Spider web-like platforms were inserted on top and halfway down the tower to further increase the surface area for cells to attach to and for neuronal somas to remain stationary. Two different designs for the spider webs were tested: the dense web comprising three concentric polygons with 5 µm line spacing and the sparse web comprising two concentric polygons with 10 µm spacing.

As a comparison, hollow microtowers with and without openings were also designed. In total, six different microtower designs were drawn: designs I & II (Figure 27(a & b)) had elliptical openings with dense or sparse webs, designs III & IV (Figure 27(c & d)) had rectangular openings with dense or sparse webs, design V (Figure 27(e)) was a hollow cylinder with rectangular openings, and design VI (Figure 27(f)) was a hollow cylinder without any openings.

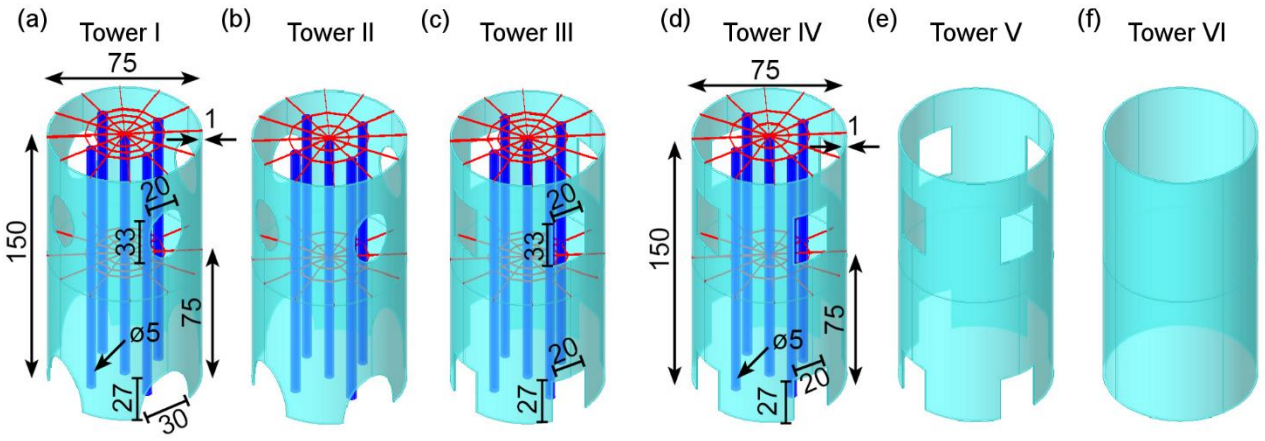

Figure 27. Microtower designs: (a) design I with elliptical openings and dense webs, (b) design II with elliptical openings and sparse, (c) design III with rectangular openings and dense webs, (d) design IV with rectangular openings and sparse webs, (e) design V with rectangular openings, and (f) design VI without openings. The dimensions are given in micrometers.

The microtower designs I–VI were polymerized using the 50× objective. The cylinders and pillars were fabricated using the multipath scanning method, in which the cylinder walls were formed by two nested contours separated by a distance of 1 µm, and the micropillars by three nested contours separated by a distance of 1 µm. Because the spider webs were polymerized as single line scans, a moderate scanning speed of 150 µm/s had to be used in order to achieve robust and untwisted threads. For the cylinders and pillars, scanning speeds of 350 µm/s and 550 µm/s were tested to optimize the fabrication time versus surface quality of the structures. For each scanning speed, the average laser power corresponding to the predetermined 70% of the polymerization window was used. In order to explore the intraluminal architecture of the microtowers with SEM imaging, longitudinal cross-sections of design II and IV towers were also fabricated with the scanning speeds of 350 µm/s and 550 µm/s.

4.7 Characterization of microstructures

The optical microscope included in all of the fabrication setups was used for sample imaging and analysis before and after development. The 50× oil immersion objective used in polymerization was also used for real-time monitoring of the polymerization process and for pre-development sample imaging. After the development procedure, a 20× air objective was utilized for imaging and visual evaluation of the sample quality. Scanning electron microscopy (SEM), atomic force microscopy (AFM), and wide-field fluorescence microscopy were used for more detailed characterization of the fabricated microstructures.

4.7.1 Scanning electron microscopy

In Publication I, PCL-o and PEGda structures were sputter coated with gold (S 150 Sputter Coater, Edwards Ltd., UK) in an argon atmosphere to a coating thickness of approximately 60 nm and imaged by SEM (Philips XL-30, Philips Electron Optics, the Netherlands). The dimensions of voxels, lines

and lattices were measured from the top view (0° tilt) or side view (25° to 30° tilt) SEM images with the free image processing software, GIMP 2.6 (GNU Image Manipulation Program, The GIMP Team). From the SEM images of the voxel arrays, complete, but still surface-bound voxels were selected for measurement purposes. As robust and measurable arrays of lines could only be fabricated from PEGda-1.5 and PEGda-1, simple lattice structures were used to study the combined effect of the average laser power and scanning speed on achievable feature sizes. The dimensions of the lattice walls were estimated from the side view SEM images.

In Publication II, protein samples were fixed in 5% (v/v) glutaraldehyde for 15 min, and then dehydrated by sequential immersion for 15 min in ion-exchanged water, 1:1 ethanol/H_2O, 100% (v/v) ethanol, 1:1 ethanol/methanol and 100% (v/v) methanol (twice). After overnight drying in a desiccator, the samples were sputter coated with gold in an argon atmosphere to a nominal thickness of 75 nm or 15 nm (S 150 Sputter Coater or SCD 050 Sputter Coater, BAL-TEC AG, Liechtenstein). The samples were imaged using either Philips XL-30 or JEOL JSM-6390 LV (JEOL Ltd., Japan) SEM. The line widths were measured from the top view (0° tilt) SEM images and the line heights from the side view (45° tilt) images with GIMP 2.6. The topography of the 2D and 3D protein patterns was also analyzed visually by comparing the SEM images of structures fabricated with the two different laser sources and different protein compositions.

Avidin and bBSA neuron guidance patterns crosslinked in the presence of Irgacure® 2959 (unpublished data) were sputter coated with gold to a nominal thickness of 38 nm (S 150 Sputter Coater) without any preceding fixation or dehydration steps. The samples were imaged with Zeiss ULTRA Plus FESEM (Carl Zeiss Microscopy GmbH, Germany) and the pattern dimensions were measured from the top view (0° tilt) and side view (60° tilt) SEM images with GIMP 2.8.

In Publication III, the fabrication accuracy of neurocages with the 2PP-DLW setup was evaluated by examining type III neurocages with SEM and by comparing the measured dimensions with the original CAD design. For SEM imaging, samples were sputter coated with gold in an argon atmosphere to a nominal thickness of 113 nm (S 150 Sputter Coater). Imaging was performed with a Philips XL-30 SEM. The acquired SEM images were analyzed with GIMP 2.8. The neurocage node diameter, channel length, channel width, and wall thickness were measured from the top view (0° tilt), and wall height from the side view (90° tilt) SEM images. The surface texture of the cages fabricated with the scanning speed of 120 μm/s was evaluated from the SEM images taken with a tilt angle of 60° by measuring the width of the ridges.

In Publication IV, the dimensions of the fabricated Ormocomp® suspended line structures and microtowers were analyzed by SEM imaging with Philips XL-30. Prior to imaging, the samples were sputter coated with gold in an argon atmosphere either to a nominal thickness of 113 nm (S 150 Sputter Coater) or 60 nm (SCD 050 Sputter Coater). The feature dimensions were measured from top (0° tilt) and side (90° tilt) view SEM images with GIMP 2.8. The degree of voxel overlap for the chosen contour distances was calculated as the product of voxel displacement in axial and lateral directions according to the following equation:

$$\delta = \frac{w - dx}{w} \times \frac{h - dz}{h}, \tag{13}$$

where δ is the degree of the voxel overlap, *w* and h are the width and height of the voxel, and *dx* and *dz* are the lateral and axial voxel distances, respectively (Žukauskas *et al.* 2012).

4.7.2 Atomic force microscopy

In Publication II, patterns of concentric squares of avidin and BSA were also studied by non-contact mode AFM (XE-100, Park Systems Inc., USA) before SEM imaging to verify the dimension measurements from SEM images and to study the surface topography of the structures. Measurements were performed using silicon probes (ACTa-910M, Applied NanoStructures Inc., USA) with a nominal resonance frequency of 300 kHz, spring constant of 4 N/m, a pyramidal-shaped tip (radius < 10 nm) and an aluminum reflective coating. Images were acquired with a scan speed of 0.15 Hz or 0.40 Hz. The dimensions and surface topography were analyzed from AFM images with the XEI image processing software (Park Systems Inc., USA).

In Publication IV, the surface roughness of the microtower cylinder walls was investigated by non-contact mode AFM (XE-100). For the imaging, the coverslip containing the microtowers was mounted in upright position on the xy-scanning stage in order to access the surface of the walls of the towers with the AFM cantilever. Measurements were performed using silicon probes (ACTa) with a nominal resonance frequency of 300 kHz, spring constant of 40 N/m, a tetrahedral pyramidal-shaped tip with a face angle of 18°. Images were acquired with a scan rate of 1.0 Hz. Areas of 10 µm × 10 µm in size were imaged from the cylindrical walls of each tower design (IV, V, and VI). From the two designs with the openings, images were acquired from two different locations of the cylinder: the sections with smoother surface and the sections located between the openings with a seemingly rougher texture. The roughness of the surface was analyzed from AFM images with the XEI image processing software (version 1.8.0, Park Systems Inc., USA). The curvature resulting from the cylindrical shape of the tower wall was removed from the acquired images by utilizing the flattening tool with second order fitting curve in the x-direction. As the microtowers appeared to be tilted in the y-direction to some extent, the slope was eliminated by also flattening the images in the vertical direction with a first order-fitting curve. The surface roughness was defined as the average areal surface roughness (R_a).

The stiffness of the polymerized structures is mainly expressed by the Young's modulus of the used material. It should be at a sufficient level for the microstructures to withstand the handling and cell culture procedures without failure. Thus, force spectroscopy measurements were performed with AFM to estimate the Young's modulus of Ormocomp®. The elastic properties of the sample were investigated with AFM force curves by recording the applied force and the depth of indentation as the tip was pushed against the sample surface (Heinz & Hoh 1999). Force-indentation curves were recorded at three points from each tower design by scanning areas of 15 µm × 15 µm from the upper

rim of the cylinder with a scan rate of 0.5 Hz. For comparison, similar sized areas were also recorded from the three UV-cured Ormocomp® thin films.

One of the most commonly used models for deriving the elastic modulus from force curve data is the Hertz model (Hertz 1882), which gives the force on a spherical tip as a function of the elastic properties of the material, the radius of the tip, and the indentation depth (Johnsson 1985). A modified Hertz model (Bilodeau 1992) for a four-sided pyramidal indenter is as follows:

$$F = \frac{E}{1-\nu^2}\frac{\tan\alpha}{\sqrt{2}}\delta^2, \tag{14}$$

where F is the indentation force applied to the sample, E is the Young's modulus, ν is the Poisson's ratio of the sample (was set to 0.35 according to (Li *et al.* 2014)), δ is the indentation depth, and α is the face angle of the pyramidal tip (18° in our case). The cantilever deflection during the indentation was taken into account in XEI by transforming the Force-Z displacement curve to Force-Separation curve via cantilever's spring constant value (k). The spring constant of the cantilever was not calibrated prior to the analysis. Instead, the nominal value of k = 40 N/m quoted by the manufacturer was used. Stiffness data was calculated automatically with XEI from the slopes of the force curves after fitting with the Hertz model.

4.7.3 Fluorescence microscopy

The ability of avidin and bBSA to retain their bioactivity and to form avidin-biotin complexes after photocrosslinking with the Nd:YAG laser was demonstrated in Publication II. Avidin microstructures were incubated in 2 μM DY-634-Biotin label (Dyomics GmbH, Germany) and bBSA structures in 20 μg/ml DyLight® 649 Streptavidin conjugate label (Vector Laboratories, Inc., USA) for 30 min. Afterwards, the excess fluorescence label was removed by immersing the labelled structures in ion-exchanged water for 1 h. Wide-field fluorescence imaging was performed on an Eclipse TS100 inverted microscope (Nikon) equipped with a mercury lamp excitation source and a 20× dry objective (NA = 0.40, Nikon). Fluorescence emission was collected by using a BrightLine® LF635-A-NQF filter set (Semrock, Inc., USA) and detected using a digital camera (SPOT RT TM SE6 Slider, Diagnostic Instruments, USA) with a 12-bit 1360 × 1024 Sony ICX-285AL CCD. Image acquisition was accomplished using SPOT Software 4.6 (Diagnostic Instruments, Inc., USA) and the data were processed with the ImageJ image analysis software (Version 1.39, U. S. National Institutes of Health, USA).

4.8 Statistical analysis

Most of the quantitative data is represented as the arithmetic mean ± standard deviation. In addition, in Publication IV, statistical tests were performed with IBM SPSS-software (version 23, IBM, USA) to highlight the significant differences between the variables. Statistical analysis was performed using

nonparametric Kruskall-Wallis test followed by Dunn-Bonferroni tests or Mann-Whitney U test. The $p < 0.05$ or $p < 0.01$ was considered significant.

4.9 Cell culture experiments

In Publication I and in co-authored publication about the microfabrication of Ormocomp® (Käpylä *et al.* 2010), the possible cytotoxicity and suitability of the used material-photoinitiator combinations (PEGda, PCL-o and Ormocomp® with Irgacure® 127) for neuronal cell culture was evaluated by utilizing the UV-cured thin films as culture substrates for hPSC-derived neuronal cells. In order to disinfect the samples for the cell culture experiment, UV-cured films were immersed into 70% (v/v) ethanol twice for 15 min and 30 min. After the disinfection, the samples were immersed in sterile Na-PBS buffer solution for three times 30 min. Four parallel disinfected samples of each material and control laminin (mouse origin, solution 10 µg/ml, Sigma-Aldrich Finland Oy) coated polystyrene surfaces were used as substrates for cell culture.

A total of 14 polymerized protein samples with 4 × 4 arrays of 2D single neuron guidance patterns (12 × bBSA and 2 × avidin) were disinfected with 70% ethanol for 15 min and used to study how the individual hPSC-derived neuronal cells attach, grow, and orient on top of the patterns (unpublished data). In Publication III, the ability of 3D confinement microstructures fabricated from Ormocomp® to control the location of neurons and direct the growth of neurites on predefined axes was assessed by culturing hPSC-derived neuronal cells on samples containing two different types of these neurocage structures. Four parallel samples with four or six pieces of type I neurocages, and four samples with four pieces of type III neurocages were polymerized on microscope glass slides. Samples were disinfected with 70% (v/v) ethanol for 15 min. Additionally, all samples with type I neurocages were also immersed in Dulbecco's phosphate buffered saline (DPBS, Lonza Group Ltd., Switzerland) for approximately 65 h.

In Publication IV, three of the six microtower designs (designs IV–VI) were investigated for their ability to support the adhesion, migration and orientation of hPSC-derived neuronal cells. Six parallel samples per time point with an array of nine microtowers comprising three pieces of each design (IV, V, and VI) were fabricated on MAPTMS-coated round glass coverslips (Ø = 9 mm). The distance between individual towers of the same design was ~90 µm and between different designs of towers ~260 µm. Cover slips containing microtowers were disinfected with 70% (v/v) ethanol for 15 min, immersed in DPBS for 2 hours at +4 °C, and let to air dry.

4.9.1 Functionalization of protein patterns

The patterns of avidin and bBSA were functionalized with ECM-derived peptide sequences via avidin-biotin interaction (unpublished data). These peptide sequences were intended to replace the nonspecific coating of the cell culture plates with the major protein component of the ECM, laminin, which is known to be essential for the attachment of neurons on glass surfaces. Thus, the tested biotinylated peptides included laminin-derived peptide sequences: biotin-(LC)-

CSRARKQAAS**IKVAV**SADR (TAG Copenhagen A/S, Copenhagen, Denmark), biotin-(LC)-CDPG**YIGSR** (TAG Copenhagen A/S), biotin-(LC)-G**RGD**S (Nordic BioSite AB, Täby, Sweden), and biotin-labeled laminin (α1β1γ1) with a 14 atom spacer (Cytoskeleton Inc., Denver, USA). Samples were inserted into 6-well plates and PDMS chambers with a round cell-attachment area in the middle (Ø = 2 mm, h = 0.5 mm) and a larger cell medium reservoir (Ø = 12 mm, h = 6 mm) were put on the patterned coverslips. bBSA patterns were first treated with avidin (1.0 mg/ml) for 2 min at room temperature. Avidin was washed once with sterile PBS. Sterile filtered biotin-linked peptide solutions (10 µg/ml) were incubated on avidin treated protein patterns for 30 min at +37 °C. Finally, the peptide solutions were washed off with PBS. The sample compositions for cell culture are summarized in Table 3. Biotinylated BSA patterns with or without avidin treatment, and avidin patterns, served as negative controls. Two parallel samples of each composition were used.

Table 3. Tested compositions of proteins and ECM-derived peptides for cell culture.

Composition	Pattern material	Avidin treatment	Peptide functionalization
1	Biotinylated BSA	yes	IKVAV
2	Biotinylated BSA	yes	YIGSR
3	Biotinylated BSA	yes	RGD
4	Biotinylated BSA	yes	Biotinylated laminin
5	Biotinylated BSA	yes	–
6	Biotinylated BSA	no	–
7	Avidin	no	–

4.9.2 Application of laminin

In order to provide essential attachment points for neurons, samples were coated with laminin, a key glycoprotein component of the ECM, in Publications III and IV. In Publication III, laminin was applied with a semi-automatic microinjection system consisting of the joystick-controlled MANi-PEN micromanipulator (developed at the Department of Automation Science and Engineering, Tampere University of Technology, Finland), a pressure injector (MPPI-2, Applied Scientific Instruments, USA), a vision system (a Nikon Eclipse TS100F inverted microscope, Nikon), and software (Viigipuu & Kallio 2004). The micromanipulator was equipped with capillaries with tip diameters of approximately 5 µm or 10 µm. The neurocages on the sample were located under the microscope and the nodes were filled with laminin solution by carefully moving the capillary tip over the neurocages. A solution of 50 µg/ml laminin (Sigma-Aldrich Finland Oy) in DPBS was applied with injection pressure of 150 mbar and a pressure pulse of 6000 ms. In order to prevent the crystallization of the laminin, a humidified atmosphere was created by placing the samples in a hot water bath for the application phase. After the application of laminin, samples were kept at +4 °C overnight to enable proper coating of the glass surface inside the neurocages. In Publication IV, microtower samples were coated using mouse laminin (10 µg /ml, Sigma-Aldrich Finland Oy). The laminin coating solution was incubated on samples for 72 hours at +4 °C.

4.9.3 Plating and culturing of cells

The stem cells had been pre-differentiated for 8 weeks (Publications I, IIII, & unpublished data) or 13 weeks (Publication IV) towards neuronal fate in neural differentiation medium (NDM) in the presence of basic fibroblast growth factor (bFGF) as described in (Lappalainen *et al.* 2010; Skottman 2010). Two different cell-plating methods were used for the experiments: administration of cell aggregates and plating as a droplet of a single cell suspension. Administration of cell aggregates involved cutting of neurospheres into smaller aggregates comprising more than 90% of young neurons, some astrocytes and non-neural, epithelial-like flat cells (Publication I). In the single cell suspension method, neurospheres were enzymatically dissociated into single cell solution using TrypLE™ Select 1× (Thermo Fisher Scientific Corporation, USA) as in Publications III, IV, and in an unpublished protein study, or trypsin 1× (Lonza Group Ltd.) as in Publication III and plated as a droplet on top of the sample surface. In the unpublished protein pattern study, cells were plated at a density of ~13 000 cells/cm^2. In Publication III, approximately 1×10^5 cells were applied on the neurocage samples yielding to a density of ~130 000 cells/ cm^2, and in Publication IV a density of ~35 000 cells/cm^2 was used.

Neuronal cells were plated in NDM without bFGF in order to initiate neuronal maturation. Between day two and five, NDM was replaced with 5+NDM containing bFGF (4 ng/ml, R&D Systems Inc., USA) and brain-derived neurotrophic factor (BDNF, 5 ng/ml, ProSpec-Tany TechnoGene Ltd., Israel) to enhance the cell growth. In Publication III, for cells in type I neurocages, conditioned NDM was added to enhance the viability of the small neuronal cell population. Cells were cultured on samples for five days (Publication III, type I neurocages), seven days (Publication I), eight days (Publication III, type III neurocages), 14 days (unpublished protein pattern study), or 28 days (Publication IV). The cell culture medium was changed three times a week.

4.9.4 Evaluation of viability

After the culture period of 7 days (Publications I & IV), 14 days, or 28 days (Publication IV), the viability of the cells was evaluated using a Live/Dead® Viability/Cytotoxicity Kit for mammalian cells (Thermo Fisher Scientific). Live cells were dyed with calcein acetoxymethyl ester (0.1 μM, green fluorescence) and dead cells with ethidium homodimer-1 (0.4 μM, red/yellow fluorescence). After 30 min of incubation at +37 °C, stained samples were visualized with a fluorescent microscope (Olympus IX51, Olympus Corporation, Japan).

4.9.5 Characterization via immunocytochemical staining

In Publications III and IV, and in the unpublished protein study, cell cultures were analyzed with immunocytochemistry. Cells were fixed for 20 min or 30 min using 4% paraformaldehyde (Fluka, Italy) and stained with neuronal, astrocytic, and cytoskeletal markers. Unspecific staining was blocked and cell membranes were permeabilized for 30 min or 45 min at room temperature with a solution containing 1% BSA, 10% normal donkey serum (NDS), and 0.1% saponin or Triton-X 100

in DPBS (all from Sigma-Aldrich Finland Oy). After blocking, samples were washed once with 1% NDS, 0.1% saponin or Triton-X 100, and 1% BSA in DPBS. Next, primary antibodies were incubated with cells at +4 °C overnight. The following day, the cells were washed three times with 1% BSA in DPBS and incubated with secondary antibodies for 1 hour at room temperature. The used primary and secondary antibodies are collated in Table 4. In Publication III and in the protein study, the samples were then washed three times with DPBS and mounted with VECTASHIELD® Mounting Media with 4′,6-diamidino-2-phenylindole (DAPI, Vector Laboratories Inc., USA). In Publication IV, DAPI (0.2 µg/ml, Sigma-Aldrich Finland Oy) in DPBS was added to the microtower samples and incubated for 15 min. Finally, the cells were washed twice with DPBS and mounted with TDE Mounting media (Abberior GmbH, Germany), 2,2'-thiodiethanol-based embedding media with a refractive index of 1.518 that matched perfectly with the refractive index of Ormocomp®. The embedding media was used to minimize the spherical aberration that causes a scattering of light and a blurring of the images. In Publication III and in the unpublished protein study, immunostained samples were immediately imaged with a microscope (IX51, Olympus Corporation) equipped with a fluorescence unit.

Table 4. Primary and secondary antibodies used for immunocytochemical staining.

Primary antibody abbreviation	Primary antibody full name	Origin	Supplier	Dilution	Secondary antibody	Supplier	Publication
MAP-2	Microtubule-associated protein, for neuronal dendrites	Rabbit	Merck Millipore	1:400	Alexa Fluor® 488 donkey anti-rabbit	Thermo Fisher Scientific	Unpublished data, III & IV
β-tub	β-tubulin isotype III, for neuronal axons	Rabbit	Sigma Aldrich Finland Oy	1:1000	Alexa Fluor® 488 donkey anti-rabbit	Thermo Fisher Scientific	Unpublished data
				1:1250	Alexa Fluor® 568 donkey anti-sheep		IV
GFAP	Glial fibrillary acidic protein antibody, for astrocytes	Sheep	R&D Systems	1:2000	Alexa Fluor® 568 donkey anti-sheep	Thermo Fisher Scientific	Unpublished data
				1:800			III
Phalloidin	Alex Fluor® 680 phalloidin, for actin fibers in cytoskeleton	Mushroom	Thermo Fisher Scientific	1:200	–	–	Unpublished data

4.9.6 Confocal imaging and image analysis

In Publication IV, confocal images were acquired with a Zeiss LSM 780 mounted into an inverted Cell Observer microscope (Carl Zeiss, Germany) using 63× (N.A. = 1.40, Zeiss Plan Apochromat, Carl Zeiss) and 25× (N.A. = 0.80, Zeiss LD LCI Plan-Apochromat, Carl Zeiss) objectives. The confocal data was visualized with the ZEN Black 2012 SP1 software (version 8.1, Carl Zeiss) and

ImageJ (U. S. National Institutes of Health). For cell number analysis, confocal image stacks were divided into 15 µm thick substacks, and cell nuclei were counted with the Cell Counter ImageJ plugin. The data were further rearranged to represent the proportion of cells attached to smooth and rough surfaces, the total cell number in the microtowers, and the proportion and longitudinal distribution of cells inside the towers.

For analyzing neurite orientation inside the microtowers, orthogonal projections were created from confocal image stacks. To exclude the cells growing on the outer surface of the towers, cropped slices representing only the center part of the towers were analyzed. These slices were projected into 2D via the maximum intensity projection function in ImageJ. The projection represented 50% of the total microtower volume. Orthogonal projections were analyzed with a spectral analysis software tool, CytoSpectre (Kartasalo *et al.* 2015), to quantify the circular variance and mean orientation of the neurites inside the towers. Circular variance is a measure of the uniformity of the orientation distribution. It varies from 0 to 1. The value of 1 describes a situation where the neurites are spread evenly in all angles lacking a dominant direction, whereas a value of 0 signifies a case of perfect alignment along a single orientation angle. In addition, the orientation angles of all neurite segments having a length of ≥ 5 µm were traced and measured manually with ImageJ from the same orthogonal projections. In total, ~3200 neurite segments were measured. The angle of each segment was calculated relative to the vertical plane and all orientation angles across the 0° to 90° spectrum were then binned in 10° sections. This method was adapted from Tuft *et al.* (Tuft *et al.* 2014). A lack of neurite alignment would thus be supported by a relatively equal distribution of neurite segment angles across the whole angle spectrum, whereas strong alignment to the longitudinal direction would be evidenced by a high incidence of neurite segments with angles $\leq 20°$.

4.9.7 Analysis of cells by SEM Imaging

The 3D morphology and organization of neuronal cells were assessed by SEM imaging in Publication IV. Prior to imaging, samples were fixed with 5% glutaraldehyde (Sigma-Aldrich Finland Oy) in DPBS (pH 7.4) at room temperature for 1 hour. Afterwards, the samples were immersed in ion-exchanged water for 15 min. Next, the samples were dehydrated using an ascending series of ethanol concentrations (10%, 20%, 40%, 60%, 80%, 99.5%, v/v) for 10 min each. Finally, the samples were air dried and stored under vacuum. After drying, the samples were sputter coated with gold in an argon atmosphere (S 150 Sputter Coater) to a coating thickness of approximately 75 nm. Samples were analyzed by SEM imaging with a Philips XL-30.

5 RESULTS

5.1 Comparison of photosensitive materials

To assess the suitability of several photosensitive materials and photoinitiators for the efficient fabrication of microstructured cell culture platforms by 2PP-DLW, optimal processing parameters, overall processability, achievable feature size, retention of bioactivity after processing, and possible cytotoxicity of the used material-photoinitiator combinations were studied. Investigated materials were compared according to the results and the most promising candidates were chosen for subsequent cell culture studies.

5.1.1 Absorption spectra

The suitability of the chosen photoinitiators, Irgacure® 127 and FMN, for 2PP-DLW with the wavelength of 532 nm was verified by the measuring of their UV-Vis absorption spectra (Publications I & II). The absorption spectra measured for PCL-o and PEGda with and without Irgacure® 127 are shown in Figure 28.

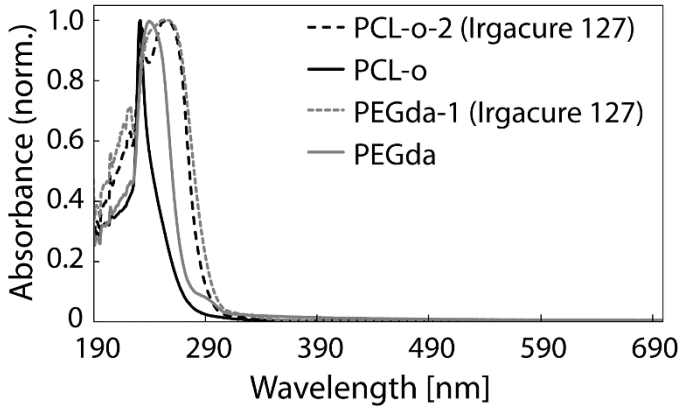

Figure 28. Normalized UV–Vis absorption spectra of PCL-o and PEGda with and without the Irgacure® 127 photoinitiator.

The absorption spectra in Figure 28 show that neither PCL-o nor PEGda with 2 wt% or 1 wt% of photoinitiator exhibited absorption at the spectral region near 532 nm, which demonstrated that both materials are transparent to the laser beam and that single-photon absorption was not involved in the polymerization process. However, both resins showed strong absorption even without photoinitiator, indicating absorption at the double bonds. The addition of the photoinitiator into the resins shifted the absorption maxima towards the wavelength of 260 nm, where the 2PA window for the Nd:YAG laser lies.

The absorption spectrum of FMN in water is shown in Figure 29.

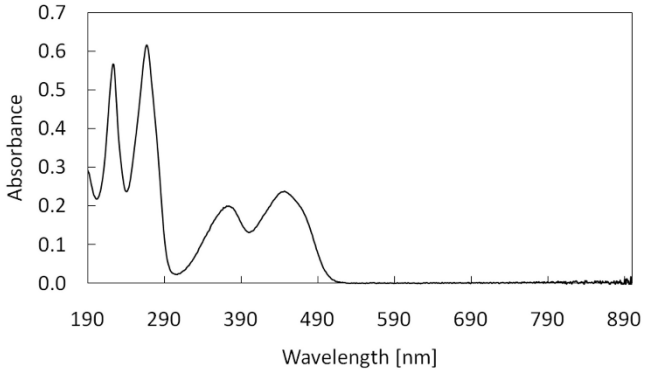

Figure 29. Normalized UV-Vis absorption spectrum of FMN in water.

FMN has four linear absorption maxima at 223 nm, 267 nm, 374nm, and 447 nm. It exhibits no absorption above 527 nm but absorbs strongly in the UV region, where the two-photon absorption windows of the lasers utilized in Publication II are located.

5.1.2 Evaluation of achievable feature size and optimal process parameters

The characterization of voxel scaling is fundamental, because the lines can be defined as a continuum of voxels. However, it is important to also figure out the scaling of the line dimensions with the laser power and scanning speed, since the fidelity of the fabricated structures depends on the line dimensions. The fabrication precision is in turn a trade off with the writing time and the desired outcome can be achieved with various combinations of laser power and scanning speed. (Guney & Fedder 2016) Because the biodegradable poly(ε-caprolactone)-based oligomer (PCL-o) had not been previously processed with 2PP-DLW, it was essential to investigate the overall processability of the material as well the achievable feature size with the used fabrication setup (Publication I). Also, 2PP-DLW fabrication of PEGda hydrogel with a picosecond Nd:YAG laser had not been previously reported. The dimensions of voxels created with an ascending scan method were measured from SEM images. The effect of photoinitiator concentration on feature size is demonstrated in Figure 30, which presents the voxel width and voxel height as a function of the average laser power. Voxels polymerized from PCL-o-α (α = 2, 3 or 5 wt%), PEGda-0.5, and PEGda-1.5 were measured.

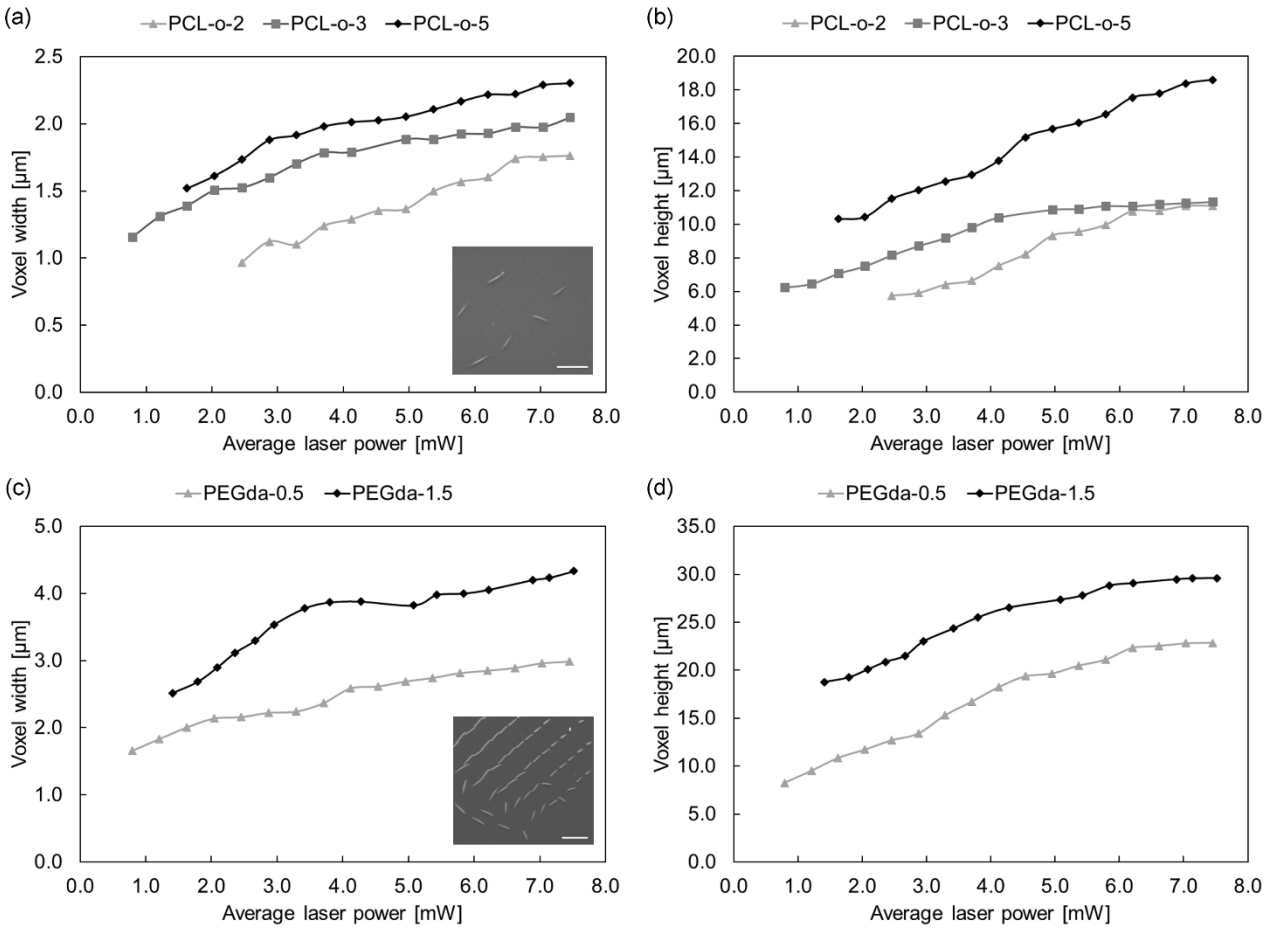

Figure 30. Voxel dimensions as a function of the average laser power measured before objective for (a, b) PCL-o-2, PCL-o-3 and PCL-o-5, and for (c, d) PEGda-0.5 and PEGda-1.5. Inserts show SEM images of the smallest voxels fabricated from PCL-o-2 (a) and PEGda-0.5 (c). Scale bars represent 20 µm.

As expected, the voxel dimensions increased approximately linearly with laser power in all investigated material-PI compositions as the exposure dose at the focal spot increased leading to a higher amount of polymerization. On some occasions, the voxel dimensions have even started to saturate as the monomer or PI concentration has dropped in the confined volume around the focal spot. However, this phenomenon is not present in all curves, as the saturation point could not be achieved because only a few attenuators were available, which limited the adjustability of the laser power range.

Voxel dimensions also increased with increasing PI concentration because of the increased formation of initiating radicals per unit volume. This led to spreading of the polymerization process across a larger volume as the concentration of the initiating radicals was increased above the polymerization threshold also in the Gaussian wings of the beam intensity profile.

Overall, PCL-o produced smaller voxels than PEGda within the available laser power range used for the polymerization of the voxels. The smallest voxel polymerized from PCL-o-2 had a width of 1.0 µm and a height of 5.7 µm, whereas the smallest PEGda voxel had a width of 1.7 µm and a height

of 8.2 µm. The aspect ratio (i.e., the voxel height divided by the voxel width) of the polymerized voxels varied from 5.0 to 8.1 for PCL-o and from 4.8 to 8.0 for PEGda. The width of the diffraction-limited focal spot can be estimated as the size of the Airy disc: $d_{zero} = 1.22\lambda/NA$ = 720 nm. Hence, even the smallest fabricated voxels were wider than the diffraction-limited focal spot suggesting that the minimum achievable voxel size could not be reached in this study by fine-tuning only the laser power with the pump diode current.

The scaling of the line dimensions with the average laser power and scanning speed was studied by polymerizing line arrays and lattice-like structures from PCL-o and PEGda. Examples of the line arrays polymerized from PEGda-1 with a constant scanning speed and by increasing the laser power are shown in Figure 31.

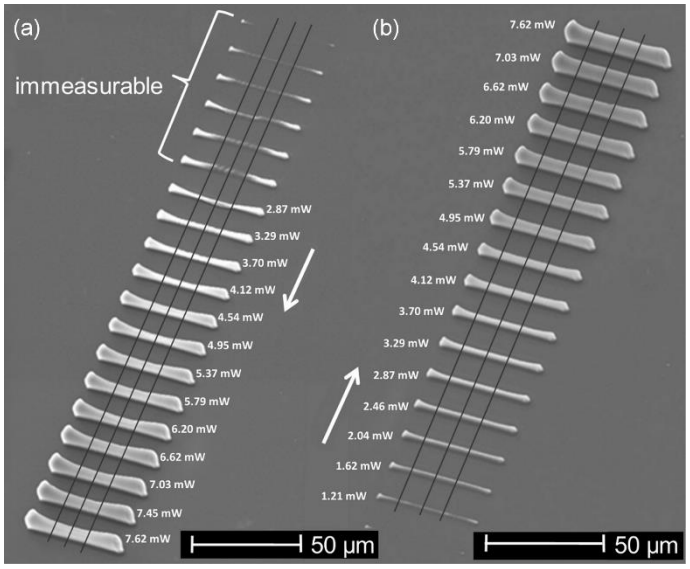

Figure 31. SEM images of PEGda-1 line arrays polymerized with the constant scanning speed of (a) 100 µm/s and (b) 50 µm/s by increasing the average laser power (measured before objective) in the direction of the white arrows. The black lines perpendicular to the polymerized lines mark the points of measurements. The word "immeasurable" denotes the lines that were not completely polymerized and were thus omitted from the analysis.

Line arrays robust enough for feature size analysis could only be fabricated from PEGda-1.5 and PEGda-1. Lines fabricated from PEGda-1.5 and all PCL-o compositions collapsed immediately after the polymerization. These lines were very thin and, apparently, were not mechanically robust enough to sustain their original shape. Thus, lattice-like structures were fabricated instead of line arrays for the feature size measurements. As can be seen from the SEM images of PEGda-0.5 and PCL-o-2 lattices (Figure 32), the increase in the line height as a function of the average laser power was substantial (from 1.6 µm to 4.0 µm for PEGda-0.5 and from 3.4 µm to 10.3 µm for PCL-o-2). On the contrary, the increase in the line width was quite modest as a function of the laser power (from 1.8 µm to 2.2 µm for PEGda-0.5 and from 1.7 µm to 3.6 µm for PCL-o-2).

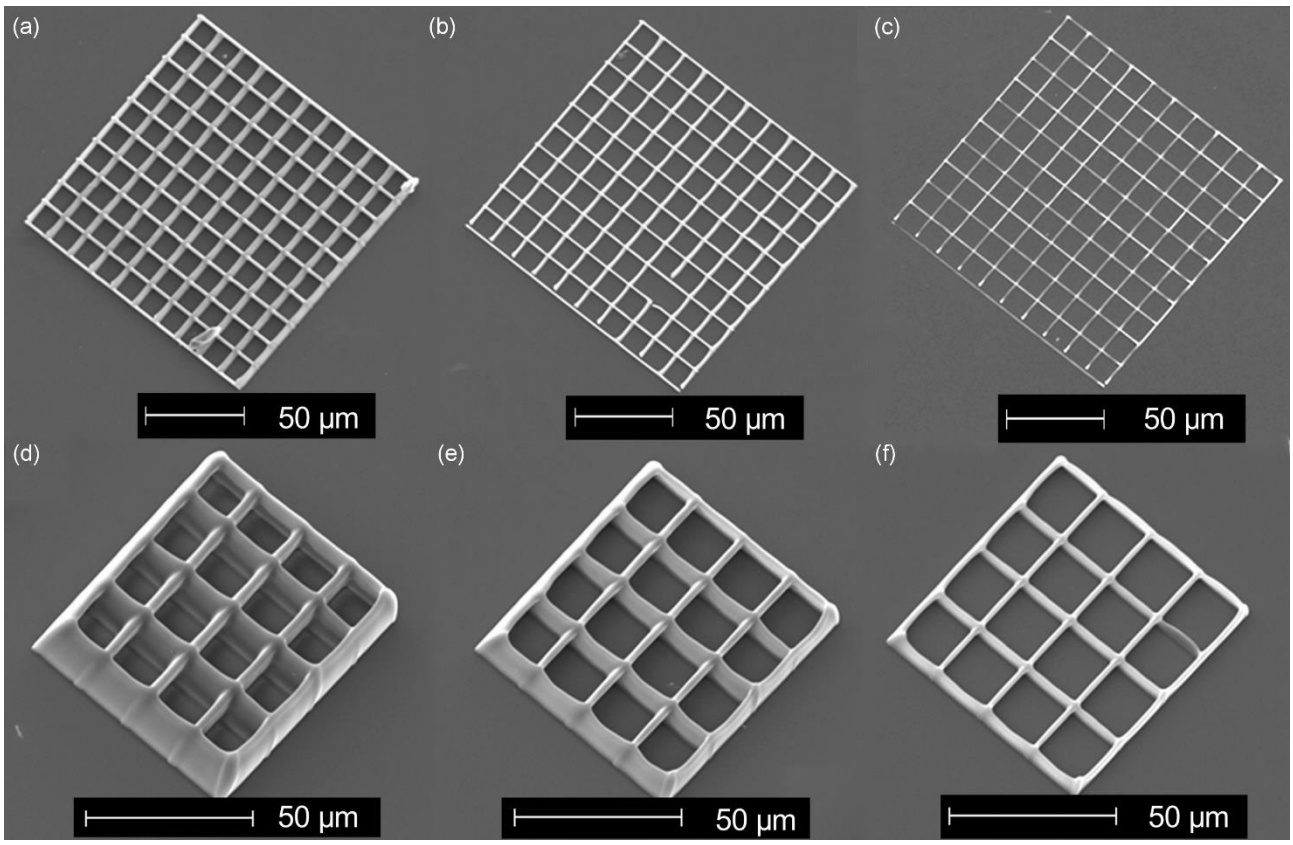

Figure 32. SEM images of lattices polymerized from PEGda-0.5 (a–c) using constant scanning speed of 30 µm/s and laser powers of (a) 6.6 mW, (b) 4.1 mW, and (c) 3.3 mW. PCL-o-2 lattices (d–f) polymerized using constant scanning speed of 5 µm/s and laser powers of (d) 6.6 mW, (e) 4.9 mW, and (f) 3.3 mW.

Similar lattice structures were also used for the determination of optimal scanning speed (varied from 1 µm/s to 150 µm/s) for each material composition. The scanning speed of 2 µm/s was found sufficient for the polymerization of PCL-o-5 (Figure 33(a)). A perfectly symmetrical lattice with sharp edges and intersections could be produced using this scanning speed and an average laser power of 1.6 mW (Figure 33d). Already the increase of the scanning speed to 5 µm/s produced some visible distortions in the middle part of the lattice (Figure 33(b)). The scanning speed of 10 µm/s was too high for the complete polymerization of the material (Figure 33(c)).

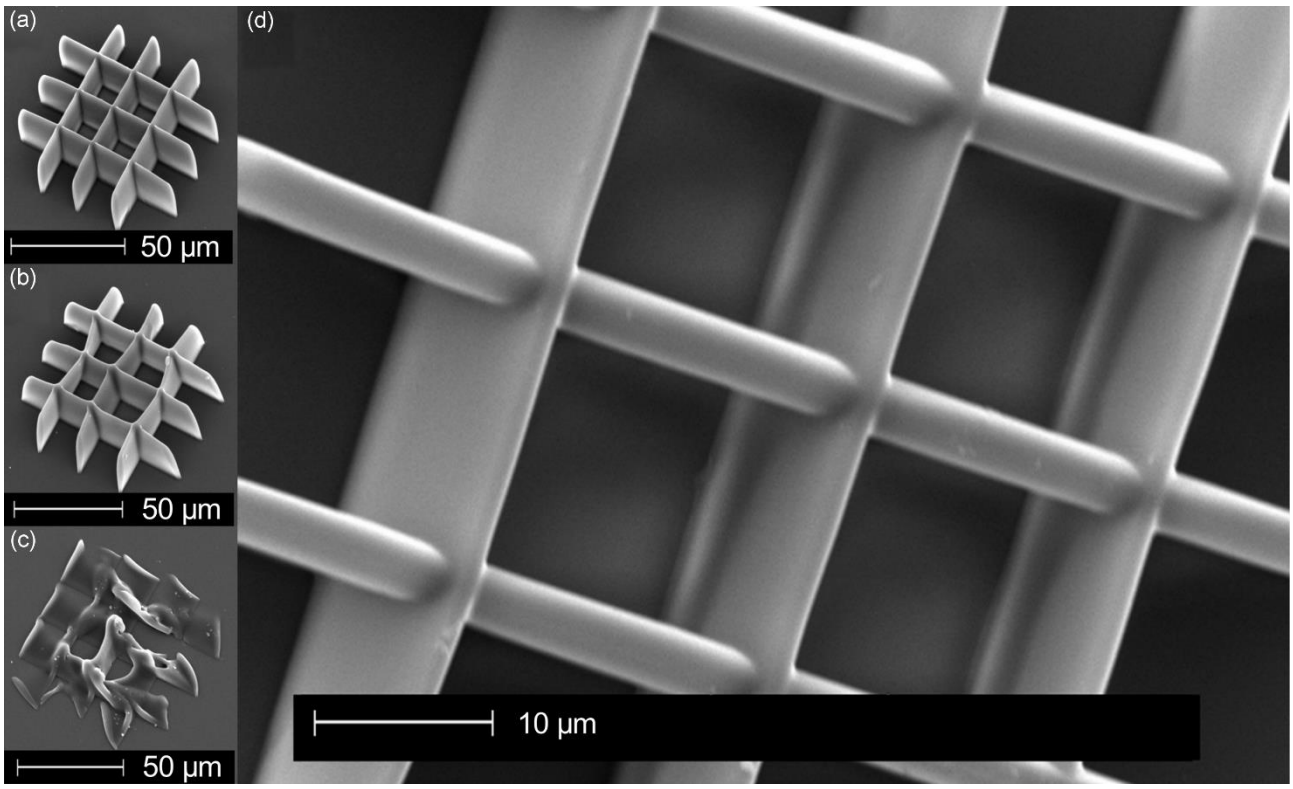

Figure 33. SEM images of PCL-o-5 lattice structures polymerized using ascending scanning speed: (a) 2 µm/s, (b) 5 µm/s, and (c) 10 µm/s. (d) Close-up of lattice (a).

An essential difference was observed in the optimal scanning speed when comparing PCL-o with PEGda. With PCL-o, the scanning speed needed to be at least 10 times slower than with PEGda to achieve complete polymerization. Typical scanning speeds for PEGda compositions varied from 20 µm/s to 100 µm/s, whereas scanning speeds of 2 µm/s to 10 µm/s were used for PCL-o. After optimizing the polymerization processing parameters, more complex 3D structures were fabricated according to CAD models. An example of a bonfire-type structure polymerized from PEGda-1 using a scanning speed of 70 µm/s and a laser power of 2.5 mW is shown in Figure 34.

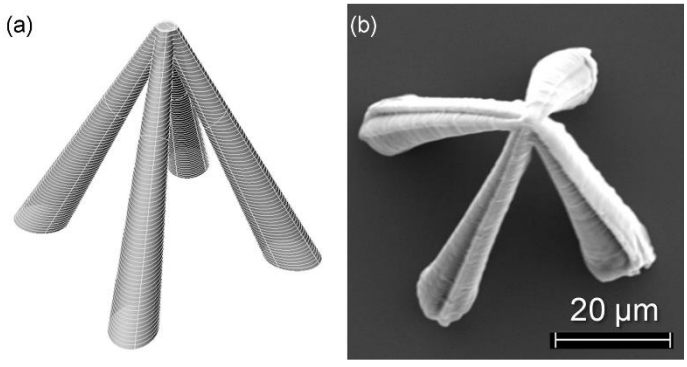

Figure 34. A hollow bonfire-type microstructure as (a) a CAD model with contours and having a layer spacing of 0.7 µm and (b) a SEM image of the polymerized structure. The bonfire-type microstructure was polymerized from PEGda-1 using a scanning speed of 70 µm/s and a laser power of 2.5 mW.

With regard to the overall processability of PCL-o and PEGda, the main difference between the two materials was the higher viscosity of PCL-o. The lower viscosity of PEGda made the sample preparation easier and more precise. Moreover, the PCL-o prepolymer solution tended to crystallize at room temperature. Therefore, all PCL-o samples had to be heated to a temperature of > 30 °C to melt the crystallized oligomers and make the solution transparent before the polymerization could take place. Of course, this additional preparation step added to the total fabrication time. However, neither of the materials was proven to be superior to the other in terms of sample preparation or handling.

In Publication II, several different protein and photosensitizer concentrations in combination with different average laser power and scanning speed values were tested to determine the range of fabrication conditions suitable for protein crosslinking. With the Nd:YAG laser, avidin could only be crosslinked into surface patterns with the protein concentration of 400 mg/ml and photosensitizer content between 1 mM and 4 mM. In order to produce continuous protein lines, the scanning speed of either 5 μm/s or 10 μm/s had to be used regardless of the photosensitizer concentration. Scanning with the speed of 20 μm/s or 40 μm/s mainly produced discontinuous protein fragments. As for the laser power, even the average laser power of 0.7 mW led to adequate crosslinking of the avidin with the scanning speed of 5 μm/s. Higher laser power values (from 3.9 mW to 6.1 mW) led to the distortion of the protein patterns due to the tilting of the protein lines with a high aspect ratio. The solution of 100 mg/ml of bBSA and 100 mg/ml of BSA with 4 mM FMN could be efficiently crosslinked into surface patterns with scanning speeds of 5 μm/s, 10 μm/s, and 20 μm/s using average laser power between 1.8 mW and 5.7 mW (Figure 35). A slightly higher laser power (2.9 mW) and slower scanning speed (5 μm/s or 10 μm/s) had to be utilized for the bBSA/BSA solutions with FMN concentration of 2 mM or 1 mM. However, without the additional photosensitizer, crosslinking of 100 mg/ml of bBSA together with 100 mg/ml of BSA solution was not observed. Also, the pure bBSA (100 mg/ml with 0 mM to 4 mM of FMN) crosslinked very poorly even with the slowest scanning speed and highest laser power. The crosslinking of BSA was not thoroughly investigated, but the protein was successfully crosslinked from a fabrication solution containing 200 mg/ml of BSA and 4 mM of FMN with an average laser power of 5.7 mW and a scanning speed of 10 μm/s (Figure 36(d)).

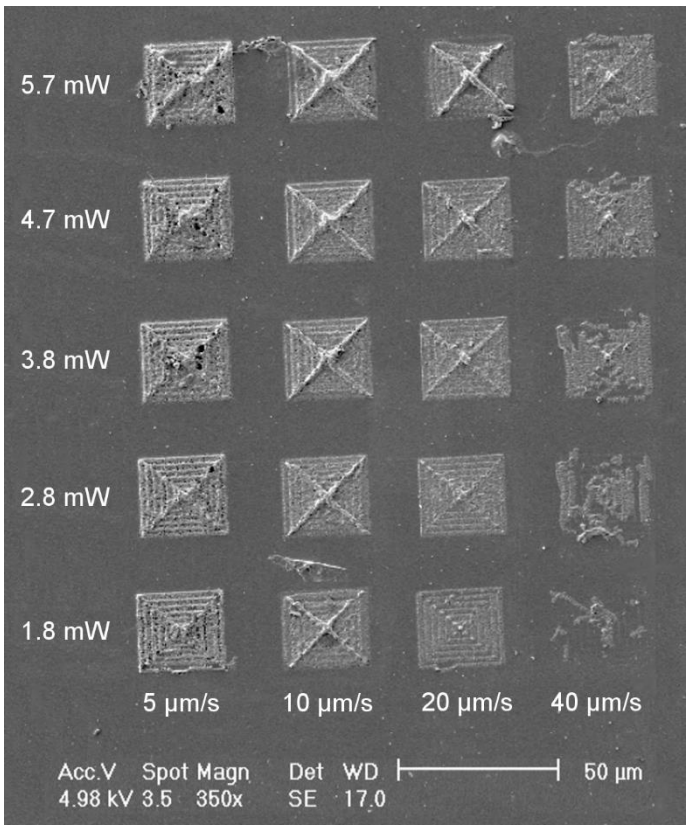

Figure 35. SEM image of a surface pattern array fabricated using the Nd:YAG laser from a protein solution containing 100 mg/ml of bBSA and 100 mg/ml of BSA with 4 mM of FMN. The scanning speed was varied from 5 µm/s to 40 µm/s and average laser power from 1.8 mW to 5.7 mW.

Samples of avidin and BSA patterns were also AFM imaged (Figure 36(a & b)) in order to assess the structure dimensions and surface topography, but it was concluded that the estimation of the line widths and heights could be done more reliably from the acquired SEM images. Furthermore, the measured dimensions do not represent the absolute minimum or maximum values for the line width and height as the degree of line truncation under the glass substrate was not taken into account by performing an ascending scan. Instead, the lines were fabricated at a randomly selected focal plane near enough the substrate surface to attach the protein lines to a solid support, and thus preventing them from floating away during the development phase. The SEM analysis of the surface structures crosslinked from avidin having a concentration of 400 mg/ml with 2 mM of FMN (1.8 mW, 5 µm/s) indicated that the average width of the thinnest lines was 270 nm ± 14 nm (Figure 36(c)). According to the measurements made from a SEM image taken from a 45° tilt, the average height of the lines was 550 nm ± 9.0 nm. This gives an average aspect ratio of 2.1 for the avidin lines. According to the SEM analysis of the concentric squares fabricated from 100 mg/ml of bBSA together with 100 mg/ml of BSA and 4 mM of FMN, the height of the surface adherent protein lines increased slightly from 1.4 µm ± 0.20 µm to 2.0 µm ± 0.39 µm as the average laser power increased from 1.8 mW to 5.7 mW. The original width of the lines could not be estimated because all the lines toppled over during the development procedure.

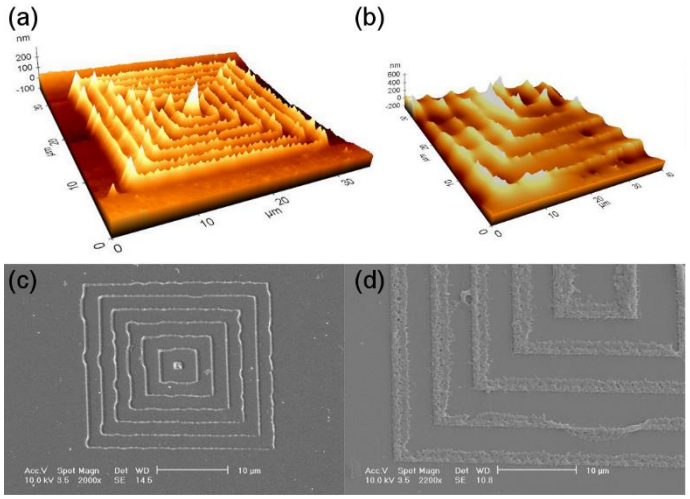

Figure 36. AFM (a) and SEM (c) images of the surface patterns photocrosslinked with the Nd:YAG laser from avidin (400 mg/ml of protein with 2 mM of FMN) using a laser power of 1.8 mW and a scanning speed of 5 μm/s. AFM (b) and SEM (d) images of part of the concentric squares fabricated from BSA (200 mg/ml of protein with 4 mM of FMN) using an average laser power of 5.7 mW and a scanning speed of 10 μm/s. Scale bars represent 10 μm.

Figure 36(b) and (d) show an AFM and a SEM image of a BSA structure (200 mg/ml of BSA with 4 mM of FMN) obtained by scanning the laser beam at 10 μm/s with a laser power of 5.7 mW. As can be seen from the Figure 36(d), the protein lines have toppled over on their sides during the development phase, and thus the original line width could only be estimated from a few parts. According to the SEM analysis, the average width of the BSA lines was 750 nm ± 100 nm and the height was 1.8 μm ± 0.16 μm resulting in an aspect ratio of 2.4.

In order to compare the processing capability of the low-cost Nd:YAG picosecond laser to the more commonly used femtosecond laser sources, protein structures were also fabricated with a Ti:sapphire laser setup by varying the average laser power and scanning speed. Crosslinking of avidin was investigated with a fabrication solution containing 400 mg/ml of avidin and 2 mM of FMN. The laser beam was scanned with the speed of 10 μm/s and the average laser power was varied from 38 mW to 123 mW. Based on the measurements from SEM images, the width of the avidin lines increased only slightly as a function of the laser power, ranging from 200 nm ± 30 nm to 310 nm ± 28 nm. The height of the lines could only be measured from a few patterns since most of the SEM images were taken from above and not from a 45° tilt. The lines fabricated with the laser power of 38 mW had an average height of 300 nm ± 2 nm. This results in an aspect ratio of 1.5 for the avidin lines fabricated with the Ti:sapphire laser, which is somewhat lower than the aspect ratio of the avidin lines fabricated with the Nd:YAG laser. However, this difference can be due to the difference in focusing height levels between the two experiments or it may result from the higher numerical aperture objective utilized with the Ti:sapphire laser, which leads to more spherical-shaped voxels instead of elongated spinning ellipsoids.

The solution of 100 mg/ml of bBSA and 100 mg/ml of BSA with 4 mM of FMN was studied by scanning the sample with a speed from 10 μm/s to 40 μm/s and by varying the laser power from 38 mW to 123 mW. An example of the fabricated square patterns is shown in Figure 37. In principle,

the width of the protein lines decreased at faster scanning speeds although the slight variance in the initial focus position between patterns produced some inconsistency to the measurements. For example, lines fabricated with an average laser power of 56 mW had an average width of 420 nm ± 36 nm at a scanning speed of 10 μm/s, 410 nm ± 52 nm at a speed of 20 μm/s, 310 nm ± 31 nm at a speed of 30 μm/s, and 270 nm ± 22 nm at a speed of 40 μm/s.

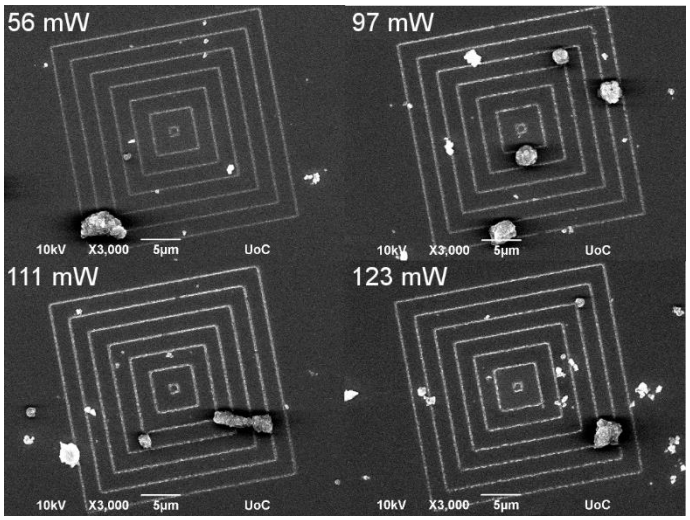

Figure 37. SEM images of an array of concentric squares fabricated with the Ti:sapphire laser from a solution of 100 mg/ml of bBSA and 100 mg/ml of BSA with 4 mM of FMN. The laser beam was scanned at a speed of 40 μm/s and the average laser power was varied from 56 mW to 123 mW. Scale bars represent 5 μm

The solution containing 200 mg/ml of BSA with 4 mM of FMN was also fabricated into surface patterns by varying the average laser power from 38 mW to 123 mW and by scanning the sample with a speed of 30 μm/s. The width of the BSA lines increased only marginally and within the error limits as a function of the laser power. For example, the lines crosslinked with an average laser power of 38 mW had an average width of 250 nm ± 26 nm, whereas lines fabricated with a power of 123 mW had a width of 270 nm ± 16 nm.

The achievable feature size and the optimal processing parameters of Ormocomp® using the second-generation fabrication setup has been previously reported by our research group (Käpylä *et al.* 2011). The data are collated in Table 5 together with the fabrication data of the other studied photosensitive materials.

Table 5. Summary of the suitable processing parameters and achievable lateral feature sizes for all the studied material-photoinitiator combinations.

Material	Photoinitiator	Laser	Optimal processing parameters	Achievable lateral feature size	Publication
Avidin	1 mM – 4 mM FMN	Nd:YAG (800 ps)	1.8 mW – 6.1 mW 5 μm/s – 10 μm/s	270 nm	II
	0.6 wt% Irgacure® 2959	Fiber laser (200 fs)	5.8 mW – 17 mW 14 μm/s – 24 μm/s	n.a.	Unpublished data
Biotinylated BSA	1 mM – 4 mM FMN	Nd:YAG (800 ps)	1.8 mW – 5.7 mW 5 μm/s –20 μm/s	750 nm	II
	0.6 wt% Irgacure® 2959	Fiber laser (200 fs)	8.0 mW – 15 mW 25 μm/s – 75 μm/s	n.a.	Unpublished data
Ormocomp®	2 wt% Irgacure® 127	Nd:YAG (800 ps)	0.4 mW – 1.6 mW 10 μm/s – 150 μm/s	210 nm	(Käpylä *et al.* 2011)
		Fiber laser (200 fs)	0.3 mW – 5.4 mW 150 μm/s – 550 μm/s	n.a.	IV
PCL-o	2 wt% – 5 wt% Irgacure® 127	Nd:YAG (800 ps)	0.8 mW – 7.6 mW 2 μm/s – 10 μm/s	1 μm	I
PEGda	0.5 wt% – 1.5 wt% Irgacure® 127	Nd:YAG (800 ps)	0.8 mW – 7.6 mW 20 μm/s – 100 μm/s	1.7 μm	I

5.1.3 Assessment of surface topography

The surface topography of the 2D and 3D crosslinked protein structures was analyzed by comparing the SEM images of structures fabricated with the two different laser sources and different protein compositions in Publication II. The SEM images revealed some differences in the surface topography of the different protein structures. Avidin appeared to form quite uniform and dense lines when processed either with the Nd:YAG (Figure 38(a)) or with the Ti:sapphire laser setup (Figure 38(b)). The very high protein concentration (400 mg/ml) enabling the efficient crosslinking of the protein and thus small mesh size of the matrix may contributed to the formation of the smooth surfaces of the avidin structures.

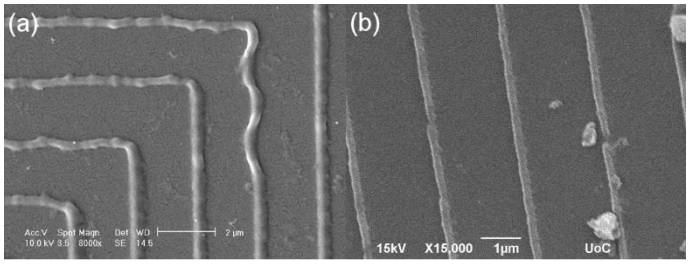

Figure 38. Close-up SEM images of avidin lines crosslinked from 400 mg/ml of avidin with 2 mM of FMN. (a) A line structure fabricated with the Nd:YAG laser setup using a scanning speed of 5 μm/s and an average laser power of 1.8 mW.(b) A line structure fabricated with the Ti:sapphire laser setup at a scanning speed of 10 μm/s using an average laser power of 97 mW. Scale bars represent 2 μm and 1 μm, respectively.

In contrast to avidin, the structures fabricated from a solution of 100 mg/ml of bBSA and 100 mg/ml of BSA with 2 mM or 4 mM of FMN had more porous and highly textured surface topography, as seen in Figure 39. Especially, the patterns photocrosslinked with the Nd:YAG laser showed highly

textured surfaces. The reduced crosslinking density of the more dilute BSA solution compared with the more concentrated avidin solution could explain the difference. The Ti:sapphire laser setup produced structures with somewhat less porous texture than the Nd:YAG laser, as shown in Figure 39(b).

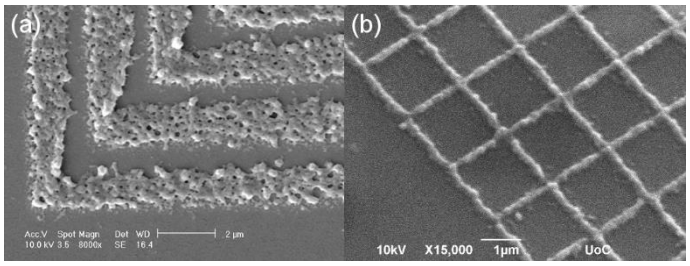

Figure 39. SEM images of surface patterns fabricated from a solution of 100 mg/ml of bBSA and 100 mg/ml of BSA with 2 mM or 4 mM of FMN, respectively. (a) A structure produced with the Nd:YAG laser using a scanning speed of 5 µm/s and an average laser power of 1.8 mW. (b) A grid fabricated with the Ti:sapphire laser by scanning the sample with a speed of 40 µm/s and an average laser power of 123 mW. Scale bars represent 2 µm and 1 µm, respectively.

3D fabrication was also demonstrated by crosslinking BSA into a simple woodpile structure with the Nd:YAG laser (Figure 40). The crosslinked BSA structure reproduced the CAD image of the woodpile in the xy-direction quite accurately, although in the z-direction, the individual rods fused together instead of forming separate layers of rods. The dimensions of the CAD model were 40 µm × 40 µm × 10 µm and, according to the measurements from the SEM image, the glass-bound bottom part of the fabricated structure had virtually no dimensional changes. However, the top part of the woodpile shrank from 40 µm to 35 µm, thus having a shrinkage rate of 13%. The anisotropic shrinkage is a result of the uneven shrinkage rates of the top and bottom parts of the woodpile during the development and dehydration procedures due to the attachment of the bottom part to the glass substrate. The measured height of the woodpile was only about 5.3 µm, which gives a shrinkage rate of 47% in the z-direction. The pronounced collapse of the structure could be a result of the non-ideal inter-layer distance in the z-direction, which in the original CAD model was 1 µm. Utilization of smaller layer spacing could have resulted in less sponge-like surface texture and thus a mechanically more stable woodpile.

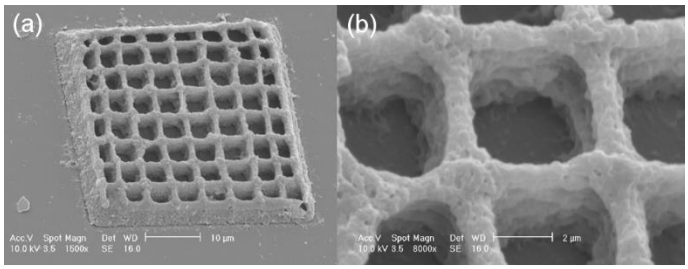

Figure 40. (a) SEM image of a woodpile structure crosslinked from a solution of 200 mg/ml of BSA with 4 mM of FMN using Nd:YAG laser. The sample was scanned with a speed of 10 µm/s and using an average laser power of 5.7 mW. (b) A close-up of the surface topography of the woodpile. Scale bars represent 10 µm and 2 µm, respectively.

5.1.4 Retention of ligand-binding ability of the avidin-biotin complex

It is important to verify whether the bioactivity of proteins is retained during the exposure to the high laser intensities required for efficient 2PA of the photosensitizer. Thus, fluorescence imaging was used as a qualitative tool to show that the microfabricated patterns of avidin and bBSA retained their ability to bind either biotinylated or streptavidin conjugated fluorescence labels after photocrosslinking with the Nd:YAG laser. Of course, the limitation of this simple assay is its inability to prove that the entire protein has been preserved in its native conformation; instead, it only shows that the ligand-binding sites of the protein are still functional. Arrays of surface-bound concentric squares were fabricated from avidin (400 mg/ml) with 1 mM, 2 mM, or 4 mM of FMN, from 100 mg/ml of bBSA with 1 mM, 2 mM, or 4 mM of FMN, and from the solution of 100 mg/ml of bBSA and 100 mg/ml of BSA with 1 mM, 2 mM, or 4 mM of FMN. Each set of squares was crosslinked with a different combination of process parameters (i.e., average laser power and scanning speed). A representative fluorescence image (Figure 41) shows that DY-634-biotin-labeled avidin structures (400 mg/ml of avidin with 2 mM of FMN) have an emission signal to background ratio as high as 10:1 over the baseline fluorescence of the negative control of BSA labeled with DyLight® 649 Streptavidin conjugate. The strong fluorescence implies that the crosslinked avidin was not significantly denatured during the fabrication process and retained its ability to bind biotinylated molecules. The corresponding surface plot profiles of the fluorescence intensities show that the biotin binding capacity of avidin fabricated with a scanning speed of 5 μm/s diminished approximately 80% as the laser power decreased from 6.1 mW to 0.71 mW. Thus, the decrease in the average laser power resulted in a lower amount of crosslinked protein and fewer available biotin binding sites in the avidin structure. Similarly, the increase in scanning speed from 5 μm/s to 40 μm/s using a constant laser power of 6.1 mW attenuated the immobilization of the biotin by about 80%. As expected, avidin patterns photocrosslinked from 400 mg/ml avidin with only 1 mM of FMN expressed lower biotin binding capacity and thus lower fluorescence intensities than the ones fabricated from avidin with 2 mM of FMN (data not shown). This is a consequence of the lower amount of protein incorporated in the patterns due to the lower photosensitizer concentration.

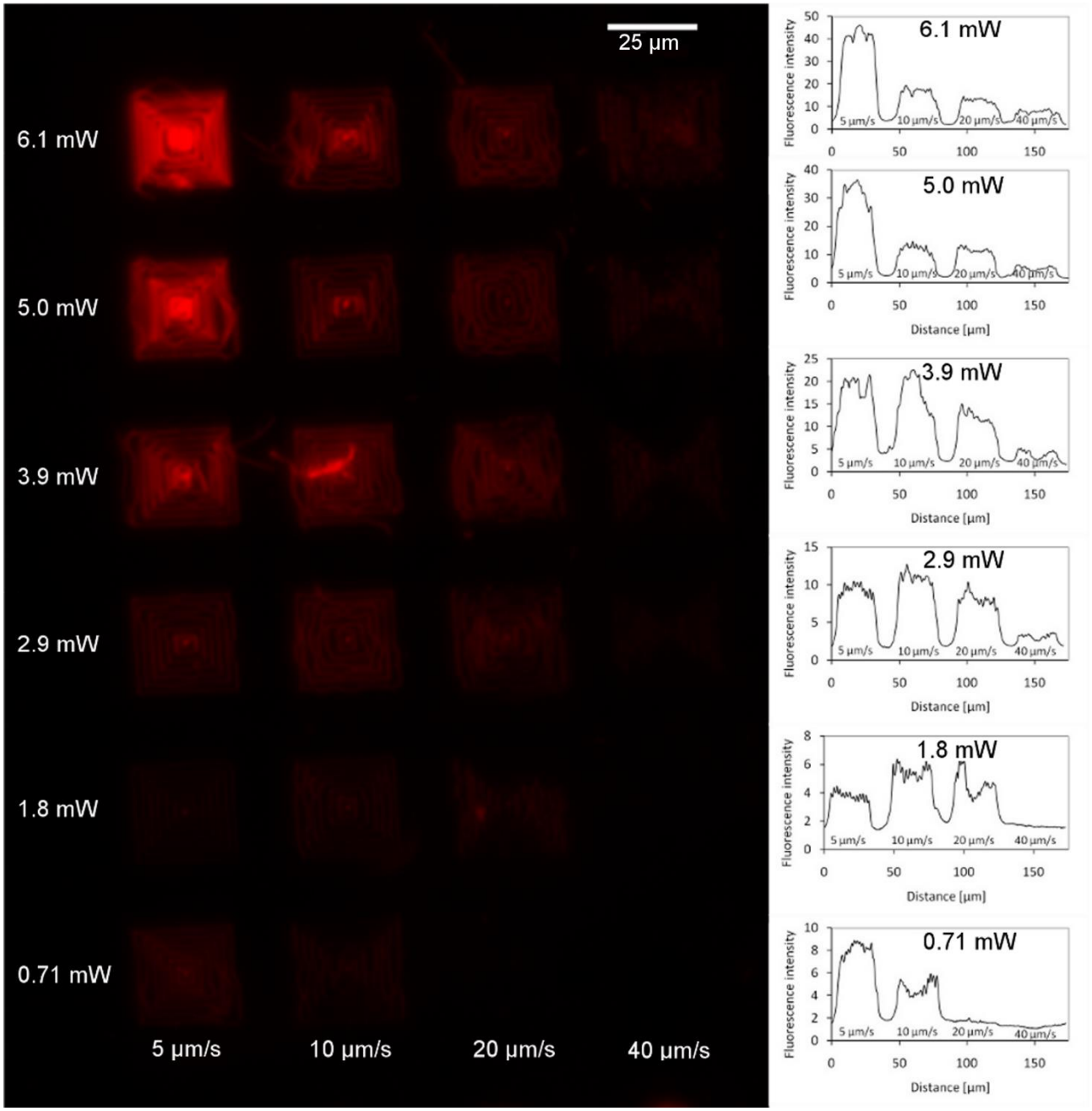

Figure 41. Fluorescence image of an array of concentric squares fabricated with the Nd:YAG laser from a solution containing 400 mg/ml of avidin with 2 mM of FMN by varying the average laser power and scanning speed, and subsequently stained with the DY-634-biotin label. Corresponding plots represent the surface intensity profiles for square pattern sets crosslinked with a constant average laser power by varying the scanning speed. The data were created by using an exposure of 5.26 s without binning.

The square patterns photocrosslinked from the solution of 100 mg/ml of bBSA with 1 mM to 4 mM of FMN contained too little protein to efficiently bind the streptavidin-conjugated label. The streptavidin binding capacity of the biotinylated BSA structures was decreased as the average laser power was lowered or the scanning speed was raised. Overall, the ligand-binding study demonstrated that the biotinylated BSA also retained its capability to bind avidin after the fabrication process.

5.1.5 Neuronal cell viability and migration tests on 2D UV-cured films

The suitability of the studied material-photoinitiator combinations for neuronal cell culture purposes was evaluated by culturing hPSC-derived neuronal cells on Ormocomp® (Käpylä *et al.* 2010), PEGda (Publication I), and PCL-o (Publication I) UV-cured thin films for seven days (Figure 42).

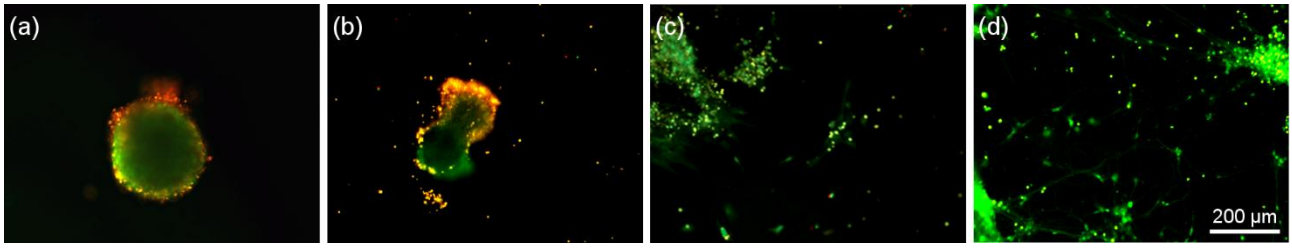

Figure 42. Fluorescence microscopy images of live/dead stained neuronal cells on surfaces of (a) PCL-o, (b) PEGda, (c) Ormocomp®, and (d) laminin control. Live cells are stained green, whereas dead cells are stained red/yellow. Figure (c) is reprinted by permission of Eureka Science Ltd., from Ref. Käpylä, E., Turunen, S. & Kellomäki, M. Two-Photon Polymerization of a Polymer-Ceramic Hybrid Material with a Low-Cost Nd:YAG Laser: Preliminary Resolution Study and 3D Fabrication. Micro and Nanosystems 2(2010)2, pp. 87-99. © 2010 Bentham Science Publishers Ltd.

Fluorescence microscopy images of the live/dead stained cells show that on PCL-o and PEGda samples cell aggregates attached to the surface, but no migration of cells or outgrowth of neurites could be observed. Both live and dead cells were found on these surfaces. On Ormocomp® thin films, cell aggregates were also able to attach to the surface and the majority of the cells remained viable during the seven-day culture period. Furthermore, Ormocomp® promoted cell migration to some extent; however, the morphology of the cells appeared non-neural. On the laminin-coated polystyrene control sample, extensive migration of cells was detected and the morphology of the cells was neuronal-like.

5.2 Selection of photosensitive materials

The hybrid inorganic-organic resin Ormocomp® has been proven to be an excellent non-degradable photosensitive material for 2PP-DLW in earlier studies by our research group (Käpylä *et al.* 2010; Käpylä *et al.* 2011). The ECM protein-binding properties and the biocompatibility of Ormocomp® as demonstrated with the hPSC-derived neuronal cells make it a good photosensitive material candidate for the fabrication of microstructures for cell growth guidance. On the other hand, the protein-repelling properties of PEGda and the inability of PEGda and PCL-o to support the migration or functionality of neuronal cells, make them undesirable alternatives for cell culture purposes. Furthermore, the issue of slow polymerization reaction observed with PCL-o needs to be addressed before any larger structures could be fabricated.

Thus, due to its superior photocrosslinking properties, ease of fabrication, and the ability to support neuronal cell migration, Ormocomp® was selected as a photosensitive material instead of PCL-o and PEGda for the fabrication of cell growth guidance structures. In addition to synthetic Ormocomp®, avidin and biotinylated BSA proteins were chosen to be further investigated as materials for

2PP-DLW since they are inherently cytocompatible and biomimetic by nature, and they are easily further functionalized with bioactive signals via avidin-biotin interaction.

5.3 2PP-DLW fabrication of bioactive protein surface patterns

Avidin and bBSA combined with Irgacure® 2959 were photocrosslinked into 2D single neuron guidance patterns. Examples of avidin and bBSA patterns are shown in Figure 43. The SEM imaged patterns were not fabricated with exactly the same fabrication parameters as the patterns used for cell culture experiments. However, the laser exposure dose in the case of bBSA patterns was nearly the same for both cases (~130 mW·s for SEM imaged patterns vs. ~140 mW·s for cell-cultured patterns). For avidin patterns, the laser exposure doses were more unequal, but in the same order on both occasions (200 mW·s for SEM imaged patterns vs. ~100 mW·s for cell-cultured patterns).

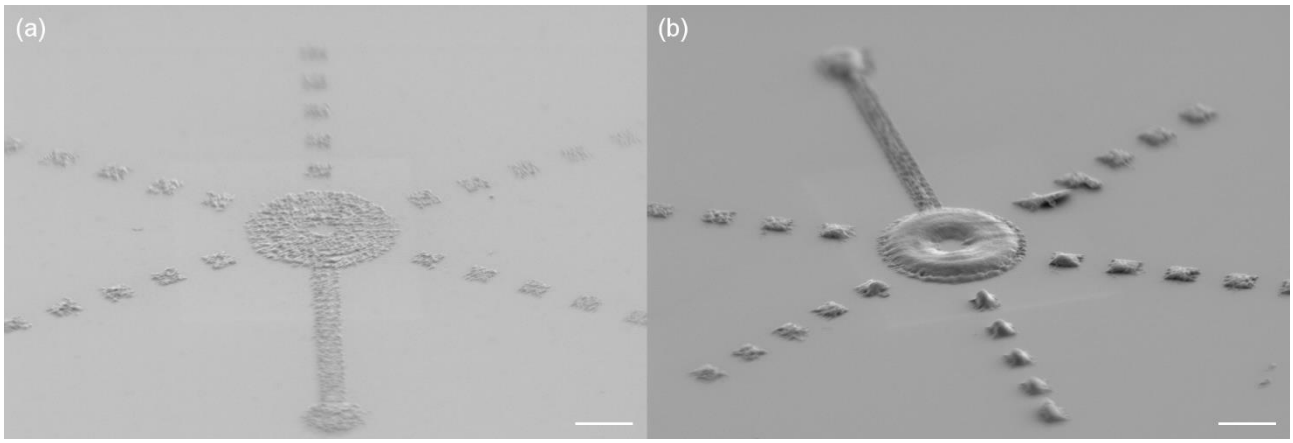

Figure 43. SEM images of protein surface patterns taken from a tilt angle of 60°. (a) Avidin pattern fabricated using a scanning speed of 24 μm/s and an average laser power of 5.8 mW. (b) bBSA surface pattern crosslinked using a scanning speed of 50 μm/s and an average laser power of 14.6 mW. Scale bars represent 10 μm.

The accuracy of the photocrosslinked protein patterns was evaluated by measuring the dimensions from the top view SEM images and comparing them with the dimensions of the CAD design (Table 6).

Table 6. Theoretical and experimental dimensions of avidin and bBSA surface patterns measured from the top view (0° tilt) SEM images. The data represent mean ± standard deviation (n = 3).

		Avidin		bBSA	
	CAD dimensions [µm]	**Measured dimensions [µm]**	**Deviation [%]**	**Measured dimensions [µm]**	**Deviation [%]**
Big circle diameter	25.0	26.1 ± 0.4	4.5 ± 1.5	25.5 ± 0.0	2.1 ± 0.0
Small circle diameter	10.0	10.0 ± 0.2	1.2 ± 1.0	10.1 ± 0.2	1.8 ± 0.0
Continuous line length	45.0	46.9 ± 0.1	4.2 ± 0.2	47.4 ± 0.1	5.3 ± 0.2
Continuous line width	4.0	4.2 ± 0.3	5.4 ± 5.4	4.3 ± 0.1	8.6 ± 2.6
Interrupted line length	5.0	4.3 ± 0.2	13.3 ± 4.6	5.0 ± 0.4	5.8 ± 3.6
Interrupted line width	4.0	4.2 ± 0.4	6.8 ± 7.3	4.3 ± 0.1	7.3 ± 3.0

The dimensions of the fabricated protein patterns coincided closely with those of the CAD design. However, several problems were encountered while fabricating arrays of protein surface patterns, which impeded the reproducibility of the process. The position of the laser focal spot in the z-direction tended to shift either too deep inside the glass surface or too far away from the surface, which resulted in poorly polymerized parts or detachment of the patterns from the glass substrate. Overall, the adhesion of the protein patterns to the glass surface was quite weak. As slow scanning speeds had to be used to achieve good polymerization results, the crosslinking of a single surface pattern from avidin or bBSA took ~11 min or ~5 min, respectively. Thus, the fabrication of large arrays of patterns was not very feasible.

5.4 2PP-DLW fabrication of 3D confinement microstructures

In Publication III, several of the first fabricated neurocage structures suffered from the collapse of the upper parts of the channel walls during the post-fabrication development phase (Figure 44(a)). The phenomenon is caused by the evaporation of the rinse solvent, 2-propanol, which generates a pulling force on the walls and binds them together. As the effect of the collapse force can be reduced by using a rinsing liquid with lower surface tension (Park *et al.* 2008), 2-propanol was replaced with HMDS in the subsequent experiments with improved results as illustrated in Figure 44(b).

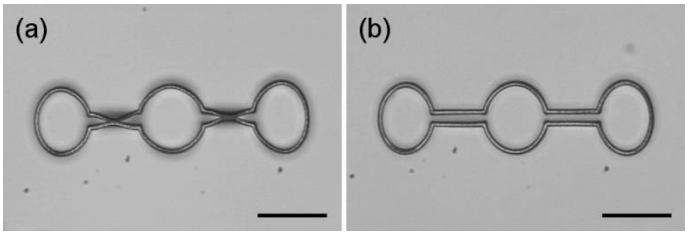

Figure 44. Bright field micrographs of type I neurocages rinsed with (a) 2-propanol resulting in the collapse of the channels, and with (b) HMDS resulting in intact channel walls. Scale bars represent 50 µm.

To minimize the polymerization time of the neurocages while still obtaining relatively smooth surface texture, a scanning speed of 120 µm/s was chosen for the fabrication of the structures. It was observed that higher scanning speeds led to more pronounced surface roughness (data not shown). The surface texture of the cages fabricated with the scanning speed of 120 µm/s was evaluated from the SEM images taken with a tilt angle of 60° (Figure 45) by measuring the width of the ridges (highlighted with arrows in Figure 45(b)). With this method of measurement, the polymerized neurocages had an average lateral surface feature size of 680 nm ± 60 nm.

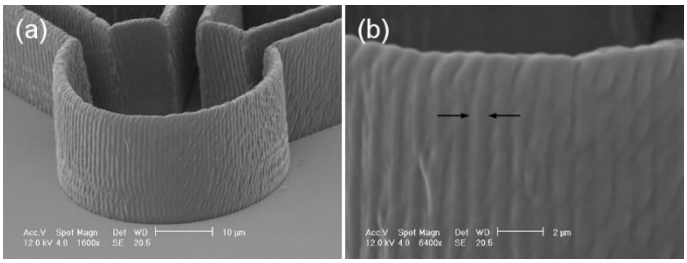

Figure 45. (a) SEM image of the corner node from a type III neurocage fabricated with a scanning speed of 120 µm/s and (b) a close-up of the surface texture of the wall. The arrows point out the method of measuring the width of the ridges. The images have been taken from a 60° tilt and the scale bars are 10 µm in (a) and 2 µm in (b).

By scanning the laser beam at 120 µm/s, the polymerization of a type I neurocage (Figure 46(a)) took approximately 5 min, type II (Figure 46(b)) 25 min and type III (Figure 46(c)) 21 min.

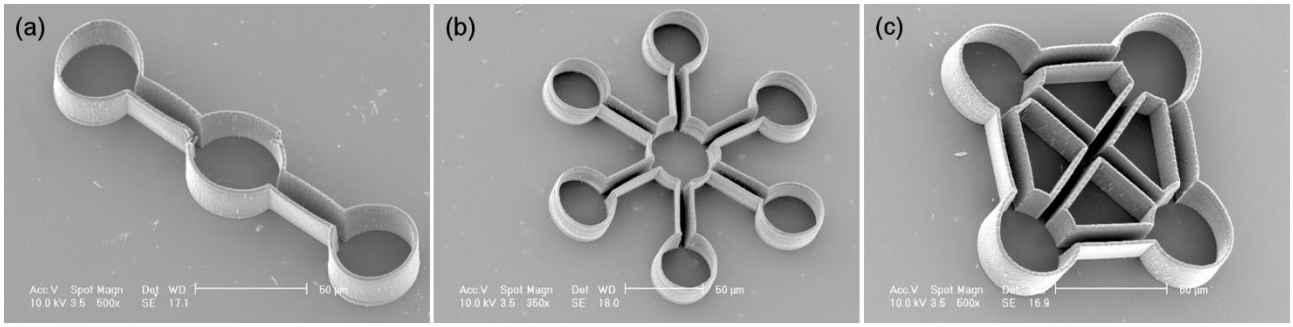

Figure 46. SEM images of neurocages fabricated on untreated microscope slides with a scanning speed of 120 µm/s: (a) type I, (b) type II, and (c) type III. The images show the neurocages from the tilt angle of 30° and the scale bars represent 50 µm.

The fabrication accuracy of neurocages with the 2PP-DLW setup was evaluated by examining type III neurocages with SEM and by comparing the measured dimensions with the original CAD design. The neurocage node diameter, channel length, channel width, and wall thickness were measured from the top view (0° tilt), and wall height from the side view (90° tilt) SEM images. Table 7 presents the results in comparison with the dimensions of the CAD design.

Table 7. Theoretical and experimental dimensions of type III neurocage. The data represent mean ± standard deviation (n = 8).

	CAD dimensions [µm]	Measured dimensions [µm]	Deviation [%]
Node diameter	40.0	36.2 ± 0.9	9.5 ± 2.3
Channel length	40.0	41.7 ± 0.6	4.2 ± 1.5
Channel width	5.0	3.7 ± 0.6	25.1 ± 12.2
Wall thickness	1.0	2.0 ± 0.2	98.1 ± 15.3
Wall height	25.0	19.4 ± 0.4	22.3 ± 1.7

5.5 2PP-DLW fabrication of 3D tubular microtowers

In order to fabricate Ormocomp® microtowers with good structural quality, i.e., without the emergence of damaging microexplosions, the applicable average laser power range (i.e., the polymerization window) for polymerization was first determined in Publication IV. The measured values are collated in Table 8. The threshold values for the examined scanning speeds were almost identical, and resulted in very similar polymerization window ranges.

Table 8. Polymerization (P_{th}) and damage threshold (P_D) power values as well as the calculated polymerization windows (P_w) and the power values corresponding to 70% of the polymerization window for the tested scanning speeds. The measured data represent mean ± standard deviation (n = 4).

Scanning speed [µm/s]	P_{th} [mW]	P_D [mW]	P_w [mW]	70% P_w [mW]
150	0.3 ± 0.04	5.4 ± 0.5	5.1 ± 0.5	3.8 ± 0.4
350	0.3 ± 0.04	5.3 ± 0.2	5.0 ± 0.2	3.9 ± 0.2
550	0.3 ± 0.06	5.4 ± 0.2	5.0 ± 0.2	3.9 ± 0.2

SEM images of suspended line structures polymerized with scanning speeds of 150 µm/s, 350 µm/s, and 550 µm/s are shown in Figure 47.

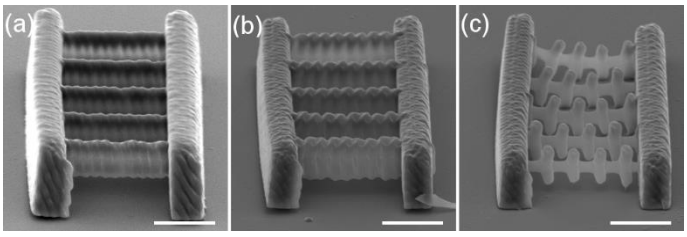

Figure 47. SEM images of suspended lines polymerized on top of supporting walls with scanning speeds of (a) 150 µm/s, (b) 350 µm/s, and (c) 550 µm/s. Images were taken from a 60° tilt. Scale bars represent 10 µm.

The measured linewidths and heights for the three scanning speeds are summarized in Table 9. Although the voxel dimensions remained nearly constant, the uniformity of the lines decreased and the surface roughness increased with scanning speed. As the fabrication time can be reduced by taking advantage of the axial height of the voxels and setting the layer distance to match the voxel height, the axial voxel distance of the microtower cylinder was set to 3.0 µm and the micropillars to 4.0 µm.

In order to achieve relatively smooth surface roughness, the lateral voxel distance was set to 1.0 µm. The lateral, axial, and overall voxel overlap degrees calculated for the cylinder according to Equation 13 are presented in Table 9. The voxel overlap ratios were not determined for the scanning speed 150 µm/s as it was only used for single line scans when polymerizing the spider webs. According to the results of previous studies, the lateral surface roughness tends to saturate when the voxel overlap ratio is over 0.5 due to self-smoothing effect (Liao 2008; Wu *et al.* 2010). For the scanning speeds of 350 µm/s and 550 µm/s, the lateral voxel overlap ratios were over 0.5 suggesting that similar surface roughness would be achieved with both scanning speeds.

Table 9. Measured line widths and heights for scanning speeds of 150 µm/s, 350 µm/s, and 550 µm/s, and calculated voxel overlap ratios. The data represent mean ± standard deviation (n = 5).

Scanning speed [µm/s]	**Line width [µm]**	**Line height [µm]**	**Lateral voxel distance [µm]**	**Lateral voxel overlap**	**Axial voxel distance [µm]**	**Axial voxel overlap**	**Overall voxel overlap degree**
150	1.9 ± 0.2	7.5 ± 0.2	n.a.	n.a.	n.a.	n.a.	n.a.
350	2.1 ± 0.1	7.4 ± 0.2	1.0	0.53	3.0	0.59	0.31
550	2.1 ± 0.2	6.8 ± 0.6	1.0	0.51	3.0	0.56	0.29

After the determination of the polymerization windows and voxel dimensions, the microtower designs I & II were polymerized with scanning speeds of 350 µm/s and 550 µm/s (Figure 48) to determine the optimal scanning speed for the fabrication and to evaluate whether the elliptically shaped openings would give round openings. However, as the axial contour distance was quite large (i.e., 3 µm), the elliptical shape of the openings was not traced properly, especially with the scanning speed of 550 µm/s. As predicted by the similar voxel overlap degrees, both scanning speeds resulted in comparable surface quality.

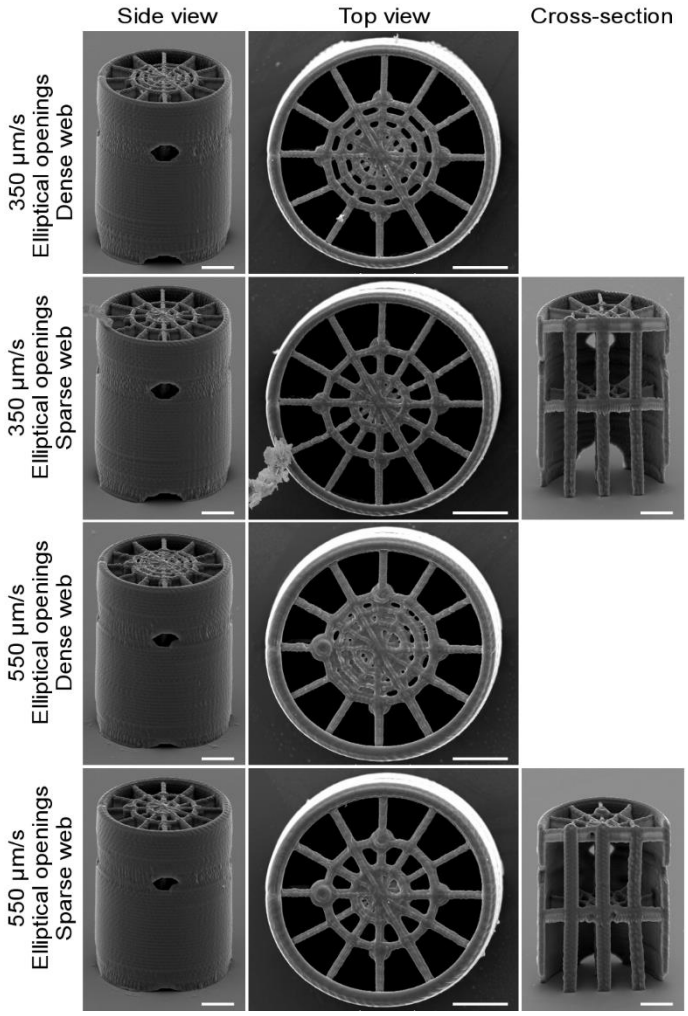

Figure 48. SEM images of microtowers with elliptical openings and with dense (design I) or sparse (design II) webs fabricated with scanning speeds of 350 µm/s or 550 µm/s. The images show the towers from the tilt angles of 60° (first column) and 0° (second column). The third column shows the longitudinal cross-sections of the towers from the tilt angle of 60°. Scale bars represent 20 µm.

The rectangular shape of the openings (designs III & IV) was reproduced quite accurately with both scanning speeds (Figure 49). Figure 48 and Figure 49 show that some of the gaps in the spider webs were enclosed by self-polymerized membranes (designs I & III) that formed in-between the web threads as the scanned lines were packed densely enough. These designs were considered to be too closed to allow efficient cell migration.

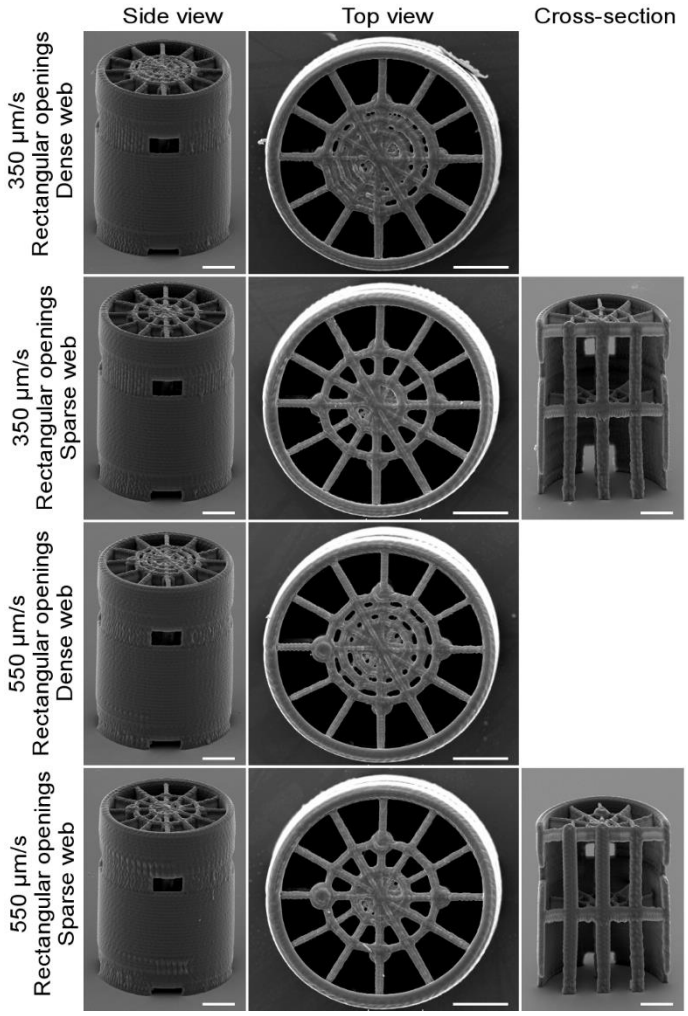

Figure 49. SEM images of microtowers with rectangular openings and with dense (design III) or sparse (design IV) webs fabricated with scanning speeds of 350 µm/s or 550 µm/s. The images show the towers from the tilt angles of 60° (first column) and 0° (second column). The third column shows the longitudinal cross-sections of the towers from the tilt angle of 60°. Scale bars represent 20 µm.

Finally, microtower design IV (Figure 50(a)) together with the reference structure designs V (Figure 50(b)) and VI (Figure 50(c)) were selected as the optimal models for the cell culture experiments.

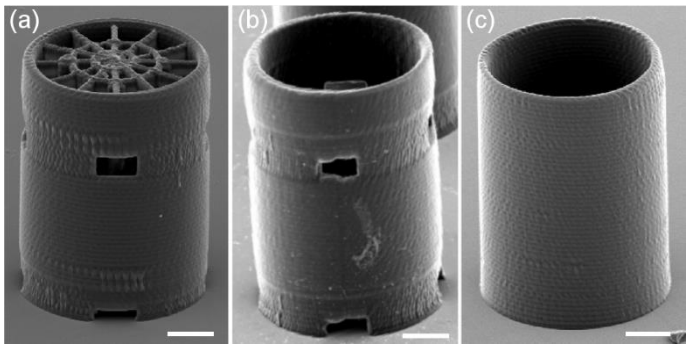

Figure 50. SEM images of the microtowers: (a) design IV with rectangular openings and sparse webs, (b) design V with rectangular openings, and (c) design VI without openings. The images show the towers from the tilt angle of 60°. Scale bars represent 20 µm.

The fabrication of a single design IV tower using scanning speeds of 350 μm/s (the cylinder and pillars) and 150 μm/s (the webs) took approximately 7 min 32 s. Increasing the scanning speed from 350 μm/s to 550 μm/s reduced the fabrication time by 22 s to 7 min 10 s. As there was no essential difference in the surface quality of the towers, the samples for the cell culture experiments were fabricated with the scanning speed of 550 μm/s. In addition, the reference microtowers (designs V & VI) were fabricated with the same scanning speed. The fabrication of design V took only 3 min 49 s and design VI 4 min 30 s. Design VI towers had a smooth uniform surface morphology with surface roughness $R_a = 11.2 \pm 0.4$ nm (henceforth denoted as "smooth surface") as the cylinder comprised only closed circular contours. The surface roughness ($R_a = 30.9 \pm 6.6$ nm, henceforth denoted as "rough surface") was higher in designs IV and V at the opening layers. The higher surface roughness was caused by the fluctuation of the laser dose due to the acceleration and deceleration of the scanner producing variation in voxel size. Other layers of the design IV and V towers had a smooth surface as in design VI. Figure 51 shows examples of AFM 3D topography images and the line scan profiles of the smooth and rough parts of the tower walls.

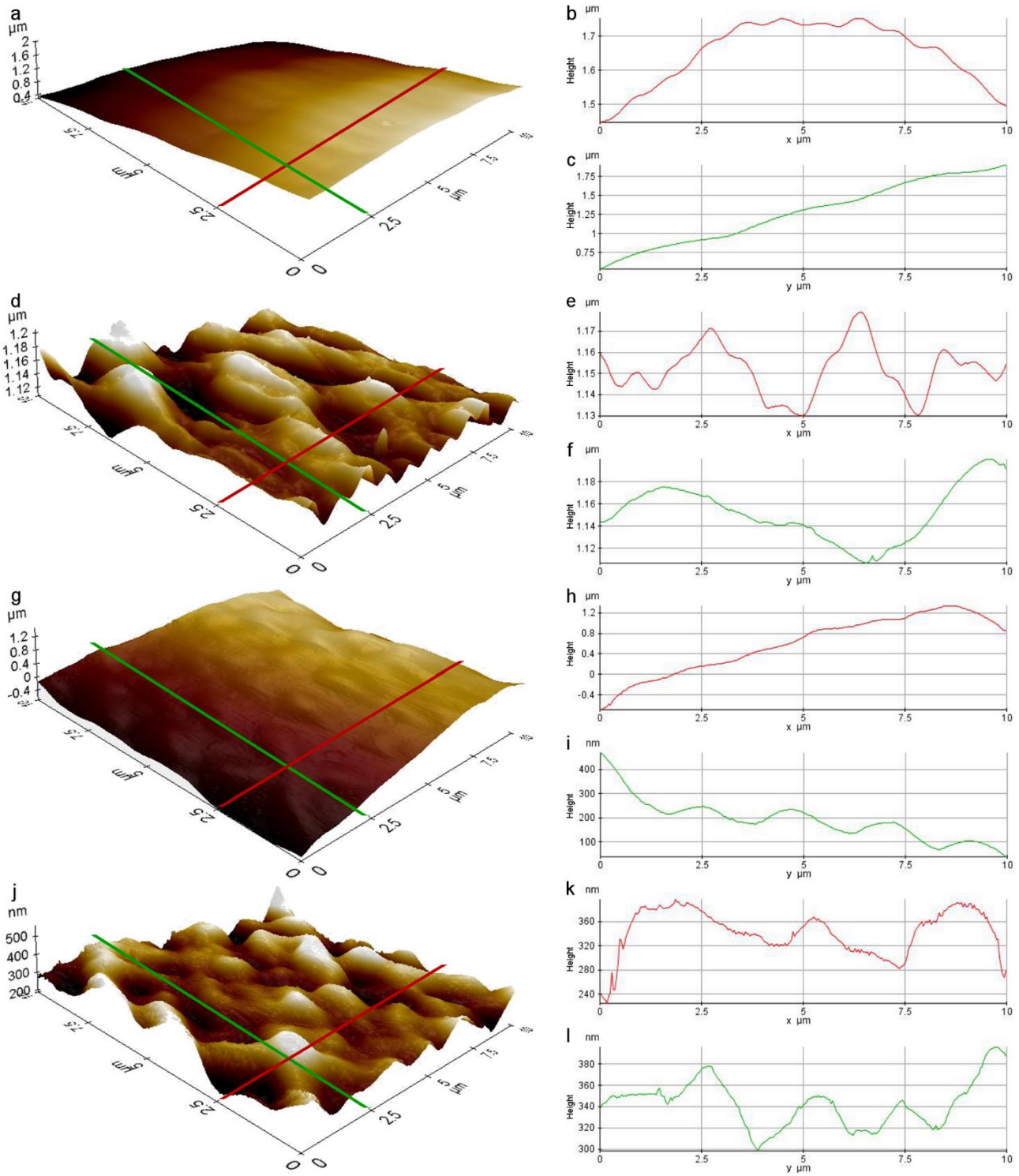

Figure 51. AFM topography images (10 µm × 10 µm) of the outer surface of the cylindrical tower walls. (a) An example 3D image of the wall section with smooth surface before performing the flattening procedure to remove the curvature in the x-direction resulting from the cylindrical shape of the tower wall and the tilt in the y-direction. (b) Line scan profiles of the unprocessed image along the red line in the x-direction and (c) green line in the y-direction. (d) The 3D topography image of the same area after flattening and (e, f) the corresponding line profiles. (g) Topography image of the wall section located between the openings with rough texture and its line profiles in the (h) x- and (i) y-directions. (j) The rough surface after flattening process and (k, l) the corresponding line profiles.

Fabrication accuracy using the 2PP-DLW setup was assessed by measuring the dimensions of the design IV microtowers from SEM images and comparing them with the theoretical dimensions of the CAD model (Table 10).

Table 10. Theoretical and experimental dimensions of design IV microtower. The measured data represent the mean ± standard deviation (n = 5).

	CAD dimensions [µm]	**Measured dimensions [µm]**	**Deviation [%]**
Cylinder height	150.0	119.2 ± 4.5	20.5 ± 3.0
Lower opening height	27.0	11.9 ± 4.2	55.9 ± 15.6
Lower opening width	20.0	18.6 ± 0.3	7.2 ± 1.3
Upper opening height	33.0	10.1 ± 0.4	69.4 ± 1.1
Upper opening width	20.0	18.1 ± 0.1	9.3 ± 0.7
Cylinder inner diameter	75.0	71.7 ± 0.4	4.3 ± 0.6
Pillar diameter	5.0	8.5 ± 0.8	70.6 ± 15.9

The comparison revealed that the microtowers had shrunk in both xy- and z-directions on average by 4% and 21%, respectively. The Young's modulus of Ormocomp® processed by 2PP-DLW was estimated via force spectroscopy measurements performed with AFM at the upper rim of the microtower cylinder. For comparison, the Young's modulus was also measured from UV-polymerized Ormocomp® thin films. According to the Hertz model, the average Young's modulus of the microstructures was E = 140 ± 18 MPa, whereas in the UV-cured Ormocomp® thin films it was E = 2.4 ± 0.18 GPa underlining a significant difference between the two differently cured specimens (two-tailed Mann-Whitney U test, p < 0.001, n = 9). Examples of the force versus indentation depth plots are shown in Figure 52.

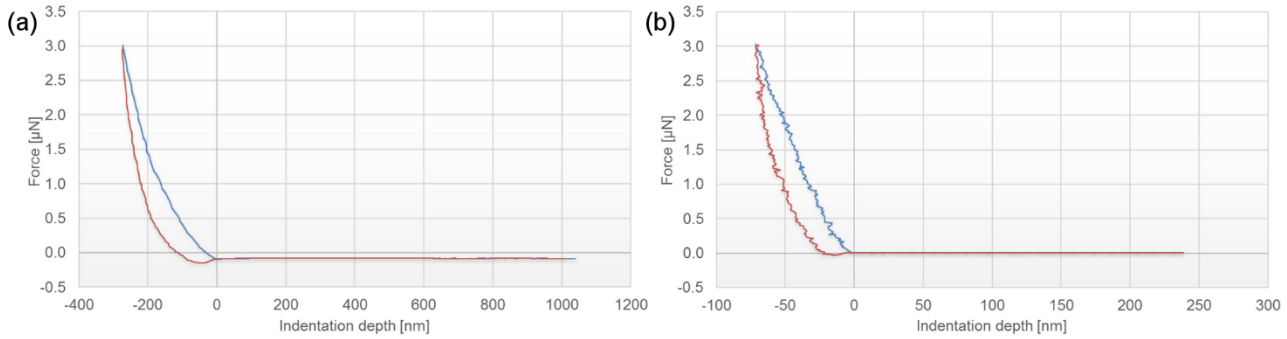

Figure 52. Representative force versus indentation depth plots from the AFM force spectroscopy measurements performed on (a) microtower and (b) Ormocomp® thin film samples. Trace (blue) and retrace (red) curves clearly show hysteresis owing to the plastic behavior of the samples instead of being absolutely elastic as assumed by the Hertz model.

5.6 Cell culture on 2D protein patterns

hPSC-derived neuronal cells were cultured on peptide-functionalized protein patterns for 14 days. The cell attachment and migration on the patterned samples was monitored with bright field microscopy. Figure 53 shows examples of bright field micrographs of each tested sample composition after 1 day, 8 days, and 14 days in culture. During the first day in culture, cells were attached to the surface but only slight neurite outgrowth occurred. Nevertheless, by day 8, cells had attached to sample surfaces and started to extend their neurites and form connections. By day 14, extensive proliferation could be observed and most of the sample surfaces were covered with large cell aggregates.

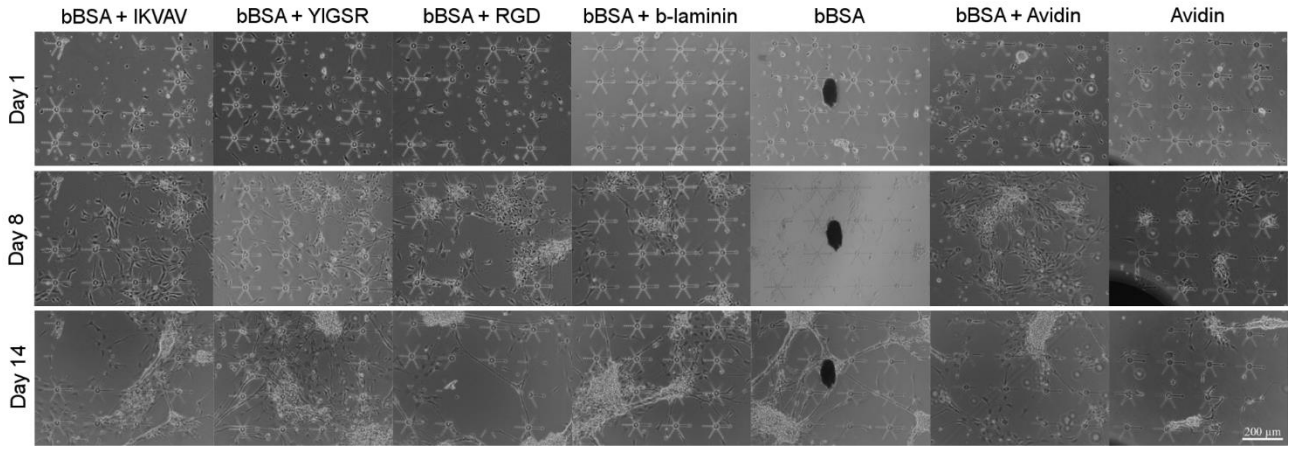

Figure 53. Bright field micrographs of 2D protein patterns functionalized with ECM peptides and reference samples without peptides after 1, 8, and 14 days in culture. Scale bar represents 200 µm.

After 14 days in culture, cells were fixed and immunocytochemically stained (Figure 54). Less than half of the cells were MAP-2- and β-tubulin III-positive neurons (visual estimation, not counted). The rest of the cells were a contaminating cell population of non-astrocytic or non-neuronal cells. The number of GFAP-positive cells on the samples was low (data not shown). The cells seemed to thrive on all samples, in fact, cell proliferation was perhaps too aggressive, and thus it was hard to distinguish, whether the neurites actually followed the patterns. Overall, only a few neurites were aligned along the edges of the patterns. In addition, the somas were not located on the round node areas intended to promote their attachment. None of the tested ECM peptides appeared superior to the others in attracting cells or neurites to the patterns. However, untreated avidin patterns seemed to have the smallest number of cells even at the 14-day time point.

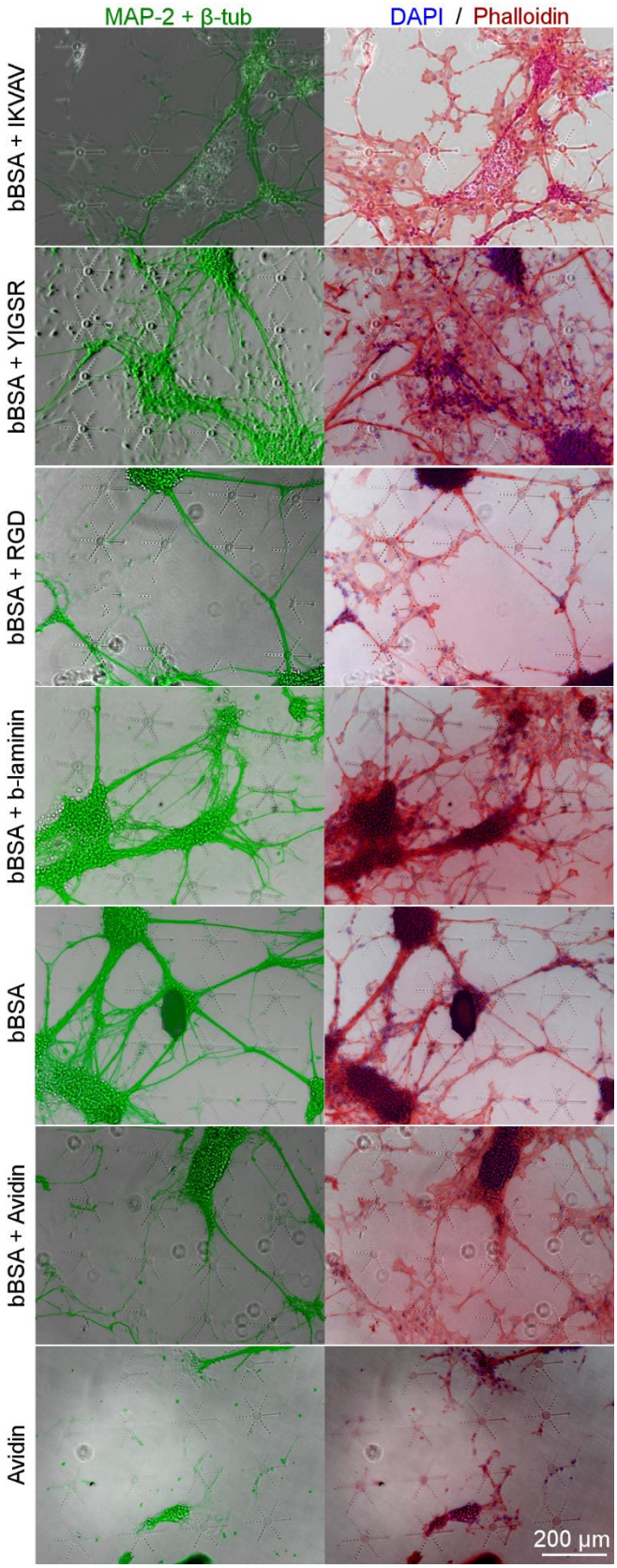

Figure 54. Fluorescence micrographs of immunostained cells on 2D protein patterns. Immunocytochemical markers MAP-2+ β-tubulin III (green), Phalloidin (red), and DAPI (blue).

5.7 Cell culture in 3D confinement microstructures

In Publication III, the laminin solution was applied successfully into the type I neurocages with the MANiPEN micromanipulator. Initially, the very small volume of laminin solution caused rapid evaporation of water from the suspension leaving crystallized laminin and other solutes in the nodes of the neurocages. However, the introduction of a hot water bath dish for the application phase provided a humidified atmosphere and solved the crystallization issue. The application of laminin into the nodes of type III neurocages was found to be more complicated than into type I neurocages. The laminin solution appeared to evaporate or otherwise disappear from the nodes although no crystallization of the protein was observed. Thus, the solution had to be added several times to each node and the repeated injection with a capillary tip distorted some of the neurocage structures.

Type I and type III neurocages were seeded with hPSC-derived neuronal cells to study the cell attachment, migration and directed growth on these samples. The initial cell attachment and migration on the samples containing type I neurocages was evaluated qualitatively with bright field microscopy after two and three days in culture (Figure 55). It was observed that the cells attached readily onto the samples and formed elaborate networks after only two days in culture. During the five-day *in vitro* culture, the cells were found to migrate towards and into the neurocages. Furthermore, when the cells attached to the laminin-coated surface inside the cages, they often extended their neurites along the channels connecting the nodes. However, it was also evident that the neurocages were not able to restrict the cell growth to the area inside the cage walls as cells also grew successfully outside the neurocages even without the laminin coating. This result was also confirmed by immunostaining. Judging by the immunostaining of the cells against MAP-2 (for neuronal cells, stained green) and GFAP (for glial cells, stained red), the majority of the cells were MAP-2 positive, indicating neuronal phenotype. Similar to the bright field microscope images, the immunostained images showed cells extending neurites towards the neurocage structures and some neurites aligned along the exterior walls of the neurocages (Figure 55). Interestingly, the cells also migrated into the neurocages from the small gaps formed in the cage walls.

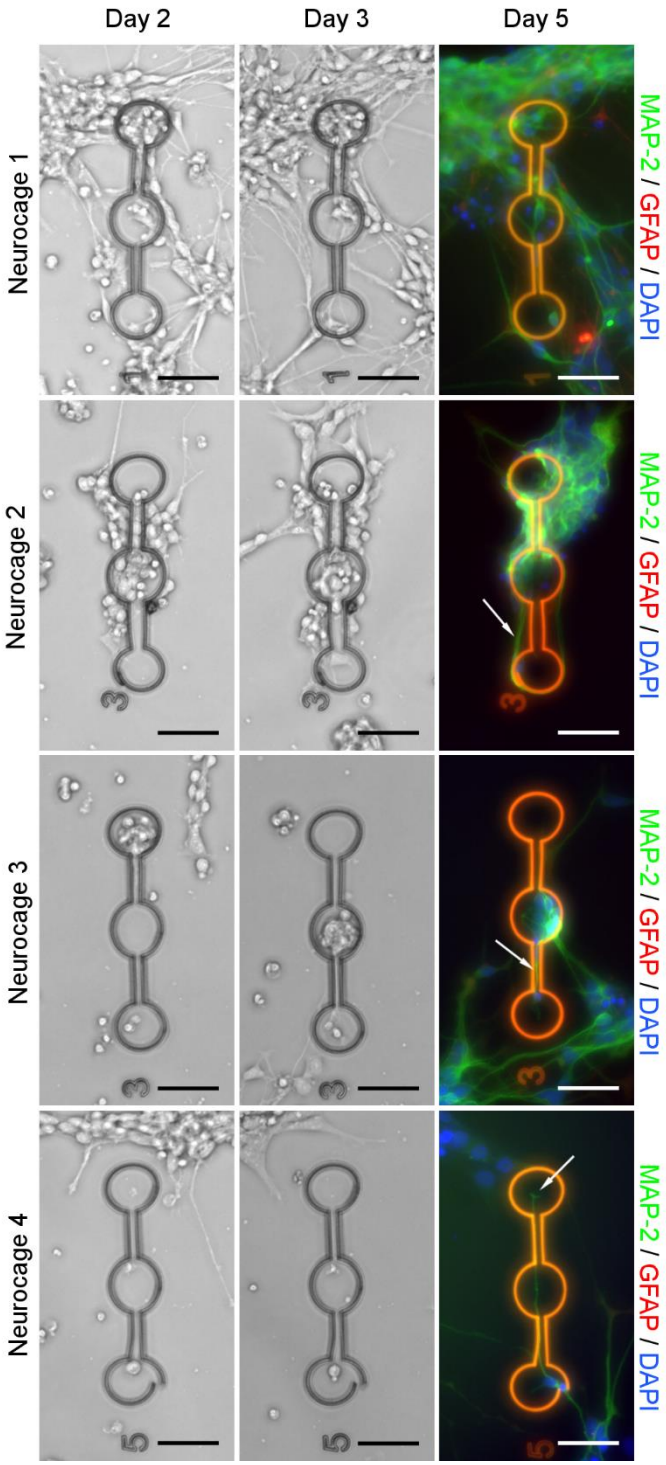

Figure 55. Bright field micrographs of neurocages after two and three days in culture, and fluorescence micrographs of immunostained cells in four parallel neurocages after five days in culture. Neuronal cells are stained green (MAP-2) and astrocytes red (GFAP). Cell nuclei were counterstained blue with DAPI. The neurocages appeared in red due to nonspecific binding of the stains on the structures. Neurites oriented along the exterior of neurocage 2, a neurite oriented along a channel in neurocage 3, and a sprouting growth cone in neurocage 4, are highlighted with arrows. Scale bars represent 50 μm.

The attachment and migration of cells in type III neurocages was followed by bright field imaging of the samples after four and six days in culture (Figure 56). During the first four days in culture, mainly unattached cell aggregates were present on all the samples. The immunocytochemical staining of the cells after eight days in culture showed that there were viable neuronal cells on the samples and even entwined neurites of several neurons, as shown in Figure 56. However, it was impossible to determine from the immunofluorescence images whether the neurites were actually attached to the bottom of the neurocages or were just migrating on top of the cage walls.

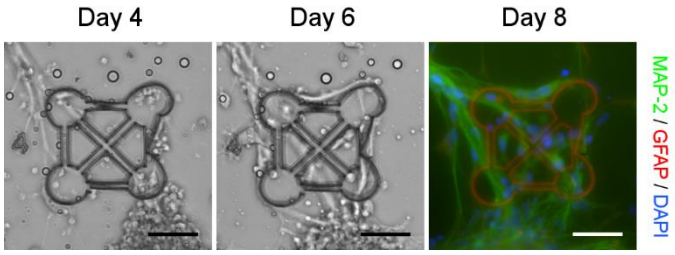

Figure 56. Bright field micrographs of type III neurocage after four and six days in culture, and fluorescence micrographs of immunostained cells after eight days in culture. Neuronal cells are stained green (MAP-2) and astrocytes red (GFAP). Cell nuclei were counterstained blue with DAPI. The neurocage appeared in red due to nonspecific binding of the stains on the structures. Scale bars represent 50 µm.

5.8 Cell culture in 3D tubular microtowers

5.8.1 Applicability of the Microtower Structures for Cell Culture Purposes

In Publication IV, the applicability of microtowers for cell culture purposes was assessed by cell viability analysis. Cells grew in close vicinity to and inside the towers throughout the four-week experiment (Figure 57(a)). The viability of the cells was not affected by the microtowers. In addition, cell growth on the outer surface of the towers was studied to further ensure the suitability of the surface texture for cell attachment (Figure 57(b & c)). The outer surface of the towers at the height of 75 µm to 90 µm representing either rough (R_a = 31 nm) or smooth (R_a = 11 nm) surface texture was closely examined. Visual inspection showed no differences between the different textures. This was confirmed by also comparing the proportions of cells attached to the analyzed areas. There were no statistically significant differences in cell attachment among surfaces with different roughness. Therefore, microtowers fabricated by 2PP-DLW provided a suitable environment for cells.

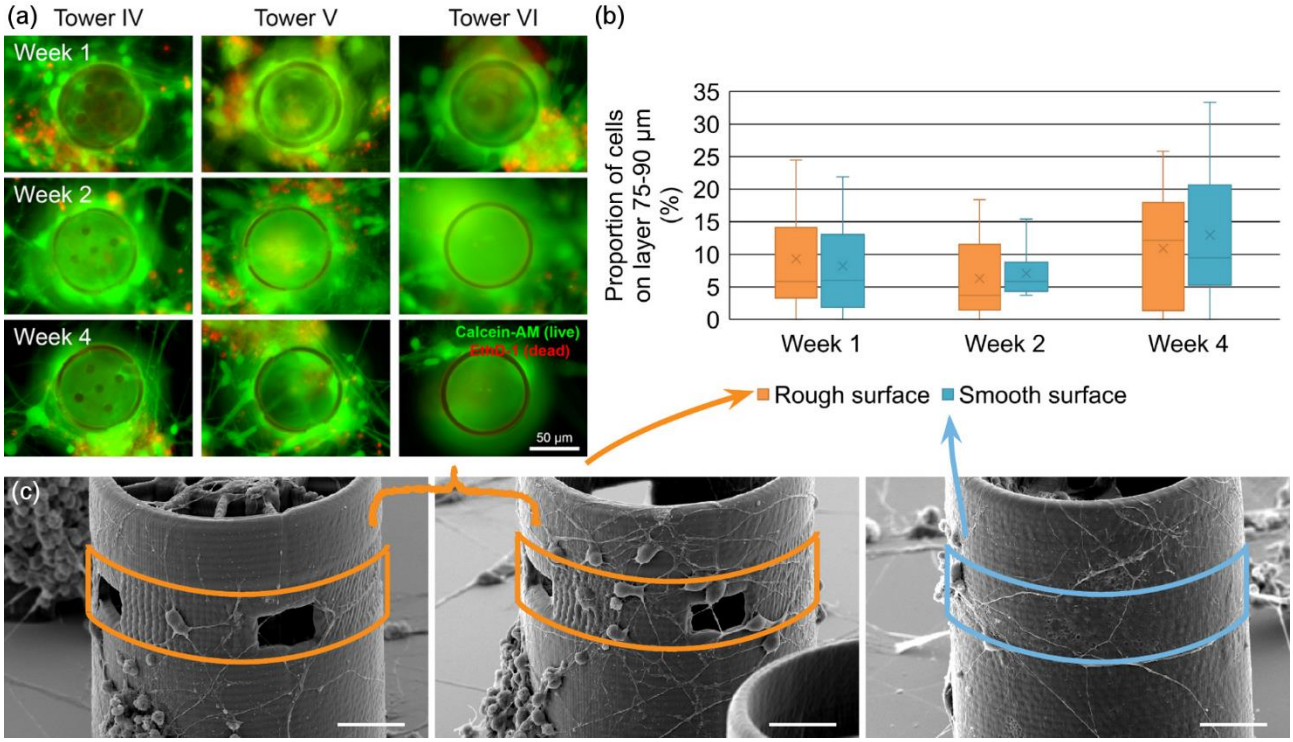

Figure 57. Applicability of the direct laser written microtower structures for cell culture purposes: (a) fluorescence images of live/dead stained cells at different time points, (b) proportion of cells attached to the outer surface layer at height 75 µm to 90 µm representing either rough or smooth surface texture. The cell numbers on the rough surface have been counted by combining the data of tower designs IV and V. The cell numbers on the smooth surface represent the data of tower design VI. There was no statistically significant difference in cell attachment among surfaces with different roughness ($p > 0.05$, two-tailed Mann-Whitney U test, $n = 8–18$), (c) SEM images of microtower designs IV, V, and VI from one-week time point illustrating the surface area used for analysis of cell attachment on differently textured surfaces. Scale bars represent 20 µm.

5.8.2 Neuronal Cell Distribution in Microtowers

Cell phenotype was confirmed as neuronal via immunocytochemical staining against the neuronal markers MAP-2 and β-tubulin III (Figure 58(a)). Cell growth inside and outside the microtowers was studied by counting cell nuclei from confocal image stacks. At the one-week time point, the total cell growth in all the studied tower designs was quite similar (Figure 58(b)). At the two-week time point, the total cell number increased in designs IV and V, whereas the number remained constant in design VI. By week four, the total cell number decreased in designs IV and V, but increased in design VI. Most of the cells, regardless of tower design, were located on the outside walls but there was a high variation in cell number (945 ± 424 cells), whereas the cell number on the inside was lower, but interestingly with less variation (440 ± 158 cells). As the inside of the tower provided a more stable microenvironment for the cells, we next calculated the relative proportion of cells inside the tower from the total cell number. Despite the dramatic changes in cell number outside of design IV, the proportion of cells inside increased significantly from week one to week four (Figure 58(b & c)). In addition, the portion of cells inside tower design IV was a significantly higher compared with design VI at the four-week time point.

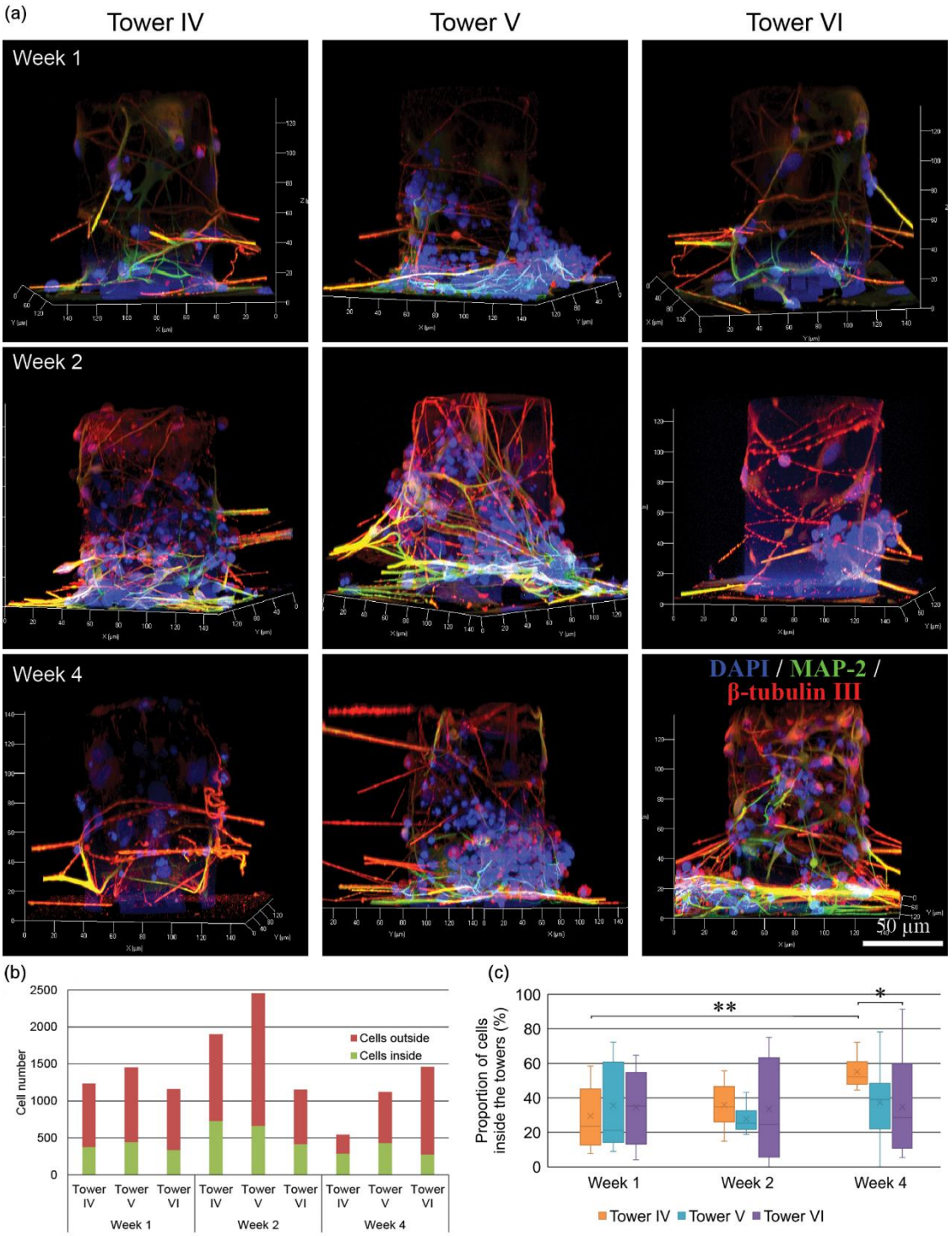

*Figure 58. Total cell number in microtowers. (a) Representative 3D renderings of confocal image stacks with immunocytochemical staining against neuronal markers MAP-2 (green), β-tubulin III (red), and DAPI (blue) for nuclei. (b) Total cell number in microtowers and (c) proportions of cells inside the towers (*p = 0.041 < 0.05, **p = 0.007 < 0.01, n = 7–9, Kruskal-Wallis test followed by post-hoc Dunn-Bonferroni tests).*

The cell distribution inside the towers was analyzed based on six layers. Each layer represented different regions of design IV: from 0 µm to 15 µm lower openings, from 15 µm to 60 µm pillars, from 60 µm to 75 µm lower web, from 75 µm to 90 µm upper openings, from 90 µm to 120 µm pillars,

and from 120 µm to 135 µm upper web. Figure 59(a) presents examples of confocal z-projections of samples at the two-week time point.

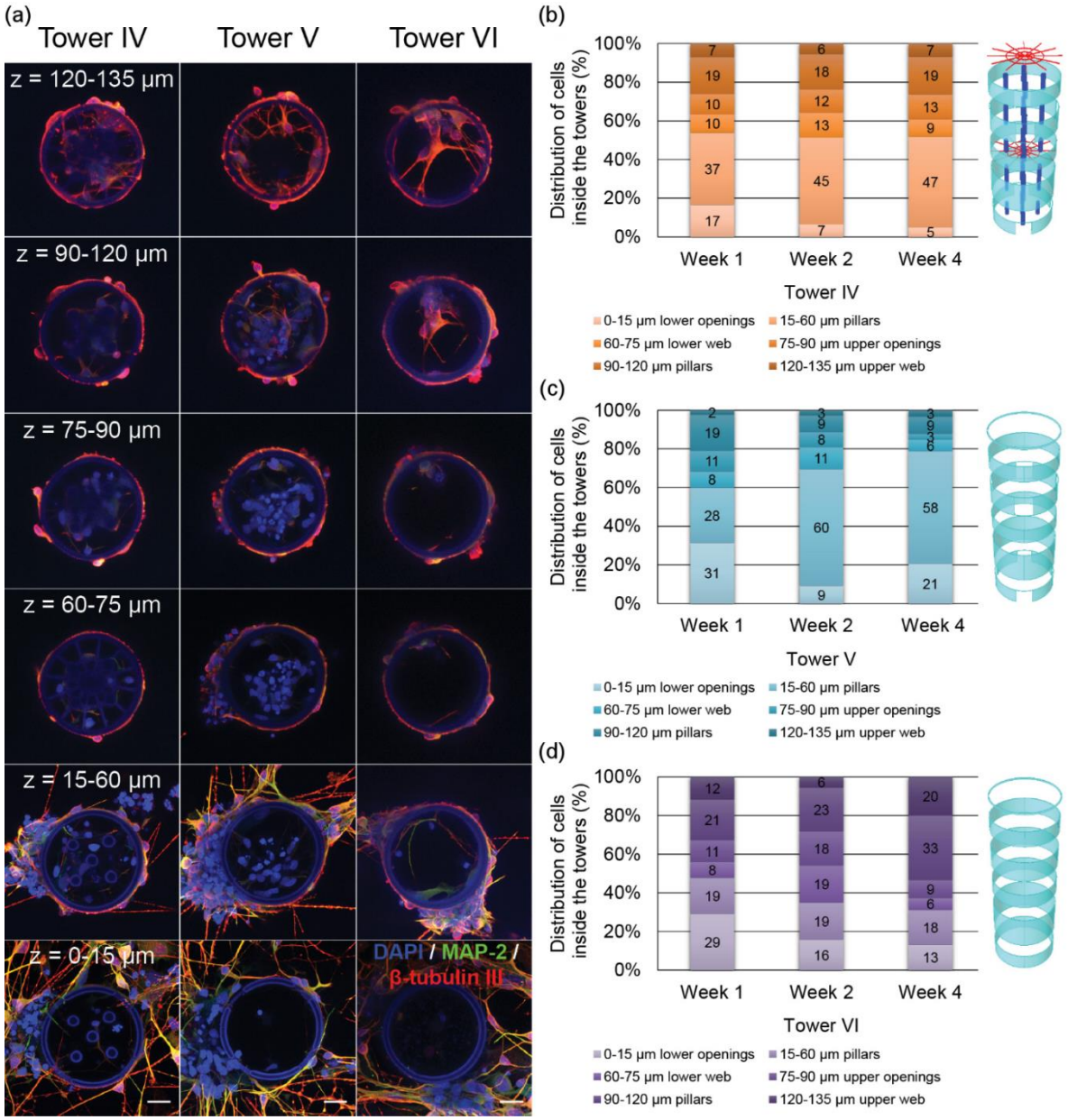

Figure 59. Distribution of cells inside the towers. The counted nuclei data were regrouped into six layers representing different regions of interest present in tower design IV. (a) Illustrative projections of confocal microscopy images from immunocytochemically stained samples representing the six layers of interest. Average cell number per layer inside microtower (b) design IV, (c) design V, and (d) design VI. Immunocytochemical markers MAP-2 (green), β-tubulin III (red), and DAPI (blue). Scale bars represent 20 µm.

In design IV, the cell distribution at the upper half (from 60 µm to135 µm) of the tower remained rather similar throughout the four weeks (Figure 59(b)). Whereas in the lower layers (from 0 µm to 60 µm), the cell localization was observed to shift from the lowest layer (from 0 µm to 15 µm) to the next layer (from 15 µm to 60 µm) over time. However, this movement upward was halted at the layer containing the lower web (from 60 µm to 75 µm). In design V, most of the cells were located in the

lower half of the tower throughout the study (Figure 59(c)). In design VI, the cells were quite evenly distributed throughout the height of the tower during the first two weeks (Figure 59(d)). By week four, the majority of the cells had migrated to the upper parts of the tower.

5.8.3 Orientation of Neurites along Microtowers

The orientation of neurites along the microtowers was first analyzed with automated analysis. Then, a more detailed analysis was performed manually to investigate the distribution of neurite orientation angles. As an example, plots of the neurite orientation distributions from the automated analysis and projections demonstrating manual neurite tracing are shown in Figure 60(a–c). According to automated CytoSpectre analysis of circular variances, all tower designs had cases of high orientation (circular variance ≤ 0.6). However, there was a large variation between parallel samples (Figure 60(d)). The dominant orientation for each tower design is represented as a box plot of mean orientation angles between 0° and 180° in Figure 60(e). The longitudinal axis of the tower is at the angle of 90°, and the neurites following this angle were considered to be perfectly oriented. The majority of the measured mean orientation angles represented ±10° deviation from the longitudinal axis throughout the experiment indicating the presence of longitudinally oriented neurites.

In the manual analysis, the lengths of the traced neurite segments were summed and compared with the total cell number (Figure 60(f)). The main finding was that design IV had the highest neurites to cell number ratio at one and four weeks. Therefore, design IV provided the most promising environment for neurite growth. Figure 60(g–i) shows the distribution of the manually measured neurite segment angles. During the first week (Figure 60(g)), all the tower designs demonstrated similar neurite orientation behavior; the highest neurite occurrence was found in the 10° bin. Throughout the experiment, design IV had the highest incidence of neurite segments (41% to 46%) with an alignment angle of $\leq 20°$ indicating orientation along the longitudinal direction. At the two-week time point (Figure 60(h)), design V had a fairly equal distribution of neurite segment angles across the bins demonstrating quite random orientation, whereas in design VI the highest neurite incidence was detected in bins 10°, 20°, and 40°. All the tower designs had approximately the same number of longitudinally orientated neurites (~40%) at the four-week time point, indicating that the cylindrical shape itself enhanced orientation in long-term culture (Figure 60(i)). Overall, in all the tower designs throughout the experiment, the highest incidence of neurites was located in the 10° to 20° bins indicating good longitudinal orientation.

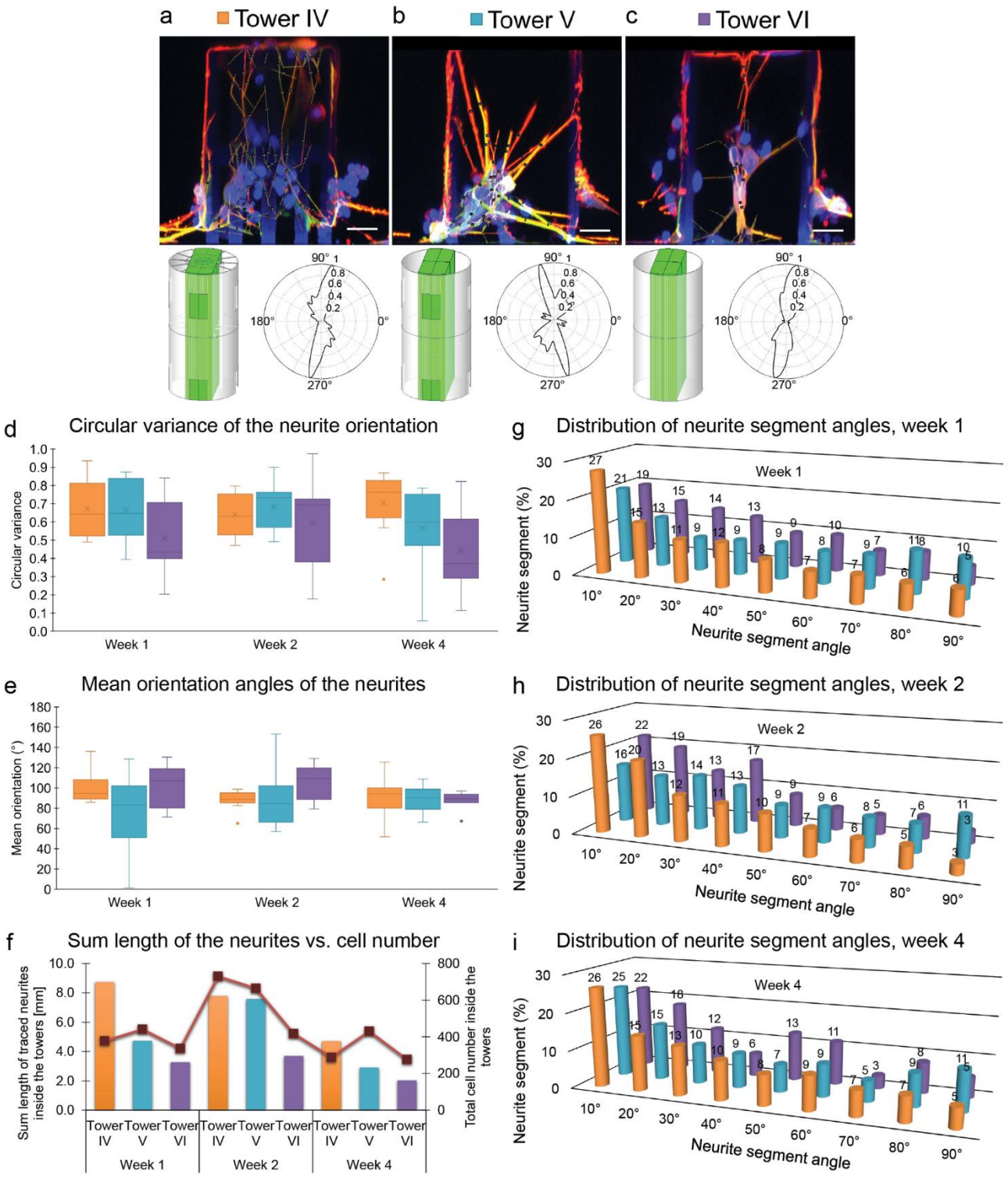

Figure 60. Orientation of neurites inside the towers was determined by measuring the angles of neurite segments from the longitudinal projections taken from the confocal microscopy image stacks of the microtowers. Representative projections of confocal micrographs from the two-week time point with traced neurites marked with yellow lines inside the microtower (a) design IV, (b) design V, and (c) design VI. For each design, the CAD model illustrates the analyzed volume utilized for the neurite angle measurements (marked with green). In addition, plots of orientation distribution created with CytoSpectre software are shown for each case. The distance from the origin represents the relative frequency of the corresponding angle. Value 1 has been designated to the angle with highest incidence. (d) Box plot of the circular

variance of the neurite orientation obtained with CytoSpectre. (e) Box plot of the mean orientation angles of neurites (from 0° to 180°, the longitudinal axis of the tower is at 90°) analyzed with CytoSpectre. (f) Sum length of traced neurites inside each microtower design at different time points and the total cell number (marked with red line). (g–i) Distribution of neurite angles relative to the vertical plane measured from all neurite segments with length 5 µm or more. The longitudinal axis is set to 0°, while horizontal axis is denoted as 90°. Scale bars represent 20 µm.

5.8.4 Formation of 3D Networks

The cell morphology and organization of neuronal networks were assessed by SEM imaging. In all microtower designs, neurons grew in close contact with the 2PP-DLW fabricated towers spreading neurites along the inner and outer surfaces, as shown in Figure 61. On the outer surface of the towers, neurons and neurites extended across the total height of the towers. Neurites as well as neurons migrated between the outer and inner surface through the wall openings in designs IV and V. In addition, similar behavior was seen in all designs at the upper rim of the cylinder, where cells formed connections between outer and inner populations by migrating over the edge (Figure 61, Top view). Interestingly, neurons formed 3D networks with suspended bridges between the adjacent microtowers and between tower walls and bottom surfaces (Figure 61, Last row). These bridges were mostly formed from several neurites intertwined into bundles. Based on the known distance between towers, several suspended neurite bridges were estimated to be ~90 µm long and the longest bridges found were ~260 µm.

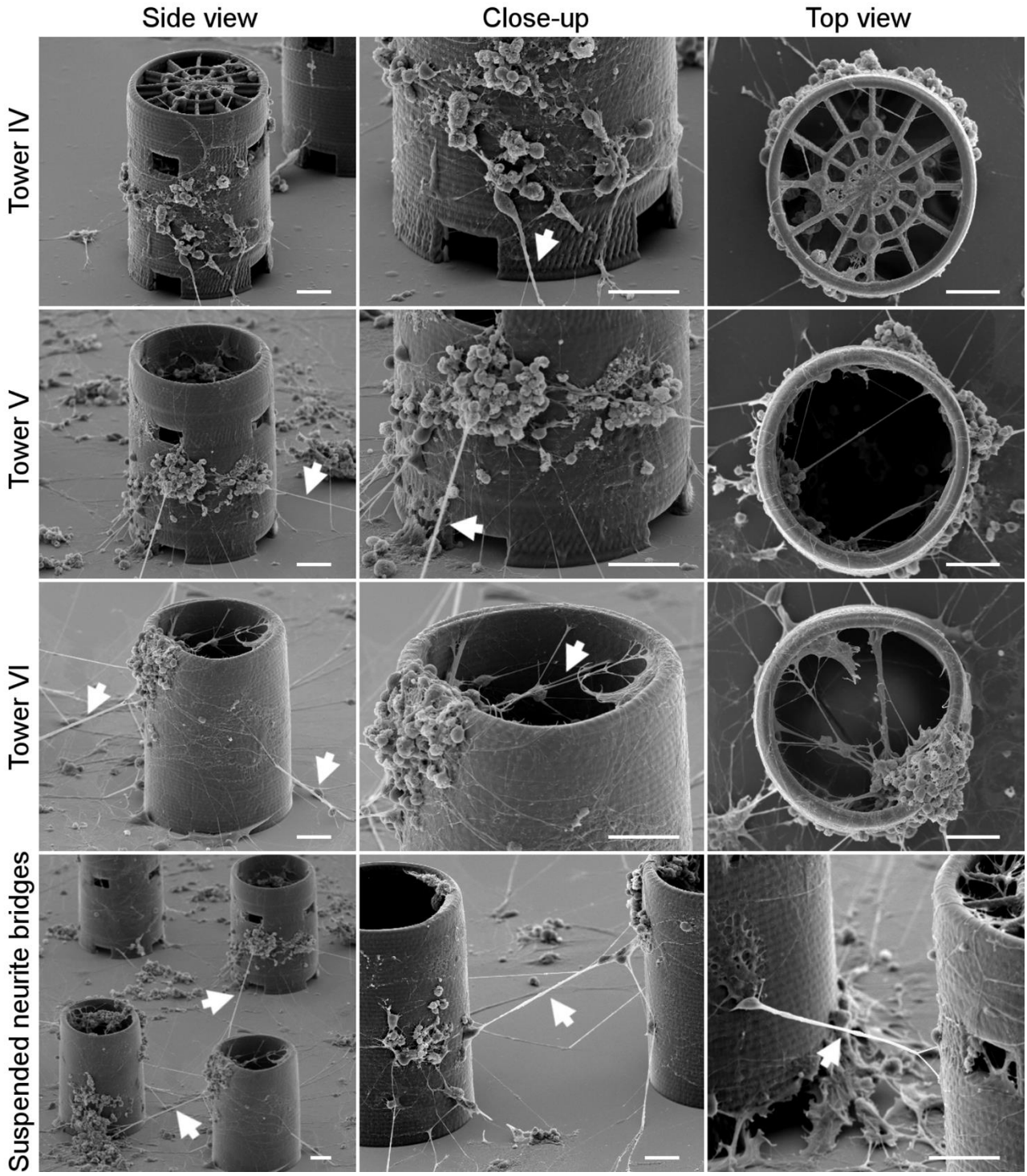

Figure 61. SEM images of neuronal cells inside and outside of different microtower designs at the one-week time point. The images of the three upper rows show the towers from the tilt angles of 60° (first and second column) and 0° (third column). The last row illustrates the close-ups of the suspended neurite bridges extending between adjacent towers. Suspended neurite bridges are marked with arrowheads. Scale bars represent 20 µm.

6 DISCUSSION

6.1 Processing and performance of PCL-o and PEGda structures

Publication I introduced a new photosensitive, non-cytotoxic, and biodegradable polycaprolactone-based resin for 2PP-DLW. Its overall processability and achievable feature size were compared with the performance of PEGda. The evaluation of voxel and line dimensions showed that the dimensions of voxels increase with increasing PI concentration with both materials. It was also concluded that within the utilized average laser power range, PCL-o produced smaller voxels than PEGda. Presumably, the larger size of the PCL-o molecules and the significantly greater viscosity compared with those of PEGda contributed to the smaller size of the PCL-o voxels. More specifically, it can be presumed that radical diffusion of the PI was more restricted in PCL-o than in the low-viscosity PEGda resulting in the formation of smaller structures.

The obtained minimum PCL-o voxel width was in the order of 1 µm, which is in good accordance with the line width reported previously by Clayessens *et al.* (Claeyssens *et al.* 2009) for a novel biodegradable triblock copolymer of PCL, PEG, and trimethylenecarbonate (PTMC). In their study, a Ti:sapphire femtosecond laser together with a 40× objective (N.A. = 0.95) was used to polymerize lattices with a line width of ~4 µm. Evidently, the accuracy of the first generation fabrication setup together with an affordable Nd:YAG laser was adequate for micrometer scale fabrication of structures for cell growth guidance purposes. Furthermore, as the current minimum feature sizes were gained with a picosecond laser and with non-optimized optics, significantly smaller features could be expected for both PEGda and PCL-o when processed with a femtosecond laser system and a high numerical aperture microscope objective.

The adjustability of the laser power range was limited by the available attenuators. Thus, the polymerization window characterized by the 2PP threshold and the laser-induced damage zone could not be determined. As the smallest achieved voxels were wider than the diffraction-limited focal spot the results did not offer any verification whether the initiation mechanism of the polymerization process actually was two-photon absorption. Another drawback was the variance in the data range between the samples at the lower laser powers, which is due to the creeping tendency of the laser at the lower diode current values.

Typically, increasing the number of functional groups in the monomer results in an increased polymerization rate (Decker1996). Therefore, it was assumed that PCL-o with four functional groups would polymerize more rapidly than PEGda with only two functional groups. Obviously, this did not apply to our study, and two possible reasons for this are proposed. Firstly, the methacrylate moieties of the PCL-o can be less reactive than the acrylate moieties of PEGda due to the steric hindrance at the radical center associated with the methyl group on the methacrylate (Schork & Tsavalas 2004). Secondly, the difference in polymerization rate can also be attributed to the higher viscosity of the PCL-o resulting from its larger molecular weight compared with the viscosity of PEGda (Anseth *et*

al. 1994). However, a comprehensive kinetic polymerization study of the polymerization reactions including *in situ* characterization would be needed in order to fully understand the crosslinking phenomenon in these two materials.

The neuronal cell viability and migration test on UV-cured PCL-o and PEGda films demonstrated that these materials are not cytotoxic but do not promote neuronal cell migration either. Thus, the microstructures fabricated from these materials could be used for cell culture purposes if an additional material functionalization or coating is performed. However, in order to be able to reproducibly fabricate series of polymerized samples for cell culture experiments, the microfabrication process should to be fast, effective, and reliable. Therefore, the issue of slow polymerization observed with PCL-o should be addressed before any larger structures for biomedical applications can be fabricated.

6.2 Processing and performance of protein structures

In Publication II, the pico- and femtosecond laser-induced photocrosslinking of protein microstructures was studied. The capability of a picosecond Nd:YAG laser to promote two-photon excited crosslinking of proteins was evaluated by fabricating 2D and 3D microstructures of avidin, BSA, and bBSA. The 2PA-induced photocrosslinking of proteins was demonstrated for the first time using a non-toxic biomolecule flavin mononucleotide (FMN) as the photosensitizer. The shape of the 2PA spectrum of FMN is similar to that of FAD, but the 2PA cross-sections (δ) of FMN are approximately nine times higher than that of FAD (Xu *et al.* 1996). For example, FMN has the maximum $\delta \approx 0.8$ GM at 700 nm (So *et al.* 2000), whereas FAD has the maximum $\delta = 0.085$ GM at 720 nm (Huang *et al.* 2002). Thus, as FMN could be more efficiently excited than FAD, at least with the Ti:sapphire laser operating at the IR region, it was selected as the photosensitizer in Publication II in order to try to enhance the crosslinking rate of the proteins.

The dependence of the protein crosslinking efficiency on the photosensitizer concentration suggested that FMN is not regenerated during the reaction and thus the crosslinking of the proteins probably proceeds via a hydrogen abstraction mechanism (Type I). The addition of a hydrogen atom to the triplet state FMN destroys its ability to generate long-lived triplet states and it can no longer act as a photosensitizer for the crosslinking reaction (Pitts *et al.* 2000). The crosslinking of the proteins via the Type I reaction mechanism is also supported by the experimental conditions (i.e., pH ~7.4), which according to Spikes *et al.* suggests that the FMN-sensitized photo-oxidation is mediated by mechanisms not involving singlet oxygen (Spikes *et al.* 1999).

BSA has also previously been shown to crosslink without any additional photosensitizer with picosecond Nd:YAG lasers (532 nm, ~600 ps, 7.65 kHz; 532 nm 550 ps, 7 kHz) (Kaehr *et al.* 2006; Engelhardt *et al.* 2011b). However, in Publication II crosslinking was not observed when irradiating a solution of 100 mg/ml of bBSA and 100 mg/ml of BSA without the additional photosensitizer. This difference in crosslinking behavior could be attributed to the different laser peak intensities at the focal point of the lasers used in these studies. However, it is impossible to reliably compare the laser intensities of these fabrication setups due to the variation in the measuring methods of the average

laser power (measurement before the objective versus after the objective). Most likely the maximum laser peak intensity of our laser system (460 GW/cm^2) was not high enough to initiate 2PP in the protein solution without the aid of an additional photosensitizer. It was also concluded that the protein concentration of 100 mg/ml was not high enough to produce uniform structures.

The achievable feature sizes for the crosslinked structures of avidin and BSA with a Nd:YAG laser has not been reported by others in detail. However, according to Kaehr *et al*. (Kaehr *et al.* 2006) the width of protein lines is typically less than 0.5 μm when using a laser power of 1 mW and about 0.75 μm at a laser power of 2 mW. In addition, Engelhardt *et al.* (Engelhardt *et al.* 2011b) has reported that voxels polymerized from BSA solution (400 mg/ml) had a minimum height of approximately 1 μm at the average laser power of 2.1 mW measured after the objective. Thus, the line widths and heights of the protein structures achieved in Publication II correspond well to the previously reported values.

The minimum feature size for BSA structures fabricated with a Ti:sapphire laser has been reported to be in the lateral direction ~200 nm (using a 1.3 N.A. objective) (Chan *et al.* 2014). In the axial direction, reported dimensions vary from 1 μm (using a 1.3 N.A. objective) (Nielson *et al.* 2009) to 3.5 μm (using a 0.75 N.A. objective) (Basu *et al.* 2004). Thus, the line widths obtained in Publication II are in good accordance with the previously reported results. Surprisingly, the Nd:YAG laser was able to produce avidin lines with comparable lateral dimensions with the Ti:sapphire laser (270 nm vs. 200 nm). However, the very small lateral dimensions of the protein lines crosslinked with the Nd:YAG laser led to the collapse of the structures during the post-fabrication rinsing phase. In future, this problem could possibly be avoided by using an objective lens with a higher numerical aperture and by selecting the initial position of the laser focal spot more accurately.

bBSA produced a more porous and highly textured surface topography than avidin. A similar surface texture has also been reported previously for a solution of BSA with Rose Bengal as photosensitizer (Pitts *et al.* 2000). A less porous texture could be produced with the Ti:sapphire laser setup than with the Nd:YAG laser. A similar difference in the surface texture of BSA (200 mg/ml, 4 mM of Rose Bengal) has also been discovered by Kaehr *et al.* in their experiments with Nd:YAG (P_{ave} = 0.5 mW) and Ti:sapphire lasers (P_{ave} = 11 mW) (Kaehr *et al.* 2006). This difference could be explained by the higher peak intensities of Ti:sapphire lasers creating a higher number of photosensitizer radicals and enabling more dense crosslinking of the proteins. In Publication II, the substantially higher peak intensity of the Ti:sapphire laser than that of the Nd:YAG laser (43 000 GW/cm^2 vs. 460 GW/cm^2) also allowed the fabrication of continuous protein patterns using 2- to 10-fold faster scanning speeds than with the Nd:YAG laser.

The shrinkage of hydrophilic protein microstructures during the drying phase as the trapped water evaporates is a common disadvantage related to mechanically weak 3D protein structures. The shrinkage phenomenon has also been described by Engelhardt *et al.* for BSA cubes (150 mg/ml, 3 mM of Rose Bengal) fabricated with a femtosecond Ti:sapphire laser (Engelhardt *et al.* 2011a). The edges of the cube shrank from 50 μm to 30 μm, which corresponds to a shrinkage of 40%. Hence, the

cube had a greater shrinkage rate in the xy-direction than the woodpile structure fabricated in Publication II, which is probably a result of lower protein concentration and thus lower crosslinking density used for the fabrication of the cube. In future experiments, the shrinkage of the fabricated structures during the solvent removal could also be reduced by using either a freeze-drying or a critical point drying process instead of the ethanol–methanol dehydration procedure. This would help to eliminate the collapsing force owing to the pressure difference due to the surface tension of the volatile rinsing material.

A similar fluorescence assay as in Publication I has been previously performed by Kaehr *et al.* for avidin (400 mg/ml, no additional photosensitizer) photocrosslinked with a frequency-doubled (532 nm) Nd:YAG laser with a pulse width of ~600 ps (Kaehr *et al.* 2006). They demonstrated that avidin matrices fabricated using an average laser power of 1.7 mW and a scanning speed of 5 μm/s retained their biotin binding capacity and showed fluorescence emission at least tenfold more intense than the negative BSA control. Hence, the ratio of emission of the labeled avidin to the baseline fluorescence of BSA detected by Kaehr *et al.* is the same as the emission ratios observed in Publication II. However, the effect of the average laser power, scanning speed, and photosensitizer concentration on the ligand-binding ability of the avidin-biotin complex photocrosslinked with a Nd:YAG laser with a pulse duration as long as 800 ps was reported by us for the first time.

Overall, the fluorescence intensity plots demonstrated that avidin and biotinylated BSA retained their capability to bind biotin and streptavidin after the fabrication process. This is also supported by the fact that if extensive thermal damage had occurred during the polymerization, less binding of the biotin or streptavidin conjugated label would have been expected at higher values of the laser power and at lower values of the scanning speed, which was not the case according to results. The effect of laser intensities and scan speeds on avidin-biotin complex formation has also been investigated by Seidlits *et al*. with a femtosecond Ti:sapphire laser tuned to 740 nm (Seidlits *et al.* 2009). According to their observations, the amount of NeutrAvidin (deglycosylated version of avidin) bound by the bBSA matrix (200 mg /ml) can be adjusted over at least a 3.5-fold range by varying the laser intensity and scanning speed during the fabrication process. These findings are in good accordance with our results, which show that the amount of bound DyLight® 649 Streptavidin conjugate can be controlled about 1.9-fold by varying the laser power and 5.5-fold by the scanning speed.

The emergence of the third generation fabrication setup and the change of photosensitizer from FAD to Irgacure® 2959 enabled a slightly more efficient crosslinking of protein structures for cell culture purposes. A series of bBSA and avidin 2D single neuron guidance patterns could be fabricated, although several difficulties were encountered during the processing and cell culture. Relatively slow scanning speeds still had to be used, which made the fabrication of a 4×4 array quite time-consuming. In addition, the random detachment of protein patterns from the glass surface during the polymerization process or afterwards damaged many pattern arrays. As very high protein concentrations had to be used for efficient crosslinking, a high degree of nonspecific protein adsorption on the unprotected glass surface was inevitable. Thus, in practice the entire sample surface was coated with protein and ECM peptides used for functionalization, which did not make the actual

protein patterns very attractive for cells to attach exclusively on them. For more reliable cell culture experiments about the effectiveness of the patterns for cell guidance, the substrates need to be pre-passivated with protein-repelling BSA or random graft co-polymer of a poly(L-lysine) and poly(ethylene glycol) (PLL-*g*-PEG). In addition, extensive post-functionalization washing procedures should be used.

Neuronal networks on 2PP-DLW fabricated guidance structures have previously been studied mostly with dissociated rat neurons. This is likely due to their wide availability and the existence of a large literature base describing their electrophysiology and methods for cell culture. Nevertheless, human cells are a more relevant model for example in neurotoxicity studies (Ylä-Outinen *et al.* 2010). Especially hPSC-derived neural cells provide an unlimited source of cells for cell-based therapies and disease modeling, as they are capable of differentiating into the various cell types that make up the CNS (Brafman 2015). Thus, in this thesis, it was appropriate to choose hPSC-derived neuronal cells as the cell type to be tested with the cell growth guidance structures fabricated by 2PP-DLW.

Similar kinds of pattern design as in our unpublished protein study have been successfully used for growth guidance of hippocampal pyramidal neurons by Greene *et al.*, with the essential difference that in their study the pattern was etched as trenches in glass substrates and subsequently functionalized with PLL together with HMDS background. This method combining both chemical and topographical guidance cues was very effective in promoting the polarization of neurons, whereas our approach proved to be quite ineffective in guiding the growth of neuronal cells. Apparently, trenches work better for guidance purposes, as the cells cannot easily escape from them, and isolating individual neurons into single-cell patterns allows one to study the cell response to guidance patterns without the interruptive presence of synaptically connected neurons in the networks. In our study, the cells obviously preferred the formation of connections between neurons to the possibility of growing on top of or along the protein patterns. The virtual height of the protein patterns could also have negatively affected the willingness of the cells to climb and attach on top of the patterns. Instead of being completely flat as chemical guidance cues generally are, our polymerized patterns exhibited heights as high as 1 μm to 2 μm.

In our study, the differentiation of neurites into axons or dendrites due to continuous or interrupted line structures could not be distinguished as the MAP-2- and β-tub-labels were administered as a cocktail and both labelled with Alexa Fluor® 488, and thus could not be detected separately. Furthermore, by day 14 in culture, the cells had overgrown the whole sample surface making it difficult to examine whether they had actually followed the patterns or not. None of the tested ECM peptides seemed to be as effective as the traditional laminin coating in providing suitable culture conditions for the neuronal cell attachment and proliferation. However, the untreated avidin patterns appeared to have the smallest number of cells, which could imply that the cells preferred the patterns of bBSA to avidin.

Overall, the efficiency for the formation of crosslinks between the photo-oxidizable amino acid residues of proteins is much more limited than the conventional chain growth polymerization of

synthetic polymers. Thus, only single cells or small cell clusters can be targeted with photocrosslinked natural protein structures as the fabrication of larger patterns or structures is not economically feasible.

6.3 Processing and performance of Ormocomp® structures

Polymer-ceramic hybrid material Ormocomp® was used as photosensitive material in Publications III and IV for the fabrication of physical confinement microstructures for cells and novel 3D neuronal cell culture platforms based on tubular microtowers. In Publication III, three different models of confining neurocage microstructures were designed and successfully fabricated on microscope slides. The initial problems concerning the collapse of the channel walls at the post-fabrication development phase were mostly solved by replacing 2-propanol with HMDS as rinsing solvent. In Publication IV, six different microtower designs were successfully fabricated. To study the relevance of the intraluminal infrastructure (design IV) for cell growth, two designs without internal structures (designs V and VI) were used for comparison. The process was optimized by defining the operational polymerization windows for Ormocomp® for the tested scanning speeds of 150 μm/s, 350 μm/s, and 550 μm/s. Microtower designs with dense spider webs (I and III) were excluded from further study because some web threads were agglutinated due to a self-polymerization phenomenon (Malinauskas *et al.* 2010b). This phenomenon results from the existence of a sub-activated region surrounding the solid voxel in which the concentration of active radicals is below the polymerization threshold (Jariwala *et al.* 2010). If the two sub-activated regions overlap as a consequence of closely situated scanning paths, the laser-generated radical concentration can exceed the threshold value, which leads to self-assembly of oligomers into features sustaining the post-exposure development (Malinauskas *et al.* 2010b). According to Uppal and Shiakolas, with a diffraction-limited laser spot having a lateral diameter of 1 μm, the radius of the sub-activated region is approximately 5 μm (Uppal & Shiakolas 2008). In our case, the lateral diameter of the diffraction-limited laser spot can be estimated as $d = 1.22\lambda/NA = 720$ nm, where λ is the wavelength of the laser (532 nm) and NA is the numerical aperture of the objective lens (0.90). Thus, in our case the radius of the sub-activated region can be estimated to be approximately 3.6 μm. The offset between the two adjacent threads of web radiating from the center varied from 0 μm to 5.2 μm, so it can be concluded that the overlap of sub-activated regions occurred especially inside the innermost polygons.

Two of the neurocage designs (types I and III) were chosen to be tested with cells as they were also the fastest to fabricate. Based on the preliminary findings, the microtower designs IV, V, and VI were selected as the most optimal models for the cell culture experiments. The scanning speed of 120 μm/s was chosen for the fabrication of neurocages since it produced a smooth enough surface texture and allowed the polymerization of a single type I neurocage in just 5 min. The fabricated neurocages and microtowers were characterized by SEM imaging and the measured dimensions were compared to CAD data in order to evaluate the fabrication accuracy. The node diameter and the channel length of the neurocages retained their dimensions well, having only 9% and 4% deviation from the original CAD models, respectively. The width of the channels and the thickness of the walls deviated

significantly from the CAD dimensions (25% and 98%, respectively), which can be explained by the fabrication of the structures with the multipath scanning method with 1 μm distance between the two contours. The doubling of the wall thickness as compared with the CAD model is thus a direct result from the scanning of the two separate paths. Furthermore, the increased wall thickness narrowed down the channels on each side, which explains the diminished channel width. The polymerized neurocages also deviated from the original design in the z-direction as the wall height had shrunk 22% on average. This results from a common issue related to the polymerization of negative tone photoresists, such as Ormocomp® (Ovsianikov *et al.* 2007d). If the structuring is performed slightly above the 2PP threshold intensity, the polymerization yield is not 100%. Hence, after the removal of the unpolymerized material, a sponge-like material is left behind. The collapse of the material at the molecular level leads to distortion of the structure due to shrinkage. (Ovsianikov *et al.* 2009) The height of the microtower cylinder (design IV) shrunk ~21% because of the low polymerization yield caused by high scanning speed and relatively large axial contour distance. However, these rather high shrinkage rates are in line with the previous published results for Ormocomp® scaffolds reporting up to 24% shrinkage in the z-direction (Käpylä *et al.* 2012). The diameters of the micropillars had broadened 71% (~3.5 μm), which is more than the width of a voxel (~2 μm). The difference could be explained by the overcuring phenomenon resulting from the multipath scanning with three nested contours separated by a distance of 1.0 μm. The overlap of the sub-activated regions (r ~3.6 μm) due to the closely situated contours led to broadening of the diameter of the micropillars. The overcuring could be avoided by taking into account the spot size of the laser beam when preparing the CAD designs and carefully selecting optimal offset between the nested contours. The height of the lower openings of the microtower deviated from the theoretical height considerably (56%) because the glass-photoresist interface, i.e., the initial focal spot height, had to be manually set for each structure. The experimental width of the lower and upper openings corresponded well with the CAD model when taking into account the overcuring caused by the size of the laser beam. The height of the upper openings shrunk substantially (69%). This finding cannot be solely explained by the height of the voxel (6.8 μm). Presumably, the shrinkage is a consequence of several phenomena such as material shrinkage and overcuring occurring at the lower and upper edges of the openings. The inner diameter of the microtower cylinder deviated from the theoretical value by only 4%. The shrinkage effect could be eliminated by using numerical pre-compensation of the CAD model (Sun *et al.* 2004; Ovsianikov *et al.* 2007d) or a single (Maruo *et al.* 2009a) or multi-anchor (Ovsianikov *et al.* 2009) supporting methods. Another way to reduce shrinkage is to develop improved photoresist materials, such as zirconium containing sol-gel material SZ2080 (Ovsianikov *et al.* 2008b; Sun *et al.* 2010b), which yield to mechanically stronger polymers showing negligible shrinkage. In conclusion, although the acknowledged limiting factors that impair the fabrication accuracy of 2PP-DLW and other photolithographic fabrication methods are the material shrinkage induced deviations (Ovsianikov *et al.* 2008b; Jipa *et al.* 2013; Koseki *et al.* 2013), from the point of view of our test arrangements, the shrinkage had no essential effect on the usability of the structures for cell culture.

In Publication IV, the photocured Ormocomp® was also characterized by AFM. The measured Young's modulus of the UV-cured Ormocomp® thin film specimens (E = 2.4 ± 0.18 GPa) were in

the same order as that reported earlier by Schizas and Karalekas (Schizas & Karalekas 2011) and Li *et al.* (Li *et al.* 2014), 1.27 GPa and 1.58 GPa, respectively. However, the average Young's modulus of the microtowers (E = 140 ± 18 MPa) was considerably smaller when compared with the thin film specimens**.** This finding is the result of the lower crosslinking degree of polymer chains achieved via 2PP-DLW when compared with the UV-curing process (Bayindir *et al.* 2005; Schizas & Karalekas 2011). The only reported Young's modulus for Ormocomp® microstructures fabricated by 2PP-DLW is E = 800 MPa (Klein *et al.* 2010), which is considerably larger than that measured here. The difference can be partially explained by the higher scanning speed (550 µm/s vs. from 50 µm/s to 250 µm/s) and the lower laser power values (3.9 mW vs. from 10 mW to 17 mW) used in our fabrication process. These factors resulted in reduction of the exposure, a decrease of the crosslinking degree of the polymer, and the lower Young's modulus. Nevertheless, the level of stiffness was adequate for the fabricated microtowers to withstand all the handling and cell culture procedures without major shape distortions.

In 2PP-DLW, the laser exposure dose (i.e., the scanning speed and average laser power) determines the resulting voxel size. Voxel size combined with the chosen contour distance for the CAD model define the final surface topography of the structure (Burmeister *et al.* 2015). Thus, the surface roughness of the microstructures can be tuned by changing these parameters. Depending on the microtower layer, the surface roughness was either ~11 nm or ~31 nm due to the fluctuation of the laser dose caused by different contour geometries. The achieved surface roughness is, nevertheless, in line with previous studies; Malinauskas *et al.* have reported a roughness of ~30 nm ± 3 nm for sol-gel photopolymer SZ2080 (Malinauskas *et al.* 2010d) and Takada *et al.* found a roughness of 4 nm to 11 nm for urethane acrylate resin SCR500 (Takada *et al.* 2005). It has been suggested that the higher surface roughness resulting in an increase of the surface area can promote the attachment of glioblastoma cells (Zamani *et al.* 2013). In Publication IV, there was no significant difference in cell adhesion between the smooth and the rough areas of the tower wall. This is in accordance with previous results stating that the neurons of substantia nigra can adhere to a surface with R_a ranging from 20 nm to 50 nm, whereas on surfaces with R_a < 10 nm or > 70 nm adherence is negatively affected (Fan *et al.* 2002). Contrary to the studies mentioned above utilizing uncoated surfaces (Fan *et al.* 2002; Zamani *et al.* 2013), we studied surface topographies coated with laminin. As reported previously by Käpylä *et al.* (Käpylä *et al.* 2014), protein coating levels off differences in the surface roughness of Ormocomp®, which in our case resulted in similar cell behavior on both roughnesses. Furthermore, the surface chemistry of Ormocomp® appears to have a stronger effect on cell attachment compared with surface roughness. Consequently, although the surface quality of the structures prepared by the 2PP-DLW technique is very susceptible to any variation in fabrication conditions, small changes in the surface roughness were assumingly compensated by the laminin coating.

Interestingly, surface roughness has been shown to dramatically affect cell behavior by Limongi *et al.* (Limongi *et al.* 2013). In their study, nanopatterned micropillar (h = 10 µm, Ø = 10 µm) arrays supported the formation of 3D networks via suspended neurite bridges, whereas smooth pillars

promoted only the formation of a flat sparse neuronal network on the bottom surface as well as at the root of the pillars (surface roughness not reported for either case). In our study, however, the smooth surface of the microtowers appeared to be very attractive for human-derived neuronal cells. Moreover, 3D neuronal networks and suspended bridges were able to form throughout the tower height, along, and between the tower walls. To some extent, a similar formation of suspended neurite bridges has also been reported with microfibers (Sharifi *et al.* 2016) and 2PP-DLW fabricated microstructures (Koroleva *et al.* 2012; Timashev *et al.* 2016). Thus, it can be concluded that with the 2PP-DLW fabrication method no additional patterning phase is needed to enhance cell growth.

The suitability of neurocage structures for the growth guidance of cells was demonstrated by a proof-of-concept cell culture experiment with hPSC-derived neuronal cells (Publication III). Two-photon polymerized structures, such as low-profile barrier structures (Kaehr *et al.* 2004; Kaehr *et al.* 2006), guidance paths (Seidlits *et al.* 2009), and scaffolds (Melissinaki *et al.* 2011; Koroleva *et al.* 2012), have been previously used for neuronal cell guidance studies. However, to the best of our knowledge, we were the first to culture hPSC-derived neuronal cells inside 2PP-fabricated 3D confinement microstructures. The neurocages were assessed in reference to their ability to support neuronal cell attachment, migration, and orientation by light microscopy and fluorescence microscopy. The cells were applied on the samples by injecting the cell suspension into the cell culture medium, which resulted in random quantities of cells inside the neurocages between the parallel samples. However, during the first few days in culture, the cell count inside the cages levelled off due to the continuous migration of cells in and out of the structures. Surprisingly, the meticulous application of laminin with the micromanipulator inside the neurocage nodes did not appear to have the anticipated influence of restricting the cell growth to only inside the structures. Instead, the cells proliferated successfully outside the neurocages even without the laminin coating, which has been considered as a necessity for their adhesion on surfaces. On the other hand, the formation of complex neuronal networks after only two days in culture suggests that the use of conditioned medium had a definite effect on the viability of the cells on the samples containing type I neurocages. Indeed, the cells cultured in type III neurocages without the conditioned medium preferred to stay as aggregates and did not sprout neurites and form networks as readily as in type I neurocages with the conditioned medium. Thus, such small cell populations need additional growth factor supply provided by the conditioned medium as also suggested by Erickson and co-workers (Erickson *et al.* 2008).

Overall, the cell confining properties of the neurocages were found insufficient, as the cells were able to migrate freely in and out of the structures. Apparently, the height of the walls (19.4 μm) was not high enough to prevent the cells climbing in and out of the structures. The appropriate wall height for cell confinement has not been thoroughly studied for human stem cell-derived neuronal cells, but Béduer *et al.* have reported that most of the cultured primary adult human neural stem cells stayed inside microchannel grooves having a wall height of 25 μm (Béduer *et al.* 2012). Despite the confinement issue, the preliminary cell culture tests showed that neurons had a tendency to migrate towards the neurocages and even make their way into the structures through small openings in the walls. In addition, the neurite guidance properties of the structures appeared quite promising as the

neurons inside the cages readily extended and oriented their neurites along the edges and channels of the structures. Hence, the neurite guidance capabilities of the neurocages shown in Publication III represented a basic but yet important step towards designing more sophisticated structures for the manipulation of migration and orientation of neuronal cells towards a predefined direction.

Microtowers with intraluminal guidance cues in Publication IV provided a more advanced approach to study the growth guidance of neuronal cells. According to the cell behavior, the tower structures seemed to create different microenvironments for the cells: one on the inner and the other on the outer surface of the towers. The lumen provided a more stable, enclosed environment, as seen by the relatively constant cell number throughout the experiment. Although the cell number in lumen of all tower designs was similar, the distribution of cells was affected by the microtower design. The openings in the tower wall seemed to have an impact on the extent of cell migration or proliferation inside the towers, whereas the existence of the spider webs did not considerably alter the cell localization. Moreover, cells inside design VI without the openings were more equally distributed throughout the tower height indicating a homogeneous microenvironment.

Based on the automatic and manual analysis of the neurite orientation angles, the microtower structures were able to orientate neurites. The more detailed manual analysis showed that during the first two weeks in culture, the longitudinal orientation of the neurites was enhanced by the intraluminal infrastructure, most probably by the micropillars (design IV). By week four, the differences in the degree of orientation leveled off in all tower designs. Overall, the intraluminal structures appeared promising for orientation purposes, but the design clearly needs more optimization. It has been reported that 2PP-DLW fabricated guidance structures (Ø = 10 µm to 20 µm) successfully oriented rodent neuroblastoma-glioma cells, although quantitative verification was not conducted (Melissinaki *et al.* 2011). Fibers (Ø = 7 µm to 8 µm) have been shown to effectively orient rat neural cells as 63% of the cells had a dominant growth direction of ≤ 10° compared with the longitudinal direction of the fibers (Sharifi *et al.* 2016). Our results suggest a similar kind of behavior even though we analyzed the orientation of all neurite segments instead of measuring only the main angles for single neurons. Thus, micropillar structures can be used effectively as components of scaffolds for orientation purposes.

Similar microtower structures as in Publication IV without an intraluminal infrastructure (h = 250 µm, Ø = 200 µm) embedded in hydrogel have been used to study rodent neural cell interactions and distribution at the tower interface in 3D (Cullen *et al.* 2011). In that study, cells accumulated to the towers and formed 3D neural networks around and across the towers. Our study showed surprisingly similar results without the support of the hydrogel matrix. We consider this finding to be important as the use of microstructure-supported cell cultures instead of random 3D cultures in a gel matrix could enhance the reproducibility of the experiments *in vitro*.

7 CONCLUSIONS AND OUTLOOK

The aims of this thesis were to choose a suitable photosensitive material for the fabrication of neuronal cell culture platform via 2PP-DLW, design efficient guidance cue structures for the cells, and determine the optimal processing parameters for the feasible fabrication of the designed structures. Furthermore, the efficiency of the fabricated guidance structures for guiding the attachment, growth and orientation of neuronal cells was evaluated by conducting cell culture experiments with hPSC-derived neuronal cells. The following conclusions were made based on the findings of Publications I–IV and the unpublished data:

Comparison and selection of photosensitive materials for 2PP-DLW (Publications I & II):

- Methacrylated poly(ε-caprolactone)-based oligomer and PEGda can be successfully fabricated into simple 2D and 3D structures with a low frequency Nd:YAG laser
- Micrometer-scale features are achievable with both materials, and the realized feature sizes are at an adequate scale for the cell growth guidance applications.
- An extremely low scanning speed (~2 μm/s) is required for the complete polymerization of PCL-o, which severely impedes the fabrication of any relevant, larger-scale structures for biomedical purposes.
- Both, PCL-o and PEGda, are biocompatible materials as shown by the neuronal cell culture test on the UV-cured thin films. However, neither of them supports the migration of cells or outgrowth of neurites.
- Avidin and biotinylated BSA proteins can be structured into 2D and 3D microstructures having submicron feature sizes with Nd:YAG and Ti:sapphire lasers and using FMN as photosensitizer.
- Very high protein concentrations (> 100 mg/ml) are needed to produce uniform structures.
- The substantially higher peak intensity of the Ti:sapphire laser than that of the Nd:YAG laser allows the fabrication of continuous protein patterns using 2- to 10-fold faster scanning speeds than with the Nd:YAG laser.
- Both proteins retain the ligand-binding ability of the avidin-biotin complex after photocrosslinking with the Nd:YAG laser.
- Ormocomp® is an an excellent non-degradable photosensitive material for 2PP-DLW as shown our earlier studies because it offers the fabrication of structures with submicron feature sizes and promotes neuronal cell migration to some extent. Thus, Ormocomp® together with avidin and bBSA proteins are eligible photosensitive materials for further studies.

2PP-DLW fabrication and performance of bioactive protein surface patterns (Publication II & Unpublished data):

- Avidin and bBSA together with Irgacure® 2959 as photosensitizer can be fabricated into surface patterns having dimensions that coincide well with those of the CAD design.

- Protein patterns can be further functionalized with ECM-derived peptide sequences via avidin-biotin interaction.
- Several unsolved issues, such as the detachment of the polymerized patterns from the glass substrate, and the requirement for the use of low scanning speed, complicate the fabrication of arrays of protein surface patterns.
- Peptide-functionalized bBSA and avidin 2D single neuron guidance patterns do not efficiently attract neuronal cells to grow on top of or along the patterns.

2PP-DLW fabrication and performance of Ormocomp® 3D confinement microstructures (Publication III):

- Several designs of confining neurocage microstructures can be successfully fabricated from Ormocomp® without collapsing channel walls if the post-fabrication development solvent 2-propanol is replaced with HMDS.
- The polymerized neurocages suffer from shrinkage, especially in the z-direction, which induces deviations from the original CAD model.
- The meticulous application of laminin with the micromanipulator inside the neurocage nodes does not restrict the cell growth to only inside the structures; instead, the cells proliferate successfully outside the neurocages even without the laminin coating.
- The cell confining properties of the neurocages are insufficient, as the cells can migrate freely in and out of the structures.
- However, the neurite guidance properties of the structures appear quite promising as the neurons inside the cages readily extend and orient their neurites along the edges and channels of the structures.

2PP-DLW fabrication of Ormocomp® 3D tubular microtowers with or without intraluminal guidance cues (Publication IV):

- Several designs of microtowers having complicated intraluminal guidance structures can be feasibly fabricated from Ormocomp®.
- The fabricated microtowers suffer from shrinkage because of the low polymerization yield caused by high scanning speed and relatively large axial contour distance.
- Although the surface roughness of the tower cylinders is rather smooth (either ~11 nm or ~31 nm), the towers are capable of attracting neuronal cells to attach and form suspended neurite bridges between the tower walls.
- The average Young's modulus of the microtowers (E = 140 ± 18 MPa) is considerably smaller when compared with the UV-cured film specimens (E = 2.4 ± 0.18 GPa)**.**
- The microtower structures are able to orientate neurites, and especially during the first two weeks in culture, the longitudinal orientation of the neurites is enhanced by the intraluminal infrastructure.
- The microtowers with intraluminal infrastructure show great potential to be used in long-term 3D culture of neuronal cells without the need to use any additional supportive hydrogel matrix.

Additive manufacturing is revolutionizing the way of producing all kind of products for various application fields ranging from the automotive to the electrical industry and all the way to medical technology. Beyond doubt, 2PP-DLW is one of the state-of-the art fabrication technologies for miniaturization having the greatest potential to create microscale, complex, structures. It is a relatively new microfabrication technique as it was developed about 15 years ago. However, already dozens of research groups around the world have published studies about 2PP-DLW, most of them using their own homemade fabrication setups. Although femtosecond Ti:sapphire lasers have been the workhorse for 2PP-DLW especially in academia, their high acquisition costs may have been a significant obstacle to the adoption of this technology in laboratories lacking specialist knowledge in optics. Thus, also in this thesis a more affordable Q-switched microschip Nd:YAG laser was investigated as a light source for 2PP-DLW (Publications I–III) in addition to a more high-end femtosecond Ti:sapphire laser (Publications III and IV). With both laser sources, a diverse set of biocompatible synthetic monomers and natural proteins could be fabricated into 2D and 3D microstructures having similar feature sizes and structural integrity. The purpose of this thesis was to develop an efficient microscale platform based on topographical or chemical guidance cues to control the attachment, growth and orientation of neuronal cells *in vitro*. Although PCL-o offered an interesting biodegradable alternative to traditional material choices, the extremely slow scanning speed required for the polymerization prevented its further use for cell culture microstructures.

The protein patterns created by 2PP-DLW in Publication II and in the unpublished research study displayed desirable properties such as inherent biomimicry and retention of native functionality to some degree providing effective means for further functionalization. However, several processing-related issues impeded the reproducibility of the process and made the fabrication of protein pattern arrays unfeasible. In addition, the outcome of the neuronal cell culture experiment with these patterns was quite disappointing as none of the studied protein-ECM peptide combinations proved to be effective in guiding cell growth.

Eventually, the polymer-ceramic hybrid material Ormocomp® turned out to be a superior photosensitive material for the fabrication of guidance structures for cells due to its ease of use and the mechanical robustness of the fabricated structures. It also demonstrated good cytocompatibility and promoted neuronal cell migration to some extent. As the most crucial property of neuronal cells is their ability to form functional neuronal networks capable of electrical signaling, the development of *in vitro* 3D culture models for studying the network formation in a controlled environment is vital. Furthermore, as the axonal alignment is an important goal for neural tissue engineering in CNS and PNS injuries and deficits, microscale guidance channels, i.e., the neurocages and microtowers, offer a novel solution to investigate the orientation of neurites along topographical guidance cues. Although the neurocages were unable to efficiently confine cells inside the structures, this limitation was to an extent compensated by their tendency to attract the cells. Furthermore, the neurite guidance properties of the cages were proven adequate as the cells readily extended their neurites along the tunnels and nodes of the structures. Thus, by implementing some changes to the designs and to cell plating, the

neurocage structures could in future be used to create small neuronal networks to study the network formation and function.

However, the observations in Publication IV support the use of microtower-based platforms to facilitate the efficient long-term 3D culturing of human neuronal cells. Microtowers were proven to support neurite orientation and 3D network formation via suspended neurite bridges. The proposed culturing concept could be used as a substitute for the hydrogel matrix commonly used to mechanically support the 3D growth of cells. Hence, it offers a promising concept for future 3D cultures in the field of neuroscience. However, before the fabrication of cell culture platforms on a larger scale can be realized, a few key issues need to be resolved. These involve the relatively long fabrication times due to the serial nature of the process and the limited size of scanning area and the structure height set by the field of view and the working distance of the objective lens. In addition, spherical aberrations arising from the refractive index mismatch and geometrical distortion aberrations produced by low-quality objectives need to be corrected or compensated for in order to enable high-quality fabrication. Thus, it appears that the mass production capabilities of 2PP-DLW are still some years away.

REFERENCES

Abbe, E. Beiträge zur Theorie des Mikroskops und der Mikroskopischen Wahrnehmung. Archiv für Mikroskopische Anatomie 9(1873)1, pp. 413-418.

Al-Hiyasat, A., Darmani, H. & Milhem, M.M. Cytotoxicity Evaluation of Dental Resin Composites and their Flowable Derivatives. Clinical Oral Investigations 9(2005)1, pp. 21-25.

Allen, R., Nielson, R., Wise, D.D. & Shear, J.B. Catalytic Three-Dimensional Protein Architectures. Analytical Chemistry 77(2005)16, pp. 5089-5095.

Anseth, K.S., Wang, C.M. & Bowman, C.N. Reaction Behaviour and Kinetic Constants for Photopolymerizations of Multi(Meth)Acrylate Monomers. Polymer 35(1994)15, pp. 3243-3250.

Antonov, E.N., Bagratashvili, V.N., Whitaker, M.J., Barry, J.J.A., Shakesheff, K.M., Konovalov, A.N., Popov, V.K. & Howdle, S.M. Three-Dimensional Bioactive and Biodegradable Scaffolds Fabricated by Surface-Selective Laser Sintering. Advanced Materials 17(2005)3, pp. 327-330.

Aura, S., Sikanen, T., Kotiaho, T. & Franssila, S. Novel Hybrid Material for Microfluidic Devices. Sensors and Actuators B: Chemical 132(2008)2, pp. 397-403.

Bakar, A.A., Chengzhi Hu, Nakajima, M., Tajima, H. & Fukuda, T. Fabrication of 3D Photo-Resistive Structure for Artificial Capillary Blood Vessel. International Symposium on Micro-NanoMechatronics and Human Science (MHS), 2012, November 4-7, 2012. 2012, IEEE. pp. 244-248.

Balasubramanian, D., Du, X. & Zigler, J.S. The Reaction of Singlet Oxygen with Proteins, with Special Reference to Crystallins. Photochemistry and Photobiology 52(1990)4, pp. 761-768.

Baldacchini, T., Snider, S. & Zadoyan, R. Two-Photon Polymerization with Variable Repetition Rate Bursts of Femtosecond Laser Pulses. Optics Express 20(2012)28, pp. 29890-29899.

Basu, S. & Campagnola, P.J. Enzymatic Activity of Alkaline Phosphatase Inside Protein and Polymer Structures Fabricated via Multiphoton Excitation. Biomacromolecules 5(2004)2, pp. 572-579.

Basu, S., Wolgemuth, C.W. & Campagnola, P.J. Measurement of Normal and Anomalous Diffusion of Dyes within Protein Structures Fabricated via Multiphoton Excited Cross-Linking. Biomacromolecules 5(2004)6, pp. 2347-2357.

Bayer, E., A. & Wilchek, M. Avidin-Biotin Technology. In: Manson, M.M. (ed.). Immunochemical Protocols. Totowa, NJ, USA 1992, Humana Press. pp. 137-142.

Bayindir, Z., Sun, Y. & Naughton, M.J. Polymer Microcantilevers Fabricated via Multiphoton Absorption Polymerization. Applied Physics Letters 86(2005)6, pp. 064105.

Béduer, A., Vieu, C., Arnauduc, F., Sol, J., Loubinoux, I. & Vaysse, L. Engineering of Adult Human Neural Stem Cells Differentiation through Surface Micropatterning. Biomaterials 33(2012)2, pp. 504-514.

Belfield, K.D., Yao, S. & Bondar, M.V. Two-Photon Absorbing Photonic Materials: From Fundamentals to Applications. In: Marder, S., R. & Lee, K. (ed.). Photoresponsive Polymers I. Berlin, Germany 2008, Springer Berlin Heidelberg. pp. 97-156.

Bezwada, R.S., Jamiolkowski, D.D., Lee, I.Y., Agarwal, V., Persivale, J., Trenka-Benthin, S., Erneta, M., Suryadevara, J., Yang, A. & Liu, S. Monocryl® Suture, a New Ultra-Pliable Absorbable Monofilament Suture. Biomaterials 16(1995)15, pp. 1141-1148.

Bilodeau, G.G. Regular Pyramid Punch Problem. Journal of Applied Mechanics 59(1992)3, pp. 519-523.

Bischel, W.K., Kelly, P.J. & Rhodes, C.K. High-Resolution Doppler-Free Two-Photon Spectroscopic Studies of Molecules. I. the ν_3 Bands of $^{12}CH_3F$. Physical Review A 13(1976)5, pp. 1817-1828.

Boiko, Y. Z-Scan Approach for Measuring a Threshold of Two-Photon Photopolymerization. Optical Memory and Neural Networks 17(2008)2, pp. 126-130.

Brafman, D.A. Generation, Expansion, and Differentiation of Human Pluripotent Stem Cell (hPSC) Derived Neural Progenitor Cells (NPCs). In: Turksen, K. (ed.). Stem Cell Renewal and Cell-Cell Communication: Methods and Protocols. New York, NY 2015, Springer New York. pp. 87-102.

Britland, S., Perridge, C., Denyer, M., Morgan, H., Curtis, A. & Wilkinson, C. Morphogenetic Guidance Cues Can Interact Synergistically and Hierarchically in Steering Nerve Cell Growth. Experimental Biology Online 1(1996)2, pp. 1-15.

Bryant, S.J. & Anseth, K.S. Hydrogel Properties Influence ECM Production by Chondrocytes Photoencapsulated in Poly(Ethylene Glycol) Hydrogels. Journal of Biomedical Materials Research 59(2002)1, pp. 63-72.

Bryant, S., Chowdhury, T., Lee, D., Bader, D. & Anseth, K. Crosslinking Density Influences Chondrocyte Metabolism in Dynamically Loaded Photocrosslinked Poly(Ethylene Glycol) Hydrogels. Annals of Biomedical Engineering 32(2004)3, pp. 407-417.

Buividas, R., Rekstyte, S., Malinauskas, M. & Juodkazis, S. Nano-Groove and 3D Fabrication by Controlled Avalanche using Femtosecond Laser Pulses. Optical Materials Express 3(2013)10, pp. 1674-1686.

Burdick, J.A. & Anseth, K.S. Photoencapsulation of Osteoblasts in Injectable RGD-Modified PEG Hydrogels for Bone Tissue Engineering. Biomaterials 23(2002)22, pp. 4315-4323.

Burmeister, F., Steenhusen, S., Houbertz, R., Zeitner, U.D., Nolte, S. & Tünnermann, A. Materials and Technologies for Fabrication of Three-Dimensional Microstructures with sub-100 nm Feature Sizes by Two-Photon Polymerization. Journal of Laser Applications 24(2012)4, pp. 042014.

Burmeister, F., Steenhusen, S., Houbertz, R., Asche, T.S., Nickel, J., Nolte, S., Tucher, N., Josten, P., Obel, K., Wolter, H., Fessel, S., Schneider, A.M., Gartner, K.H., Beck, C., Behrens, P., Tunnermann, A. & Walles, H. Two-Photon Polymerization of Inorganic-Organic Polymers for Biomedical and Microoptical Applications. In: Konig, K. & Ostendorf, A. (ed.). Optically Induced Nanostructures: Biomedical and Technical Applications. Berlin, Germany 2015, De Gruyter. pp. 239-266.

Byatt, J. Laser Beam Control. In: Jones, Julian, D., C. & Webb, C., E. (ed.). Handbook of Laser Technology and Applications. 2003, Taylor & Francis. pp. 135-160.

Chan, B.P., Ma, J.N., Xu, J.Y., Li, C.W., Cheng, J.P. & Cheng, S.H. Femto-Second Laser-Based Free Writing of 3D Protein Microstructures and Micropatterns with Sub-Micrometer Features: A Study on Voxels, Porosity, and Cytocompatibility. Advanced Functional Materials 24(2014)3, pp. 277-294.

Chen, X., Brewer, M.A., Zou, C. & Campagnola, P.J. Adhesion and Migration of Ovarian Cancer Cells on Crosslinked Laminin Fibers Nanofabricated by Multiphoton Excited Photochemistry. Integrative Biology 1(2009)7, pp. 469-476.

Chong, Z.Z., Shang, Y.C., Wang, S. & Maiese, K. Shedding New Light on Neurodegenerative Diseases through the Mammalian Target of Rapamycin. Progress in Neurobiology 99(2012) pp. 128-148.

Chuenjitkuntaworn, B., Inrung, W., Damrongsri, D., Mekaapiruk, K., Supaphol, P. & Pavasant, P. Polycaprolactone/Hydroxyapatite Composite Scaffolds: Preparation, Characterization, and in Vitro and in Vivo Biological Responses of Human Primary Bone Cells. Journal of Biomedical Materials Research Part A 94A(2010)1, pp. 241-251.

Claeyssens, F., Hasan, E.A., Gaidukeviciute, A., Achilleos, D.S., Ranella, A., Reinhardt, C., Ovsianikov, A., Shizhou, X., Fotakis, C., Vamvakaki, M., Chichkov, B.N. & Farsari, M. Three-Dimensional Biodegradable Structures Fabricated by Two-Photon Polymerization. Langmuir 25(2009)5, pp. 3219-3223.

Cló, E., Snyder, J.W., Ogilby, P.R. & Gothelf, K.V. Control and Selectivity of Photosensitized Singlet Oxygen Production: Challenges in Complex Biological Systems. ChemBioChem 8(2007)5, pp. 475-481.

Cullen, D.K., Tang-Schomer, M.D., Struzyna, L.A., Patel, A.R., Johnson, V.E., Wolf, J.A. & Smith, D.H. Microtissue Engineered Constructs with Living Axons for Targeted Nervous System Reconstruction. Tissue Engineering. Part A 18(2012)21-22, pp. 2280-2289.

Cullen, D.K., Wolf, J.A., Vernekar, V.N., Vukasinovic, J. & LaPlaca, M.C. Neural Tissue Engineering and Biohybridized Microsystems for Neurobiological Investigation in Vitro (Part 1). Critical Reviews™ in Biomedical Engineering 39(2011)3, pp. 201-240.

Danilevičius, P., Rekštytė, S., Balčiūnas, E., Kraniauskas, A., Širmenis, R., Baltriukienė, D., Bukelskienė, V., Gadonas, R., Sirvydis, V., Piskarskas, A. & Malinauskas, M. Laser 3D Micro/Nanofabrication of Polymers for Tissue Engineering Applications. Optics & Laser Technology 45(2013)February, pp. 518-524.

Decker, C. Photoinitiated Crosslinking Polymerisation. Progress in Polymer Science 21(1996)4, pp. 593-650.

Denk, W., Strickler, J. & Webb, W. Two-Photon Laser Scanning Fluorescence Microscopy. Science 248(1990)4951, pp. 73-76.

Deubel, M., von Freymann, G., Wegener, M., Pereira, S., Busch, K. & Soukoulis, C.M. Direct Laser Writing of Three-Dimensional Photonic-Crystal Templates for Telecommunications. Nature Materials 3(2004)7, pp. 444-447.

Doraiswamy, A., Jin, C., Narayan, R.J., Mageswaran, P., Mente, P., Modi, R., Auyeung, R., Chrisey, D.B., Ovsianikov, A. & Chichkov, B. Two Photon Induced Polymerization of Organic-Inorganic Hybrid Biomaterials for Microstructured Medical Devices. Acta Biomaterialia 2(2006)3, pp. 267-275.

Doraiswamy, A., Ovsianikov, A., Gittard, S.D., Monteiro-Riviere, N.A., Crombez, R., Montalvo, E., Shen, W., Chichkov, B.N. & Narayan, R.J. Fabrication of Microneedles using Two Photon Polymerization for Transdermal Delivery of Nanomaterials. Journal of Nanoscience and Nanotechnology 10(2010)10, pp. 6305-6312.

Dow, J.A.T., Clark, P., Connolly, P., Curtis, A.S.G. & Wilkinson, C.D.W. Novel Methods for the Guidance and Monitoring of Single Cells and Simple Networks in Culture. Journal of Cell Science 1987(1987)Supplement 8, pp. 55-79.

Dubbelman, T.M.A.R., De Goeij, A.F.P.M. & Van Steveninck, J. Photodynamic Effects of Protoporphyrin on Human Erythrocytes. Nature of the Cross-Linking of Membrane Proteins. Biochimica et Biophysica Acta (BBA) - Biomembranes 511(1978)2, pp. 141-151.

Engelhardt, S., Hoch, E., Borchers, K., Meyer, W., Kruger, H., Tovar, G.E. & Gillner, A. Fabrication of 2D Protein Microstructures and 3D Polymer-Protein Hybrid Microstructures by Two-Photon Polymerization. Biofabrication 3(2011a)2, pp. 025003.

Engelhardt, S., Hu, Y., Seiler, N., Riester, D., Meyer, W., Krüger, H., Wehner, M., Bremus-Köbberling, E. & Gillner, A. 3D-Microfabrication of Polymer-Protein Hybrid Structures with a Q-Switched Microlaser. Journal of Laser Micro/Nanoengineering 6(2011b)1, pp. 54-58.

Erickson, J., Tooker, A., Tai, Y.C. & Pine, J. Caged Neuron MEA: A System for Long-Term Investigation of Cultured Neural Network Connectivity. Journal of Neuroscience Methods 175(2008)1, pp. 1-16.

Fan, Y.W., Cui, F.Z., Hou, S.P., Xu, Q.Y., Chen, L.N. & Lee, I.S. Culture of Neural Cells on Silicon Wafers with Nano-Scale Surface Topography. Journal of Neuroscience Methods 120(2002)1, pp. 17-23.

Farsari, M., Vamvakaki, M. & Chichkov, B.N. Multiphoton Polymerization of Hybrid Materials. Journal of Optics 12(2010)12, pp. 124001.

Farsari, M., Claret-Tournier, F., Huang, S., Chatwin, C.R., Budgett, D.M., Birch, P.M., Young, R.C.D. & Richardson, J.D. A Novel High-Accuracy Microstereolithography Method Employing an Adaptive Electro-Optic Mask. Journal of Materials Processing Technology 107(2000)1-3, pp. 167-172.

Farsari, M. & Chichkov, B.N. Materials Processing: Two-Photon Fabrication. Nature Photonics 3(2009)8, pp. 450-452.

Fischer, J. & Wegener, M. Three-Dimensional Direct Laser Writing Inspired by Stimulated-Emission-Depletion Microscopy. Optical Materials Express 1(2011)4, pp. 614-624.

Fischer, J., Mueller, J.B., Kaschke, J., Wolf, T.J.A., Unterreiner, A. & Wegener, M. Three-Dimensional Multi-Photon Direct Laser Writing with Variable Repetition Rate. Optics Express 21(2013)22, pp. 26244-26260.

Fischer, J. & Wegener, M. Three-Dimensional Optical Laser Lithography Beyond the Diffraction Limit. Laser & Photonics Reviews 7(2013)1, pp. 22-44.

Fisher, W.G., Partridge, W.P., Dees, C. & Wachter, E.A. Simultaneous Two-Photon Activation of Type-I Photodynamic Therapy Agents. Photochemistry and Photobiology 66(1997a)2, pp. 141-155.

Fisher, W.G., Wachter, E.A., Armas, M. & Seaton, C. Titanium:Sapphire Laser as an Excitation Source in Two-Photon Spectroscopy. Applied Spectroscopy 51(1997b)2, pp. 218-226.

Flemming, R.G., Murphy, C.J., Abrams, G.A., Goodman, S.L. & Nealey, P.F. Effects of Synthetic Micro- and Nano-Structured Surfaces on Cell Behavior. Biomaterials 20(1999)6, pp. 573-588.

Fuchs, U., Zeitner, U.D. & Tünnermann, A. Hybrid Optics for Focusing Ultrashort Laser Pulses. Optics Letters 31(2006)10, pp. 1516-1518.

Gittard, S.D., Narayan, R.J., Jin, C., Ovsianikov, A., Chichkov, B.N., Monteiro-Riviere, N.A., Stafslien, S. & Chisholm, B. Pulsed Laser Deposition of Antimicrobial Silver Coating on Ormocer Microneedles. Biofabrication 1(2009)4, pp. 041001.

Gittard, S.D. & Narayan, R.J. Laser Direct Writing of Micro- and Nano-Scale Medical Devices. Expert Review of Medical Devices 7(2010)3, pp. 343-356.

Gittard, S.D., Ovsianikov, A., Akar, H., Chichkov, B., Monteiro-Riviere, N.A., Stafslien, S., Chisholm, B., Shin, C.C., Shih, C.M., Lin, S.J., Su, Y.Y. & Narayan, R.J. Two Photon Polymerization-Micromolding of Polyethylene Glycol-Gentamicin Sulfate Microneedles. Advanced Engineering Materials 12(2010)4, pp. B77-B82.

Gittard, S.D., Koroleva, A., Nguyen, A.K., Fadeeva, E., Gaidukeviciute, A., Schlie-Wolter, S., Narayan, R.J. & Chichkov, B. Two-Photon Polymerization Microstructuring in Regenerative Medicine. Frontiers in Bioscience (Elite Edition) 5(2013) pp. 602-609.

Gittard, S.D., Miller, P.R., Boehm, R.D., Ovsianikov, A., Chichkov, B.N., Heiser, J., Gordon, J., Monteiro-Riviere, N. & Narayan, R.J. Multiphoton Microscopy of Transdermal Quantum Dot Delivery using Two Photon Polymerization-Fabricated Polymer Microneedles. Faraday Discussions 149(2011a)January, pp. 171-185.

Gittard, S.D., Nguyen, A., Obata, K., Koroleva, A., Narayan, R.J. & Chichkov, B.N. Fabrication of Microscale Medical Devices by Two-Photon Polymerization with Multiple Foci via a Spatial Light Modulator. Biomedical Optics Express 2(2011b)11, pp. 3167-3178.

Göppert-Mayer, M. Über Elementarakte mit zwei Quantensprüngen. Annalen der Physik 401(1931)3, pp. 273-294.

Greene, A.C., Washburn, C.M., Bachand, G.D. & James, C.D. Combined Chemical and Topographical Guidance Cues for Directing Cytoarchitectural Polarization in Primary Neurons. Biomaterials 32(2011)34, pp. 8860-8869.

Greiner, A.M., Richter, B. & Bastmeyer, M. Micro-Engineered 3D Scaffolds for Cell Culture Studies. Macromolecular Bioscience 12(2012)10, pp. 1301-1314.

Greiner, A.M., Jäckel, M., Scheiwe, A.C., Stamow, D.R., Autenrieth, T.J., Lahann, J., Franz, C.M. & Bastmeyer, M. Multifunctional Polymer Scaffolds with Adjustable Pore Size and Chemoattractant Gradients for Studying Cell Matrix Invasion. Biomaterials 35(2014)2, pp. 611-619.

Grossmann, T., Schleede, S., Hauser, M., Beck, T., Thiel, M., von Freymann, G., Mappes, T. & Kalt, H. Direct Laser Writing for Active and Passive High-Q Polymer Microdisks on Silicon. Optics Express 19(2011)12, pp. 11451-11456.

Guney, M.G. & Fedder, G.K. Estimation of Line Dimensions in 3D Direct Laser Writing Lithography. Journal of Micromechanics and Microengineering 26(2016)10, pp. 105011-105021.

Guo, R., Xiao, S., Zhai, X., Li, J., Xia, A. & Huang, W. Micro Lens Fabrication by Means of Femtosecond Two Photon Photopolymerization. Optics Express 14(2006)2, pp. 810-816.

Haas, K.H. & Wolter, H. Synthesis, Properties and Applications of Inorganic-Organic Copolymers (ORMOCER®s). Current Opinion in Solid State and Materials Science 4(1999)6, pp. 571-580.

Haas, K.H. Hybrid Inorganic/Organic Polymers Based on Organically Modified Si-Alkoxides. Advanced Engineering Materials 2(2000)9, pp. 571-582.

Harrison, R.G. The Reaction of Embryonic Cells to Solid Structures. Journal of Experimental Zoology 17(1914)4, pp. 521-544.

Haske, W., Chen, V.W., Hales, J.M., Dong, W., Barlow, S., Marder, S.R. & Perry, J.W. 65 Nm Feature Sizes using Visible Wavelength 3-D Multiphoton Lithography. Optics Express 15(2007)6, pp. 3426-3436.

Heinz, W.F. & Hoh, J.H. Spatially Resolved Force Spectroscopy of Biological Surfaces using the Atomic Force Microscope. Trends in Biotechnology 17(1999)4, pp. 143-150.

Helminen, A.O., Korhonen, H. & Seppälä, J.V. Cross-Linked Poly(ε-caprolactone/D,L-lactide) Copolymers with Elastic Properties. Macromolecular Chemistry and Physics 203(2002)18, pp. 2630-2639.

Hertz, H. Ueber die Berührung fester elastischer Körper. Journal für die reine und angewandte Mathematik 92(1882), pp. 156-171.

Hidai, H., Jeon, H., Hwang, D.J. & Grigoropoulos, C.P. Self-Standing Aligned Fiber Scaffold Fabrication by Two Photon Photopolymerization. Biomedical Microdevices 11(2009)3, pp. 643-652.

Horner, P.J. & Gage, F.H. Regenerating the Damaged Central Nervous System. Nature 407(2000)6807, pp. 963-970.

Hou, Y., Schoener, C.A., Regan, K.R., Munoz-Pinto, D., Hahn, M.S. & Grunlan, M.A. Photo-Cross-Linked $PDMS_{star}$-PEG Hydrogels: Synthesis, Characterization, and Potential Application for Tissue Engineering Scaffolds. Biomacromolecules 11(2010)3, pp. 648-656.

Houbertz, R., Steenhusen, S., Stichel, T. & Sextl, G. Two-Photon Polymerization of Inorganic-Organic Hybrid Polymers as Scalable Technology using Ultra-Short Laser Pulses. In: Duarte, F.J. (ed.). Coherence and Ultrashort Pulse Laser Emission. Rijeka, Croatia 2010, InTech. pp. 583-608.

Huang, S., Heikal, A.A. & Webb, W.W. Two-Photon Fluorescence Spectroscopy and Microscopy of NAD(P)H and Flavoprotein. Biophysical Journal 82(2002)5, pp. 2811-2825.

Ikegami, T., Stocker, M.P., Monaco, K., Fourkas, J.T. & Maruo, S. Fabrication of Three-Dimensional Metalized Movable Microstructures by the Combination of Two-Photon Microfabrication and Electroless Plating. Japanese Journal of Applied Physics 51(2012)6, pp. 06FL17.

Ito, Y. Surface Micropatterning to Regulate Cell Functions. Biomaterials 20(1999)23-24, pp. 2333-2342.

Jariwala, S., Venkatakrishnan, K. & Tan, B. Single Step Self-Enclosed Fluidic Channels via Two Photon Absorption (TPA) Polymerization. Optics Express 18(2010)2, pp. 1630-1636.

Jhaveri, S.J., Senaratne, W., Hynd, M.R., Turner, J.N., Sengupta, P., Shain, W. & Ober, C.K. Defining the Biology-Materials Interface using both 2D and 3D Lithography. Journal of Photopolymer Science and Technology 19(2006)4, pp. 435-440.

Jipa, F., Zamfirescu, M., Velea, A., Popescu, M. & Dabu, R. Femtosecond Laser Lithography in Organic and Non-Organic Materials. In: Sumio, H. (ed.). Updates in Advanced Lithography. 2013, InTech. pp. 66-94.

Johnsson, K.L. Contact Mechanics. Cambridge, U.K. 1985, Cambridge University Press. 486 p.

Juodkazis, S., Mizeikis, V. & Misawa, H. Three-Dimensional Microfabrication of Materials by Femtosecond Lasers for Photonics Applications. Journal of Applied Physics 106(2009)5, pp. 051101-1-051101-14.

Juodkazis, S., Mizeikis, V. & Misawa, H. Three-Dimensional Structuring of Resists and Resins by Direct Laser Writing and Holographic Recording. In: Marder, S. & Lee, K. (ed.). Photoresponsive Polymers I. Berlin, Germany 2008, Springer Berlin Heidelberg. pp. 157-206.

Kaehr, B., Allen, R., Javier, D.J., Currie, J. & Shear, J.B. Guiding Neuronal Development with in Situ Microfabrication. Proceedings of the National Academy of Sciences of the United States of America 101(2004)46, pp. 16104-16108.

Kaehr, B. & Shear, J.B. Multiphoton Fabrication of Chemically Responsive Protein Hydrogels for Microactuation. Proceedings of the National Academy of Sciences of the United States of America 105(2008)26, pp. 8850-8854.

Kaehr, B., Ertas, N., Nielson, R., Allen, R., Hill, R.T., Plenert, M. & Shear, J.B. Direct-Write Fabrication of Functional Protein Matrixes using a Low-Cost Q-Switched Laser. Analytical Chemistry 78(2006)9, pp. 3198-3202.

Kaiser, W. & Garrett, C.G.B. Two-Photon Excitation in CaF_2:Eu^{2+}. Physical Review Letters 7(1961)6, pp. 229-231.

Kam, L., Shain, W., Turner, J.N. & Bizios, R. Axonal Outgrowth of Hippocampal Neurons on Micro-Scale Networks of Polylysine-Conjugated Laminin. Biomaterials 22(2001)10, pp. 1049-1054.

Kane, R.S., Takayama, S., Ostuni, E., Ingber, D.E. & Whitesides, G.M. Patterning Proteins and Cells using Soft Lithography. Biomaterials 20(1999)23-24, pp. 2363-2376.

Käpylä, E., Turunen, S., Pelto, J., Viitanen, J. & Kellomäki, M. Investigation of the Optimal Processing Parameters for Picosecond Laser-Induced Microfabrication of a Polymer-Ceramic Hybrid Material. Journal of Micromechanics and Microengineering 21(2011)6, pp. 065033.

Käpylä, E., Aydogan, D.B., Virjula, S., Vanhatupa, S., Miettinen, S., Hyttinen, J. & Kellomäki, M. Direct Laser Writing and Geometrical Analysis of Scaffolds with Designed Pore Architecture for Three-Dimensional Cell Culturing. Journal of Micromechanics and Microengineering 22(2012)11, pp. 115016.

Käpylä, E., Sorkio, A., Teymouri, S., Lahtonen, K., Vuori, L., Valden, M., Skottman, H., Kellomäki, M. & Juuti-Uusitalo, K. Ormocomp-Modified Glass Increases Collagen Binding and Promotes the Adherence and Maturation of Human Embryonic Stem Cell-Derived Retinal Pigment Epithelial Cells. Langmuir 30(2014)48, pp. 14555-14565.

Käpylä, E., Turunen, S. & Kellomäki, M. Two-Photon Polymerization of a Polymer-Ceramic Hybrid Material with a Low-Cost Nd:YAG Laser: Preliminary Resolution Study and 3D Fabrication. Micro and Nanosystems 2(2010)2, pp. 87-99.

Kartasalo, K., Pölönen, R., Ojala, M., Rasku, J., Lekkala, J., Aalto-Setälä, K. & Kallio, P. CytoSpectre: A Tool for Spectral Analysis of Oriented Structures on Cellular and Subcellular Levels. BMC Bioinformatics 16(2015)1, pp. 344.

Kato, J., Takeyasu, N., Adachi, Y., Sun, H. & Kawata, S. Multiple-Spot Parallel Processing for Laser Micronanofabrication. Applied Physics Letters 86(2005)4, pp. 044102.

Kawata, S., Sun, H.B., Tanaka, T. & Takada, K. Finer Features for Functional Microdevices. Nature 412(2001)6848, pp. 697-698.

Kim, R.H. & Lee, K. 3D Stereolithography by using Two-Photon Photopolymerization. Macromolecular Symposia 298(2010)1, pp. 25-33.

Klein, F., Striebel, T., Fischer, J., Jiang, Z., Franz, C.M., von Freymann, G., Wegener, M. & Bastmeyer, M. Elastic Fully Three-Dimensional Microstructure Scaffolds for Cell Force Measurements. Advanced Materials 22(2010)8, pp. 868-871.

Kleinfeld, D., Kahler, K. & Hockberger, P. Controlled Outgrowth of Dissociated Neurons on Patterned Substrates. The Journal of Neuroscience 8(1988)11, pp. 4098-4120.

Koji, S. & Ya, C. A Tutorial on Optics for Ultrafast Laser Materials Processing: Basic Microprocessing System to Beam Shaping and Advanced Focusing Methods. Advanced Optical Technologies 1(2012)5, pp. 353-364.

Kondo, T., Juodkazis, S. & Misawa, H. Reduction of Capillary Force for High-Aspect Ratio Nanofabrication. Applied Physics A 81(2005)8, pp. 1583-1586.

Koroleva, A., Gill, A.A., Ortega, I., Haycock, J.W., Schlie, S., Gittard, S.D., Chichkov, B.N. & Claeyssens, F. Two-Photon Polymerization-Generated and Micromolding-Replicated 3D Scaffolds for Peripheral Neural Tissue Engineering Applications. Biofabrication 4(2012)2, pp. 025005.

Koseki, K., Sakamaki, H. & Jeong, K.M. In Situ Measurement of Shrinkage Behavior of Photopolymers. Journal of Photopolymer Science and Technology 26(2013)4, pp. 57-572.

Koutsopoulos, S. & Zhang, S. Long-Term Three-Dimensional Neural Tissue Cultures in Functionalized Self-Assembling Peptide Hydrogels, Matrigel and Collagen I. Acta Biomaterialia 9(2013)2, pp. 5162-5169.

Kufelt, O., El-Tamer, A., Sehring, C., Schlie-Wolter, S. & Chichkov, B.N. Hyaluronic Acid Based Materials for Scaffolding via Two-Photon Polymerization. Biomacromolecules 15(2014)2, pp. 650-659.

Kumi, G., Yanez, C.O., Belfield, K.D. & Fourkas, J.T. High-Speed Multiphoton Absorption Polymerization: Fabrication of Microfluidic Channels with Arbitrary Cross-Sections and High Aspect Ratios. Lab on a Chip 10(2010)8, pp. 1057-1060.

LaFratta, C.N., Fourkas, J.T., Baldacchini, T. & Farrer, R.A. Multiphoton Fabrication. Angewandte Chemie International Edition 46(2007)33, pp. 6238-6258.

Lai, Y., Cheng, K. & Kisaalita, W. Three Dimensional Neuronal Cell Cultures More Accurately Model Voltage Gated Calcium Channel Functionality in Freshly Dissected Nerve Tissue. PloS One 7(2012)9, pp. e45074.

Lanasa, S.M., Hoffecker, I.T. & Bryant, S.J. Presence of Pores and Hydrogel Composition Influence Tensile Properties of Scaffolds Fabricated from Well-Defined Sphere Templates. Journal of Biomedical Materials Research. Part B, Applied Biomaterials 96(2011)2, pp. 294-302.

LaPlaca, M.C., Vernekar, V.N., Shoemaker, J.T. & Cullen, D.K. Three-Dimensional Neuronal Cultures. In: Berthiaume, F. & Morgan, J.R. (ed.). 3D Tissue Engineering. (First Edition). Boston, USA 2010, Artech House. pp. 187-204.

Lappalainen, R.S., Salomäki, M., Ylä-Outinen, L., Heikkilä, T.J., Hyttinen, J.A., Pihlajamäki, H., Suuronen, R., Skottman, H. & Narkilahti, S. Similarly Derived and Cultured hESC Lines show Variation in their Developmental Potential towards Neuronal Cells in Long-Term Culture. Regenerative Medicine 5(2010)5, pp. 749-762.

Lee, K.S., Yang, D.Y., Park, S.H. & Kim, R.H. Recent Developments in the use of Two-Photon Polymerization in Precise 2D and 3D Microfabrications. Polymers for Advanced Technologies 17(2006)2, pp. 72-82.

Lee, K.S., Kim, R.H., Prabhakaran, P., Yang, D.Y., Lim, T.W. & Park, S.H. Two-Photon Stereolithography. Journal of Nonlinear Optical Physics and Materials 16(2007)1, pp. 59-73.

Lee, K.S., Kim, R.H., Yang, D.Y. & Park, S.H. Advances in 3D Nano/Microfabrication using Two-Photon Initiated Polymerization. Progress in Polymer Science 33(2008)6, pp. 631-681.

Li, Y., Qi, F., Yang, H., Gong, Q., Dong, X. & Duan, X. Nonuniform Shrinkage and Stretching of Polymerized Nanostructures Fabricated by Two-Photon Photopolymerization. Nanotechnology 19(2008)5, pp. 055303-1-055303-5.

Li, Z., Brand, U. & Ahbe, T. Towards Quantitative Modelling of Surface Deformation of Polymer Micro-Structures Under Tactile Scanning Measurement. Measurement Science and Technology 25(2014)4, pp. 044010.

Li, N., Tourovskaia, A. & Folch, A. Biology on a Chip: Microfabrication for Studying the Behavior of Cultured Cells. Critical Reviews in Biomedical Engineering 31(2003)5-6, pp. 423-488.

Liao, C. Product Model Creation and Simulation for Two-Photon Polymerization Micro-Manufacturing. Ph.D. Thesis. 2008. Joseph Fourier University / National Taiwan University. 222 p.

Limongi, T., Cesca, F., Gentile, F., Marotta, R., Ruffilli, R., Barberis, A., Dal Maschio, M., Petrini, E.M., Santoriello, S., Benfenati, F. & Di Fabrizio, E. Nanostructured Superhydrophobic Substrates Trigger the Development of 3D Neuronal Networks. Small 9(2013)3, pp. 402-412.

Liu, Y., Yang, J., Nie, Y., Lu, C., Huang, E., Shin, C., Baldeck, P. & Lin, C. A Simple and Direct Reading Flow Meter Fabricated by Two-Photon Polymerization for Microfluidic Channel. Microfluidics and Nanofluidics 18(2015)3 pp. 427-431.

Livnat, N., Sarig-Nadir, O., Zajdman, R., Seliktar, D. & Shoham, S. A Hydrogel-Based Nerve Regeneration Conduit with Sub-Micrometer Feature Control. Proceedings of the 3rd International IEEE/EMBS Conference on Neural Engineering, Kohala Coast, Hawaii, USA, May 2-5, 2007. IEEE. pp. 101-103.

Majorek, K.A., Porebski, P.J., Dayal, A., Zimmerman, M.D., Jablonska, K., Stewart, A.J., Chruszcz, M. & Minor, W. Structural and Immunologic Characterization of Bovine, Horse, and Rabbit Serum Albumins. Molecular Immunology 52(2012)3-4, pp. 174-182.

Malinauskas, M., Gilbergs, H., Žukauskas, A., Purlys, V., Paipulas, D. & Gadonas, R. A Femtosecond Laser-Induced Two-Photon Photopolymerization Technique for Structuring Microlenses. Journal of Optics 12(2010a)3, pp. 035204.

Malinauskas, M., Bičkauskaitė, G., Rutkauskas, M., Paipulas, D., Purlys, V. & Gadonas, R. Self-Polymerization of Nano-Fibres and Nano-Membranes Induced by Two-Photon Absorption. Lithuanian Journal of Physics 50(2010b)1, pp. 135-140.

Malinauskas, M., Purlys, V., Rutkauskas, M., Gaidukevičiute, A. & Gadonas, R. Femtosecond Visible Light Induced Two-Photon Photopolymerization for 3D Micro/Nanostructuring in Photoresists and Photopolymers. Lithuanian Journal of Physics 50(2010c)2, pp. 201-207.

Malinauskas, M., Gilbergs, H., Zukauskas, A., Belazaras, K., Purlys, V., Rutkauskas, M., Bickauskaite, G., Momot, A., Paipulas, D., Gadonas, R., Juodkazis, S. & Piskarskas, A. Femtosecond Laser Fabrication of Hybrid Micro-Optical Elements and their Integration on the Fiber Tip. Proceedings of SPIE 7716, Micro-Optics 2010, April 12-16, 2010. Bellingham, Washington, USA, 2010d, SPIE.

Malinauskas, M., Žukauskas, A., Bičkauskaitė, G., Gadonas, R. & Juodkazis, S. Mechanisms of Three-Dimensional Structuring of Photo-Polymers by Tightly Focussed Femtosecond Laser Pulses. Optics Express 18(2010e)10, pp. 10209-10221.

Malinauskas, M., Danilevicius, P. & Juodkazis, S. Three-Dimensional Micro-/Nano-Structuring via Direct Write Polymerization with Picosecond Laser Pulses. Optics Express 19(2011)6, pp. 5602-5610.

Malinauskas, M., Farsari, M., Piskarskas, A. & Juodkazis, S. Ultrafast Laser Nanostructuring of Photopolymers: A Decade of Advances. Physics Reports 533(2013)1, pp. 1-31.

Marino, A., Ciofani, G., Filippeschi, C., Pellegrino, M., Pellegrini, M., Orsini, P., Pasqualetti, M., Mattoli, V. & Mazzolai, B. Two-Photon Polymerization of Sub-Micrometric Patterned Surfaces: Investigation of Cell-Substrate Interactions and Improved Differentiation of Neuron-Like Cells. ACS Applied Materials & Interfaces 5(2013)24, pp. 13012-13021.

Maruo, S., Nakamura, O. & Kawata, S. Three-Dimensional Microfabrication with Two-Photon-Absorbed Photopolymerization. Optics Letters 22(1997)2, pp. 132-134.

Maruo, S., Hasegawa, T. & Yoshimura, N. Single-Anchor Support and Supercritical CO_2 Drying Enable High-Precision Microfabrication of Three-Dimensional Structures. Optics Express 17(2009a)23, pp. 20945-20951.

Maruo, S., Takaura, A. & Saito, Y. Optically Driven Micropump with a Twin Spiral Microrotor. Optics Express 17(2009b)21, pp. 18525-18532.

McKinnon, D.D., Kloxin, A.M. & Anseth, K.S. Synthetic Hydrogel Platform for Three-Dimensional Culture of Embryonic Stem Cell-Derived Motor Neurons. Biomaterials Science 1(2013)5, pp. 460-469.

Melissinaki, V., Gill, A.A., Ortega, I., Vamvakaki, M., Ranella, A., Haycock, J.W., Fotakis, C., Farsari, M. & Claeyssens, F. Direct Laser Writing of 3D Scaffolds for Neural Tissue Engineering Applications. Biofabrication 3(2011)4, pp. 045005.

Middleton, J.C. & Tipton, A.J. Synthetic Biodegradable Polymers as Orthopedic Devices. Biomaterials 21(2000)23, pp. 2335-2346.

Miller, C., Jeftinija, S. & Mallapragada, S. Synergistic Effects of Physical and Chemical Guidance Cues on Neurite Alignment and Outgrowth on Biodegradable Polymer Substrates. Tissue Engineering 8(2002)3, pp. 367-378.

Mizeikis, V., Seet, K.K., Juodkazis, S. & Misawa, H. Three-Dimensional Woodpile Photonic Crystal Templates Forthe Infrared Spectral Range. Optics Letters 29(2004)17, pp. 2061-2063.

Mueller, J.B., Fischer, J., Mange, Y.J., Nann, T. & Wegener, M. *In-Situ* Local Temperature Measurement during Three-Dimensional Direct Laser Writing. Applied Physics Letters 103(2013)12, pp. 123107.

Namatsu, H., Kurihara, K., Nagase, M., Iwadate, K. & Murase, K. Dimensional Limitations of Silicon Nanolines Resulting from Pattern Distortion due to Surface Tension of Rinse Water. Applied Physics Letters 66(1995)20, pp. 2655-2657.

Narayan, R.J., Doraiswamy, A., Chrisey, D.B. & Chichkov, B.N. Medical Prototyping using Two Photon Polymerization. Materials Today 13(2010)12, pp. 42-48.

Nguyen, K.T. & West, J.L. Photopolymerizable Hydrogels for Tissue Engineering Applications. Biomaterials; Injectable Polymeric Biomaterials 23(2002)22, pp. 4307-4314.

Nguyen, Q.T., Hwang, Y., Chen, A.C., Varghese, S. & Sah, R.L. Cartilage-Like Mechanical Properties of Poly (Ethylene Glycol)-Diacrylate Hydrogels. Biomaterials 33(2012)28, pp. 6682-6690.

Nielson, R., Kaehr, B. & Shear, J.B. Microreplication and Design of Biological Architectures using Dynamic-Mask Multiphoton Lithography. Small 5(2009)1, pp. 120-125.

Obi, S. Replicated Optical Microstructures in Hybrid Polymers: Process Technology and Applications. Dissertation. Neuchâtel, Switzerland 2006. University of Neuchâtel. 110 p.

Oliva, A.A.,Jr, James, C.D., Kingman, C.E., Craighead, H.G. & Banker, G.A. Patterning Axonal Guidance Molecules using a Novel Strategy for Microcontact Printing. Neurochemical Research 28(2003)11, pp. 1639-1648.

Ovsianikov, A., Chichkov, B., Adunka, O., Pillsbury, H., Doraiswamy, A. & Narayan, R.J. Rapid Prototyping of Ossicular Replacement Prostheses. Applied Surface Science 253(2007a)15, pp. 6603-6607.

Ovsianikov, A., Chichkov, B., Mente, P., Monteiro-Riviere, N.A., Doraiswamy, A. & Narayan, R.J. Two Photon Polymerization of Polymer-Ceramic Hybrid Materials for Transdermal Drug Delivery. International Journal of Applied Ceramic Technology 4(2007b)1, pp. 22-29.

Ovsianikov, A., Schlie, S., Ngezahayo, A., Haverich, A. & Chichkov, B.N. Two-Photon Polymerization Technique for Microfabrication of CAD-Designed 3D Scaffolds from Commercially Available Photosensitive Materials. Journal of Tissue Engineering and Regenerative Medicine 1(2007c)6, pp. 443-449.

Ovsianikov, A., Gaidukeviciute, A., Chichkov, B.N., Oubaha, M., MacCraith, B.D., Sakellari, I., Giakoumaki, A., Gray, D., Vamvakaki, M., Farsari, M. & Fotakis, C. Two-Photon Polymerization of Hybrid Sol-Gel Materials for Photonics Applications. Laser Chemistry 2008(2008a), Article ID 493059.

Ovsianikov, A., Malinauskas, M., Schlie, S., Chichkov, B., Gittard, S., Narayan, R., Löbler, M., Sternberg, K., Schmitz, K.,P. & Haverich, A. Three-Dimensional Laser Micro- and Nano-Structuring of Acrylated Poly(Ethylene Glycol) Materials and Evaluation of their Cytoxicity for Tissue Engineering Applications. Acta Biomaterialia 7(2011)3, pp. 967-974.

Ovsianikov, A., Passinger, S., Houbertz, R. & Chichkov, B. Three Dimensional Material Processing with Femtosecond Lasers. In: Phipps, C. (ed.). Laser Ablation and Its Applications. New York, USA 2007d, Springer Science. pp. 121-157.

Ovsianikov, A. & Chichkov, B.N. Two-Photon Polymerization – High Resolution 3D Laser Technology and Its Applications. In: Korkin, A. & Rosei, F. (ed.). Nanoelectronics and Photonics. New York, USA 2008, Springer New York. pp. 427-446.

Ovsianikov, A., Viertl, J., Chichkov, B., Oubaha, M., MacCraith, B., Sakellari, I., Giakoumaki, A., Gray, D., Vamvakaki, M., Farsari, M. & Fotakis, C. Ultra-Low Shrinkage Hybrid Photosensitive Material for Two-Photon Polymerization Microfabrication. ACS Nano 2(2008b)11, pp. 2257-2262.

Ovsianikov, A., Shizhou, X., Farsari, M., Vamvakaki, M., Fotakis, C. & Chichkov, B.N. Shrinkage of Microstructures Produced by Two-Photon Polymerization of Zr-Based Hybrid Photosensitive Materials. Optics Express 17(2009)4, pp. 2143-2148.

Park, S., Kim, K.H., Lim, T.W., Yang, D. & Lee, K. Investigation of Three-Dimensional Pattern Collapse Owing to Surface Tension using an Imperfection Finite Element Model. Microelectronic Engineering 85(2008)2, pp. 432-439.

Paz, V.F., Emons, M., Obata, K., Ovsianikov, A., Peterhänsel, S., Frenner, K., Reinhardt, C., Chichkov, B., Morgner, U. & Osten, W. Development of Functional Sub-100 nm Structures with 3D Two-Photon Polymerization Technique and Optical Methods for Characterization. Journal of Laser Applications 24(2012)4, pp. 042004-1-042004-7.

Peppas, N.A., Bures, P., Leobandung, W. & Ichikawa, H. Hydrogels in Pharmaceutical Formulations. European Journal of Pharmaceutics and Biopharmaceutics 50(2000)1, pp. 27-46.

Pins, G.D., Bush, K.A., Cunningham, L.P. & Campagnola, P.J. Multiphoton Excited Fabricated Nano and Micro Patterned Extracellular Matrix Proteins Direct Cellular Morphology. Journal of Biomedical Materials Research - Part A 78(2006)1, pp. 194-204.

Pitts, J.D., Campagnola, P.J., Epling, G.A. & Goodman, S.L. Submicron Multiphoton Free-Form Fabrication of Proteins and Polymers: Studies of Reaction Efficiencies and Applications in Sustained Release. Macromolecules 33(2000)5, pp. 1514-1523.

Puschmann, T.B., de Pablo, Y., Zanden, C., Liu, J. & Pekny, M. A Novel Method for Three-Dimensional Culture of Central Nervous System Neurons. Tissue Engineering. Part C, Methods 20(2014)6, pp. 485-492.

Raimondi, M.T., Eaton, S.M., Nava, M.M., Laganà, M., Cerullo, G. & Osellame, R. Two-Photon Laser Polymerization: From Fundamentals to Biomedical Application in Tissue Engineering and Regenerative Medicine. Journal of Applied Biomaterials and Biomechanics 10(2012)1, pp. 56-66.

Rajnicek, A., Britland, S. & McCaig, C. Contact Guidance of CNS Neurites on Grooved Quartz: Influence of Groove Dimensions, Neuronal Age and Cell Type. Journal of Cell Science 110(1997)23, pp. 2905-2913.

Rajnicek, A. & McCaig, C. Guidance of CNS Growth Cones by Substratum Grooves and Ridges: Effects of Inhibitors of the Cytoskeleton, Calcium Channels and Signal Transduction Pathways. Journal of Cell Science 110(1997)23, pp. 2915-2924.

Rekštytė, S., Jonušauskas, L., Žukauskas, A., Gervinskas, G., Malinauskas, M. & Juodkazis, S. Three-Dimensional Nanostructuring of Polymer Materials by Controlled Avalanche using Femtosecond Laser Pulses. *Proc. SPIE* 8972, Frontiers in Ultrafast Optics: Biomedical, Scientific, and Industrial Applications XIV, San Francisco, California, USA, February 2-5, 2014. San Francisco, California, USA 2014, SPIE. pp. 897210.

Rich, J., Korhonen, H., Hakala, R., Korventausta, J., Elomaa, L. & Seppälä, J. Porous Biodegradable Scaffold: Predetermined Porosity by Dissolution of Poly(Ester-Anhydride) Fibers from Polyester Matrix. Macromolecular Bioscience 9(2009)7, pp. 654-660.

Rill, M.S., Plet, C., Thiel, M., Staude, I., von Freymann, G., Linden, S. & Wegener, M. Photonic Metamaterials by Direct Laser Writing and Silver Chemical Vapour Deposition. Nature Materials 7(2008)7, pp. 543-546.

Ritschdorff, E.T. & Shear, J.B. Multiphoton Lithography using a High-Repetition Rate Microchip Laser. Analytical Chemistry 82(2010)20, pp. 8733-8737.

Rumi, M. & Perry, J.W. Two-Photon Absorption: An Overview of Measurements and Principles. Advances in Optics and Photonics 2(2010)4, pp. 451-518.

Sakellari, I., Kabouraki, E., Gray, D., Purlys, V., Fotakis, C., Pikulin, A., Bityurin, N., Vamvakaki, M. & Farsari, M. Diffusion-Assisted High-Resolution Direct Femtosecond Laser Writing. ACS Nano 6(2012)3, pp. 2302-2311.

Sanchez, C., Ribot, F. & Lebeau, B. Molecular Design of Hybrid Organic-Inorganic Nanocomposites Synthesized via Sol-Gel Chemistry. Journal of Materials Chemistry 9(1999)1, pp. 35-44.

Schizas, C., Melissinaki, V., Gaidukeviciute, A., Reinhardt, C., Ohrt, C., Dedoussis, V., Chichkov, B., Fotakis, C., Farsari, M. & Karalekas, D. On the Design and Fabrication by Two-Photon Polymerization of a Readily Assembled Micro-Valve. The International Journal of Advanced Manufacturing Technology 48(2010)5-8, pp. 435-441.

Schizas, C. & Karalekas, D. Mechanical Characteristics of an Ormocomp® Biocompatible Hybrid Photopolymer. Journal of the Mechanical Behavior of Biomedical Materials 4(2011)1, pp. 99-106.

Schlie, S., Ngezahayo, A., Ovsianikov, A., Fabian, T., Kolb, H.A., Haferkamp, H. & Chichkov, B.N. Three-Dimensional Cell Growth on Structures Fabricated from ORMOCER by Two-Photon Polymerization Technique. Journal of Biomaterials Applications 22(2007)3, pp. 275-287.

Schmidt, H. New Type of Non-Crystalline Solids between Inorganic and Organic Materials. Journal of Non-Crystalline Solids 73(1985)1-3, pp. 681-691.

Schork, F.J. & Tsavalas, J. The Morphology of Alkyd/Acrylate Latexes Produced via Hybrid Miniemulsion Polymerization: Grafting Mechanisms. In: Tauer, K. (ed.). Aqueous Polymer Dispersions. Berlin, Heidelberg 2004, Springer Berlin Heidelberg. pp. 126-130.

Seidlits, S.K., Schmidt, C.E. & Shear, J.B. High-Resolution Patterning of Hydrogels in Three Dimensions using Direct-Write Photofabrication for Cell Guidance. Advanced Functional Materials 19(2009)22, pp. 3543-3551.

Serbin, J., Egbert, A., Ostendorf, A., Chichkov, B.N., Houbertz, R., Domann, G., Schulz, J., Cronauer, C., Fröhlich, L. & Popall, M. Femtosecond Laser-Induced Two-Photon Polymerization of Inorganic Organic Hybrid Materials for Applications in Photonics. Optics Letters 28(2003)5, pp. 301-303.

Serbin, J., Ovsianikov, A. & Chichkov, B. Fabrication of Woodpile Structures by Two-Photon Polymerization and Investigation of their Optical Properties. Optics Express 12(2004)21, pp. 5221-5228.

Sharifi, F., Patel, B.B., Dzuilko, A.K., Montazami, R., Sakaguchi, D.S. & Hashemi, N. Polycaprolactone Microfibrous Scaffolds to Navigate Neural Stem Cells. Biomacromolecules 17(2016)10, pp. 3287-3297.

Shen, H., Spikes, J.D., Kopeceková, P. & Kopecek, J. Photodynamic Crosslinking of Proteins. I. Model Studies using Histidine- and Lysine-Containing N-(2-Hydroxypropyl) Methacrylamide Copolymers. Journal of Photochemistry and Photobiology B: Biology 34(1996a)2-3, pp. 203-210.

Shen, H., Spikes, J.D., Kopecková, P. & Kopecek, J. Photodynamic Crosslinking of Proteins II. Photocrosslinking of a Model Protein-Ribonuclease A. Journal of Photochemistry and Photobiology B: Biology 35(1996b)3, pp. 213-219.

Shen, H., Spikes, J.D., Smith, C.J. & Kopecek, J. Photodynamic Cross-Linking of Proteins: V. Nature of the Tyrosine–Tyrosine Bonds Formed in the FMN-Sensitized Intermolecular Cross-Linking of N-Acetyl-L-Tyrosine. Journal of Photochemistry and Photobiology A: Chemistry 133(2000)1-2, pp. 115-122.

Sherborne, C.R., Pateman, C.J. & Claeyssens, F. Direct Laser Writing of Neural Tissue Engineering Scaffolds for Biohybrid Devices. Living Machines, Barcelona, Spain, July 9-12, 2012. Berlin, Germany 2012, Springer Berlin Heidelberg. pp. 392-393.

Skottman, H. Derivation and Characterization of Three New Human Embryonic Stem Cell Lines in Finland. In Vitro Cellular and Developmental Biology - Animal 46(2010)3-4, pp. 206-209.

Slaughter, B.V., Khurshid, S.S., Fisher, O.Z., Khademhosseini, A. & Peppas, N.A. Hydrogels in Regenerative Medicine. Advanced Materials 21(2009)32-33, pp. 3307-3329.

So, P.T.C., Dong, C.Y., Masters, B.R. & Berland, K.M. Two-Photon Excitation Fluorescence Microscopy. Annual Review of Biomedical Engineering 2(2000)1, pp. 399-429.

Spangenberg, A., Hobeika, N., Stehlin, F., Jean-Pierre Malval, Wieder, F., Prabhakaran, P., Baldeck, P. & Soppera, O. Recent Advances in Two-Photon Stereolithography. In: Hosaka, S. (ed.). Updates in Advanced Lithography. 2013, InTech. pp. 35-63.

Sparrow, C.M. On Spectroscopic Resolving Power. Astrophysical Journal 44(1916) pp. 76-86.

Spikes, J.D., Shen, H., Kopecková, P. & Kopecek, J. Photodynamic Crosslinking of Proteins. III. Kinetics of the FMN- and Rose Bengal-Sensitized Photooxidation and Intermolecular Crosslinking of Model Tyrosine-Containing N-(2-Hydroxypropyl)Methacrylamide Copolymers. Photochemistry and Photobiology 70(1999)2, pp. 130-137.

Spivey, E.C., Ritschdorff, E.T., Connell, J.L., McLennon, C.A., Schmidt, C.E. & Shear, J.B. Multiphoton Lithography of Unconstrained Three-Dimensional Protein Microstructures. Advanced Functional Materials 23(2013)3, pp. 333-339.

Stampfl, J. & Liska, R. Polymerizable Hydrogels for Rapid Prototyping: Chemistry, Photolithography, and Mechanical Properties. In: Bártolo, P., Jorge (ed.). Stereolithography. New York, USA 2011, Springer US. pp. 161-182.

Stoneman, M., Fox, M., Zeng, C. & Raicu, V. Real-Time Monitoring of Two-Photon Photopolymerization for use in Fabrication of Microfluidic Devices. Lab on a Chip 9(2009)6, pp. 819-827.

Strickler, J.H. & Webb, W.W. Three-Dimensional Optical Data Storage in Refractive Media by Two-Photon Point Excitation. Optics Letters 16(1991)22, pp. 1780-1782.

Su, P.J., Tran, Q.A., Fong, J.J., Eliceiri, K.W., Ogle, B.M. & Campagnola, P.J. Mesenchymal Stem Cell Interactions with 3D ECM Modules Fabricated via Multiphoton Excited Photochemistry. Biomacromolecules 13(2012)9, pp. 2917-2925.

Suggs, L., Moore, S. & Mikos, A. Synthetic Biodegradable Polymers for Medical Applications. In: Mark, J., E. (ed.). Physical Properties of Polymers Handbook. New York, USA 2007, Springer New York. pp. 939-950.

Sun, Q., Juodkazis, S., Murazawa, N., Mizeikis, V. & Misawa, H. Freestanding and Movable Photonic Microstructures Fabricated by Photopolymerization with Femtosecond Laser Pulses. Journal of Micromechanics and Microengineering 20(2010a)3, pp. 035004-1-035004-5.

Sun, H.B., Tanaka, T. & Kawata, S. Three-Dimensional Focal Spots Related to Two-Photon Excitation. Applied Physics Letters 80(2002)20, pp. 3673.

Sun, H.B., Maeda, M., Takada, K., Chon, J.W.M., Gu, M. & Kawata, S. Experimental Investigation of Single Voxels for Laser Nanofabrication via Two-Photon Photopolymerization. Applied Physics Letters 83(2003a)5, pp. 819-821.

Sun, H.B., Takada, K., Kim, M.S., Lee, K.S. & Kawata, S. Scaling Laws of Voxels in Two-Photon Photopolymerization Nanofabrication. Applied Physics Letters 83(2003b)6, pp. 1104-1106.

Sun, H.B. & Kawata, S. Two-Photon Photopolymerization and 3D Lithographic Microfabrication. In: NMR • 3D Analysis • Photopolymerization. Berlin, Germany 2004, Springer Berlin Heidelberg. pp. 169-273.

Sun, H., Suwa, T., Takada, K., Zaccaria, R.P., Kim, M., Lee, K. & Kawata, S. Shape Precompensation in Two-Photon Laser Nanowriting of Photonic Lattices. Applied Physics Letters 85(2004)17, pp. 3708-3710.

Sun, Q., Juodkazis, S., Murazawa, N., Mizeikis, V. & Misawa, H. Femtosecond Laser Photopolymerization of Photonic and Free-Movable Microstructures in Sol-Gel Hybrid Resist. Advanced Fabrication Technologies for Micro/Nano Optics and Photonics III, January 23, 2010. 2010b, SPIE. pp. 75910K.

Sun, Q., Ueno, K. & Misawa, H. In Situ Investigation of the Shrinkage of Photopolymerized Micro/Nanostructures: The Effect of the Drying Process. Optics Letters 37(2012)4, pp. 710-712.

Sun, Y., Dong, W., Niu, L., Jiang, T., Liu, D., Zhang, L., Wang, Y., Chen, Q., Kim, D. & Sun, H. Protein-Based Soft Micro-Optics Fabricated by Femtosecond Laser Direct Writing. Light: Science & Applications 3(2014)January, pp. e129.

Takada, K., Sun, H.B. & Kawata, S. Improved Spatial Resolution and Surface Roughness in Photopolymerization-Based Laser Nanowriting. Applied Physics Letters 86(2005)7, pp. 1-3.

Tanaka, T., Sun, H.B. & Kawata, S. Rapid Sub-Diffraction-Limit Laser Micro/Nanoprocessing in a Threshold Material System. Applied Physics Letters 80(2002)2, pp. 312-314.

Tanaka, T., Morigami, M. & Atoda, N. Mechanism of Resist Pattern Collapse. Journal of the Electrochemical Society 140(1993)7, pp. L115-L116.

Temenoff, J.S., Athanasiou, K.A., LeBaron, R.G. & Mikos, A.G. Effect of Poly(Ethylene Glycol) Molecular Weight on Tensile and Swelling Properties of Oligo(Poly(Ethylene Glycol) Fumarate) Hydrogels for Cartilage Tissue Engineering. Journal of Biomedical Materials Research 59(2002)3, pp. 429-437.

Terzaki, K., Kissamitaki, M., Skarmoutsou, A., Fotakis, C., Charitidis, C.A., Farsari, M., Vamvakaki, M. & Chatzinikolaidou, M. Pre-Osteoblastic Cell Response on Three-Dimensional, Organic-Inorganic Hybrid Material Scaffolds for Bone Tissue Engineering. Journal of Biomedical Materials Research. Part A 101(2013)8, pp. 2283-2294.

Thiel, M., Fischer, J., von Freymann, G. & Wegener, M. Direct Laser Writing of Three-Dimensional Submicron Structures using a Continuous-Wave Laser at 532 nm. Applied Physics Letters 97(2010)22, pp. 221102.

Timashev, P.S., Vedunova, M.V., Guseva, D., Ponimaskin, E., Deiwick, A., Mishchenko, T.A., Mitroshina, E.V., Koroleva, A.V., Pimashkin, A.S., Mukhina, I.V., Panchenko, V.Y., Chichkov, B.N. & Bagratashvili, V.N. 3D in Vitro Platform Produced by Two-Photon Polymerization for the Analysis of Neural Network Formation and Function. Biomedical Physics & Engineering Express 2(2016)3, pp. 035001.

Torgersen, J., Qin, X., Li, Z., Ovsianikov, A., Liska, R. & Stampfl, J. Hydrogels for Two-Photon Polymerization: A Toolbox for Mimicking the Extracellular Matrix. Advanced Functional Materials 23(2013)36, pp. 4542-4554.

Tuft, B.W., Xu, L., White, S.P., Seline, A.E., Erwood, A.M., Hansen, M.R. & Guymon, C.A. Neural Pathfinding on Uni- and Multidirectional Photopolymerized Micropatterns. ACS Applied Materials & Interfaces 6(2014)14, pp. 11265-11276.

Uppal, N. & Shiakolas, P.S. Modeling of Temperature-Dependent Diffusion and Polymerization Kinetics and their Effects on Two-Photon Polymerization Dynamics. Journal of Micro/Nanolithography, MEMS, and MOEMS 7(2008)4, pp. 043002-1-043002-10.

Van Steveninck, J. & Dubbelman, T.M.A.R. Photodynamic Intramolecular Crosslinking of Myoglobin. Biochimica et Biophysica Acta (BBA) - Protein Structure and Molecular Enzymology 791(1984)1, pp. 98-101.

Verweij, H., Dubbelman, T.M.A.R. & Van Steveninck, J. Photodynamic Protein Cross-Linking. Biochimica et Biophysica Acta (BBA) - Biomembranes 647(1981)1, pp. 87-94.

Viigipuu, K. & Kallio, P. Microinjection of Living Adherent Cells by using a Semi-Automatic Microinjection System. Alternatives to Laboratory Animals: ATLA 32(2004)4, pp. 417-423.

Voldman, J., Gray, M.L. & Schmidt, M.A. Microfabrication in Biology and Medicine. Annual Review of Biomedical Engineering 1(1999) pp. 401-425.

Wang, C., Zhao, P., Miao, Q., Sun, Y. & Zhou, Y. Optical Limiting and Dynamical Two-Photon Absorption of Organic Compounds for a Nanosecond Pulse. Journal of Physics B: Atomic, Molecular and Optical Physics 43(2010)10, pp. 105601.

Wang, I., Bouriau, M., Baldeck, P.L., Martineau, C. & Andraud, C. Three-Dimensional Microfabrication by Two-Photon-Initiated Polymerization with a Low-Cost Microlaser. Optics Letters 27(2002)15, pp. 1348-1350.

Wang, Y.C. & Ho, C. Micropatterning of Proteins and Mammalian Cells on Biomaterials. The FASEB Journal: Official Publication of the Federation of American Societies for Experimental Biology 18(2004)3, pp. 525-527.

Webster, A., Britton, D., Apap-Bologna, A. & Kemp, G. A Dye-Photosensitized Reaction that Generates Stable Protein-Protein Crosslinks. Analytical Biochemistry 179(1989)1, pp. 154-157.

Weiß, T., Hildebrand, G., Schade, R. & Liefeith, K. Two-Photon Polymerization for Microfabrication of Three-Dimensional Scaffolds for Tissue Engineering Application. Engineering in Life Sciences 9(2009)5, pp. 384-390.

West, J.L. & Hubbell, J.A. Photopolymerized Hydrogel Materials for Drug Delivery Applications. Reactive Polymers; Drug Delivery and Slow Release 25(1995)2, pp. 139-147.

Withers, G.S., James, C.D., Kingman, C.E., Craighead, H.G. & Banker, G.A. Effects of Substrate Geometry on Growth Cone Behavior and Axon Branching. Journal of Neurobiology 66(2006)11, pp. 1183-1194.

Witzgall, G., Vrijen, R., Yablonovitch, E., Doan, V. & Schwartz, B.J. Single-Shot Two-Photon Exposure of Commercial Photoresist for the Production of Three-Dimensional Structures. Optics Letters 23(1998)22, pp. 1745-1747.

Wollhofen, R., Katzmann, J., Hrelescu, C., Jacak, J. & Klar, T.A. 120 nm Resolution and 55 nm Structure Size in STED-Lithography. Optics Express 21(2013)9, pp. 10831-10840.

Woodruff, M.A. & Hutmacher, D.W. The Return of a Forgotten polymer–Polycaprolactone in the 21st Century. Progress in Polymer Science 35(2010)10, pp. 1217-1256.

Woodward, S.C., Brewer, P.S., Moatamed, F., Schindler, A. & Pitt, C.G. The Intracellular Degradation of Poly(ε-Caprolactone). Journal of Biomedical Materials Research 19(1985)4, pp. 437-444.

Wu, D., Chen, Q.D., Niu, L.G., Wang, J.N., Wang, J., Wang, R., Xia, H. & Sun, H.B. Femtosecond Laser Rapid Prototyping of Nanoshells and Suspending Components towards Microfluidic Devices. Lab on a Chip 9(2009)16, pp. 2391-2394.

Wu, D., Wu, S., Niu, L., Chen, Q., Wang, R., Song, J., Fang, H. & Sun, H. High Numerical Aperture Microlens Arrays of Close Packing. Applied Physics Letters 97(2010)3, pp. 031109-1-031109-3.

Wu, P.K., Ringeisen, B.R., Krizman, D.B., Frondoza, C.G., Brooks, M., Bubb, D.M., Auyeung, R.C.Y., Piqué, A., Spargo, B., McGill, R.A. & Chrisey, D.B. Laser Transfer of Biomaterials: Matrix-Assisted Pulsed Laser Evaporation (MAPLE) and MAPLE Direct Write. Review of Scientific Instruments 74(2003)4, pp. 2546-2557.

Wu, S., Serbin, J. & Gu, M. Two-Photon Polymerisation for Three-Dimensional Micro-Fabrication. Journal of Photochemistry and Photobiology A: Chemistry 181(2006)1, pp. 1-11.

Wyart, C., Ybert, C., Douarche, C., Herr, C., Chatenay, D. & Bourdieu, L. A New Technique to Control the Architecture of Neuronal Networks in Vitro. In: Poindron, P., Piguet, P. & Förster, E. (ed.). New Methods for Culturing Cells from Nervous Tissues. Basel 2005, Karger Publishers. pp. 23-57.

Xing, J., Dong, X., Chen, W., Duan, X., Takeyasu, N., Tanaka, T. & Kawata, S. Improving Spatial Resolution of Two-Photon Microfabrication by using Photoinitiator with High Initiating Efficiency. Applied Physics Letters 90(2007)13, pp. 131106.

Xu, C., Zipfel, W., Shear, J.B., Williams, R.M. & Webb, W.W. Multiphoton Fluorescence Excitation: New Spectral Windows for Biological Nonlinear Microscopy. Proceedings of the National Academy of Sciences 93(1996)20, pp. 10763-10768.

Yang, D., Park, S.H., Lim, T.W., Kong, H., Yi, S.W., Yang, H.K. & Lee, K. Ultraprecise Microreproduction of a Three-Dimensional Artistic Sculpture by Multipath Scanning Method in Two-Photon Photopolymerization. Applied Physics Letters 90(2007)1, pp. 013113.

Ylä-Outinen, L., Heikkilä, J., Skottman, H., Suuronen, R., Äänismaa, R. & Narkilahti, S. Human Cell-Based Micro Electrode Array Platform for Studying Neurotoxicity. Frontiers in Neuroengineering 3(2010) pp. 111.

Zamani, F., Amani-Tehran, M., Latifi, M. & Shokrgozar, M.A. The Influence of Surface Nanoroughness of Electrospun PLGA Nanofibrous Scaffold on Nerve Cell Adhesion and Proliferation. Journal of Materials Science: Materials in Medicine 24(2013)6, pp. 1551-1560.

Zein, I., Hutmacher, D.W., Tan, K.C. & Teoh, S.H. Fused Deposition Modeling of Novel Scaffold Architectures for Tissue Engineering Applications. Biomaterials 23(2002)4, pp. 1169-1185.

Zhang, Y., Chen, Q., Xia, H. & Sun, H. Designable 3D Nanofabrication by Femtosecond Laser Direct Writing. Nano Today 5(2010)5, pp. 435-448.

Zhou, W., Kuebler, S.M., Braun, K.L., Yu, T., Cammack, J.K., Ober, C.K., Perry, J.W. & Marder, S.R. An Efficient Two-Photon-Generated Photoacid Applied to Positive-Tone 3D Microfabrication. Science 296(2002)5570, pp. 1106-1109.

Žukauskas, A., Malinauskas, M., Reinhardt, C., Chichkov, B.N. & Gadonas, R. Closely Packed Hexagonal Conical Microlens Array Fabricated by Direct Laser Photopolymerization. Applied Optics 51(2012)21, pp. 4995-5003.

ORIGINAL PUBLICATIONS

Publication I

Koskela, J., Turunen, S., Ylä-Outinen, L., Narkilahti, S. & Kellomäki, M.

Two-photon microfabrication of poly(ethylene glycol) diacrylate and a novel biodegradable photopolymer – comparison of processability for biomedical applications

Polymers for Advanced Technologies 23(2012)6, pp. 992-1001

Research article

polymers advanced technologies

Received: 26 January 2011, Revised: 4 April 2011, Accepted: 5 April 2011, Published online in Wiley Online Library: 25 May 2011

(wileyonlinelibrary.com) DOI: 10.1002/pat.2002

Two-photon microfabrication of poly(ethylene glycol) diacrylate and a novel biodegradable photopolymer—comparison of processability for biomedical applications

Jenni E. Koskela[a], Sanna Turunen[a]*, Laura Ylä-Outinen[b,c], Susanna Narkilahti[b] and Minna Kellomäki[a]

Two-photon polymerization (2PP) is a versatile microfabrication tool for biomedical applications as it provides unparalleled resolution for accurate three-dimensional (3D) replication of biological microstructures. To widen the selection of biomaterials suitable for 2PP, this paper presents the processing of a methacrylated poly(ε-caprolactone)-based oligomer (PCL-o) and a poly(ethylene glycol) diacrylate (PEGda) hydrogel into microstructures. PCL-o is a novel biodegradable photopolymer that has not been previously processed with 2PP, and the fabrication of both polymers with an Nd:YAG laser is reported here for the first time. The overall 2PP processability and achievable resolution were studied by polymerizing arbitrary microstructures on glass substrates. The samples were characterized with scanning electron microscopy. Additionally, the effect of photoinitiator concentration on the resolution was investigated. Also, a preliminary cell attachment test was performed with UV cured films in order to investigate the impact of the used material–initiator combination on cell viability and migration. As a result, laser-induced polymerization of both PCL-o and PEGda was successfully demonstrated, and the Nd:YAG laser was proven adequate for the 2PP processing of the novel biodegradable photoresist. Resolution in the order of 1 μm was achieved with PCL-o. With the easy processing of both PEGda and PCL-o, these materials have great potential for different biomedical applications. Copyright © 2011 John Wiley & Sons, Ltd.

Keywords: Nd:YAG laser; two-photon polymerization; poly(ethylene glycol) diacrylate; polycaprolactone; biodegradable photopolymer

INTRODUCTION

Two-photon polymerization (2PP), which is induced by optically non-linear absorption of pulsed laser energy, can be used to fabricate 3D objects in essentially any shape on size scales ranging from submicron to millimeter. Compared with traditional, inherently planar photofabrication methods such as photolithography, 2PP has the advantage that the light beam can be focused into the volume of the photosensitive material. The polymer-curing phenomenon in 2PP is based on two-photon absorption (2PA), in which a photoinitiator (PI) molecule is excited from a lower quantum state to an excited state by the simultaneous absorption of two photons. Because of a quadratic dependence of the absorption rate on laser intensity, 2PP only occurs in the confined focal volume when the intensity of light at the laser focus exceeds a certain threshold value for 2PA. Thus, 2PP enables the fabrication of microstructures with resolution well beyond the diffraction limit of the focusing optics.[1–5]

Even though the physical phenomenon behind 2PP technology was first predicted already in 1930s and confirmed experimentally 30 years later along the invention of lasers, the most vigorous development around 2PP has been carried out within the past two decades.[1] The primary application of 2PP has been the fabrication of 3D photonic crystals, first proposed and demonstrated by Maruo *et al.*[6] in 1997. To date, application areas of 2PP include micromechanical systems, microfluidic devices, micro-optical components, and plasmonic components. In addition to its success in these areas, 2PP has also shown great promise for biological applications including tissue engineering, drug delivery, medical implants, and medical sensors.[1,3,7,8]

2PP is commonly driven by ultrafast lasers such as the Ti:sapphire laser, which produces pulses of a few tens of femtoseconds in duration at high frequency.[9] Although excellent in their properties, femtosecond lasers are quite expensive for routine fabrication work performed in the laboratories worldwide. Inspired by research of Kaehr and co-workers,[10] fabrication

* *Correspondence to: S. Turunen, Tampere University of Technology, Department of Biomedical Engineering, PO Box 692, 33101, Tampere, Finland. E-mail: sanna.turunen@tut.fi*

a *J. E. Koskela, S. Turunen, M. Kellomäki*
Tampere University of Technology, Department of Biomedical Engineering, PO Box 692, 33101, Tampere, Finland

b *L. Ylä-Outinen, S. Narkilahti*
Regea—Institute for Regenerative Medicine, University of Tampere and Tampere University Hospital, Biokatu 12, 33520, Tampere, Finland

c *L. Ylä-Outinen*
The Science Center of Pirkanmaa Hospital District, Tampere, Finland

polymers advanced technologies

equipment based on a diode-pumped Q-switched Nd:YAG picosecond pulsed laser has been successfully utilized for research work in our laboratory.[11,12]

Commercial photoresists commonly utilized in 2PP include acrylic polymers, epoxy-based photoresist SU-8, and inorganic–organic hybrid materials such as Ormocer®s.[1,6,13] Among these, SU-8 and Ormocer®s have been proven biocompatible and applicable in biomedical applications.[14,15] However, processing of these polymers involves the use of toxic organic solvents, such as propylene glycol methyl ether acetate and 4-methyl-2-pentanone. Incomplete removal of such solvents, especially from thick scaffolds, may result in harmful residues, causing the final product to fail the tests on the basis of ISO 10993 standards for establishing the presence and nature of any extractables that have toxic potential in the human body.[14] Thus, there is a great interest towards the development and utilization of water-soluble resins, which offer a safe alternative for biological applications.

To date, several photosensitive synthetic and natural polymers have already been processed with traditional photolithographic techniques and utilized in biodegradable biomedical devices. These materials have been synthesized, for example, of polycaprolactone, polylactide, and trimethylenecarbonate precursors.[16–19] Unfortunately, the activity to investigate more suitable synthetic biomaterials for the biomedical applications of 2PP has remained low, apart from some exceptions such as the study by Clayessens *et al.*[20]

Natural proteins, on the other hand, have been introduced to 2PP research as suitable materials for biological applications. Bovine serum albumin, avidin,[21–24] fibrinogen,[22] and collagen[25] have been successfully crosslinked by means of 2PP. Besides proteins, 2PP micropatterning of hydrogels, especially those based on poly(ethylene glycol) (PEG), has been demonstrated.[26–29]

In this paper, we demonstrate 2PP microfabrication of two different photopolymers with properties suitable for various biological applications. One of the materials is a biodegradable poly(ε-caprolactone)-based oligomer (PCL-o) which has not been previously processed with 2PP. The other studied material is a PEG diacrylate (PEGda) hydrogel, whose 2PP with a Nd:YAG laser has not been reported earlier. In this study, PEGda serves as a reference material for PCL-o. By comparing the resolution and processability of the two photoresins, we show that both of these materials can be successfully processed into micron-scale 3D structures with 2PP.

EXPERIMENTAL

Fabrication setup

A diode-pumped passively Q-switched Nd:YAG microchip laser (PULSELAS-P-1064-300-FC, Alphalas, Goettingen, Germany) with the pulse duration of 800 ps, maximum repetition rate of 15 kHz, and wavelength of 532 nm, was used in the experiments to induce 2PA. The beam was directed through a microscope (Nikon ECLIPSE ME 600, Nikon, Tokyo, Japan) into a ×50 oil immersion objective. Laser exposure of the samples was controlled with a mechanical shutter and its controller (SH05 Beam Shutter and TSC001 T-Cube Shutter Controller, Thorlabs, Munich, Germany). A motorized the *xyz*-stage (SCAN 130 × 85, Märzhäuser Wetzlar, Wetzlar, Germany) with a controller (Corvus TT, ITK Dr. Kassen, Lahnau, Germany) was employed to enable accurate 3D fabrication.

The power range of the laser was roughly adjusted before fabrication by using an attenuator with a 25% transmittance of the incident light. During the polymerization process, the laser power could be adjusted by varying the laser diode from 1.70 to 2.52 A. Furthermore, in this laser system, the laser pulse frequency also changed linearly as a function of the laser diode current. The pulse frequency increased from 5 to 15 kHz as the laser current value changed from 1.80 A to the maximum of 2.52 A.

Materials and sample preparation

Water-soluble low-viscosity PEGda with M_n of 575 g/mol was purchased from Sigma-Aldrich (Schnelldorf, Germany). The biodegradable, methacrylated PCL-o was custom synthesized at the Laboratory of Polymer Technology in Aalto University School of Chemical Technology (Espoo, Finland) by the group of Professor Seppälä.[30] The star-shaped oligomer with four arms was purified by dissolution in dichloromethane and precipitation in hexane resulting in a product that was a water-insoluble, highly viscous transparent liquid with a molecular weight of slightly over 1000 g/mol. The biodegradation of thermally cured networks of PCL-o has been evaluated by Helminen and co-workers, and according to their studies, PCL-o with molecular weight of 11,550 g/mol crosslinked in the presence of dibenzoyl peroxide as radical initiator showed water absorption of under 2% and mass loss of 1% after immersion in phosphate buffer solution (pH 7.0) at 37°C for 12 weeks.[16] Similar results have been obtained with PCL-o photocured with camphorquinone by incubating the samples in phosphate buffer solution (pH 7.4) at 37°C for 3 weeks. The pure PCL-o matrix absorbed only 2.6% water in 3 weeks, and mass loss was 1%.[30] The slow degradation behavior of PCL-o originates from its partial crystallinity and high hydrophobicity.[16]

The photo-crosslinkable resins of both PEGda and PCL-o were prepared by mixing them with a commercial UV photoinitiator, Irgacure® 127 (Ciba Specialty Chemicals, Basel, Switzerland) in different concentrations. Irgacure® 127 was selected as the photoinitiator for this 2PP study, because according to the supplier, it has maximum absorbance around 260 nm, which is approximately half of the wavelength of the laser beam utilized in this research. However, to ensure the compatibility of the resins with the utilized laser wavelength of 532 nm, UV–Vis absorption spectra were measured for PCL-o and PEGda with and without the Irgacure® 127 photoinitiator. The spectra were obtained with a Unicam UV 540 UV–Vis spectrometer (Thermo Spectronic, Essex, England) in the range of 190–700 nm by diluting PCL-o in dichloromethane and PEGda in ion-exchanged water. The absorption spectra in Fig. 1 show that neither PCL-o nor PEGda with 1% or 0% photoinitiator exhibited absorption at the spectral region near 532 nm, which demonstrated that both materials are transparent to the laser beam and that single-photon absorption was not involved in the polymerization process. However, both resins showed strong absorption even without photoinitiator, indicating absorption at the double bonds. The addition of the photoinitiator into the resins shifted the absorption maxima towards the wavelength of 260 nm, where the 2PA window for the Nd:YAG laser lies.

Henceforth, the photocurable resins are referred to as PCL-o-α and PEGda-β, in which α and β denote the weight percentage of the photoinitiator for each resin. PCL-o resins of $\alpha = 2$, 3, and 5 and PEGda resins of $\beta = 0.5$, 1, and 1.5 were used in the

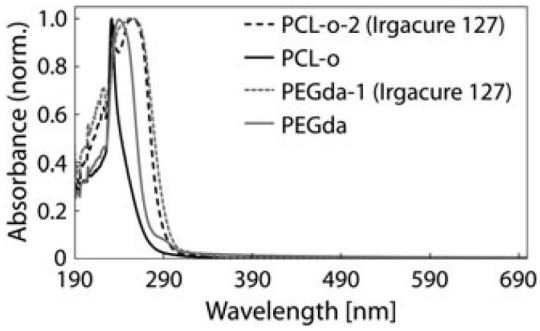

Figure 1. Normalized UV–Vis absorption spectra of PCL-o and PEGda with and without the Irgacure® 127 photoinitiator. PCL-o, poly(ε-caprolactone)-based oligomer; PEGda, poly(ethylene glycol) diacrylate.

experiments. The chemical structures of PCL-o, PEGda, and Irgacure® 127 are presented in Fig. 2.

The polymerization experiments were performed on microscope glass slides pre-treated with a coupling agent 3-(trimethoxysilyl)propyl methacrylate (MAPTMS, Sigma-Aldrich, Germany) to ensure adequate attachment of the microstructures to the substrate. Both PEGda and PCL-o samples were prepared by simple drop casting without any pre-baking or post-baking steps. A 150-µm-thick steel spacer was used to sandwich the resin between the microscope slide and a coverslip. Because of the crystallization characteristics of the PCL-o oligomer, samples of PCL-o had to be warmed to approximately 30°C before polymerization.

After polymerization, PCL-o samples were developed with dichloromethane (Sigma-Aldrich, Germany) or with Ormodev® (Micro Resist Technology, Berlin, Germany), which is a 50:50 mixture of 4-methyl-2-pentanone and 2-propanol. The PCL-o samples were also rinsed with 2-propanol (99.8%, Labscan Limited, Dublin, Ireland). PEGda samples, on the other hand, were developed with ion-exchanged water.

Computer-controlled manufacturing of microstructures

Two-dimensional (2D) microstructures, such as lines and lattices, were fabricated using the WinPos software (ITK Dr. Kassen),

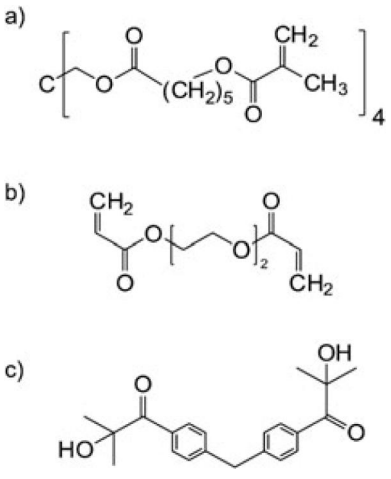

Figure 2. The chemical structures of (a) poly(ε-caprolactone)-based oligomer, (b) poly(ethylene glycol) diacrylate, and (c) Irgacure® 127.

which converted the entered data of coordinates into *xyz*-stage movements and simultaneously controlled the shutter as programmed. Simultaneously, different processing parameters such as the laser diode current and scanning speed were varied to evaluate the processability of the sample materials. In addition, arrays of volumetric pixels (voxels) were polymerized with WinPos for resolution calculation purposes. The 3D structures were fabricated by contour scanning of laterally sliced CAD models, for which layer spacing of 1–4 µm was used depending on the structure geometry. The contour data were exported to a scanning program specially designed for this project (CorvusControl), which translated the contour information into the desirable *xyz*-stage coordinates and shutter commands.

The polymerization process could be monitored in real time with a CCD camera (CV-M10RS, JAI Corporation, Yokohama-shi, Japan) and commercial visualization software called Ulead DVD Movie Factory™ 4.0 (Ulead Systems, Inc., Taipei, Taiwan). After polymerization, the samples were developed by rinsing away the remaining unpolymerized oligomer solution with a suitable solvent.

Imaging

The optical microscope included in the fabrication setup was utilized for sample imaging and analysis before and after development. The ×50 oil immersion objective used in polymerization was also used for pre-development sample imaging. After the development procedure, a ×20 air objective was utilized for imaging and visual evaluation of sample quality. A scanning electron microscope (SEM) (Philips XL-30, Philips Electron Optics, Eindhoven, the Netherlands) was employed for a more precise sample characterization. The samples were sputter coated with gold (S 150 Sputter Coater, Edwards Limited, Crawley, West Sussex, UK) for 90 s in argon atmosphere corresponding to a coating thickness of approximately 60 nm.

Resolution study

For resolution studies, arrays of voxels were polymerized by adjusting the laser diode current from 1.70 to 2.50 A, which corresponded to average laser power of 0.79–7.45 mW. Also, 2D lines were polymerized with different scanning speeds (30, 50, 60, and 100 µm/s) and by varying the laser diode current from 1.75 to 2.52 A (1.21–7.62 mW) to study the dependence of the resolution on scanning speed.

The lateral and vertical resolutions for the combination of the fabrication system and the used materials were determined from SEM images of voxel arrays. Also, the voxel aspect ratios were determined by dividing the lengths of the voxels by their diameters. Individual voxels were produced by programming the shutter to open and close periodically while the *xyz*-platform translated and descended between these commands. This ascending scan method was utilized to produce arrays, in which a series of voxels was polymerized with the same average laser power as the laser focus position was increased by 1 µm between voxels. The ascending scan was used to find the optimal focus position for creating isolated, complete voxels.

From the SEM images of the voxel arrays, complete voxels possessing an ellipsoidal-like shape were selected for resolution calculations, which were performed with free image processing software, GIMP 2.6 (GNU Image Manipulation Program, The Gimp Team). The evaluation of dimensions was based on measuring

the voxel dimensions or line heights first as pixels and then comparing the value to the scale bar length of the SEM images to obtain the dimensions in microns. Guidelines were drawn on SEM images to facilitate the measurement of the line dimensions. Three measurements were taken from each line at the points where the guidelines intersected the polymerized lines. The measurement of voxel and line dimensions is also demonstrated in Fig. 3.

Neuronal cell attachment test

A preliminary cell attachment test was performed in order to investigate the impact of the used material–initiator combination on cell viability and migration. PEGda and PCL-o prepolymer solutions containing 1.5 and 3 wt% of photoinitiator, respectively, were polymerized into thin films as described previously.[12] In brief, a drop of the resin was placed on a microscope glass slide and exposed to UV light for 10 s (300–450 nm wavelength, ~3000 mW/cm^2 intensity). Following polymerization, films were placed in water (PEGda) or the Ormodev® solvent (PCL-o) for 20 min to remove any unreacted monomer. The PCL-o samples were subsequently rinsed thoroughly with 2-propanol. The films were die cut to 6-mm-diameter samples to fit inside a 96-well plate and immersed into 70% ethanol in ultra-pure water twice for 15 and 30 min. After the disinfection, the samples were rinsed three times with sterile Na–PBS solution for 30 min. Human embryonic stem cells (hESC), which had been differentiated towards neurons for 8 weeks in neural differentiation medium (NDM) in the presence of basic fibroblast growth factor, were used in this study as previously described.[31] NDM contains Dulbecco's modified Eagle's medium/F12 (Gibco, Invitrogen, Espoo, Finland) and Neurobasal medium (Gibco) 1:1, supplemented with 2 mM GlutaMax (Gibco), 1× B27 (Gibco), 1× N2 (Gibco), 20 ng/ml fibroblast growth factor (R&D Systems, Minneapolis, MN, USA), and penicillin/streptomycin (25 U/ml, Cambrex, Verviers, Belgium). The differentiated cells were cultured on the disinfected samples. Laminin (mouse origin, solution 10 µg/ml, Sigma-Aldrich, Finland) coated polystyrene was used as a control surface, and four parallel samples were used of PEGda, PCL-o, and control. Small cell aggregates plated onto sample surfaces consisted of more than 90% of young neurons, some astrocytes and non-neural, epithelial-like flat cells.[31] Cells were cultured in NDM for 7 days at 37°C, and the medium was changed three times per week. After the culturing period, the viability of the cells was determined using a Live/Dead® Viability/Cytotoxicity Kit for mammalian cells (Sigma-Aldrich) to dye live cells with Calcein AM and dead cells with ethidium homodimer-1 that was visualized with a fluorescent microscope (Olympus IX51, Olympus, Espoo, Finland). The cell attachment was monitored using contrast phase optics.

RESULTS AND DISCUSSION

In this study, 2PP was investigated with a commercial photoinitiator and two different types of biopolymers, PCL-o and PEGda. The purpose of the study was to compare these materials in terms of processability and resolution, in order to widen the selection of 2PP processable biomaterials. In addition, a preliminary cell attachment test was performed with the sample materials.

Scanning speed

To optimize the scanning speed for each prepolymer solution, we fabricated simple 2D lattice structures by using different scanning speeds within the range of 1–150 µm/s. Figure 4 presents SEM images of PCL-o-5 lattices polymerized with different scanning speeds. The scanning speed of 2 µm/s (Fig. 4(a)) was found to be sufficient for polymerization. In Fig. 4(b), the speed was 5 µm/s, and some distortion is visible in the middle sections of the lattice. The scanning speed in Fig. 4(c) was 10 µm/s, which was too fast for complete polymerization. In all the three lattices (a–c), the average laser power was 1.62 mW. A close-up of the lattice (a) is shown in Fig. 4(d). The lattice has sharp edges and intersections and wall thickness of approximately 3 µm.

The *xyz*-stage scanning speed affects the polymerization results, as it is directly related to the exposure time. High scanning speed greatly decreases the exposure time, resulting in thinner lines. With a too fast scanning speed, the production of initiator radicals is insufficient to propagate complete polymerization throughout the irradiated volume. On the other

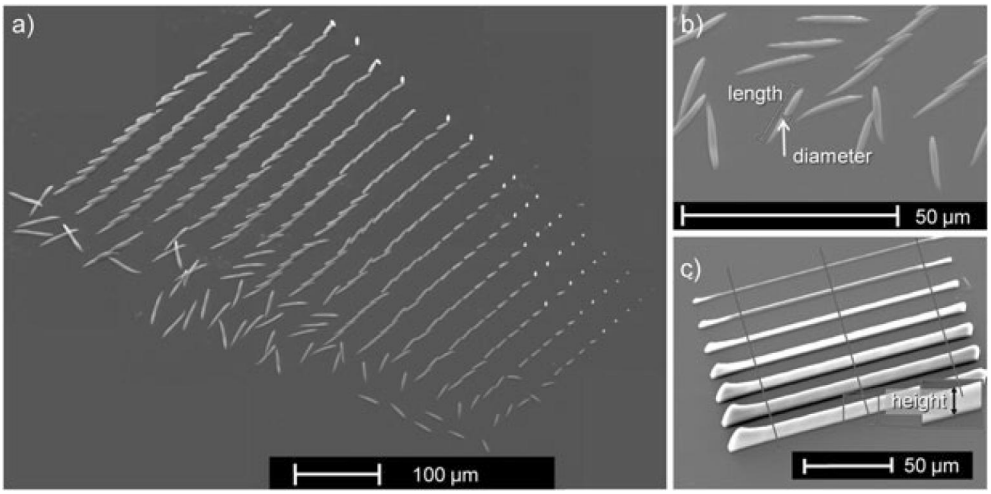

Figure 3. (a) An example of a voxel array polymerized with an ascending scan method while varying the average laser power, (b) measurement of length and diameter of individual voxels, and (c) height measurement from a line array polymerized with increasing average laser power.

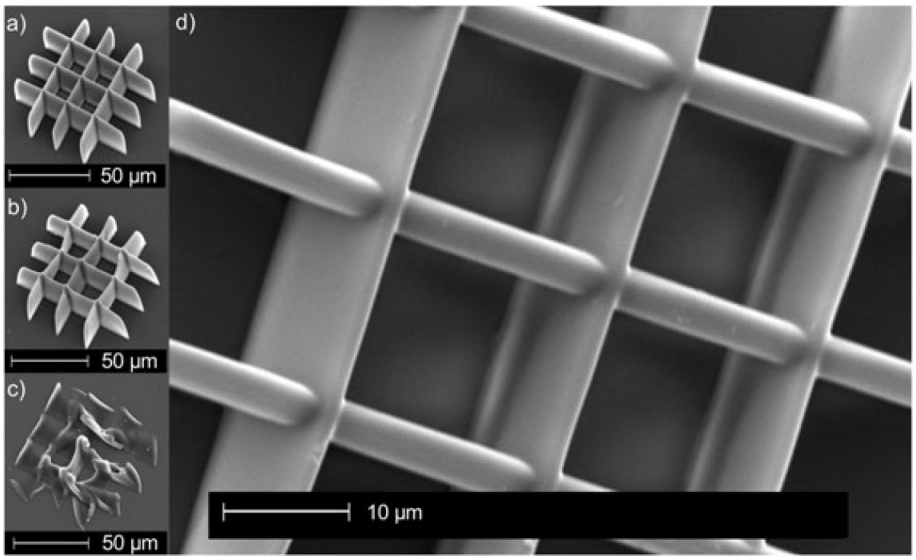

Figure 4. Scanning electron microscope images of PCL-o-5 lattice structures polymerized with different scanning speeds (v): (a) $v = 2$ µm/s, (b) $v = 5$ µm/s, and (c) $v = 10$ µm/s. Image (d) is a close-up of lattice (a).

hand, a scanning speed that is too slow will result in worsened resolution due to longer exposure time. A significant difference was observed in the optimal scanning speed when comparing PCL-o with PEGda. With PCL-o, the scanning speed had to be at least 10 times slower than with PEGda to achieve complete polymerization. Typical scanning speeds for PEGda samples varied from 20 to 100 µm/s whereas scanning speeds of 2–10 µm/s were used for PCL-o samples. Typically, increasing the amount of functional groups in the monomer results in increased polymerization rate.[13] Therefore, it could be assumed that PCL-o with four functional groups would polymerize more rapidly than PEGda with only two functional groups. Obviously, this rule does not apply to the current study, for which we propose two possible reasons. First, the methacrylate moieties of the PCL-o can be less reactive than the acrylate moieties of PEGda because of the steric hindrance at the radical center associated with the methyl group on the methacrylate.[32] Secondly, the difference in polymerization rate can also be attributed to the higher viscosity of the PCL-o oligomer because of its larger molecular weight compared with the viscosity of PEGda.[33] However, a comprehensive kinetic polymerization study of the polymerization reactions including *in situ* characterization would be needed in order to fully understand the crosslinking phenomenon in these two materials.

Because of the slow scanning speed required by PCL-o, some of the more complicated and large structures polymerized of PEGda were not tested with PCL-o. To be able to reproducibly fabricate series of polymerized samples for cell culture experiments, for instance, the microfabrication process needs to be fast, effective, and reliable. Therefore, the issue of slow polymerization observed with PCL-o needs to be addressed before any larger structures for biomedical applications can be fabricated.

Resolution study

Voxels

The fabrication equipment utilized in this study employed a Nd:YAG pulsed laser, which produces pulses of picoseconds in duration. This type of a laser is more affordable compared with the Ti:sapphire femtosecond lasers utilized in most of the reported 2PP studies and thus is a reasonable choice for research purposes. The laser pulse duration is one of the most significant laser parameters in 2PP. Longer pulse duration results in longer irradiation time, which leads to more extensive generation and consecutive diffusion of radicals at the focal point. This results in the formation of larger voxels when using a picosecond laser instead of a femtosecond laser.[34] Therefore, the secondary motive of this study was to compare the gained resolution results with results reported with more expensive laser types. Also, the goal was to evaluate the effect of photoinitiator concentration on resolution and to compare the overall voxel size between the two photopolymers. Figure 5 presents the voxel length and voxel diameter as a function of the average laser power. Voxels polymerized from PCL-o-*a*, PEGda-0.5, and PEGda-1.5 were measured.

During fabrication, the adjustability of the laser power range was limited by the available attenuators. Thus, if more data could have been gained from either end of the power range, the two-photon processing window characterized by the 2PP threshold and the laser-induced damage zone could have been determined. Another drawback is the variance in the data range between the samples at the lower laser powers, which is due to the creeping tendency of the laser at the lower diode current values. The non-linear dependence of voxel dimensions on applied laser power can be seen from Fig. 5. Because of the quadratic dependence of the 2PA rate on light intensity, the voxel dimensions first increased rapidly and then started to level off after a saturation point. However, some of the curves in Fig. 5 most likely only represent the steepest part of the resolution curves and have not yet reached the saturation level. Further observation of the curves in Fig. 5 reveals that voxel dimensions increase with increasing PI concentration, as expected. According to the achieved voxel data, PCL-o produced smaller voxels than PEGda within the available average laser power range used for the voxel polymerization and thus provided better resolution. SEM images of the smallest voxels produced with PCL-o and PEGda are shown in Fig. 5(c and f), respectively. Assumingly, the larger size of the monomer and the significantly greater

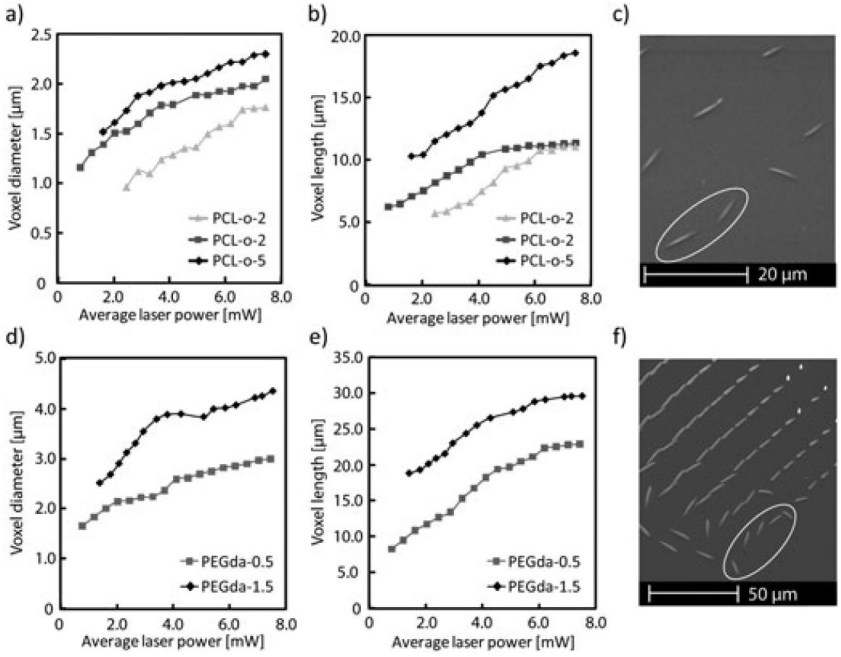

Figure 5. Voxel diameter (a, d) and voxel length (b, e) as functions of the average laser power and SEM images of the smallest voxels fabricated from PCL-o-2 (c) and PEGda-0.5 (f). The resolution was determined as an average of the dimensions measured from the circled voxels. PCL-o, poly(ε-caprolactone)-based oligomer; PEGda, poly(ethylene glycol) diacrylate.

viscosity of PCL-o compared with those of PEGda contribute to the smaller size of the PCL-o voxels. More specifically, it can be presumed that radical diffusion of the PI is more restricted in PCL-o than in the low-viscosity PEGda, which results in smaller voxels. Table 1 summarizes the smallest achieved voxels for both PEGda and PCL-o. The best overall resolution was achieved with PCL-o-2 with voxel diameter of 1.0 µm and voxel length of 5.7 µm.

Table 1 also lists the aspect ratios of the smallest voxels obtained. A large voxel aspect ratio impairs the achievable vertical resolution; therefore, a small aspect ratio is desirable for detailed submicron features. Theoretically, the aspect ratio of a voxel is mainly affected by the numerical aperture (NA) of the objective lens used. Moreover, low values of laser power will produce voxels with low aspect ratio, thus providing better resolution. With optimized fabrication setup and low initiator concentration, aspect ratio near unity can be obtained.[8] In the current study, the aspect ratio (i.e. the voxel length divided by the voxel diameter) for PCL-o voxels was between 5.0 and 8.1, whereas for PEGda voxels, it varied from 4.8 to 8.0. These values indicate that the NA used (0.9) is not ideal, and better resolution could be obtained using an objective with higher NA. These results also imply that the composition of the prepolymer solution does not have a significant effect on the ratio value, as almost similar ratios were obtained with both PCL-o and PEGda.

Minimum feature sizes down to a few hundred nanometers have been reported in 2PP-related publications, yet these studies have employed expensive Ti:sapphire lasers and SU-8 as photoresist. However, in the paper by Clayessens *et al.*,[20] which described 2PP with a novel biodegradable copolymer using a femtosecond laser, resolution of 4 µm was reported. This resolution is comparable with the results gained in the current study. Furthermore, as the current resolutions were gained with a picosecond laser and with non-optimized optics, significantly enhanced resolution could be expected for both PEGda and PCL-o when processed with a femtosecond laser system. Considering the quality of the fabrication system and the fact that these were the first 2PP studies with PCL-o, the obtained resolution values are more than satisfactory.

Table 1. Summary of the smallest voxel dimensions obtained from samples polymerized from material compositions with different PI concentrations

Smallest achieved voxel dimensions	PCL-o-2 at 2.46 mW	PCL-o-3 at 0.79 mW	PCL-o-5 at 1.62 mW	PEGda-0.5 at 0.79 mW	PEGda-1.5 at 1.41 mW
Voxel diameter (µm)	1.0	1.2	1.5	1.7	2.5
Voxel length (µm)	5.7	6.2	10.3	8.2	18.8
Voxel aspect ratio	5.7	5.2	6.9	4.8	7.5

PCL-o, poly(ε-caprolactone)-based oligomer; PEGda, poly(ethylene glycol) diacrylate.

Lines

Two-dimensionally polymerized line arrays were used to study the combined effect of the average laser power and scanning speed on resolution. Figure 6 presents the SEM images of PEGda line arrays that have been used for height measurements. Figure 6(a and b) presents lines polymerized of PEGda-1.5 whereas Fig. 6(c and d) presents lines fabricated of PEGda-1. The height of each polymerized line depended on the initial laser focus position, which could not be precisely adjusted. Therefore, comparison of the line heights between the line arrays polymerized on different samples cannot be carried out, which means that PEGda-1 results cannot be compared with results gained with PEGda-1.5.

As can be seen from the images of Fig. 6, the line height increased slightly towards the ends of the lines. This phenomenon is due to the acceleration and deceleration of the *xyz*-stage, which resulted in an increase in the exposure time at the line ends. The results from line height measurements are shown in Fig. 7, which shows the average line height of PEGda-1 and PEGda-1.5 as a function of the average laser power for different scanning speeds. The curves presented in Fig. 7 follow the same trend as observed with voxel dimensions plotted against the laser power, i.e. the line height first increased with increasing laser power until it started to level off at higher laser power values. The effect of the exposure time on line dimensions can also be interpreted via the scanning speed values. As can be seen from Fig. 7, slower scanning speed, meaning longer exposure time, resulted in taller lines for both resins. As a conclusion, longer exposure time leads to a diminished line aspect ratio, or more accurately, diminished aspect ratio of the voxels. This finding is consistent with the voxel scaling laws proposed by Sun *et al.*[35]

Robust and measurable line arrays could only be fabricated from PEGda-1.5 and PEGda-1. The problem with PEGda-0.5 and all PCL-o prepolymer solutions was that lines collapsed immediately after polymerizing, even with slow scanning speeds. The polymerized lines from these resins were very thin and, apparently, were not mechanically robust enough to maintain their original shape. To solve the issue of collapsed lines, we used lattice-like structures for the resolution study of PEGda-0.5 and PCL-o instead of simple lines.

Lattices

By varying the average laser power and scanning speed, we fabricated lattices of different aspect ratios. Figure 8 presents SEM images of PEGda-0.5 and PCL-o-2 lattices that were polymerized with three different laser power values. As can be visually estimated from Fig. 8, the increase in feature height as a function of the average laser power was substantial (from 1.6 to 4.0 µm for PEGda-0.5 and from 3.4 to 10.3 µm for PCL-o-2), whereas a dimensional increase in the lateral direction was quite modest (from 1.8 to 2.2 µm for PEGda-0.5 and from 1.7 to 3.6 µm for PCL-o-2). This behavior is observed with both materials, and thus, it can be assumed to be characteristic to the 2PP phenomenon and not material dependent. Furthermore, the optical characteristics of the objective lens used for the polymerization further add to this behavior. The polymerization process for lattices presented in Fig. 8 is fast, easy, and readily variable. Fabrication of one such lattice takes only a couple of minutes. These simple lattices can be polymerized on top of each other to form truly 3D scaffold-like structures. Furthermore, lattice dimensions can be individually adjusted for each layer to form, for example, microscaffolds with varying pore sizes.

After optimizing the polymerization processing parameters, more complex structures were fabricated according to CAD models using the CorvusControl software. The 3D CAD models were first sliced into horizontal layers with contours. With PCL-o, layer spacing of 0.5, 1, 2, and 4 µm were tested, whereas PEGda

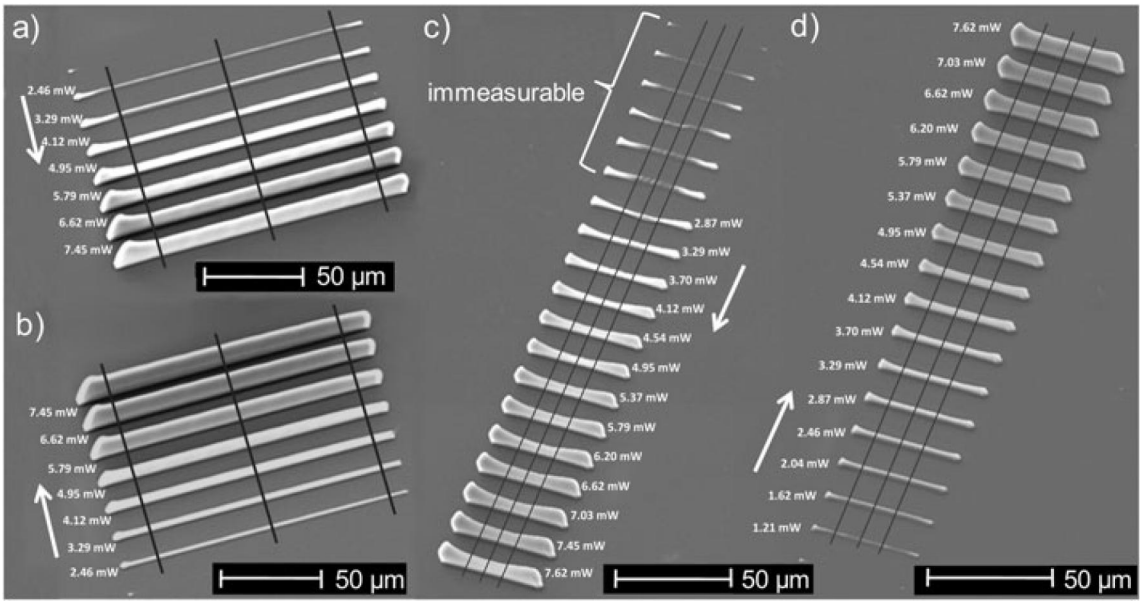

Figure 6. PEGda lines polymerized with increasing average laser power using different scanning speeds (*v*): (a) PEGda-1.5, $v = 60$ µm/s; (b) PEGda-1.5, $v = 30$ µm/s; (c) PEGda-1, $v = 100$ µm/s; and (d) PEGda-1, $v = 50$ µm/s. The lines perpendicular to the polymerized lines mark the points of height measurements whereas the arrows point out the direction of increasing laser power. In image (c), the word 'immeasurable' denotes lines that have not been completely polymerized and could not be used for height measurements. PEGda, poly(ethylene glycol) diacrylate.

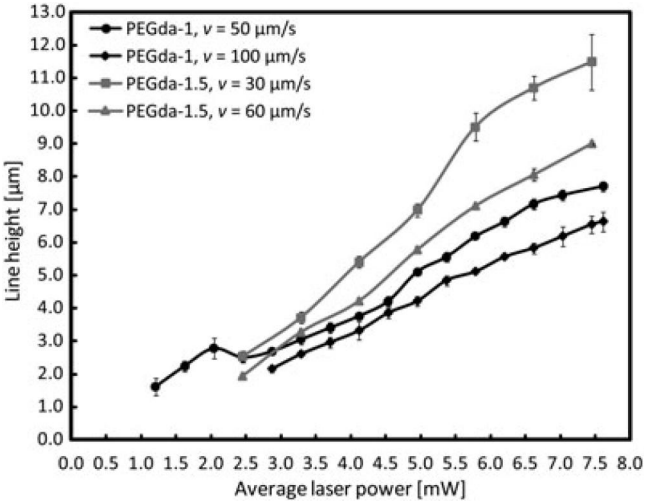

Figure 7. Line heights of PEGda-1 and PEGda-1.5 as a function of the average laser power with different scanning speeds (*v*). Data points represent the mean of three measurements ± standard deviation. PEGda, poly(ethylene glycol) diacrylate.

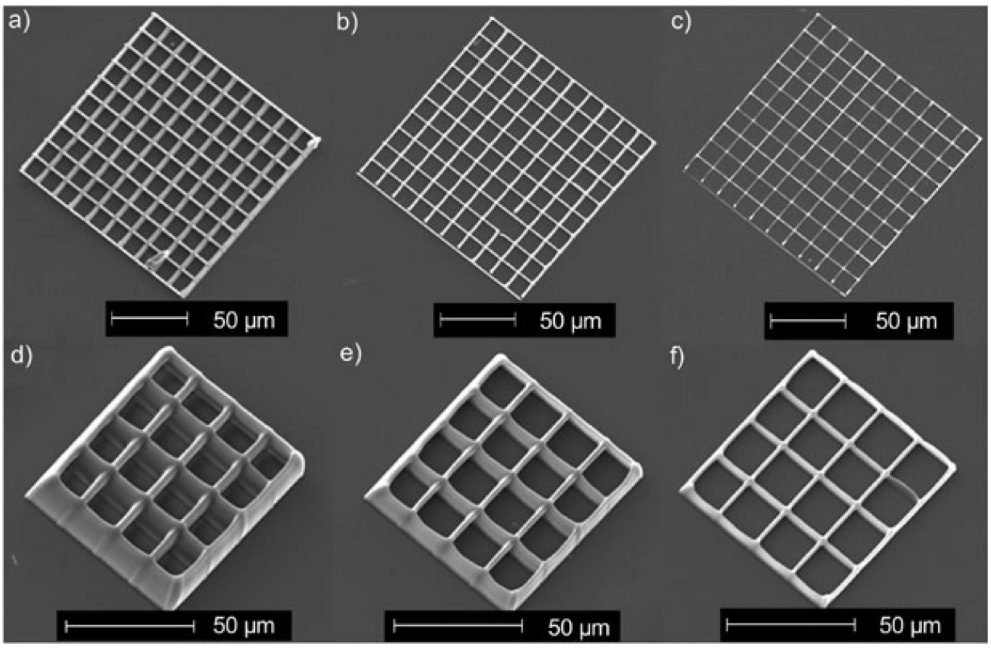

Figure 8. Scanning electron microscope images of lattices. Images (a–c) present PEGda-0.5 lattices polymerized with constant scanning speed of 30 µm/s and laser powers of (a) 6.62, (b) 4.12, and (c) 3.29 mW; (d–f) present PCL-o-2 lattices polymerized with constant scanning speed of 5 µm/s and laser powers of (d) 6.62, (e) 4.95, and (f) 3.29 mW. PCL-o, poly(ε-caprolactone)-based oligomer; PEGda, poly(ethylene glycol) diacrylate.

structures were fabricated with layer spacing varying from 0.35 to 2 µm. An example of a 3D structure polymerized from PEGda-1 using scanning speed of 70 µm/s and laser power of 2.46 mW is shown in Fig. 9.

Overall processability

One of the main goals of this study was to evaluate and compare the overall processability of PCL-o and PEGda with 2PP technique. Besides resolution, other important aspects of processability include the ease of sample preparation and handling, toxicity of the solvents used in the fabrication process, and sample shelf life. Most of the differences between PEGda and PCL-o in terms of processability arise from the very different viscosity values of the resins. For example, sample preparation was easier and more precise with PEGda because of its lower viscosity. On the other hand, the higher viscosity of PCL-o effectively prevented flow in the unpolymerized solution, which occasionally occurred in PEGda samples during polymerization. However, the viscosity of PEGda could be tailored by increasing the molecular weight of the PEG moiety, but the effect of the molecular weight of PEGda on processability and polymerization efficiency was not examined in this study. Moreover, the PCL-o prepolymer solution exhibited crystallization behavior below a

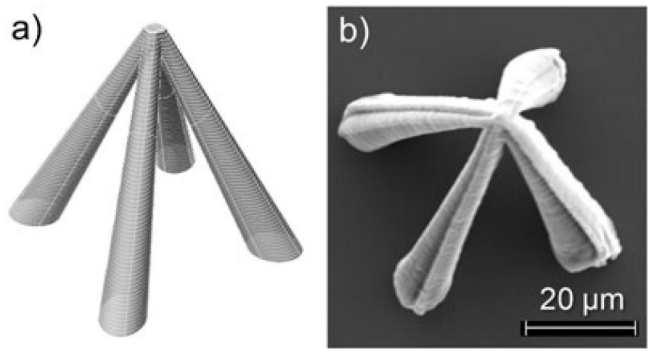

Figure 9. A hollow bonfire-type microstructure as (a) a sliced CAD model using layer spacing of 0.7 µm and (b) an SEM image of the polymerized structure. The structure was fabricated from PEGda-1 by using a scanning speed of 70 µm/s and a laser power of 2.46 mW.

temperature of 30°C. Therefore, all PCL-o samples had to be warmed before polymerization to melt the crystallized oligomers in order make the solution transparent and polymerizable. This was an additional preparation step, which added to the total fabrication time. Overall, neither PCL-o nor PEGda was superior to the other in terms of sample preparation or handling.

The development procedure is a critical step in the fabrication process. For PEGda and PCL-o, similar procedures were used, but because of the very different solubility characteristics of these materials, different solvents were utilized. Uncrosslinked PEGda is a water-soluble viscous liquid, and thus ion-exchanged water can be used for development of the polymerized structures. The use of water as a solvent increases the biocompatibility of the overall process, as no toxic solvent residues will be left in the polymer network. Furthermore, water is safe, cheap, and easy to handle. Removal of the uncrosslinked PCL-o, on the other hand, requires the use of a specific organic solvent such as dichloromethane. Residues of these substances may cause cytotoxic effects that cannot be predicted before cell testing.

Despite of the obvious superiority of water as a development solvent, some problems arose with PEGda samples also. Firstly, the silane treatment of the microscope glasses made the glass surface hydrophobic, which resulted in difficulties during development. The hydrophobicity of the surface caused the water droplets to roll over the surface without wetting it. Therefore, careful rinsing with excess water had to be performed multiple times to ensure that the uncrosslinked polymer had been thoroughly washed away. Furthermore, heavy rinsing occasionally caused the polymerized structures to detach from the substrate.

After development, polymerized samples were stored for SEM imaging in a sealed yet not airproof box. Time of the storage varied from a few days to several weeks. Within this time scale, no visible changes in structure or dimensions were observed in the samples of either PEGda or PCL-o when imaged with an optical microscope. Consequently, the shelf life of the crosslinked structures made of both materials seems appropriate at least for research purposes.

Cell tests

PEGda is a known biocompatible material[27] used in different biomedical applications. PCL-o, on the other hand, is a novel photopolymerizable material, and no previous cell-based testing has been performed with this material. However, PCL, the precursor material for PCL-o, is well known for its good biocompatibility.[36] In this study, the suitability of the materials for cell scaffolds was verified by cell culturing experiments with hESC-derived neuronal cells followed by a Live/Dead staining analysis. Similar results were attained with PEGda and PCL-o in the cytotoxicity and attachment testing. With both materials, cell aggregates attached to the sample surface, but no outgrowth of neurites could be observed. Both live and dead cells were found in all samples. On the laminin control, on the other hand, extensive migration was observed on all sample surfaces, and the morphology of the cells was neuronal like. Images from the Live/Dead analysis are shown in Fig. 10.

As seen in Fig. 10, majority of the cells cultured on PEGda and PCL-o surfaces remained viable in the cell aggregates whereas most of the cells outside the aggregates were dead. Thus, the typical neuronal cell migration was prevented in these materials compared with the laminin surface control. These results indicate that the hESC-derived neuronal cells are able to attach to the surface of both materials, but the materials do not promote cell migration. Because of the verified cell attachment and non-cytotoxicity of PEGda and PCL-o with hESC-derived neuronal cells, the fabricated microstructures have potential for neural cell culture applications as guidance structures after additional material functionalization.

CONCLUSIONS

This study demonstrated the applicability of two photosensitive biomaterials for microfabrication by the means of two-photon-induced polymerization. This study successfully introduced a

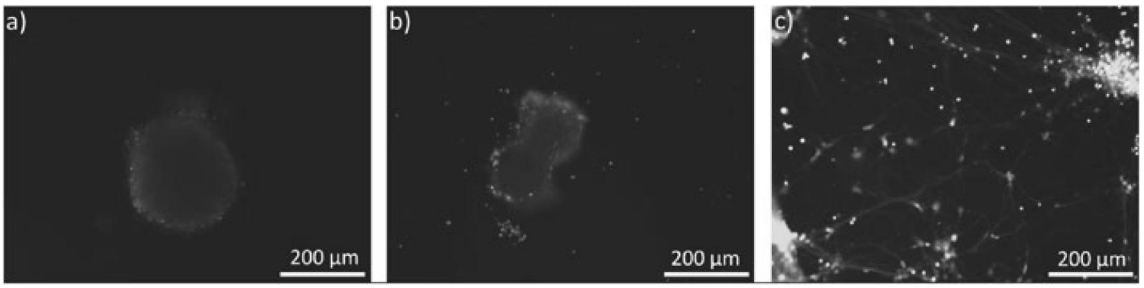

Figure 10. The viability of neural cells on surfaces of (a) poly(ε-caprolactone)-based oligomer, (b) poly(ethylene glycol) diacrylate, and (c) laminin control. Dead cells are stained as red/yellow whereas live cells are stained as green.

new photosensitive, non-cytotoxic, and biodegradable resin for 2PP fabrication. The studied materials, PEGda and a novel methacrylated PCL-based photosensitive oligomer, were compared in terms of resolution and processability. Neither of the two materials, PCL-o or PEGda, turned out to be superior to the other in terms of sample preparation or handling. The resolution study showed that the voxel dimensions increase with increasing PI concentration with both materials. It was also concluded that within the utilized average laser power range, PCL-o produced smaller voxels than PEGda and thus provided better resolution. The obtained minimum resolution was in the order of 1 μm, which is an appropriate scale for cell growth guidance applications. On the other hand, larger features up to a hundred microns in height could be fabricated using the same fabrication system. Therefore, the 2PP setup based on an affordable picosecond laser was shown to be suitable for the fabrication of biocompatible microstructures for different cell-based applications.

Acknowledgements

The authors would like to gratefully acknowledge Sanna Siljander for SEM imaging, Prof. Jouko Viitanen for 2PP setup expertise, and Elli Käpylä, M.Sc. (Eng.), for the assistance with the manuscript preparation.

REFERENCES

[1] S. Wu, J. Serbin, M. Gu, *J. Photochem. Photobiol., A* **2006**, *181*, 1.
[2] K. S. Lee, R. H. Kim, D.-Y. Yang, S. H. Park, *Prog. Polym. Sci.* **2008**, *33*, 631.
[3] A. Ostendorf, B. Chichkov, *Photonics Spectra* **2006**, *40*, 72.
[4] C. LaFratta, J. Fourkas, T. Baldacchini, R. Farrer, *Angew. Chem. Int. Ed.* **2007**, *46*, 6238.
[5] S. Peltola, F. Melchels, D. Grijpma, M. Kellomäki, *Ann. Med.* **2008**, *40*, 4.
[6] S. Maruo, O. Nakamura, S. Kawata, *Opt. Lett.* **1997**, *22*, 132.
[7] A. Ovsianikov, B. Chichkov, *Two-Photon Polymerization—High Resolution 3D Laser Technology and Its Applications, Nanoelectronics and Photonics, Part II*. Springer, New York, **2008**.
[8] T. Bąk, Two Photon Microstereolithography of Polymers for Tissue Engineering, Doctoral Dissertation, Twente, the Netherlands, the University of Twente, **2009**.
[9] K. S. Lee, D-Y. Yang, S. H. Park, R. H. Kim, *Polym. Adv. Technol.* **2006**, *17*, 72.
[10] B. Kaehr, N. Ertas, R. Nielson, R. Allen, R. T. Hill, M. Plenert, J. Shear, *Anal. Chem.* **2006**, *78*, 3198.
[11] S. Peltola, M. Kellomäki, J. Viitanen, ICALEO, 27th International Congress on Applications of Lasers & Electro-optics, Temecula, CA, USA, **2008**, pp. 93–98.
[12] E. Käpylä, S. Turunen, M. Kellomäki, *Micro Nanosyst.* **2010**, *2*, 87.
[13] C. Decker, *Prog. Polym. Sci.* **1996**, *21*, 593.
[14] G. Kotzar, M. Freas, P. Abel, A. Fleischman, S. Roy, C. Zorman, J. M. Moran, J. Melzak, *Biomaterials* **2002**, *23*, 2737.
[15] S. Schlie, A. Ngezahayo, A. Ovsianikov, T. Fabian, H.-A. Kolb, H. Haferkamp, B. N. Chichkov, *J. Biomater. Appl.* **2007**, *22*, 275.
[16] A. Helminen, H. Korhonen, J. Seppälä, *Macromol. Chem. Phys.* **2002**, *203*, 2630.
[17] A. Helminen, H. Korhonen, J. Seppälä, *J. Appl. Polym. Sci.* **2002**, *86*, 3616.
[18] T. Matsuda, M. Mizutani, S. C. Arnold, *Macromolecules* **2000**, *33*, 795.
[19] T. Matsuda, M. Mizutani, *Macromolecules* **2000**, *33*, 791.
[20] F. Claeyssens, E. Hasan, A. Gaidukeviciute, A. Demetra, A. Ranella, C. Reinhardt, A. Ovsianikov, X. Shizhou, C. Fotakis, M. Vamvakaki, *et al.*, *Langmuir* **2009**, *25*, 3219.
[21] B. Kaehr, J. Shear, *Proc. Natl. Acad. Sci. U.S.A.* **2008**, *105*, 8850.
[22] B. Kaehr, R. Allen, D. Javier, J. Currie, J. Shear, *Proc. Natl. Acad. Sci. U.S.A.* **2004**, *101*, 16104.
[23] J. D. Pitts, P. J. Campagnola, G. A. Epling, S. L. Goodman, *Macromolecules* **2000**, *33*, 1514.
[24] L. P. Cunningham, M. P. Veilleux, P. J. Campagnola, *Opt. Express* **2006**, *14*, 8613.
[25] S. Basu, L. P. Cunningham, G. D. Pins, K. A. Bush, R. Taboada, A. R. Howell, J. Wang, P. J. Campagnola, *Biomacromolecules* **2005**, *6*, 1465.
[26] J. Wosnick, M. Shoichet, *Chem. Mater.* **2008**, *20*, 55.
[27] M. Hahn, J. Miller, J. West, *Adv. Mater.* **2006**, *18*, 2679.
[28] S. Seidlits, C. Schmidt, J. Shear, *Adv. Funct. Mater.* **2009**, *19*, 3543.
[29] A. Ovsianikov, A. Ostendorf, B. Chichkov, *Appl. Surf. Sci.* **2007**, *253*, 6599.
[30] J. Rich, H. Korhonen, R. Hakala, J. Korventausta, L. Elomaa, J. Seppälä, *Macromol. Biosci.* **2009**, *9*, 654.
[31] R. S. Lappalainen, M. Salomäki, L. Ylä-Outinen, T. J. Heikkilä, J. A. Hyttinen, H. Pihlajamäki, R. Suuronen, H. Skottman, S. Narkilahti, *Regen. Med.* **2010**, *5*, 749.
[32] F. J. Schork, J. Tsavalas, *Prog. Colloid Polym. Sci.* **2004**, *124*, 126.
[33] K. S. Anseth, C. M. Wang, C. N. Bowman, *Polymer* **1994**, *35*, 3243.
[34] S. Jariwala, K. Venkatakrishnan, B. Tan, *Opt. Express* **2010**, *18*, 1630.
[35] H. Sun, K. Takada, M. Kim, K. Lee, S. Kawata, *Appl. Phys. Lett.* **2003**, *83*, 1104.
[36] P. R. Selvaganapathy, In *Comprehensive Microsystems*, Vol. 1 (Eds.: Y. Gianchandani, O. Tabata, H. Zappe), Elsevier, Oxford, **2008**, pp. 75–105.

Publication II

Turunen, S., Käpylä, E., Terzaki, K., Viitanen, J., Fotakis, C., Kellomäki, M. & Farsari, M.

Pico- and femtosecond-laser induced crosslinking of protein microstructures: Evaluation of processability and bioactivity

Biofabrication 3(2011)4, pp. 045002

Biofabrication 3 (2011) 045002 (14pp) doi:10.1088/1758-5082/3/4/045002

Pico- and femtosecond laser-induced crosslinking of protein microstructures: evaluation of processability and bioactivity

S Turunen[1], E Käpylä[1,6], K Terzaki[2,3], J Viitanen[4], C Fotakis[2,5], M Kellomäki[1] and M Farsari[2]

[1] Tampere University of Technology, Department of Biomedical Engineering, PO Box 692, 33101 Tampere, Finland
[2] Institute of Electronic Structure and Laser (IESL), Foundation for Research and Technology Hellas (FORTH), N. Plastira 100, 70013, Heraklion, Crete, Greece
[3] Department of Materials Science and Technology, University of Crete, Greece
[4] VTT Technical Research Centre of Finland, PO Box 1300, 33101 Tampere, Finland
[5] Department of Physics, University of Crete, Greece

E-mail: elli.kapyla@tut.fi

Received 4 April 2011
Accepted for publication 12 August 2011
Published 9 September 2011
Online at stacks.iop.org/BF/3/045002

Abstract

This study reports the pico- and femtosecond laser-induced photocrosslinking of protein microstructures. The capabilities of a picosecond Nd:YAG laser to promote multiphoton excited crosslinking of proteins were evaluated by fabricating 2D and 3D microstructures of avidin, bovine serum albumin (BSA) and biotinylated bovine serum albumin (bBSA). The multiphoton absorption-induced photocrosslinking of proteins was demonstrated here for the first time with a non-toxic biomolecule flavin mononucleotide (FMN) as the photosensitizer. Sub-micrometer and micrometer scale structures were fabricated from several different compositions of protein and photosensitizer by varying the average laser power and scanning speed in order to determine the optimal process parameters for efficient photocrosslinking. In addition, the retention of ligand-binding ability of the crosslinked protein structures was shown by fluorescence imaging of immobilized biotin or streptavidin conjugated fluorescence labels. The surface topography and the resolution of the protein patterns fabricated with the Nd:YAG laser were compared to the results obtained with a femtosecond Ti:Sapphire laser. Quite similar grain characteristics and comparable feature sizes were achieved with both laser sources, which demonstrates the utility of the low-cost Nd:YAG microlaser for direct laser writing of protein microstructures.

(Some figures in this article are in colour only in the electronic version)

1. Introduction

Direct laser writing (DLW) by multiphoton polymerization (MPP) is a laser-based rapid prototyping technique capable of fabricating two- (2D) and three-dimensional (3D) microstructures with sub-diffraction limit resolution. Typically, the process is based on the optical phenomenon of multiphoton absorption (MPA). In MPA, the simultaneous absorption of two or more photons in a photosensitive resin triggers chemical reactions between photoinitiator molecules and monomers resulting in the polymerization of

[6] Author to whom any correspondence should be addressed.

the photoresist [1–5]. The nonlinear intensity dependence of MPA localizes the excitation and the following polymerization of the resin within the focal volume of the laser beam. Thus, the technique enables the fabrication of features with lateral resolutions below 100 nm, well beyond the diffraction limit of light [6]. Arbitrary 3D microstructures can be fabricated by slicing CAD data into suitable layers in the z direction to generate 2D scanning paths. Each sliced layer is then polymerized by accurately positioning the laser beam focus in the bulk of the photoresist along the desired scanning path. The location of the laser beam along z-axis is translated between the individual layers. These two phases are then repeated layer by layer until the complete design of the microstructure has been scanned. Afterwards, free-standing structures are obtained by washing away the unpolymerized material [7].

Very high peak intensity but low average power is required to launch MPA and to minimize thermal damage of the photopolymerizable material. Commonly, this requirement for photon density is met by utilizing Ti:Sapphire lasers as light sources for MPP. These lasers emit at infrared wavelengths and are capable of producing pulses with widths of several tens of femtoseconds (fs) [8]. However, these lasers cannot be directly diode-pumped and the need for additional pump lasers makes Ti:Sapphire lasers expensive and cumbersome to be widely used for research purposes in materials science and biomedical engineering laboratories. Consequently, some research groups have already utilized more affordable laser source options and introduced visible wavelength picosecond lasers to MPP. It has been shown that the transient power of some frequency-doubled, Q-switched Nd:YAG microchip lasers is high enough to launch MPA in a handful of synthetic [9–13] and protein-based materials [14–16]. Recently, the MPP capability of a high-repetition-rate (36.6 kHz) microchip Nd:YAG laser has been compared to the performance of a lower repetition rate laser (8.24 kHz) by fabricating simple, multilayered protein micropads from bovine serum albumin (BSA) with flavin adenine dinucleotide (FAD) as a photosensitizer [12]. Also, the generation of 3D polymer–protein hybrid structures of photosensitive diacrylate prepolymer and BSA with a small footprint, turn-key Nd:YAG laser source has been demonstrated [17]. Yet in another study by Engelhardt *et al*, the beneficial properties of proteins were combined with the mechanical stability of artificial gelatin methacrylamide (Gel-MAAm) by fabricating microscopic filter systems with a polymer backbone and BSA membranes. In addition, the cell guidance capability of Gel-MAAm 2D microstructures was demonstrated with a cell adhesion assay of porcine chondrocytes [18].

Many proteins can form inter- and intramolecular covalent crosslinks via irradiation of a suitable photosensitizer [19, 20]. Although the mechanisms involved in the photocrosslinking of proteins are not well understood, the crosslinking is believed to proceed either via free radical formation (type I) [19, 21] or via singlet oxygen generation (type II) [22, 23] depending, e.g., on the sensitizer, the reaction conditions and the wavelength and intensity of the exciting light. The singlet oxygen or the radicals interact with photooxidizable amino acid residues such as tyrosine, cysteine, histidine and tryptophan in one protein molecule to form products that react with residues in another protein molecule to promote crosslinking [24, 25]. Naturally occurring flavin mononucleotide (FMN) has been shown to sensitize crosslinking by type I and II mechanisms depending on the pH conditions. The FMN-sensitized photooxidation at pH < 8 is probably mediated by mechanisms that do not involve singlet oxygen. Instead, the reaction involves the formation of a long-lived triplet state FMN, which in turn can abstract an electron (or an H atom) from the protein to generate radicals of the sensitizer and the protein [26, 27]. The excitation of FMN to triplet state can also be achieved via absorption of the combined energy of two or multiple photons, as in the case of MPA-induced photocrosslinking. In fact, another flavin cofactor, FAD, has previously been successfully utilized as a photosensitizer for MPP of BSA and bovine heart cytochrome c (cyt c) induced by picosecond lasers [12, 14]. The shape of the two-photon excitation (TPE) spectrum of FAD is similar to that of FMN, but the TPE action cross-sections of FAD are approximately nine times smaller than that of FMN [28]. For example, FMN has the maximum TPE action cross-section of ~0.8 GM at 700 nm [29], whereas FAD has the maximum peak of 0.085 GM at 720 nm [30]. Thus, as FMN can be more efficiently excited than FAD at least with the Ti:Sapphire laser operating at the infrared (IR) region, it was selected as the photosensitizer for this MPP study in order to enhance the crosslinking rate of the proteins.

The precise control of the cellular architecture is vital for creating engineered tissue constructs. For example, functional nerves and blood vessels can form only when the cells are highly organized in a specific manner [31]. Cellular adhesion, proliferation and differentiation *in vitro* can be guided by topographical and chemical cues. Thus, photocrosslinked nano- and microscale protein topographies with biological activity offer a great opportunity to control the spatial organization of cells by affecting the cell–matrix interactions in cell culture [32–34]. However, as the fabrication speed of protein structures via MPP is very slow, the approach will probably be limited to experiments studying cell–matrix or cell–cell interactions in low cell number samples instead of creating true macroscopic tissue engineering scaffolds.

In this study, we take some fundamental steps towards creating bioactive protein cues with a compact, low-cost laser source. These protein topographies can be used for cell growth guidance purposes as already demonstrated for Chinese Hamster Ovary cells [15], primary human dermal fibroblasts [33, 35], rat brain cortical cells [14, 32], neuroblastoma-glioma (NG108-15) cells [32], rat dorsal root ganglion cells and rat hippocampal neural progenitor cells [34]. However, instead of well-established line cells or cells of animal origin, our future intention is to utilize protein topographies crosslinked via MPP for creating patterned neural networks from neurons differentiated from human embryonic stem cells (hESC). The capabilities of a picosecond pulsed Nd:YAG microlaser to promote MPA-induced photocrosslinking of proteins are evaluated by crosslinking simple 2D surface structures of avidin, bovine serum albumin (BSA) and biotinylated bovine serum albumin (bBSA). In order to

determine the optimal process parameters for efficient fabrication, the photocrosslinking of several different protein and photosensitizer concentrations is reported. In addition, the effects of the average laser power and scanning speed on the ligand-binding ability of the avidin–biotin complex are described. The achievable feature size of the structures and the performance of the Nd:YAG laser are also compared to a femtosecond Ti:Sapphire laser commonly utilized as a laser source for DLW. Also, the 3D fabrication ability of the Nd:YAG laser is demonstrated by fabricating simple woodpile microstructures.

2. Experimental methods

2.1. Fabrication setup

Two different fabrication setups were used for the fabrication of protein structures. The configuration based on the Nd:YAG laser has been described previously [36]. Briefly, a frequency-doubled (532 nm) diode-pumped *Q*-switched Nd:YAG laser (PULSELAS-P-1064-300-FC, Alphalas GmbH, Germany) with a pulse duration of 800 ps, maximum repetition rate of approximately 8 kHz and an average output power of 100 mW, was utilized. The beam was scanned in *x*–*y* direction with a fast steering mirror (FSM-300, Newport Corporation, USA) and in *z* direction with a piezoelectric objective lens positioning system (Mipos 250 SGEX, Piezosystem Jena GmbH, Germany). The sample exposure was controlled with a fast electronic shutter (Oriel 76992, Newport Corporation, USA). The laser output power was attenuated to a suitable crosslinking power of 0.71–6.09 mW measured at the back aperture of the objective. The beam was directed into a 50× oil immersion objective (NA = 0.90, Meiji Techno, Japan) situated on an upright Nikon microscope (ECLIPSE ME 600, Nikon, Japan). The objective had a transmission rate of approximately 30%. The laser beam focal spot radius was estimated at 433 nm [36], which yields the peak focal intensity of 277–321 GW cm^{-2} for the average laser power of 0.71–6.09 mW.

The fabrication setup based on the Ti:Sapphire femtosecond laser (FEMTOSOURCE^{TM} FUSION^{TM} 20, FEMTOLASERS Produktions GmbH, Austria) operating at 800 nm has been described previously [37, 38]. In brief, the laser generated sub-20 fs pulses at the focal spot in the air (measured using an autocorellator) with a repetition rate of 75 MHz and maximum output power of 450 mW. The beam movement was achieved with an *x*–*y* galvanometric mirror digital scanner (hurrySCAN® II, SCANLAB AG, Germany) and on the *z*-axis with a three-axis linear encoder stage (Physik Instrumente GmbH & Co. KG, Germany). The beam was controlled using a mechanical shutter (Uniblitz, USA) and the laser power was adjusted by a motorized attenuator (ALTECHNA Co. Ltd, Lithuania) to an appropriate crosslinking power of 38–123 mW measured before the objective. A high numerical aperture 100× objective lens (NA = 1.40, Zeiss, Germany) was used to focus the laser beam into a focal spot with a radius of 350 nm, which led to the peak intensity of 13–43 TW cm^{-2} at the focal spot. The overall transmittance of the laser beam measured after the objective was approximately 17% of the initial laser output power.

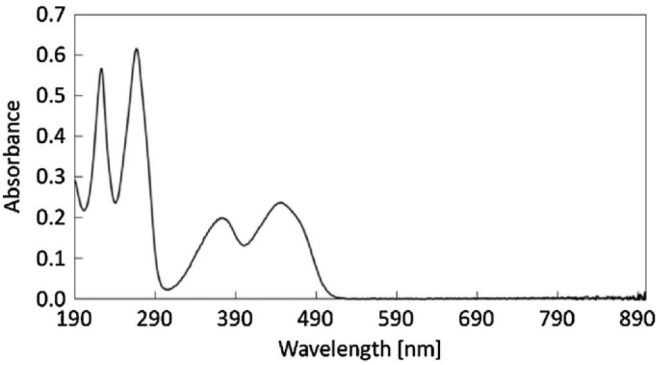

Figure 1. Normalized UV-Vis absorption spectrum of FMN in ion-exchanged water.

2.2. Materials and sample preparation

As a cofactor of vitamin B_2 [39], FMN can be used as a non-toxic photosensitizer for protein crosslinking. It also has a suitable absorption spectrum for MPA-induced photocrosslinking at 532 nm and at 800 nm, which was verified by the measurement of the UV-Vis absorption spectrum (figure 1) of FMN dissolved in ion-exchanged water to a concentration of 0.1 mM. The spectrum was obtained with a Unicam UV 540 UV-Vis spectrometer (Thermo Spectronic, England) in the range of 190–900 nm. The absorption spectrum of FMN in water has four linear absorption maxima at 223, 267, 374 and 447 nm. Also, the photosensitizer exhibits no absorption above 527 nm but absorbs strongly in the UV region, where the two-photon absorption windows of the lasers utilized in this study lie.

Photocrosslinking of three different proteins with FMN as photosensitizer was investigated in this study. The BSA (Sigma-Aldrich Finland Oy, Finland) reagent solution contained 200 mg ml^{-1} of protein and 4 mM FMN (Sigma-Aldrich Finland Oy, Finland) in phosphate-buffered saline (PBS, pH ~ 7.4). BSA was biotinylated via reaction with biotinamidohexanoyl-6-aminohexanoic acid *N*-hydroxysuccinimide ester (Sigma-Aldrich Finland Oy, Finland) in a buffer consisting of 50 mM sodium phosphate and 100 mM NaCl (pH ~ 7). bBSA was used as a solution containing 100 mg ml^{-1} of the protein with 0–4 mM FMN or together with BSA as a solution of 100 mg ml^{-1} bBSA and 100 mg ml^{-1} BSA with 0–4 mM FMN. Plain BSA was added to the solution to provide increased mechanical stability. Avidin (Belovo Chemicals, Belgium) was studied as solutions containing 50, 100, 200 or 400 mg ml^{-1} protein and 0–4 mM FMN in PBS.

2.3. Photofabrication of protein microstructures

The protein microstructures were fabricated in a chamber between a microscope slide and a coverslip with a 150 μm thick spacer. The chamber was filled with a protein solution and structures were crosslinked either downwards from the

top cover glass or upwards from the bottom microscope slide depending on the fabrication setup in question. In order to enhance the adherence of the protein structures on glass, 3-aminopropyl triethoxysilanized microscope slides (Electron Microscopy Sciences, USA) were used in some occasions with the Nd:YAG laser setup to provide a hydrophobic substrate for the proteins. Simple 2D patterns, such as arrays of seven concentric squares spaced 2 μm apart with the outer square side length of 25 μm, were fabricated from each of the protein solution by varying the average laser power and scanning speed. With the Nd:YAG laser setup, scanning speeds of 5, 10, 20 and 40 μm s^{-1} and average laser powers of 0.71–6.09 mW were tested. The average laser power for the Ti:Sapphire laser setup was varied from 38 mW to 123 mW and the samples were scanned with speeds of 10, 20, 30, 40 and 50 μm s^{-1}.

The fabrication of 3D structures was also attempted with the Nd:YAG system by crosslinking simple woodpile structures from BSA. The overall size of the CAD model of the woodpile was 40 $\times$ 40 $\times$ 10 μm. Fabrication of the 2D rods of the woodpile was executed by single line scans with a 5 μm distance between the scanning paths in the x–y direction and 1 μm between the scanning paths in the z direction. The scanning speed used for the woodpile fabrication was 10 μm s^{-1} and the average laser power was 5.67 mW. After crosslinking, all the fabricated structures were rinsed with ion-exchanged water to remove the excess protein solution and photosensitizer.

2.4. SEM imaging

For SEM imaging, the protein samples were fixed in 5% (v/v) glutaraldehyde for 15 min, and then dehydrated by sequential wash for 15 min in ion-exchanged water, 1:1 ethanol/H_2O, 100% (v/v) ethanol, 1:1 ethanol/methanol and 100% (v/v) methanol (twice). After overnight drying in a desiccator, the samples were sputter coated with gold in an argon atmosphere to a nominal thickness of 75 nm or 15 nm (S 150 Sputter Coater, Edwards Ltd, UK, or SCD 050 Sputter Coater, BAL-TEC AG, Liechtenstein). The samples were imaged using either a Philips XL-30 (Philips Electron Optics, the Netherlands) or a JEOL JSM-6390 LV (JEOL Ltd, Japan) scanning electron microscope with an acceleration voltage of 5 kV or 10 kV.

2.5. Fluorescence imaging

For bioactivity studies, avidin microstructures were incubated in 2 μM DY-634-Biotin label (Dyomics GmbH, Germany) and bBSA structures in 20 μg ml^{-1} DyLight® 649 Streptavidin conjugate (Vector Laboratories, Inc., USA) for 30 min. The previously reported washing procedures [14, 35, 40] to remove the excess fluorescence label suggest that rinsing the sample few times with buffer solution should have been adequate. However, we found that 10 rinses with a Pasteur pipette were insufficient for eliminating the unbound label completely from the protein structures. Hence, a test series was performed to determine an effective protocol for the washing by labelling five samples of crosslinked BSA with 20 μg ml^{-1} DyLight® 649 Streptavidin conjugate. One sample was simply rinsed ten times with water and others were immersed in water for a total of 30 min, 1 h (water was changed after every 15 min), 2 h or 4 h (water was changed every 30 min). According to the fluorescence imaging results, it was found that even the 4 h immersion was not sufficient to remove the label completely from the 3D structures. However, the 1 h immersion was found adequate to significantly reduce the nonspecific fluorescence of the surface patterns. Thus, the bioactivity of protein structures was evaluated by immersing the labelled structures in ion-exchanged water for 1 h.

Wide-field fluorescence imaging was performed on a Nicon Eclipse TS100 inverted microscope (Nikon, Japan) equipped with a mercury lamp excitation source and a 20$\times$ dry objective (NA = 0.40, Nikon, Japan). Fluorescence emission was collected by using a BrightLine® LF635-A-NQF filter set (Semrock, Inc., USA) and detected using a digital camera (SPOT RT™ SE6 Slider, Diagnostic Instruments, USA) with a 12-bit 1360 $\times$ 1024 Sony ICX-285AL CCD. Image acquisition was accomplished using SPOT Software 4.6 (Diagnostic Instruments, Inc., USA) and the data were processed with the NIH ImageJ image analysis software.

2.6. AFM imaging

Patterns of concentric squares of avidin, BSA and bBSA were also studied by non-contact mode atomic force (AFM) microscopy (XE-100, Park Systems Inc., USA). All measurements were performed using silicon probes (ACTa-910M, Applied NanoStructures Inc., USA) with a nominal resonance frequency of 300 kHz, spring constant of 4 N m^{-1}, a pyramid shaped tip (radius $<$ 10 nm) and an aluminum reflective coating. Images were acquired with a scan speed of 0.15 or 0.40 Hz.

3. Results and discussion

3.1. Evaluation of processability and achievable resolution

Several different protein and photosensitizer concentrations as well as average laser power and scanning speed values were tested to determine the range of fabrication conditions suitable for protein crosslinking. With the Nd:YAG laser, avidin could be crosslinked into surface patterns only with the protein concentration of 400 mg ml^{-1} and photosensitizer content of 1–4 mM. In order to produce continuous protein lines, the scanning speed of either 5 or 10 μm s^{-1} had to be used regardless of the photosensitizer concentration. Scanning with the speed of 20 or 40 μm s^{-1} mainly produced discontinuous protein fragments. As for the laser power, even the average laser power of 0.71 mW led to adequate crosslinking of the avidin with the scanning speed of 5 μm s^{-1}. Higher laser power values (3.94–6.09 mW) led to the distortion of the protein patterns due to the tilting of the protein lines with a high aspect ratio.

The solution of 100 mg ml^{-1} of bBSA and 100 mg ml^{-1} of BSA with 4 mM FMN could be efficiently crosslinked into surface patterns with scanning speeds of 5, 10 and 20 μm s^{-1} and with laser powers of 1.84–5.67 mW (figure 2). A slightly higher laser power (2.87 mW) and slower scanning speed (5 or 10 μm s^{-1}) had to be utilized for the bBSA/BSA solutions with FMN concentrations of 2 mM or 1 mM.

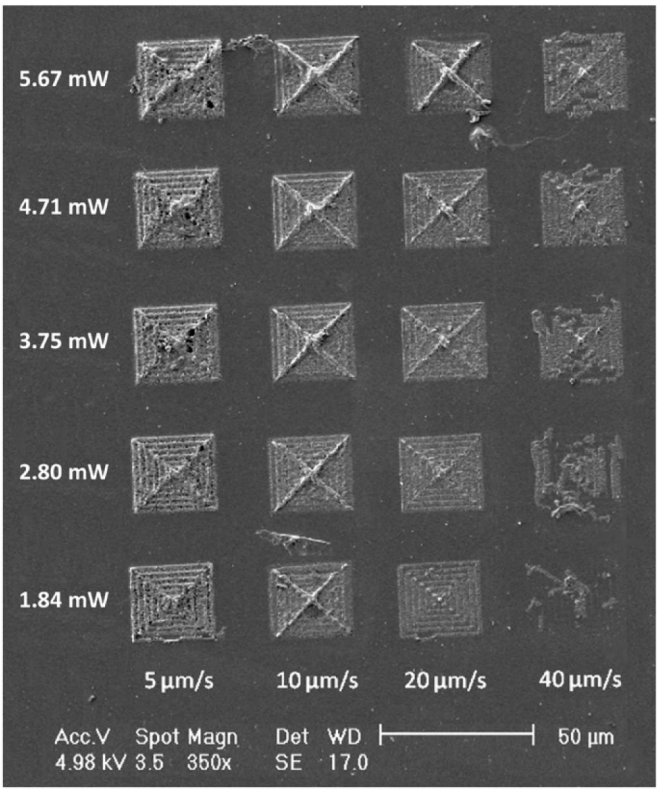

Figure 2. SEM image of a surface pattern array fabricated with the Nd:YAG laser from a solution of 100 mg ml^{-1} bBSA and 100 mg ml^{-1} BSA with 4 mM FMN by varying the scanning speed and laser power.

This dependence of the protein crosslinking efficiency on the photosensitizer concentration suggests that FMN is not regenerated during the reaction and thus the crosslinking of the proteins probably proceeds via a hydrogen abstraction mechanism (type I). The addition of a hydrogen atom to the triplet state FMN destroys its ability to generate long-lived triplet states and it no longer can act as a photosensitizer for the crosslinking reaction [41]. The speculation about the reaction mechanism being of type I is also supported by the experimental conditions (i.e., pH $\sim$ 7.4), which according to Spikes *et al* suggests that the FMN-sensitized photooxidation is mediated by mechanisms not involving singlet oxygen [26].

Although BSA has previously been shown to crosslink also without any additional photosensitizer with picosecond Nd:YAG lasers (532 nm, $\sim$ 600 ps, 7.65 kHz; 532 nm 550 ps, 7 kHz) [14, 17], in our experiments crosslinking was not observed when irradiating the solution of 100 mg ml^{-1} of bBSA and 100 mg ml^{-1} of BSA without the additional photosensitizer. This difference in crosslinking behaviour could be attributed to different laser peak intensities at the focal point of the laser setups utilized in these studies. However, it is impossible to reliably compare the laser intensities of these fabrication setups due to the variation in the measuring method of the average laser power (measurement before the objective versus after the objective). Most likely the maximum laser peak intensity of our laser system ($\sim$300 GW cm^{-2}) was not high enough to initiate MPP in the protein solution without the aid of an additional photosensitizer. Also, the pure bBSA (100 mg ml^{-1} with 0–4 mM FMN) crosslinked very poorly even with the slowest scanning speed and highest laser power. It was concluded that the protein concentration of 100 mg ml^{-1} was not high enough to produce uniform structures. The crosslinking efficiency of BSA was not thoroughly investigated but the protein was successfully crosslinked from a fabrication solution containing 200 mg ml^{-1} BSA and 4 mM FMN with an average laser power of 5.67 mW and a scanning speed of 10 μm s^{-1} (figure 3(*d*)).

Samples of avidin and BSA patterns were also AFM imaged (figure 3(*a*) and (*b*)) in order to assess the resolution and surface topography but it was concluded that the estimation of the line widths and heights could be done more reliably from the acquired SEM images. Furthermore, the resolution results presented here do not represent the absolute minimum or maximum values for the line width and height as the degree of line truncation under the glass substrate was not taken into account by performing an ascending scan [42]. Instead, the lines were fabricated at a randomly selected focal plane near enough the substrate surface to attach the protein lines to a solid support and thus preventing them from floating away during the development phase. SEM analysis of the surface structures crosslinked of 400 mg ml^{-1} avidin with 2 mM FMN (1.79 mW, 5 μm s^{-1}) indicated that the average width of the thinnest lines was 266 nm $\pm$ 14 nm (figure 3(*c*)). According to the measurements made from a SEM image taken from a 45° tilt, the average height of the lines was 548 nm $\pm$ 9 nm. This gives an average aspect ratio of 2.1 for the avidin lines. According to the SEM analysis of the concentric squares fabricated of the solution of 100 mg ml^{-1} bBSA and 100 mg ml^{-1} BSA with 4 mM FMN, the height of the surface adherent protein lines increased slightly from 1.39 μm $\pm$ 0.20 μm to 2.02 μm $\pm$ 0.39 μm as the average laser power increased from 1.84 mW to 5.67 mW. The original width of the lines could not be estimated because all the lines toppled over during the development procedure.

Figure 3(*b*) and (*d*) shows an AFM and a SEM image of a BSA structure (200 mg ml^{-1} BSA, 4 mM FMN) obtained by scanning the laser beam at 10 μm s^{-1} with the laser power of 5.67 mW. As can be seen from the figure 3(*d*) the protein lines had toppled over on their sides during the development phase and thus the original line width could only be estimated from the parts like the one marked with a black arrow. According to the SEM analysis, the average width of the BSA lines was 747 nm $\pm$ 101 nm and the height was 1.76 μm $\pm$ 0.16 μm resulting in an aspect ratio of 2.4. The achievable resolution for the crosslinked structures of avidin and BSA with a Nd:YAG laser has not been reported by others in detail, but according to Kaehr *et al* [14] the width of protein lines is typically less than 0.5 μm when using a laser power of 1 mW and about 0.75 μm at the laser power of 2 mW. Recently, Engelhardt *et al* [17] also reported that voxels polymerized of the BSA solution (400 mg ml^{-1}) had a minimum height of approximately 1 μm at the average laser power of 2.1 mW measured after the objective. Thus, the line widths and heights of the protein structures achieved in this study correspond well to the previously reported values.

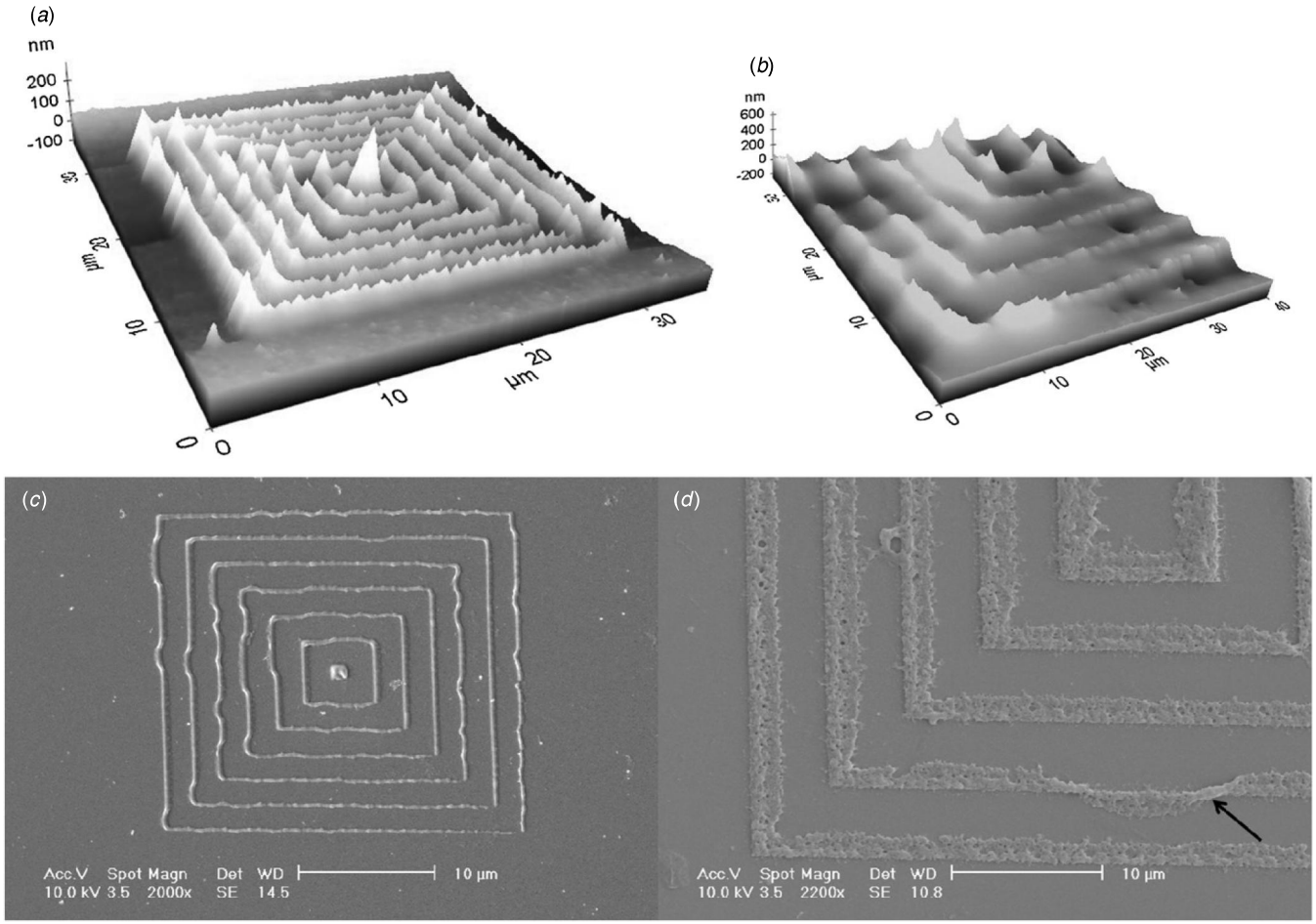

Figure 3. (*a*) and (*c*) AFM and SEM images of the surface patterns photocrosslinked with the Nd:YAG laser of 400 mg ml^{-1} avidin with 2 mM FMN with an average laser power of 1.79 mW and a scanning speed of 5 μm s^{-1}. (*b*) and (*d*) AFM and SEM images of parts of concentric squares fabricated from 200 mg ml^{-1} BSA with 4 mM FMN with an average laser power of 5.67 mW and a scanning speed of 10 μm s^{-1}. The black arrow indicates a part of the protein pattern that could be used for estimation of the original line width as most of the protein lines had toppled over during the development phase.

In order to compare the processing capability of the low-cost Nd:YAG picosecond laser to the more commonly used femtosecond laser sources, protein structures were also fabricated with a Ti:Sapphire laser setup by varying the average laser power and scanning speed. Crosslinking of avidin was investigated with a fabrication solution containing 400 mg ml^{-1} avidin and 2 mM FMN. The laser beam was scanned with the speed of 10 μm s^{-1} and the average laser power was varied from 38 mW to 123 mW. Based on the measurements from SEM images, the width of the avidin lines increased only slightly as a function of the laser power, ranging from 204 nm $\pm$ 33 nm to 309 nm $\pm$ 28 nm. The height of the lines could only be measured from a few patterns since most of the SEM images were taken from above and not from a 45° tilt. The lines fabricated with the laser power of 38 mW were found to have the average height of 304 nm $\pm$ 2 nm. This results in an aspect ratio of 1.5 for the avidin lines fabricated with the Ti:Sapphire laser, which is somewhat lower than the aspect ratio of the avidin lines fabricated with the Nd:YAG laser. However, this difference can be due to the difference in focusing height levels between the two experiments or it may result from the higher numerical aperture objective utilized with the Ti:Sapphire laser, which leads to more spherical shaped voxels instead of elongated spinning ellipsoids. The solution of 100 mg ml^{-1} bBSA and 100 mg ml^{-1} BSA with 4 mM FMN was studied by scanning the sample with a speed of 10–40 μm s^{-1} and by varying the laser power from 38 mW to 123 mW. An example of the fabricated square patterns is shown in figure 4. In principle, the width of the protein lines decreased at faster scanning speeds although the slight variance in the initial focus position between patterns produced some inconsistency to the measurements. For example, lines fabricated with an average laser power of 56 mW had an average width of 421 nm $\pm$ 36 nm at a scanning speed of 10 μm s^{-1}, 405 nm $\pm$ 52 nm at a speed of 20 μm s^{-1}, 307 nm $\pm$ 31 nm at a speed of 30 μm s^{-1} and 270 nm $\pm$ 22 nm at a speed of 40 μm s^{-1}.

The solution containing 200 mg ml^{-1} BSA with 4 mM FMN was also fabricated into surface patterns by varying the average laser power from 38 mW to 123 mW and by scanning the sample with a speed of 30 μm s^{-1}. The width of the BSA lines increased only marginally and within the error limits as a function of the laser power. For example, the lines crosslinked with an average laser power of 38 mW had an average width

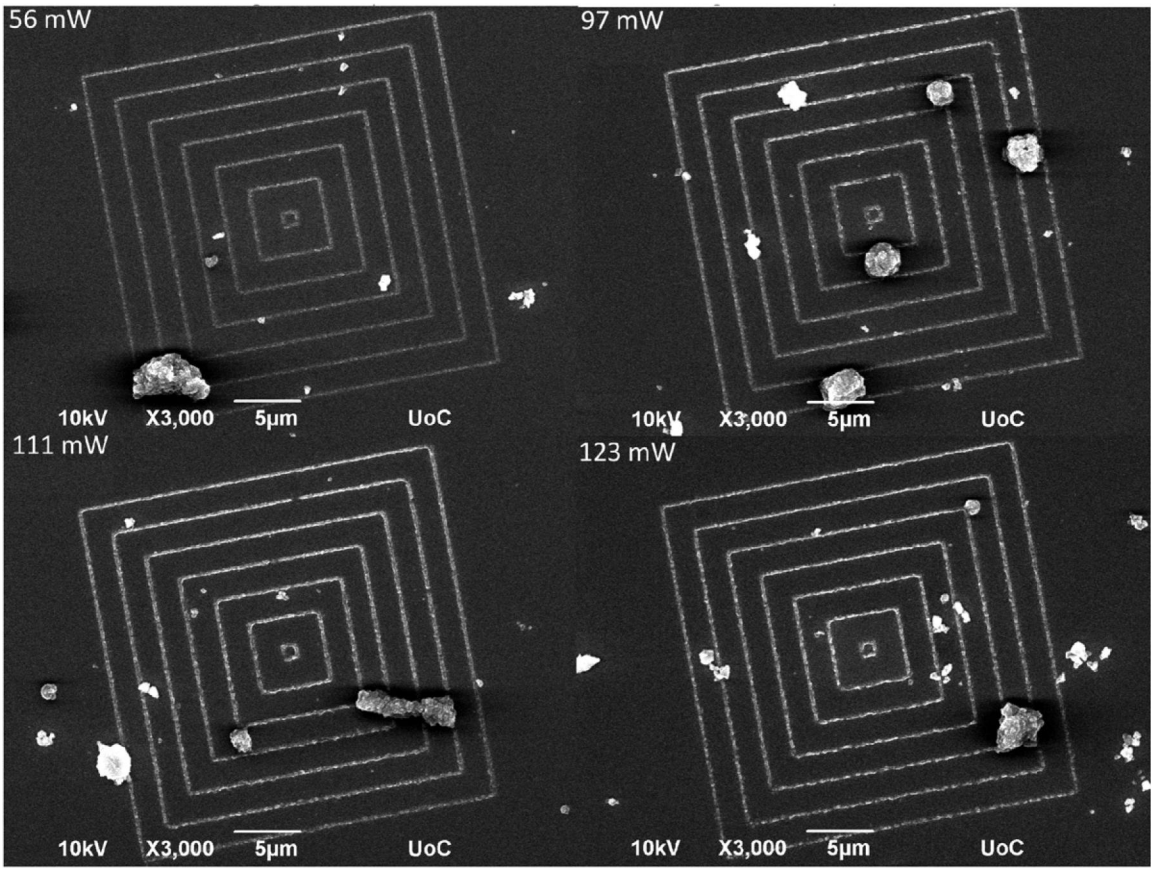

Figure 4. SEM image of an array of concentric squares fabricated with the Ti:Sapphire laser from a solution of 100 mg ml^{-1} bBSA and 100 mg ml^{-1} BSA with 4 mM FMN. The laser beam was scanned at a speed of 40 μm s^{-1} and the average laser power was varied from 56 mW to 123 mW.

of 249 nm ± 26 nm, whereas lines fabricated with a power of 123 mW had a width of 267 nm ± 16 nm. Again, the measured dimensions suffered from some inconsistency due to the variance in the initial laser beam focus position. The line heights had values close to the line widths, thus resulting in an average aspect ratio of 0.66–0.85. The minimum resolution for BSA structures fabricated with a Ti:Sapphire laser has been reported to vary in the lateral direction from 250 nm (using a 1.3 NA lens) [32] to 600–700 nm (using a 0.75 NA lens) [35], and in the axial direction from 1 μm (using a 1.3 NA lens) [43] to 3.5 μm (using a 0.75 lens) [44]. Thus, the line widths obtained in the current study are in good accordance with the previously reported results. The axial resolution is only about one fifth of the minimum line height published previously for BSA. However, this difference in heights probably results from the difference in focus positions and thus it cannot be considered as a significant result. Surprisingly, the Nd:YAG laser was able to produce avidin lines with a comparable lateral resolution with the Ti:Sapphire laser (266 nm versus 204 nm). However, the very small lateral dimensions of the protein lines crosslinked with the Nd:YAG laser led to the collapse of the structures during the post-fabrication rinsing phase. In the future, this problem could possibly be avoided by using an objective lens with a higher numerical aperture and by selecting the initial focal position more accurately. In contrast, the protein lines fabricated with the Ti:Sapphire laser had lower aspect ratios and thus the structures mainly withstood the rinsing procedure without deformation.

3.2. 2D and 3D topography

The topography of the 2D and 3D crosslinked structures was analysed by comparing the SEM images of structures fabricated with the two different laser sources and different protein compositions. The SEM images revealed some differences in the surface topography of the different protein structures. Avidin appeared to form quite uniform and dense lines when processed either with the Nd:YAG (figure 5(*a*)) or with the Ti:Sapphire laser setup (figure 5(*b*)). The very high protein concentration (400 mg ml^{-1}) enabling the efficient crosslinking of the protein and thus small mesh size of the matrix may have led to the formation of smooth surfaces of the avidin structures.

In contrast to avidin, the structures fabricated from a solution of 100 mg ml^{-1} bBSA and 100 mg ml^{-1} BSA with 2 mM or 4 mM FMN had more porous and highly textured surface topography, as seen in figure 6. Similar grain structure results have also been reported previously for a solution of BSA (1.5×10^{-4} M) with Rose Bengal (1×10^{-4} M) as photosensitizer [41]. Especially, the patterns photocrosslinked with the Nd:YAG laser showed highly textured surfaces. The difference could be explained by the reduced crosslinking

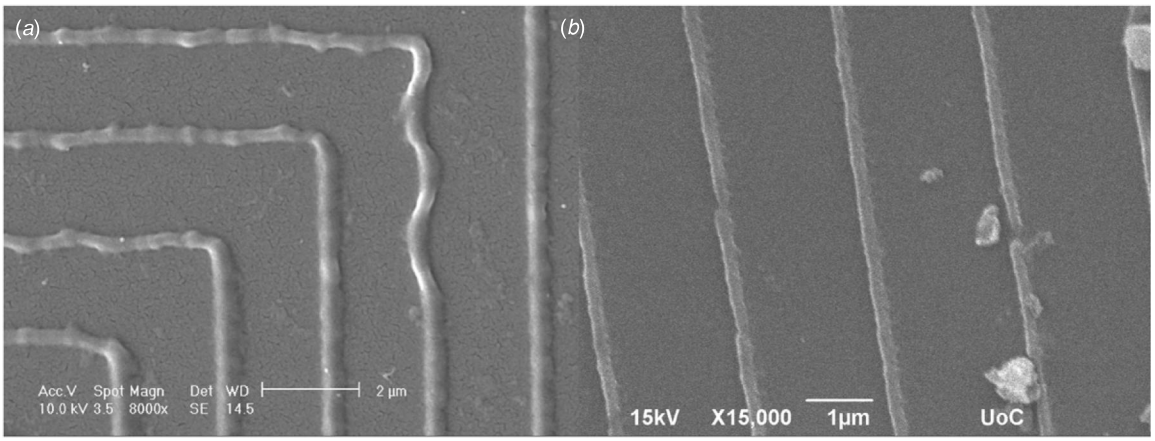

Figure 5. Close-up SEM images of avidin lines crosslinked of a solution containing 400 mg ml^{-1} avidin with 2 mM FMN. (*a*) A line structure fabricated with the Nd:YAG laser setup with a scanning speed of 5 μm s^{-1} and an average power of 1.79 mW. (*b*) A line structure fabricated with the Ti:Sapphire laser setup at a scanning speed of 10 μm s^{-1} with an average power of 97 mW.

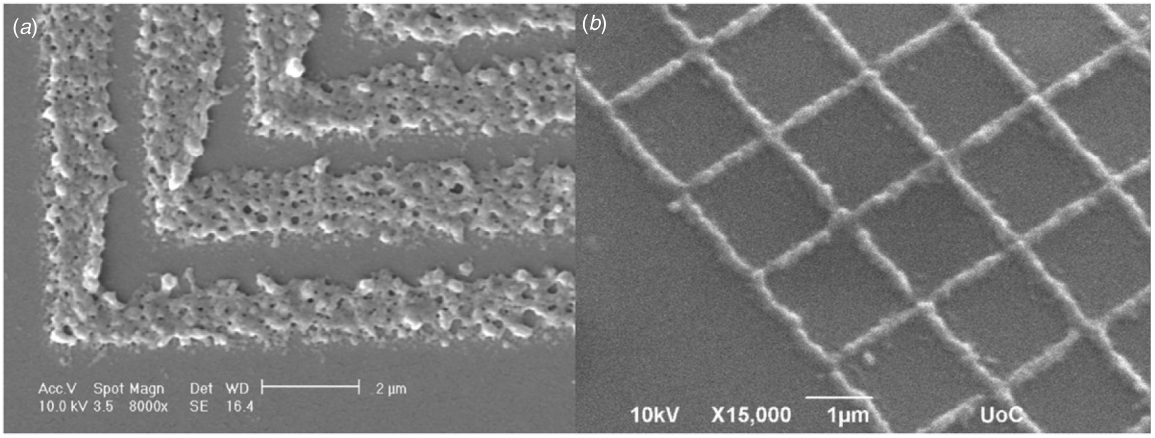

Figure 6. SEM images of surface patterns fabricated from a solution of 100 mg ml^{-1} bBSA and 100 mg ml^{-1} BSA with 2 mM or 4 mM FMN, respectively. (*a*) A structure produced with the Nd:YAG laser with a scanning speed of 5 μm s^{-1} and an average laser power of 1.79 mW. (*b*) A grid fabricated with the Ti:Sapphire laser by scanning the sample with a speed of 40 μm s^{-1} and with an average laser power of 123 mW.

density of the more dilute BSA solution compared to the more concentrated avidin solution. The Ti:Sapphire laser setup produced structures with somewhat less porous texture than the Nd:YAG laser, as can be seen from figure 6(*b*). Similar difference in grain characteristics of BSA (200 mg ml^{-1}, 4 mM Rose Bengal) has also been discovered by Kaehr *et al* in their experiments with Nd:YAG (average power, 0.5 mW) and Ti:Sapphire lasers (average power, 11 mW) [14].

The structures crosslinked of pure BSA showed similar surface topography as the structures fabricated from the solution of bBSA and BSA. Figure 7 shows an example of a star-shaped BSA surface pattern fabricated with the Ti:Sapphire laser from a solution containing 200 mg ml^{-1} BSA with 4 mM FMN. Overall, the Ti:Sapphire laser allowed the fabrication of the continuous protein patterns with 2- to 10-fold faster scanning speeds in comparison to the scanning speeds used with the Nd:YAG laser. This is likely due to the much higher repetition rate (75 MHz versus 8 kHz) and approximately 90-fold higher peak power of the Ti:Sapphire laser compared to that of the Nd:YAG laser, which enables more efficient crosslinking of proteins by creating favourable circumstances for the multiphoton absorption to occur.

3D fabrication was also demonstrated by crosslinking BSA into a simple woodpile structure with the Nd:YAG laser (figure 8). The size of the 3D structures that can be fabricated in a single scan with our Nd:YAG laser setup is limited to 310 μm in the x direction and 220 μm in y direction by the scanning range of the fast steering mirror with the 50× objective. In principle, the scanning range in the z direction is restricted by the maximum deflection of the piezoelectric positioning system (250 μm), but in practice it is limited by the height of the fabrication chamber (150 μm). If structures covering larger areas than a single scan plane are desired, multiple lateral planes can be quilted together into larger patterns as proposed by Nielson *et al* [43]. However, in our current experiment, this was not attempted as a very low scanning rate of 10 μm s^{-1} was required to produce uniform matrices with the selected protein and photosensitizer concentrations leading to a time-consuming fabrication process.

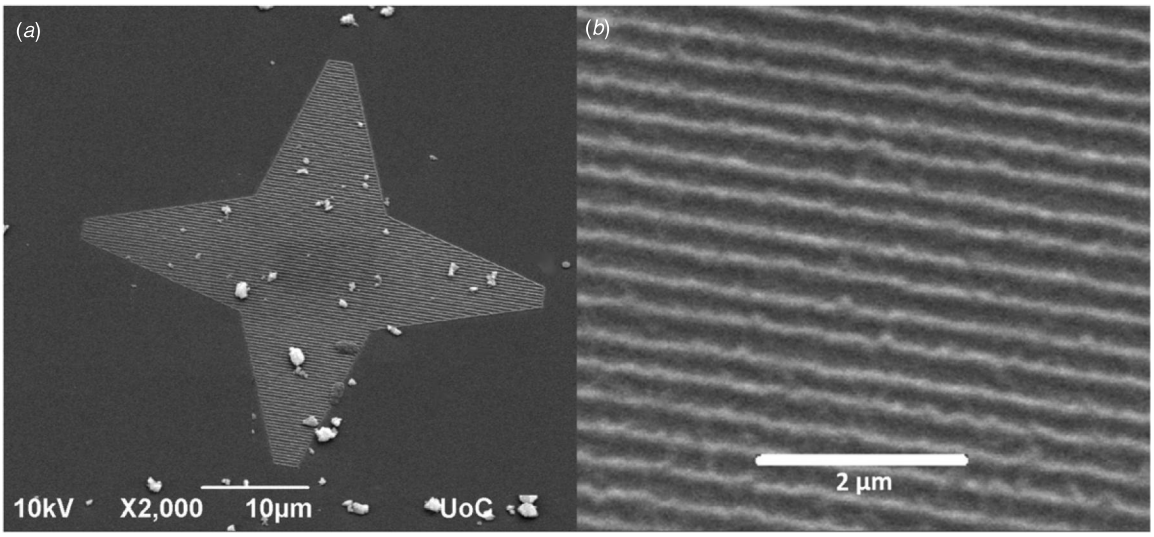

Figure 7. (*a*) SEM image of a star-shaped surface pattern fabricated from 200 mg ml^{-1} BSA with 4 mM FMN with the Ti:Sapphire laser. The scanning speed and the average laser power used were 50 μm s^{-1} and 56 mW, respectively. (*b*) A close-up of the individual protein lines within in the star.

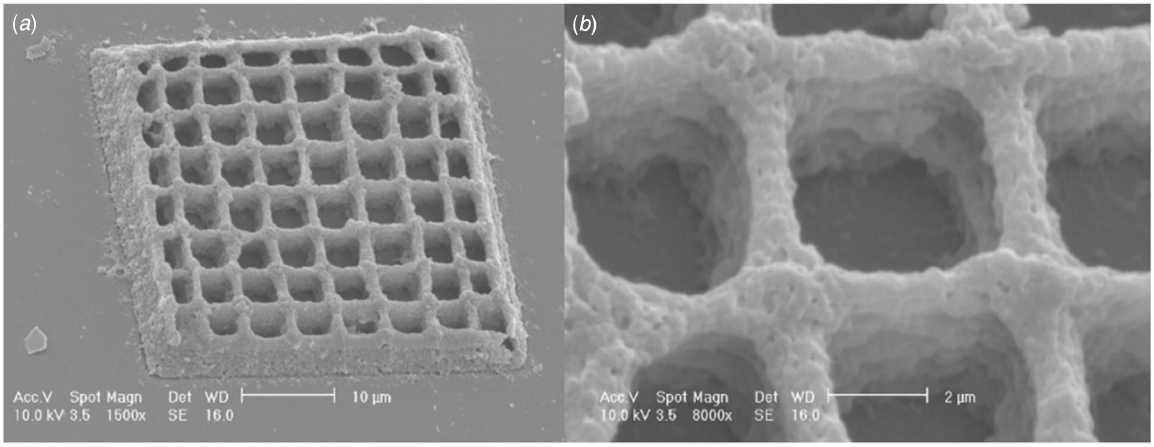

Figure 8. (*a*) SEM image of a woodpile structure cross-linked from 200 mg ml^{-1} BSA with 4 mM FMN with the Nd:YAG laser by scanning the sample with a speed of 10 μm s^{-1} and with an average laser power of 5.67 mW. (*b*) A close-up of the surface topography of the woodpile.

The crosslinked BSA structure reproduced the CAD image of the woodpile in the *x*–*y* direction quite accurately although in the *z* direction, the individual rods fused together instead of forming separate layers of rods. The dimensions of the CAD model were 40 × 40 × 10 μm and according to the measurements from the SEM image, the glass-bound bottom part of the fabricated structure had virtually no dimensional changes. However, the top part of the woodpile shrank from 40 μm to 35 μm, thus having a maximum shrinkage strain of 13%. The anisotropic shrinkage is a result of the uneven shrinkage rates of the top and bottom parts of the woodpile during the development and dehydration procedures due to the attachment of the bottom part to the glass substrate. The measured height of the woodpile was only about 5.3 μm, which gives a maximum shrinkage strain of 47% in the *z* direction. The pronounced collapse of the structure could be a result of the non-ideal inter-layer distance in the *z* direction, which in the original CAD model was 1 μm. Utilization of smaller layer spacing could have resulted in less sponge-like surface texture and thus mechanically more stable woodpile. The shrinkage of hydrophilic protein microstructures during drying phase as the trapped water evaporates is a common disadvantage related to mechanically weak 3D protein structures. The shrinkage phenomenon was also described by Engelhardt *et al* as they fabricated BSA cubes (150 mg ml^{-1}, 3 mM Rose Bengal) with a femtosecond Ti:Sapphire laser [18]. The edges of the cube shrank from 50 μm to 30 μm, which corresponds to a shrinkage strain of 40%. Hence the cube had a greater shrinkage value in the *x*–*y* direction than the woodpile structure fabricated in our study, which is probably a result of lower protein concentration and thus lower crosslinking density used for crosslinking the cube. In future experiments, the shrinkage of the fabricated structures during the solvent removal could also be reduced by using either a freeze drying or a critical point drying process instead of the ethanol–methanol dehydration procedure. This would help to eliminate the collapsing force owing to the pressure difference due to the surface tension of the volatile rinsing material.

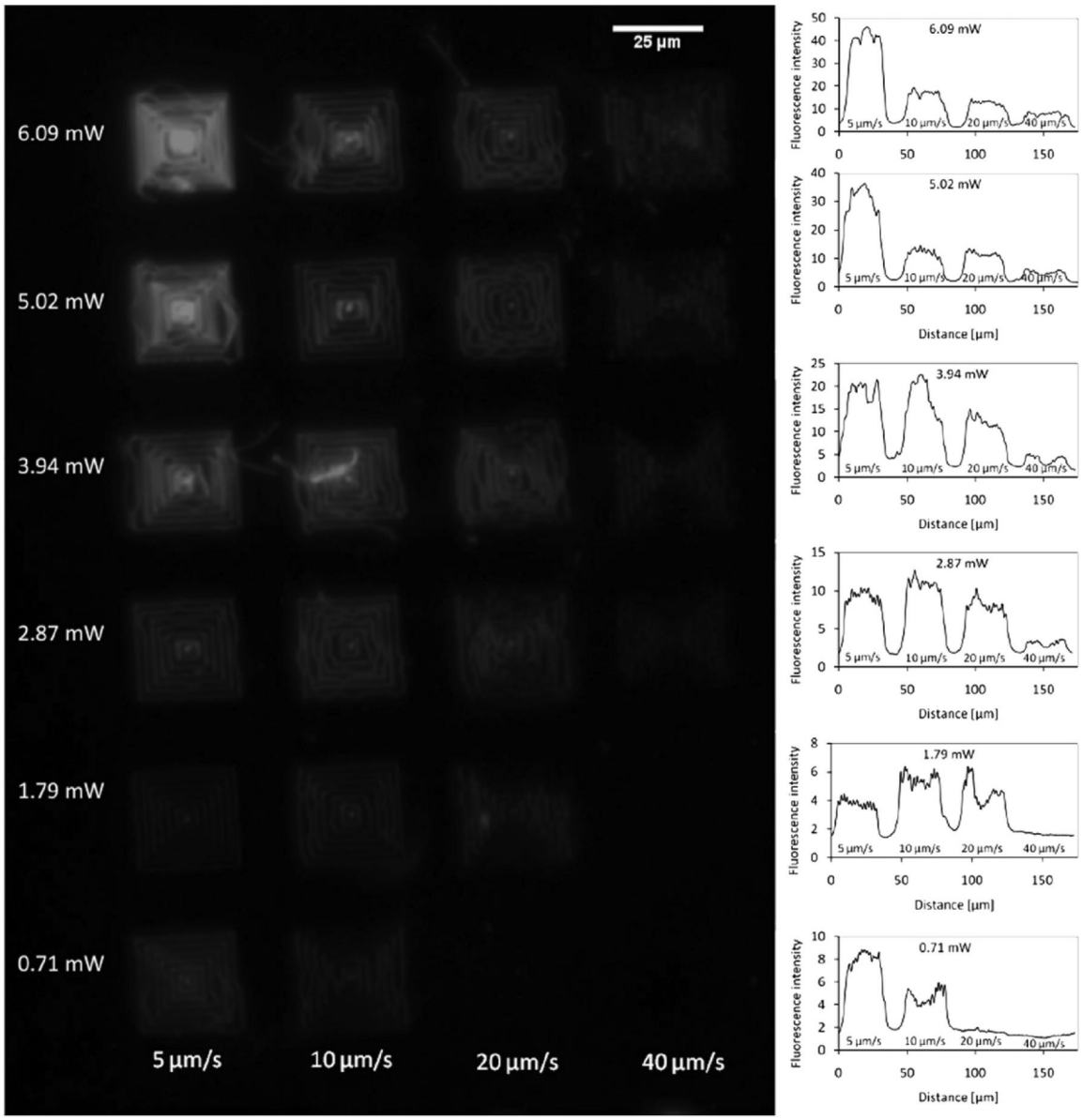

Figure 9. Fluorescence image of an array of concentric squares fabricated with the Nd:YAG laser from 400 mg ml^{-1} avidin with 2 mM FMN by varying the average laser power and scanning speed and subsequently stained with the DY-634-biotin label. Corresponding plots represent the surface intensity profiles for square pattern sets cross-linked with a constant average laser power by varying the scanning speed. The data were created by using an exposure of 5.26 s without binning.

3.3. Retention of ligand-binding ability of the avidin–biotin complex

It is important to verify whether the bioactivity of proteins is retained during the exposure to the high laser intensities required for efficient MPA of the photosensitizer. For example, it has been shown that endogenous proteins in living cells can become denatured due to accidental two- and three-photon absorption when exposed to the irradiation from a Ti:Sapphire laser with a pulse width of 190 fs, wavelength of 840 nm and a pulse repetition rate of 82 MHz [45]. Thus, fluorescence imaging was used as a qualitative tool to show that the microfabricated patterns of avidin and bBSA retained their ability to bind either biotinylated or streptavidin conjugated fluorescence labels after photocrosslinking with the Nd:YAG laser. Of course, the limitation of this simple assay is its inability to prove that the entire protein has been preserved in its native conformation; instead it only shows that the ligand-binding sites of the protein are still functional. Arrays of surface bound concentric squares were fabricated from 400 mg ml^{-1} avidin with 1 mM, 2 mM or 4 mM FMN, from 100 mg ml^{-1} bBSA with 1 mM, 2 mM or 4 mM FMN and from the solution of 100 mg ml^{-1} bBSA and 100 mg ml^{-1} BSA with 1 mM, 2 mM or 4 mM FMN. Each set of squares was crosslinked with a different combination of process parameters (i.e. average laser power and scanning speed). A representative fluorescence image (figure 9) shows that labelled avidin structures (400 mg ml^{-1} avidin with 2 mM FMN) have an emission signal to background ratio as high as of 10:1 over the baseline fluorescence of the negative control

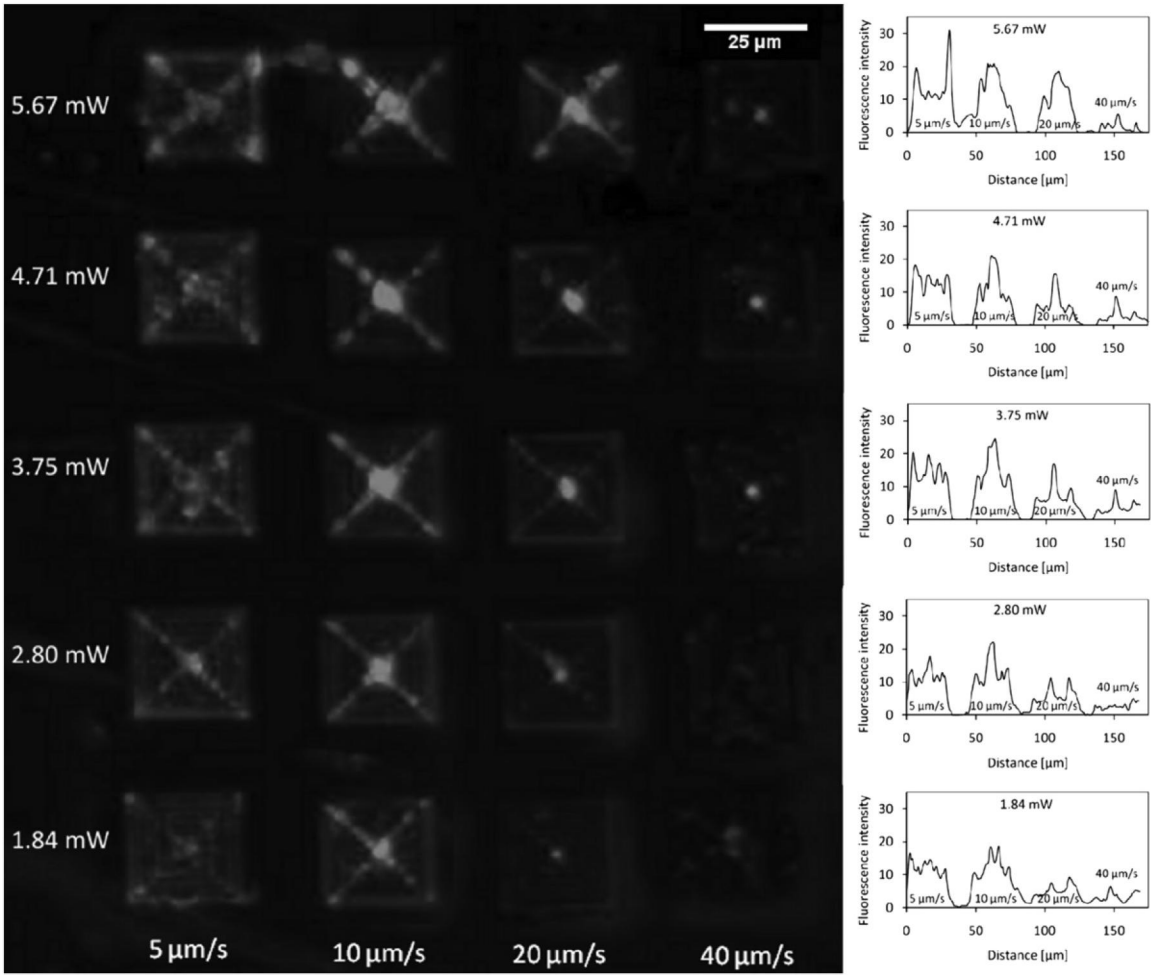

Figure 10. Fluorescence image of an array of square patterns photocrosslinked with the Nd:YAG laser of the solution of 100 mg ml^{-1} bBSA and 100 mg ml^{-1} BSA with 4 mM FMN by varying the laser power and scanning speed and subsequently stained with the DyLight® 649 Streptavidin conjugate. The corresponding fluorescence intensity surface plots are also presented. The data were collected using an exposure time of 7.00 s without binning.

of BSA labelled with DyLight® 649 Streptavidin conjugate. The strong fluorescence implies that the crosslinked avidin was not significantly denatured during the fabrication process and retained its ability to bind biotinylated molecules. Also, the corresponding surface plot profiles of the fluorescence intensities were determined for square patterns fabricated by varying the average laser power and the scanning speed. The intensity plots reveal that the biotin binding capacity of avidin fabricated with a scanning speed of 5 μm s^{-1} diminished approximately 80% as the laser power decreased from 6.09 mW to 0.71 mW. Thus the decrease in the utilized average laser power resulted in a lower amount of crosslinked protein and less available biotin binding sites in the avidin structure. Similarly, the increase in scanning speed from 5 μm s^{-1} to 40 μm s^{-1} as the laser power remained at 6.09 mW attenuated the immobilization of the biotin about 80%.

As expected, avidin patterns photocrosslinked of 400 mg ml^{-1} avidin with only 1 mM FMN expressed lower biotin binding capacity and thus lower fluorescence intensities than the ones fabricated from avidin with 2 mM FMN (data not shown). For example, the pattern crosslinked of the protein solution with 1 mM FMN with the laser power of 6.09 mW and scanning speed of 5 μm s^{-1} had 46% lower fluorescence intensity than the corresponding square pattern fabricated from the avidin with 2 mM FMN. This is a consequence of the lower amount of protein incorporated in the patterns due to the lower photosensitizer concentration. Also, the biotin binding capacity of the avidin structures fabricated with 1 mM FMN varied as a function of the laser power and scanning speed as already detected for avidin patterns crosslinked with 2 mM FMN. The fluorescence intensity diminished by 68% as the laser power decreased from 6.09 mW to 0.71 mW and the scanning speed was kept at 5 μm s^{-1}, and by 53% as the scanning speed increased from 5 μm s^{-1} to 20 μm s^{-1} at the average laser power of 6.09 mW. Similar fluorescence assay has been previously performed by Kaehr *et al* for avidin (400 mg ml^{-1}, no additional photosensitizer) photocrosslinked with a frequency-doubled (532-nm) Nd:YAG laser with a pulse width of ~600 ps [14]. They demonstrated that avidin matrices fabricated using an average laser power of 1.7 mW and a scanning speed of 5 μm s^{-1} retained their biotin binding capacity and showed fluorescence emission at least tenfold more intense than the negative BSA control. Hence, the ratio of emission of the labelled avidin to the baseline

fluorescence of BSA detected by Kaehr *et al* is same as the emission ratios observed by us. AFM measurements of the stiffness of cantilevers fabricated of avidin with a Ti:Sapphire laser operated at 730–740 nm have also indirectly proven the sustainment of the biotin binding ability of these avidin matrices [46]. However, the effect of average laser power, scanning speed and photosensitizer concentration on ligand-binding ability of the avidin–biotin complex photocrosslinked with a Nd:YAG laser with a pulse duration as long as 800 ps is reported here for the first time.

The square patterns photocrosslinked of 100 mg ml^{-1} bBSA with 1–4 mM FMN contained too little protein to efficiently bind the streptavidin conjugated label. Thus, relatively low fluorescence intensity values were detected especially for the patterns fabricated with a low laser power or high scanning speed (data not shown). An example of a fluorescence image of the surface patterns photocrosslinked of the mixture of 100 mg ml^{-1} bBSA and 100 mg ml^{-1} BSA with 4 mM FMN is presented in figure 10. Although some inconsistent variation of the intensities can be seen in the plots, generally the streptavidin binding capacity of the biotinylated BSA structures was decreased as the average laser power was lowered or the scanning speed was raised. For example, the fluorescence intensity diminished by 47% as the laser power decreased from 5.67 mW to 1.84 mW and the scanning speed was kept at 5 $\mu m\ s^{-1}$, and by 82% as the scanning speed increased from 5 $\mu m\ s^{-1}$ to 40 $\mu m\ s^{-1}$ at the average laser power of 5.67 mW. Overall, these fluorescence intensity plots demonstrate that the biotinylated BSA also retains its capability to bind avidin after the fabrication process. This is supported by the fact that if extensive thermal damage occurred during the polymerization, less binding of the streptavidin conjugated label would be expected at higher values of the laser power and at lower values of the scanning speed, which was not the case according to the figure 10. The effect of laser intensities and scan speeds on avidin–biotin complex formation has also been investigated by Seidlits *et al* with a femtosecond Ti:Sapphire laser tuned to 740 nm [34]. According to their observations, the amount of Neutravidin bound by the bBSA matrix (200 mg ml^{-1}) can be adjusted over at least a 3.5-fold range by varying the laser intensity and scanning speed during the fabrication process. These findings are in good accordance with our results, which show that the amount of bound DyLight® 649 Streptavidin conjugate can be controlled about 1.9-fold with the laser power and 5.5-fold with the scanning speed.

4. Conclusions

The experiments reported here demonstrate that sub-micrometer and micrometer scale structures can be fabricated by photocrosslinking avidin, biotinylated BSA and BSA via multiphoton excited photochemistry using the non-toxic biomolecule FMN as a photosensitizer. However, it was observed that with the Nd:YAG laser, avidin could be crosslinked into uniform surface patterns only at a protein concentration of 400 mg ml^{-1} and by utilizing scanning speed of either 5 or 10 $\mu m\ s^{-1}$. Instead, bBSA and BSA could also be efficiently crosslinked into surface patterns at a concentration of 200 mg ml^{-1} and with scanning speeds of 5, 10 and 20 $\mu m\ s^{-1}$. Most importantly, by comparing the results obtained with the Nd:YAG picosecond and Ti:Sapphire femtosecond lasers, this study shows that comparable resolution and surface characteristics can be achieved with both laser sources. Although both lasers required the utilization of quite slow scanning speeds, the Ti:Sapphire laser was able to crosslink uniform protein patterns even with a tenfold faster scanning speed than the low-repetition-rate Nd:YAG laser. However, the inexpensive and compact Nd:YAG microlaser should be considered as an alternative choice for the fabrication of protein microstructures that could be utilized as chemical and topographical cues for cells. Furthermore, the retention of the avidin–biotin complex formation after the exposure to the high laser intensities from the Nd:YAG laser was shown via fluorescence imaging of protein surface patterns immobilized with biotinylated or streptavidin-conjugated fluorescence labels. Also, the biotin or streptavidin binding capacity of the protein patterns was demonstrated to vary depending on the average laser power or scanning speed. The fabrication process based on the Nd:YAG laser requires further optimization due to the observed pattern collapse due to the high aspect ratio. In the future, the fabrication efficiency could be improved by using higher protein concentrations and a photosensitizer with a larger 2PA cross-section or higher quantum yield. Also, an objective lens with higher numerical aperture and multipath scanning method could be utilized to improve the mechanical strength of the protein microstructures.

Acknowledgments

The work was funded by the TEKES (the Finnish Funding Agency for Technology and Innovation) FinNano research program, the Finnish Foundation for Technology Promotion and the Finnish Cultural Foundation. Part of this work was supported by LaserLab Europe (ULF-FORTH001589) and FP7 European Network of Excellence for Biophotonics (photonics4life, 224 014). The authors would like to acknowledge Niina Ahola for AFM imaging, Vuokko Heino for SEM imaging as well as Jenni Leppiniemi and Vesa Hytönen for guidance and for supplying the proteins. We are also grateful to Mrs Aleka Manousaki for expert technical assistance with SEM.

References

[1] Narayan R J, Doraiswamy A, Chrisey D B and Chichkov B N 2010 Medical prototyping using two photon polymerization *Mater. Today* **13** 42–8

[2] LaFratta C N, Fourkas J T, Baldacchini T and Farrer R A 2007 Multiphoton fabrication *Angew. Chem. Int. Ed. Engl.* **46** 6238–58

[3] Drakakis T S, Papadakis G, Sambani K, Filippidis G, Georgiou S, Gizeli E, Fotakis C and Farsari M 2006 Construction of three-dimensional biomolecule structures employing femtosecond lasers *Appl. Phys. Lett.* **89** 144108

[4] Farsari M, Filippidis G and Fotakis C 2005 Fabrication of three-dimensional structures by three-photon polymerization *Opt. Lett.* **30** 3180–2

[5] Farsari M, Vamvakaki M and Chichkov B N 2010 Multiphoton polymerization of hybrid materials *J. Opt.* **12** 124001

[6] Maruo S and Fourkas J T 2008 Recent progress in multiphoton microfabrication *Laser Photon. Rev.* **2** 100–11

[7] Park S H, Yang D Y and Lee K S 2009 Two-photon stereolithography for realizing ultraprecise three-dimensional nano/microdevices *Laser Photon. Rev.* **3** 1–11

[8] Lee K S, Kim R H, Yang D Y and Park S H 2008 Advances in 3D nano/microfabrication using two-photon initiated polymerization *Prog. Polym. Sci.* **33** 631–81

[9] Martineau C, Anémian R, Andraud C, Wang I, Bouriau M and Baldeck P L 2002 Efficient initiators for two-photon induced polymerization in the visible range *Chem. Phys. Lett.* **362** 291–5

[10] Wang I, Bouriau M, Baldeck P L, Martineau C and Andraud C 2002 Three-dimensional microfabrication by two-photon-initiated polymerization with a low-cost microlaser *Opt. Lett.* **27** 1348–50

[11] Liao C, Bouriauand M, Baldeck P L, Leon J, Masclet C and Chung T 2007 Two-dimensional slicing method to speed up the fabrication of micro-objects based on two-photon polymerization *Appl. Phys. Lett.* **91** 033108

[12] Ritschdorff E T and Shear J B 2010 Multiphoton lithography using a high-repetition rate microchip laser *Anal. Chem.* **82** 8733–7

[13] Käpylä E, Turunen S and Kellomäki M 2010 Two-photon polymerization of a polymer-ceramic hybrid material with a low-cost Nd:YAG laser: preliminary resolution study and 3D fabrication *Micro Nanosystems* **2** 87–99

[14] Kaehr B, Ertas N, Nielson R, Allen R, Hill R T, Plenert M and Shear J B 2006 Direct-write fabrication of functional protein matrixes using a low-cost *Q*-switched laser *Anal. Chem.* **78** 3198–202

[15] Iosin M, Stephan O, Astilean S, Duperray A and Baldeck P L 2007 Microstructuration of protein matrices by laser-induced photochemistry *J. Optoelectron. Adv. M.* **9** 716–20

[16] Peltola S, Kellomäki M and Viitanen J 2008 Two-photon polymerization of protein patterns with Nd:YAG pulsed laser *Proc. 27th Int. Conf. on Applications of Lasers & Electro-Optics (ICALEO)* (Temecula, CA: Laser Institute of America) pp 93–8

[17] Engelhardt S, Hu Y, Seiler N, Riester D, Meyer W, Krüger H, Wehner M, Bremus-Köbberling E and Gillner A 2011 3D-microfabrication of polymer-protein hybrid structures with a *Q*-switched microlaser *J. Laser Micro/Nanoeng.* **6** 54–8

[18] Engelhardt S, Hoch E, Borchers K, Meyer W, Kruger H, Tovar G E and Gillner A 2011 Fabrication of 2D protein microstructures and 3D polymer–protein hybrid microstructures by two-photon polymerization *Biofabrication* **3** 025003

[19] Webster A, Britton D, Apap-Bologna A and Kemp G 1989 A dye-photosensitized reaction that generates stable protein-protein crosslinks *Anal. Biochem.* **179** 154–7

[20] Van Steveninck J and Dubbelman T M A R 1984 Photodynamic intramolecular crosslinking of myoglobin *Biochim. Biophys. Acta* **791** 98–101

[21] Balasubramanian D, Du X and Zigler J S 1990 The reaction of singlet oxygen with proteins, with special reference to crystallins *Photochem. Photobiol.* **52** 761–8

[22] Shen H, Spikes J D, Kopeceková P and Kopecek J 1996 Photodynamic crosslinking of proteins: I. Model studies using histidine- and lysine-containing *N*-(2-hydroxypropyl) methacrylamide copolymers *J. Photochem. Photobiol. B. Biol.* **34** 203–10

[23] Shen H, Spikes J D, Kopecková P and Kopecek J 1996 Photodynamic crosslinking of proteins II. Photocrosslinking of a model protein-ribonuclease A *J. Photochem. Photobiol.* B **35** 213–9

[24] Verweij H, Dubbelman T M A R and Van Steveninck J 1981 Photodynamic protein cross-linking *Biochim. Biophys. Acta* **647** 87–94

[25] Dubbelman T M A R, De Goeij A F P M and Van Steveninck J 1978 Photodynamic effects of protoporphyrin on human erythrocytes. Nature of the cross-linking of membrane proteins *Biochim. Biophys. Acta* **511** 141–51

[26] Spikes J D, Shen H, Kopecková P and Kopecek J 1999 Photodynamic crosslinking of proteins: III. Kinetics of the FMN- and Rose Bengal-sensitized photooxidation and intermolecular crosslinking of model tyrosine-containing *N*-(2-Hydroxypropyl)methacrylamide copolymers *Photochem. Photobiol.* **70** 130–7

[27] Shen H, Spikes J D, Smith C J and Kopecek J 2000 Photodynamic cross-linking of proteins: V. Nature of the tyrosine–tyrosine bonds formed in the FMN-sensitized intermolecular cross-linking of N-acetyl-L-tyrosine *J. Photochem. Photobiol.* A **133** 115–22

[28] Xu C, Zipfel W, Shear J B, Williams R M and Webb W W 1996 Multiphoton fluorescence excitation: new spectral windows for biological nonlinear microscopy *Proc. Natl Acad. Sci. USA* **93** 10763–8

[29] So P T C, Dong C Y, Masters B R and Berland K M 2000 Two-photon excitation fluorescence microscopy *Annu. Rev. Biomed. Eng.* **2** 399–429

[30] Huang S, Heikal A A and Webb W W 2002 Two-photon fluorescence spectroscopy and microscopy of NAD(P)H and flavoprotein *Biophys. J.* **82** 2811–25

[31] Wang Y C and Ho C C 2004 Micropatterning of proteins and mammalian cells on biomaterials *FASEB J.* **18** 525–7

[32] Kaehr B, Allen R, Javier D J, Currie J and Shear J B 2004 Guiding neuronal development with in situ microfabrication *Proc. Natl Acad. Sci. USA* **101** 16104–8

[33] Pins G D, Bush K A, Cunningham L P and Campagnola P J 2006 Multiphoton excited fabricated nano and micro patterned extracellular matrix proteins direct cellular morphology *J. Biomed. Mater. Res.* A **78A** 194–204

[34] Seidlits S K, Schmidt C E and Shear J B 2009 High-resolution patterning of hydrogels in three dimensions using direct-write photofabrication for cell guidance *Adv. Funct. Mater.* **19** 3543–51

[35] Basu S, Cunningham L P, Pins G D, Bush K A, Taboada R, Howell A R, Wang J and Campagnola P J 2005 Multiphoton excited fabrication of collagen matrixes cross-linked by a modified benzophenone dimer: bioactivity and enzymatic degradation *Biomacromolecules* **6** 1465–74

[36] Käpylä E, Turunen S, Pelto J, Viitanen J and Kellomäki M 2011 Investigation of the optimal processing parameters for picosecond laser-induced microfabrication of a polymer-ceramic hybrid material *J. Micromech. Microeng.* **21** 065033

[37] Claeyssens F *et al* 2009 Three-dimensional biodegradable structures fabricated by two-photon polymerization *Langmuir* **25** 3219–23

[38] Sakellari I, Gaidukeviciute A, Giakoumaki A, Gray D, Fotakis C, Farsari M, Vamvakaki M, Reinhardt C, Ovsianikov A and Chichkov B N 2010 Two-photon polymerization of titanium-containing sol-gel composites for three-dimensional structure fabrication *Appl. Phys.* A **100** 359–64

[39] Hustad S, McKinley M C, McNulty H, Schneede J, Strain J J, Scott J M and Ueland P M 2002 Riboflavin, flavin mononucleotide, and flavin adenine dinucleotide in human

plasma and erythrocytes at baseline and after low-dose riboflavin supplementation *Clin. Chem.* **48** 1571–7

[40] Hill R T and Shear J B 2006 Enzyme-nanoparticle functionalization of three-dimensional protein scaffolds *Anal. Chem.* **78** 7022–6

[41] Pitts J D, Campagnola P J, Epling G A and Goodman S L 2000 Submicron multiphoton free-form fabrication of proteins and polymers: studies of reaction efficiencies and applications in sustained release *Macromolecules* **33** 1514–23

[42] Sun H B, Tanaka T and Kawata S 2002 Three-dimensional focal spots related to two-photon excitation *Appl. Phys. Lett.* **80** 3673

[43] Nielson R, Kaehr B and Shear J B 2009 Microreplication and design of biological architectures using dynamic-mask multiphoton lithography *Small* **5** 120–5

[44] Basu S, Wolgemuth C W and Campagnola P J 2004 Measurement of normal and anomalous diffusion of dyes within protein structures fabricated via multiphoton excited cross-linking *Biomacromolecules* **5** 2347–57

[45] Hopt A and Neher E 2001 Highly nonlinear photodamage in two-photon fluorescence microscopy *Biophys. J.* **80** 2029–36

[46] Khripin C Y, Brinker C J and Kaehr B 2010 Mechanically tunable multiphoton fabricated protein hydrogels investigated using atomic force microscopy *Soft Matter* **6** 2842–8

Publication III

Turunen, S., Käpylä, E., Lähteenmäki, M., Ylä-Outinen, L., Narkilahti, S. & Kellomäki, M.

Direct laser writing of microstructures for growth guidance of human pluripotent stem cell derived neuronal cells

Journal of Optics and Lasers in Engineering 55(2014)April, pp. 197-204

Optics and Lasers in Engineering 55 (2014) 197–204

Contents lists available at ScienceDirect

Optics and Lasers in Engineering

journal homepage: www.elsevier.com/locate/optlaseng

Direct laser writing of microstructures for the growth guidance of human pluripotent stem cell derived neuronal cells

S. Turunen [a,b,c,*], E. Käpylä [a,b], M. Lähteenmäki [a,b], L. Ylä-Outinen [a,c,d], S. Narkilahti [a,c,d], M. Kellomäki [a,b]

[a] BioMediTech, Institute of Biosciences and Medical Technology, Biokatu 10, 33520 Tampere, Finland
[b] Tampere University of Technology, Department of Electronics and Communications Engineering, PO Box 692, 33101 Tampere, Finland
[c] NeuroGroup, Institute of Biomedical Technology, University of Tampere, 33014 Tampere, Finland
[d] The Science Center of Pirkanmaa Hospital District, PO Box 2000, 33521 Tampere, Finland

ARTICLE INFO

Article history:
Received 5 August 2013
Accepted 1 November 2013

Keywords:
Direct laser writing
Two-photon polymerization
Microstructure
Cell growth guidance
Human pluripotent stem cell derived neuronal cell

ABSTRACT

Studying neural networks *in vivo* is very laborious due to the location and immense complexity of the central nervous system. Therefore, neuronal cell culture models have become important tools to study the development of neuronal networks *in vitro*. We introduce a technique called direct laser writing (DLW) by two-photon polymerization (2PP) as a feasible method for the fabrication of microstructures for studying neuronal cell growth guidance. As human pluripotent stem cells (hPSC) can be differentiated into several cell types, such as neurons, astrocytes, and oligodendrocytes, they are a promising cell source for cell culture models. In this study, three novel designs of neurocage microstructures were fabricated for the first time by 2PP. As a proof of concept, two of the neurocage designs were seeded with hPSC derived neuronal cells to study cell attachment, migration and directed neurite growth. Although the fabricated neurocage structures could not confine the neurons, the preliminary cell culture tests showed that neurons had a tendency to migrate towards the microstructures. In addition, the neurite guidance properties of the structures appeared promising as the neurons inside the cages readily extended their processes along the channels.

1. Introduction

Computer-aided design (CAD) based direct laser writing techniques (DLW) offer a powerful tool for fabricating microscale structures for tissue engineering and regenerative medicine applications. Although traditional DLW techniques, such as UV laser stereolithography and selective laser sintering, are able to fabricate complex 3D structures, they cannot produce submicron features. In contrast, two-photon polymerization (2PP), a pulsed laser light-based rapid prototyping process, enables true 3D direct writing of predesigned structures with features beyond the diffraction limit of light [1,2]. Due to its versatility, 2PP can be used for the fabrication of customized 2D and 3D cell culture matrices, such as microstructures for neural cell growth guidance. Indeed, there exists an obvious need for new efficient methods to study and treat neurodegenerative disorders, such as Alzheimer's and Parkinson's disease, as they affect a significant portion of the world's population leading to either disability or death for almost 30 million individuals worldwide [3]. Due to the location and immense complexity of neural networks, studying these networks *in vivo* is very laborious. Therefore, the development of *in vitro* neuronal cell culture models has become an important tool to study the molecular and cellular mechanisms of central nervous system regeneration [4,5]. One approach to direct neuronal cell migration and neuritogenesis to predefined areas is to use 3D confinement microstructures [6]. Physically confining 3D microstructures, such as square chambers with rectangular channels [6] or cylindrical neurocages with tunnels on microelectrode arrays (MEA) [7–14], have been shown to control the location of neurons and limit the growth of neurites on predefined axes.

The previously reported 3D confinement structures were fabricated photolithographically by using unalterable mask masters, which limits the experimentation with different designs. Multilayer photolithography also requires precise alignment of each subsequent layer, which may result in poor feature resolution. Due to several manual steps, the fabrication process is very laborious and time-consuming. To overcome this limitation, we introduce 2PP as an alternative method for fabricating 3D confinement microstructures. 2PP is an additive process, in which complex structures are constructed according to the predesigned CAD model by moving the laser focus along the scanning path. 2PP is based on the optical phenomenon of two-photon absorption (2PA),

* Corresponding author at: Tampere University of Technology, Department of Electronics and Communications Engineering, PO Box 692, 33101 Tampere, Finland. Tel.: +358 50 301 3375.
E-mail address: sanna.turunen@tut.fi (S. Turunen).

0143-8166/$ - see front matter © 2013 Elsevier Ltd. All rights reserved.
http://dx.doi.org/10.1016/j.optlaseng.2013.11.003

in which the simultaneous absorption of two photons by photoinitiator molecules initiates the polymerization and solidification of a photosensitive resin. Due to the nonlinear intensity dependence of 2PA, the polymerization is localized within the focal volume of the laser beam, which makes 2PP an intrinsically 3D fabrication technique [15,16]. The resolution of 2PP can be tuned by the choice of the focusing optics, exposure time and laser power. With optimal parameters, lateral features below 100 nm can be achieved [17].

Due to the intrinsic ability to produce 3D structures and to process various photosensitive materials, 2PP has been used to fabricate structures for neural tissue engineering applications to study neuronal cell growth and alignment [18]. Biopolymers, such as bovine serum albumin (BSA) and laminin, have been successfully fabricated into low-profile barrier structures to guide the interactions of developing rat brain cortical neurons and neuroblastoma–glioma hybrid cells (NG108-15) in culture [19,20]. Guidance paths of biotinylated BSA functionalized with IKVAV peptides for rat dorsal root ganglion cells (DRGs) and rat hippocampal neural progenitor cells (NPCs) have also been created inside hyaluronic acid hydrogels [21]. Synthetic biodegradable polymers have also recently been used for scaffold fabrication by 2PP. Polylactide-based (PLA) photopolymer has been structured into 3D microstructures with linear guidewires for studying directed growth of NG108-15 and PC12 neuroblastoma cells [22]. Yet in another study, photopolymerizable PLA was used to produce scaffolds composed of hollow cylinders and tested as a substrate for primary rat Schwann cells [23].

Neuronal networks on 2PP guidance structures have previously been studied exclusively with dissociated rat neurons. This is likely due to their wide availability and the existence of a large literature base describing their electrophysiology and methods for cell culture. Nevertheless, human cells are a more relevant model for neurotoxicity studies [24]. Human embryonic stem cell derived neurons [25], human induced pluripotent stem cell derived neuronal cells [26] and human fetal neural stem cell derived cells [27] have been cultured in MEA format and also used in toxicological studies [24]. However, these cell types are difficult to culture and network formation in these cell cultures is random, which causes variation in results. The formation of controlled neuronal networks increases the robustness of the results, which facilitates transition to *in vivo*. In this paper, we present three novel designs for neurocage 3D confinement microstructures which were fabricated by 2PP for the first time. As a proof of concept, two of the neurocage designs were seeded with neuronal cells derived from human pluripotent stem cells (hPSC) and tested for their ability to confine cells onto specific locations and guide cell migration and neurite growth.

2. Experimental

2.1. Neurocage design

The neurocages were designed with the Rhinoceros® 4.0 CAD program (Robert McNeel & Associates, USA) and consisted of so-called nodes and channels. With our design approach, neurocage dimensions such as node diameter, channel width and length, channel angle relative to the node, cage wall height and thickness and the overall number of nodes and channels could be easily modified. We designed three different types of neurocages as shown by Fig. 1. We chose a node diameter of 40 μm so that the nodes could in the future enclose a standard 30 μm in diameter MEA electrode by MultiChannel Systems, for example. The channel width was set to 5 μm in order to ensure that neuronal processes could fit inside the channels. The cage wall height was set to 25 μm.

2.2. Neurocage fabrication by two-photon polymerization

Neurocages were fabricated with a custom-built 2PP set-up that has been previously described in [28]. Briefly, the system was based on a Nd:YAG picosecond laser (PULSELAS-P-1064-300-FC, Alphalas GmbH, Germany) emitting at 532 nm with a pulse duration of 800 ps, maximum frequency of 13 kHz and an average output power of 100 mW. The movement of the laser beam in the *xy*- and *z*-directions was controlled with a fast steering mirror scanner (FSM-300, Newport Corporation, USA) and a piezo-focusing unit (Mipos 250 SGEX, Piezosystem Jena GmbH, Germany) respectively. The beam was directed through an upright microscope frame (ECLIPSE ME 600, Nikon, Japan) to a 50× oil immersion objective (NA=0.90). The laser exposure was controlled with a fast electronic shutter (Oriel 76992, Newport Corporation, USA) and the output power was attenuated to a suitable average polymerization power of approximately 1 mW measured at the back aperture of the objective.

As the photopolymerizable material, a commercial polymer–ceramic hybrid material Ormocomp® (Micro resist technology GmbH, Germany), was used in combination with 2 wt% (w/w) of the photoinitiator Irgacure® 127 (Ciba Specialty Chemicals, Switzerland). ORMOCER® materials, such as Ormocomp®, have been shown to be noncytotoxic and biologically inert materials in several studies [29–31]. Also, in our previous study with hPSC derived neuronal cells on UV-cured Ormocomp® films, we showed that the material–initiator combination did not substantially impair with cell attachment and viability, and is thus suitable for cell growth guidance purposes [32]. A drop of Ormocomp® was sandwiched between a microscope slide and a coverslip separated by 150 μm thick stainless steel spacer. For 2PP, the neurocage models were sliced into contours in the *z*-direction in Rhinoceros®. The contour spacing was set to 1.0 μm. Neurocages were then polymerized by scanning the laser beam according to the contour coordinates with an average laser power of 0.98–1.43 mW and scanning speed of 120 μm/s. The cages were fabricated using the multipath scanning method developed by Yang et al. [33], *i.e.*, the cage walls were formed by two sets of contours separated by a distance of 1 μm. After the polymerization, the non-illuminated Ormocomp® was removed by immersing the samples in Ormodev® solvent (Micro resist technology GmbH) for approximately 3–15 min and by rinsing with either 2-propanol (Labscan Ltd, Ireland) or hexamethyldisilazane (HMDS, Sigma-Aldrich Finland Oy, Finland).

In addition to untreated microscope slides, slides coated with a dielectric layer of spin-on glass were tested as a substrate material for neurocage fabrication. This polysiloxane-based liquid material (IC1-200, Futurrex, Inc., USA) was spin-coated on glass slides at 3000 rpm for 40 s. The samples were then baked on a hot plate at 100 °C for 60 s and at 200 °C for 60 s to drive away the casting solvent. To fully establish the crosslinking, samples were annealed in a furnace at 400 °C for 30 min under ambient atmosphere. To test the compatibility of the spin-on glass film with the 2PP fabrication process, type I and type II neurocages were polymerized on it with an average laser power of 1.03 mW and scanning speed of 120 μm/s.

For the cell culture experiment, four parallel samples with four or six pieces of type I neurocages and four samples with four pieces of type III neurocages were polymerized on microscope glass slides and subsequently disinfected with 70% (v/v) ethanol for 15 min. Additionally, all samples with type I neurocages were also immersed in Dulbecco's phosphate buffered saline (DPBS, Lonza Group Ltd, Switzerland) for approximately 65 h.

2.3. SEM imaging of neurocages

For SEM imaging, the samples were sputter coated with gold for 180 s in an argon atmosphere to a nominal thickness of 113 nm

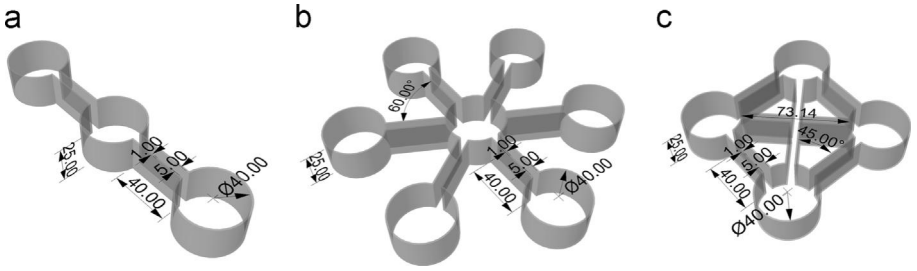

Fig. 1. Neurocage designs: (a) type I, (b) type II and (c) type III. The dimensions are given in microns.

(S 150 Sputter Coater, Edwards Ltd, UK). The imaging was performed with a Philips XL-30 (Philips Electron Optics, the Netherlands) scanning electron microscope with an accelerating voltage of 12 kV. The SEM images were analyzed with free GIMP 2.8 software.

2.4. Application of laminin

In order to provide essential attachment points for neurons, the glass surfaces were coated with laminin, a key glycoprotein component of the ECM. The laminin was applied with a semi-automatic microinjection system consisting of the joystick-controlled MANiPEN micromanipulator (developed at the Department of Automation Science and Engineering, Tampere University of Technology, Finland), a pressure injector (MPPI-2, Applied Scientific Instruments, USA), a vision system (a Nikon Eclipse TS100F inverted microscope, Nikon Corporation, Japan) and a software [34]. In this study, capillaries with tip diameters of approximately 5 or 10 μm were attached to the micromanipulator. The neurocages on the sample were located under the microscope and the nodes were filled with laminin solution by carefully moving the capillary tip over the neurocages. Solution of 50 μg/ml laminin (Sigma-Aldrich Finland Oy) in DPBS was applied with injection pressure of 150 mbar and a pressure pulse of 6000 ms. In order to prevent the crystallization of the laminin, a humidified atmosphere was created by placing the samples in a hot water bath for the application phase. After the application of laminin, samples were kept at +4 °C overnight to enable proper coating of the glass surface inside the neurocages.

2.5. Differentiation of neuronal cells and disaggregation of neurospheres

The neuronal cells used in this study were derived from human embryonic stem cell lines Regea 08/023 and Regea 06/040. Institute of Biomedical Technology has the ethical approval from Pirkanmaa Hospital District to derivate, culture, and differentiate the hPSCs (Skottman, R05116), as well as a permission for human stem cell research from the National Authority for Medicolegal Affairs (Valvira, 1426/32/300/05). The differentiation of neuronal cells was performed as described previously by Lappalainen et al. [35]. Briefly, the hPSC colonies were mechanically dissected into smaller pieces and cultured as flowing aggregates in neural differentiation medium (0NDM) containing 1:1 Dulbecco's modified Eagle's Medium/F12 (Gibco, Invitrogen, Finland) and Neurobasal Medium supplemented with 2 mM GlutaMax, 1 × B27, and 1 × N2 (all from Gibco), 20 ng/ml basic fibroblast growth factor (bFGF, R&D Systems, Minneapolis, USA), and 25 μg/ml penicillin/streptomycin (Lonza Group Ltd, Switzerland). In the suspension culture, cell aggregates formed neurospheres. The medium was changed three times a week and the spheres were mechanically passaged once a week. Neurospheres were cultured for a total of 7–9 weeks to gain a pure neuronal population.

After differentiation, the cells were enzymatically dissociated into single cell suspension either with TrypLE™ Select (Invitrogen, Finland) or with trypsin (Trypsin-Versene 10 × stock solution, 5 mg/ml trypsin, Lonza Group Ltd, Switzerland) diluted in DPBS to a 1 × working solution. For TrypLE disaggregation, the neurospheres were suspended in 100 μl of TrypLE™ Select and incubated for 15 min during which the suspension was aspirated twice. After incubation, the suspension was aspirated with 1 ml of 0NDM. For trypsin disaggregation, the neurospheres were suspended in 100 μl of 10 μg/ml trypsin solution and incubated for 5 min. Afterwards, the suspension was aspirated with 1 ml of 5% (v/v) human serum (PAA Laboratories GmbH, Austria) in DPBS. The suspension was centrifuged (200 G, 5 min) and the supernatant was removed.

2.6. Application of cell suspension and cell culture

The cell suspension was prepared by diluting the dissociated cells in 0NDM at a density of 1×10^6 cells/ml and filtering the suspension with a 70 μm Falcon filter (Becton Dickinson OY, Finland). A drop of suspension with approximately 1×10^5 cells was applied on the samples by injecting it atop the neurocages. After application, the cells were let to settle into the structures for about 15 min, after which the samples were stored in an incubator. For cells in type I neurocages, conditioned 0NDM was added to enhance the viability of the small neuronal cell population. Two days later, 0NDM was replaced with 5+NDM [0NDM with 4 ng/ml bFGF and 5 ng/ml brain derived neurotrophic factor (BDNF, Gibco, Invitrogen, Finland)] and conditioned medium (only for samples with type I neurocages). Cells were cultured for a total of five days (type I neurocages) or eight days (type III neurocages) and the medium was changed three times a week. The attachment and migration of cells was monitored by light microscope (Olympus IX51 or Olympus CK2, Olympus Corporation, Japan) in bright field mode after 2 and 3 days of culture with type I neurocages and 4 and 6 days of culture with type III neurocages.

2.7. Immunocytochemical staining

Immunocytochemical staining was conducted as previously described [35]. Briefly, cells were fixed with 4% paraformaldehyde (Sigma-Aldrich, Finland) for 20 min. Thereafter, cells were rinsed twice with DPBS, blocked with 10% of normal donkey serum, 0.1% of Triton-X 100 and 1% of bovine serum albumin (BSA) (all from Sigma-Aldrich) in DPBS for 45 min at room temperature. After blocking, the samples were washed once with primary antibody solution containing 1% of normal donkey serum, 0.1% of Triton-X and 1% of BSA in DPBS. Next, the primary antibodies, rabbit anti-microtubule associated protein (MAP-2, 1:600, Millipore, USA) and sheep anti-human glial fibrillary acidic protein (GFAP, 1:800, R&D Systems, USA), were incubated with the cells at 4 °C overnight. On the following day, the cells were washed three times with secondary antibody solution containing 1% BSA in DPBS and incubated for 1 h at room temperature with secondary antibodies: Alexa Fluor-488 donkey anti-rabbit and Alexa Fluor-568 donkey anti-sheep (all 1:400, Invitrogen, USA). The samples were then washed three times with DPBS and two times with phosphate

buffer (pH 7.0, 0.1 M, Sigma-Aldrich), and mounted with Vectashield Mounting Medium for Fluorescence with 4′,6-diamidino-2-phenylindole (DAPI, Vector Laboratories, USA). The samples were immediately viewed and imaged with an Olympus microscope (IX51, Olympus) equipped with a fluorescence unit.

3. Results

3.1. Neurocage fabrication by 2PP

Several of the first fabricated neurocage structures suffered from collapse of the upper parts of the channel walls during the post-fabrication development phase (Fig. 2(a)). The phenomenon is caused by the evaporation of the rinse solvent, 2-propanol, which generates a pulling force on the walls and binds them together. As the effect of the collapse force can be reduced by using a rinsing liquid with lower surface tension [36], 2-propanol was replaced with HMDS in the subsequent experiments with improved results as illustrated in Fig. 2(b).

To minimize the polymerization time of the neurocages while still obtaining relatively smooth surface texture, scanning speed of 120 μm/s was chosen for the fabrication of the structures. It was observed that higher scanning speeds led to more pronounced surface roughness (data not shown). The surface texture of the cages fabricated with the scanning speed of 120 μm/s was evaluated from the SEM images taken with a tilt angle of 60° (Fig. 3) by measuring the width of the ridges (highlighted with arrows in Fig. 3(b)). With this method of measurement, the polymerized neurocages had an average surface feature size of 680 nm ± 60 nm. By scanning the laser beam at 120 μm/s, the polymerization of a type I neurocage (Fig. 4(a)) took approximately 5 min, type II (Fig. 4(b)) 25 min and type III (Fig. 4(c)) 21 min.

Also, the type I and II neurocages were successfully fabricated on slides coated with dielectric layer of spin-on glass as shown in Fig. 5. Although the structures were polymerized relatively accurately on the spin-on glass film, some microbubbling, likely resulting from the absorption of the laser radiation by the dielectric film, was observed during the scanning of the layers nearest the substrate surface.

The fabrication accuracy of neurocages with the 2PP set-up was evaluated by examining type III neurocages with SEM and by comparing the measured dimensions with the original CAD design. The neurocage node diameter, channel length, channel width and wall thickness were measured from the top view (0° tilt), and wall height from the side view (90° tilt) SEM images. Table 1 presents the results in comparison to the dimensions of the CAD design.

3.2. Application of laminin

The laminin solution was applied successfully into the type I neurocages with the MANiPEN micromanipulator, which enabled easy three-dimensional navigation of the capillary and precise injection of the laminin solution into the neurocages due to the accurate pressure regulation (see Supplementary video). Initially, the very small volume of laminin solution caused rapid evaporation of water from the suspension leaving crystallized laminin and other solutes into the nodes of the neurocages. However, the introduction of a hot water bath dish for the application phase provided a humidified atmosphere and solved the crystallization issue. The application of laminin into the nodes of type III neurocages was found more complicated than into type I neurocages. The laminin solution appeared to evaporate or otherwise disappear from the nodes although no crystallization of the protein was observed. Thus, the solution had to be added several times to each node and the repeated injection with a capillary tip distorted some of the neurocage structures.

3.3. Cell attachment, migration, orientation and identification of phenotype

Type I and type III neurocages were seeded with hPSC derived neuronal cells to study the cell attachment, migration and directed

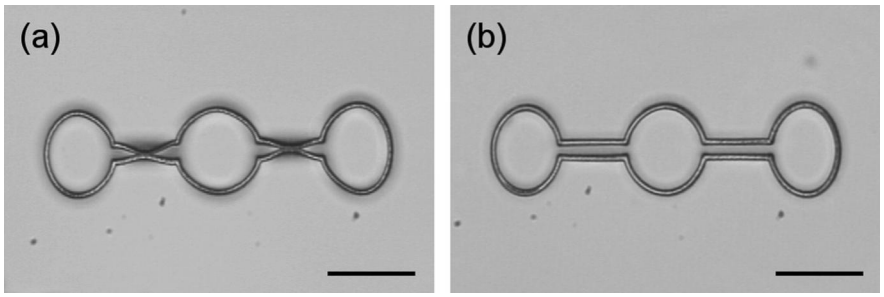

Fig. 2. Bright field micrographs of type I neurocages rinsed with (a) 2-propanol resulting in collapse of the channels, and (b) HMDS resulting in intact channel walls. The scale bars represent 50 μm.

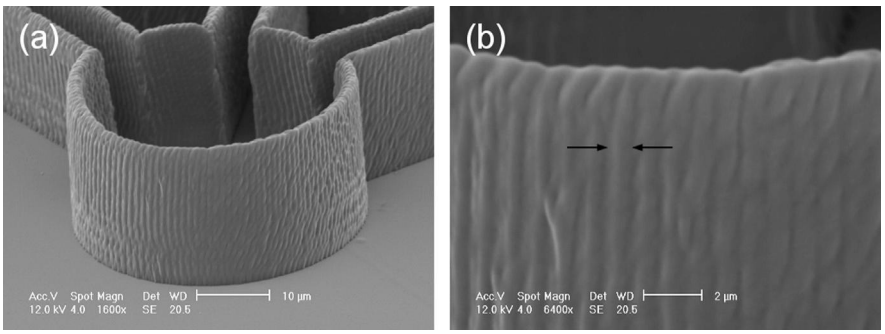

Fig. 3. (a) SEM image of the corner node from a type III neurocage fabricated with a scanning speed of 120 μm/s and (b) a close-up of the surface texture of the wall. The arrows point out the method of measuring the width of the ridges. The images have been taken from a 60° tilt and the scale bars are 10 μm in (a) and 2 μm in (b).

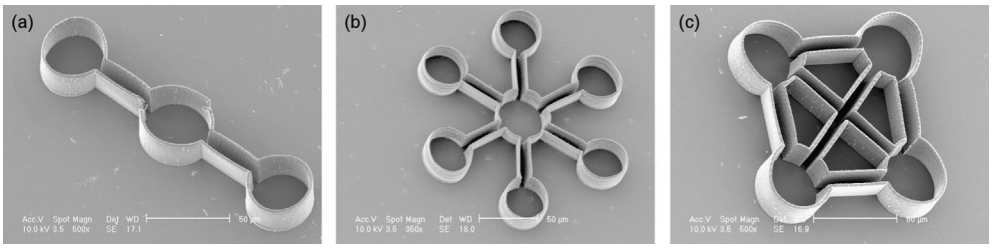

Fig. 4. SEM images of neurocages fabricated on untreated microscope slides with a scanning speed of 120 μm/s: (a) type I, (b) type II and (c) type III. The images show the neurocages from the tilt angle of 30° and the scale bars represent 50 μm.

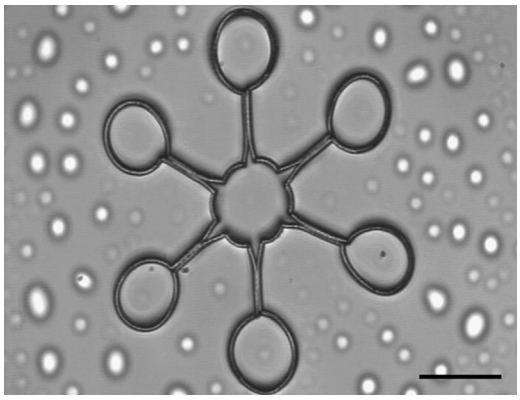

Fig. 5. A bright field micrograph of a type II neurocage polymerized on a dielectric layer of spin-on glass. The scale bar represents 50 μm.

Table 1
Dimensions of type III neurocage as defined in the CAD design and measured from the SEM images. The measured data represents the mean ± standard deviation of 8 measurements.

	CAD design [μm]	Measured dimensions [μm]	Deviation [%]
Node diameter	40	36.2 ± 0.9	9.5 ± 2.3
Channel length	40	41.7 ± 0.6	4.2 ± 1.5
Channel width	5	3.7 ± 0.6	25.1 ± 12.2
Wall thickness	1	2.0 ± 0.2	98.1 ± 15.3
Wall height	25	19.4 ± 0.4	22.3 ± 1.7

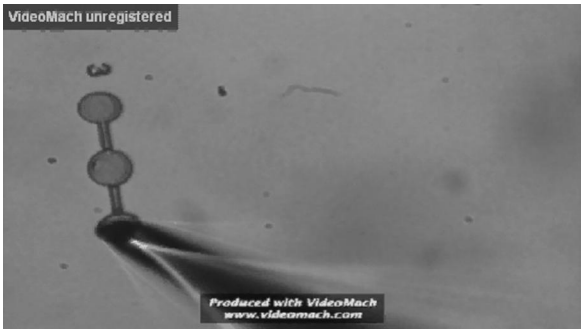

Video S1. Application of laminin solution into a type I neurocage with a semi-automatic microinjection system. A video clip is available online. Supplementary material related to this article can be found online at http://dx.doi.org/10.1016/j.optlaseng.2013.11.003.

growth on these samples. The initial cell attachment and migration on the samples containing type I neurocages was evaluated qualitatively with bright field microscopy after two and three days in culture (Fig. 6). It was observed that the cells attached readily onto the samples and formed elaborate networks after 2 days in culture. During the 5 days *in vitro* culture, the cells were found to migrate towards and into the neurocages. Furthermore, when the cells attached to the laminin-coated surface inside the cages, they often extended their neurites along the channels connecting the nodes (Fig. 6). However, it was also evident that the neurocages were not able to restrict the cell growth to the area inside the cage walls as cells also grew successfully outside the neurocages even without the laminin coating (Fig. 6). This result was also confirmed by immunostaining.

Judging by the immunostaining of the cells against MAP-2 (for neuronal cells, stained green) and GFAP (for glial cells, stained red), majority of the cells were MAP-2 positive, indicating neuronal phenotype. Similar to the bright field microscope images, the immunostained images showed cells extending processes towards the neurocage structures and some neurites aligned along the exterior walls of the neurocages (Fig. 6). Interestingly, the cells also migrated into the neurocages from the small gaps formed in the cage walls.

The attachment and migration of cells in type III neurocages was followed by bright field imaging the samples after four and six days in culture (Fig. 7). During the first four days in culture, mainly unattached cell aggregates were present on all the samples. The immunocytochemical staining of the cells after eight days in culture showed that there were viable neuronal cells on the samples and even entwined processes of several neurons as shown in Fig. 7. However, it was impossible to determine from the immunofluorescence images whether the neurites were actually attached to the bottom of the neurocages or were just migrating on top of the cage walls.

4. Discussion

In this study, we introduced direct laser writing (DLW) by two-photon polymerization (2PP) as a feasible technique for fabricating physical confinement microstructures from a photosensitive polymer–ceramic hybrid material Ormocomp®. Three different models of neurocage microstructures were designed and successfully fabricated on microscope slides as well as on a spin-on glass insulation layer. The initial problems concerning the collapse of the channel walls at the post-fabrication development phase were largely solved by replacing the 2-propanol with HMDS as rinsing solvent. Rare cases of channel collapse with HMDS, such as in Fig. 5, were most likely due to manual errors made in the development procedure, such as allowing the Ormodev® solvent to evaporate before replacement with HMDS.

The fabricated neurocages were characterized *via* SEM imaging and the measured dimensions were compared to CAD data in order to evaluate the fabrication accuracy. The node diameter and the channel length retained their dimensions well, having only 9.5% and 4.2% deviation from the original CAD models respectively. The width of the channels and the thickness of the walls deviated significantly from the CAD dimensions (25.1% and 98.1% respectively), which can be explained by the fabrication of the structures with the multipath scanning method with 1 μm distance between the two contours. The doubling of the wall thickness compared to the CAD model is thus a direct result from the scanning of the two separate paths. Furthermore, the increased wall thickness narrowed down the channels on each side, which explains the diminished channel

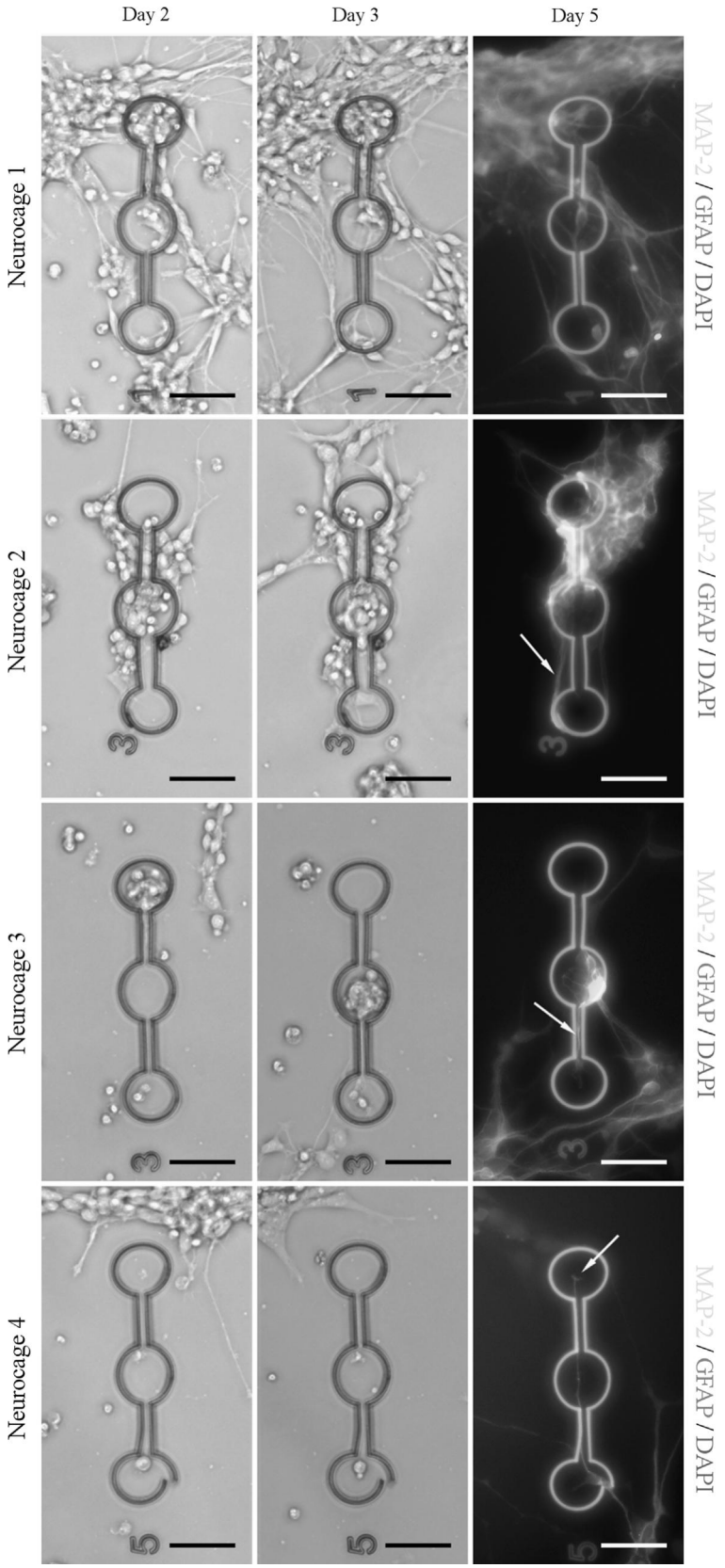

Fig. 6. Bright field and immunostained micrographs of four parallel neurocages after 2, 3 and 5 days in culture. Neuronal cells are stained green (MAP-2) and astrocytes red (GFAP). Cell nuclei were counterstained blue with DAPI. The neurocages appeared in red due to nonspecific binding of the stains on the structures. Neurites oriented along the exterior of neurocage 2, a neurite oriented along a channel in neurocage 3 and a sprouting growth cone in neurocage 4, are highlighted with arrows. Scale bars represent 50 μm.

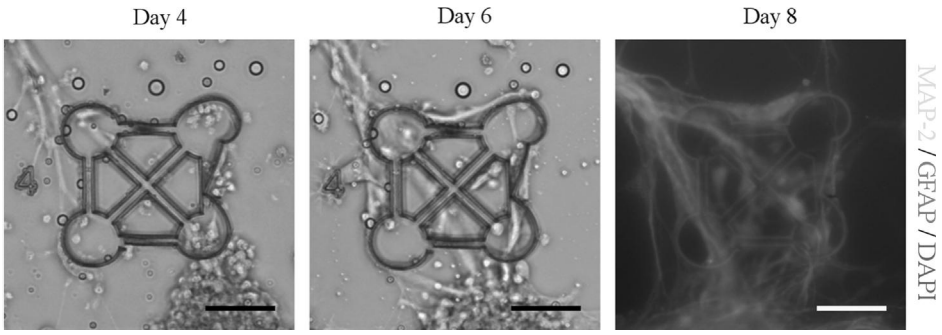

Fig. 7. Bright field and immunostained micrographs of type III neurocage after 4, 6 and 8 days in culture. Neuronal cells are stained green (MAP-2) and astrocytes red (GFAP). Cell nuclei were counterstained blue with DAPI. The neurocage appeared in red due to nonspecific binding of the stains on the structures. Scale bars represent 50 μm.

width. The polymerized neurocages also deviated from the original design in the *z*-direction as the wall height had shrunk 22.3% on average. This is a result of a common issue related to the polymerization of negative tone photoresists, such as Ormocomp® [37]. If the structuring is performed slightly above the 2PP threshold intensity, the polymerization yield is not 100%. Hence, after the removal of the unpolymerized material, a sponge-like material is left behind. The collapse of the material at the molecular level leads to distortion of the structure due to shrinkage [38]. The shrinkage of approximately 22% in the wall height is in good accordance with previously published results for organically modified ceramics, which have shown that photonic crystals [37] and scaffolds [39] fabricated of Ormocomp® can shrink laterally up to 24%. In the future, this material shrinkage could be taken into account by scaling up the wall height in the CAD design with a compensation factor.

Two of the neurocage designs (types I and III) were chosen to be tested with cells as they were also the fastest to fabricate. The scanning speed of 120 μm/s was chosen for the fabrication since it produced smooth enough surface texture and allowed the polymerization of a single type I neurocage in just 5 min. We demonstrated the suitability of these neurocage designs for neuronal cell growth guidance by a proof-of-concept cell culture experiment with hPSC derived neuronal cells. The most crucial property of neuronal cells is their ability to form functional neuronal networks capable of electrical signaling. Hence, the development of *in vitro* culture models for studying the network formation and electrophysiological properties of neuronal cells is important. Although the two-photon polymerized neurocages reported here are ultimately aimed to be incorporated onto MEA platforms, in this study, no electrodes were incorporated on the samples. However, with proper modifications, the neurocages fabricated by 2PP are adaptable to a glassy insulation layer on a microelectrode array. This was also demonstrated in our study *via* successful polymerization of neurocages on a spin-on glass insulation layer.

Although two-photon polymerized structures, such as low-profile barrier structures [19,20], guidance paths [21] and scaffolds [22,23], have previously been used in neuronal cell guidance studies, to the best of our knowledge, we have for the first time cultured hPSC derived neuronal cells with 2PP-fabricated 3D confinement microstructures. In addition, this is also the first study to report the fabrication of neurocage structures by high-resolution, maskless 2PP instead of more conventional photolithographic methods requiring the deposition of multiple sacrificial layers and etching. Biologically, the neurocages were assessed in reference to their ability to support neuronal cell attachment, migration and orientation by light microscopy and immunocytochemical staining. The cells were applied on the samples by injecting the cell suspension into the cell culture medium, which resulted in random quantities of cells inside the neurocages between the parallel samples. However, during the first few days in culture, the cell count inside the cages levelled off due to the continuous migration of cells in and out of the structures.

Surprisingly, the meticulous application of laminin with the micromanipulator inside the neurocage nodes did not appear to have the anticipated influence of restricting the cell growth only inside the neurocages. Instead, the cells proliferated successfully outside the neurocages even without the laminin coating, which has been considered as a necessity for their adhesion on surfaces. On the other hand, the formation of complex neuronal networks only after two days in culture (Fig. 6), suggests that the use of conditioned medium had a definite effect on the viability of the cells on the samples containing type I neurocages. Indeed, the cells cultured in type III neurocages without the conditioned medium preferred to stay as aggregates and did not sprout processes and form networks as readily as in type I neurocages with conditioned medium. Thus, such small cell populations need additional growth factor supply provided by conditioned medium as also suggested by Erickson and co-workers [7].

Overall, the cell confining properties of the neurocages were found insufficient, as the cells were able to migrate freely in and out of the structures. Apparently, the height of the walls (19.4 μm) was not high enough to prevent the cells climbing in and out of the structures. The appropriate wall height for cell confinement has not been thoroughly studied for human stem cell derived neuronal cells, but Béduer et al. have reported that most of the cultured primary adult human neural stem cells stayed inside microchannel grooves having a wall height of 25 μm [40]. Despite the confinement issue, the preliminary cell culture tests showed that neurons had a tendency to migrate towards the neurocages and even make their way into the structures through small openings in the walls. In addition, the neurite guidance properties of the structures appeared quite promising as the neurons inside the cages readily extended and oriented their processes along the edges and channels of the structures. Hence, the neurite guidance capabilities of the neurocages shown in this study represent a basic but yet an important step towards designing more sophisticated structures for the manipulation of the migration and neuritogenesis of hPSC derived neuronal cells to a predefined direction.

5. Conclusions

In this study, we introduced direct laser writing (DLW) by two-photon polymerization (2PP) as a feasible method for fabricating physically confining 3D microstructures called neurocages. Three novel versions of these neurocage microstructures were designed and successfully fabricated from Ormocomp® hybrid polymer–ceramic material with relatively good fabrication accuracy with respect to the original CAD models. In addition to untreated glass,

the neurocages could also be fabricated on a spin-on glass insulation layer. The cell culture experiment with two neurocage designs demonstrated that the neurocages supported the growth of hPSC derived neuronal cells. Also, the lack of efficient cell confinement properties was to an extent compensated by the observed ability of the fabricated neurocages to attract the cells. Furthermore, the neurite guidance properties of the cages were proven adequate as the cells readily extended their neurites along the tunnels and nodes of the structures. Thus, by implementing some changes to the designs, the neurocage structures could in the future be incorporated to MEA platforms to create small neuronal networks to study the network formation and function.

Acknowledgments

The study was funded by the Academy of Finland (StemFunc project), the TEKES (the Finnish Funding Agency for Technology and Innovation), the Finnish Foundation for Technology Promotion and the Finnish Cultural Foundation. The authors would like to acknowledge Prof. Jouko Viitanen for 2PP set-up expertise and M.Sc. (Eng.) Vuokko Heino and M.Sc. (Eng.) Taru Karhula for SEM imaging. We are also grateful to Prof. Pasi Kallio from the Department of Automation Science and Engineering at TUT for allowing us to access the micromanipulator set-up and to M.Sc. (Eng.) Juha Hirvonen for guidance with the apparatus.

References

[1] Gittard SD, Koroleva A, Nguyen AK, Fadeeva E, Gaidukeviciute A, Schlie-Wolter S, et al. Two-photon polymerization microstructuring in regenerative medicine. Front Biosci (Elite Ed) 2013;5:602–9.
[2] Raimondi MT, Eaton SM, Nava MM, Laganà M, Cerullo G, Osellame R. Two-photon laser polymerization: from fundamentals to biomedical application in tissue engineering and regenerative medicine. J Appl Biomater Biomech 2012;10:56–66.
[3] Chong ZZ, Shang YC, Wang S, Maiese K. Shedding new light on neurodegenerative diseases through the mammalian target of rapamycin. Prog Neurobiol 2012;99:128–48.
[4] Horner PJ, Gage FH. Regenerating the damaged central nervous system. Nature 2000;407:963–70.
[5] Wyart C, Ybert C, Douarche C, Herr C, Chatenay D, Bourdieu L. A new technique to control the architecture of neuronal networks *in vitro*. In: Poindron P, Piguet P, Förster E, editors. New methods for culturing cells from nervous tissues. Basel: Karger Publishers; 2005. p. 23–57.
[6] Francisco H, Yellen BB, Halverson DS, Friedman G, Gallo G. Regulation of axon guidance and extension by three-dimensional constraints. Biomaterials 2007;28:3398–407.
[7] Erickson J, Tooker A, Tai YC, Pine J. Caged neuron MEA: a system for long-term investigation of cultured neural network connectivity. J Neurosci Methods 2008;175:1–16.
[8] Maher M, Wright J, Pine J, Tai Y. Microstructure for interfacing with neurons: the neurochip. In: Chang HK, Zhang YT, (Eds.). Proceedings of the annual international conference of the IEEE engineering in medicine and biology, Hong Kong, China, Piscataway, NJ; 1998, p. 1698–702.
[9] Maher M, Dvorak-Carbone H, Pine J, Wright J, Tai Y. Microstructures for studies of cultured neural networks. Med Biol Eng Comput 1999;37:110–8.
[10] He Q, Meng E, Tai YC, Rutherglen CM, Erickson J, Pine J. Parylene neuro-cages for live neural networks study. In: Proceedings of the 12th international conference on transducers, solid-state sensors, actuators and microsystems, 2003, Boston, MA, Piscataway, NJ, 2003, p. 995–8.
[11] Meng E, Tai Y, Erickson J, Pine J. Parylene technology for mechanically robust neuro-cages. In: M Northrup A, K Jensen F, D Harrison J (Eds.). Proceedings of the 7th international conference on micro-total analysis systems, Squaw Valley, California, USA. Cambridge, UK: The Royal Society of Chemistry; 2003, p. 1109–1112.
[12] Tooker A, Meng E, Erickson J, Tai YC, Pine J. Development of biocompatible parylene neurocages. Proceedings of the 26th annual international conference of the IEEE engineering in medicine and biology society, San Francisco, CA, Piscataway, NJ; 2004, pp. 2542–5.
[13] Tooker A, Meng E, Erickson J, Tai YC, Pine J. Biocomplatible parylene neurocages. IEEE Eng Med Biol Mag 2005;24:30–3.
[14] Tooker A, Erickson J, Chow G, Tai YC, Pine J. Parylene neurocages for electrical stimulation on silicon and glass substrates. In: Proceedings of the 28th annual international conference of the IEEE engineering in medicine and biology society, EMBS'06, New York, NY, IEEE, Piscataway NJ; 2006, p. 4322–5.
[15] Lee KS, Kim RH, Prabhakaran P, Yang DY, Lim TW, Park SH. Two-photon stereolithography. J Nonlinear Opt Phys 2007;16:59–73.
[16] Juodkazis S, Mizeikis V, Misawa H. Three-dimensional microfabrication of materials by femtosecond lasers for photonics applications. J Appl Phys 2009;106.
[17] Takada K, Sun HB, Kawata S. Improved spatial resolution and surface roughness in photopolymerization- based laser nanowriting. Appl Phys Lett 2005;86:1–3.
[18] Ovsianikov A, Mironov V, Stampf J, Liska R. Engineering 3D cell-culture matrices: multiphoton processing technologies for biological and tissue engineering applications. Expert Rev Med Devices 2012;9:613–33.
[19] Kaehr B, Allen R, Javier DJ, Currie J, Shear JB. Guiding neuronal development with *in situ* microfabrication. Proc Natl Acad Sci USA 2004;101:16104–8.
[20] Kaehr B, Ertas N, Nielson R, Allen R, Hill RT, Plenert M, et al. Direct-write fabrication of functional protein matrixes using a low-cost Q-switched laser. Anal Chem 2006;78:3198–202.
[21] Seidlits SK, Schmidt CE, Shear JB. High-resolution patterning of hydrogels in three dimensions using direct-write photofabrication for cell guidance. Adv Funct Mater 2009;19:3543–51.
[22] Melissinaki V, Gill AA, Ortega I, Vamvakaki M, Ranella A, Haycock JW, et al. Direct laser writing of 3D scaffolds for neural tissue engineering applications. Biofabrication 2011;3:045005.
[23] Koroleva A, Gill AA, Ortega I, Haycock JW, Schlie S, Gittard SD, et al. Two-photon polymerization-generated and micromolding-replicated 3D scaffolds for peripheral neural tissue engineering applications. Biofabrication 2012;4:025005.
[24] Ylä-Outinen L, Heikkilä J, Skottman H, Suuronen R, Äänismaa R, Narkilahti S. Human cell-based micro electrode array platform for studying neurotoxicity. Front Neuroeng 2010;3:111.
[25] Heikkilä TJ, Ylä-Outinen L, Tanskanen JMA, Lappalainen RS, Skottman H, Suuronen R, et al. Human embryonic stem cell-derived neuronal cells form spontaneously active neuronal networks *in vitro*. Exp Neurol 2009;218:109–16.
[26] Äänismaa R, Ylä-Outinen L, Mikkonen JE, Narkilahti S. Human pluripotent stem cell-derived neuronal networks: their electrical functionality and usability for modelling and toxicology. In: Atwood C, editor. Methodological advances in the culture. Rijeka: Manipulation and Utilization of Embryonic Stem Cells for Basic and Practical Applications, InTech; 2011. p. 459–72.
[27] Pizzi R, Cino G, Gelain F, Rossetti D, Vescovi A. Learning in human neural networks on microelectrode arrays. BioSystems 2007;88:1–15.
[28] Käpylä E, Turunen S, Pelto J, Viitanen J, Kellomäki M. Investigation of the optimal processing parameters for picosecond laser-induced microfabrication of a polymer–ceramic hybrid material. J Micromech Microeng 2011;21:065033.
[29] Doraiswamy A, Jin C, Narayan RJ, Mageswaran P, Mente P, Modi R, et al. Two photon induced polymerization of organic–inorganic hybrid biomaterials for microstructured medical devices. Acta Biomater 2006;2:267–75.
[30] Ovsianikov A, Chichkov B, Adunka O, Pillsbury H, Doraiswamy A, Narayan RJ. Rapid prototyping of ossicular replacement prostheses. Appl Surf Sci 2007;253:6603–7.
[31] Ovsianikov A, Chichkov B, Mente P, Monteiro-Riviere NA, Doraiswamy A, Narayan RJ. Two photon polymerization of polymer–ceramic hybrid materials for transdermal drug delivery. Int J Appl Ceram Technol 2007;4:22–9.
[32] Käpylä E, Turunen S, Kellomäki M. Two-photon polymerization of a polymer-ceramic hybrid material with a low-cost Nd:YAG laser: preliminary resolution study and 3D fabrication. Micro Nanosyst 2010;2:87–99.
[33] Yang D, Park SH, Lim TW, Kong H, Yi SW, Yang HK, et al. Ultraprecise microreproduction of a three-dimensional artistic sculpture by multipath scanning method in two-photon photopolymerization. Appl Phys Lett 2007;90:013113.
[34] Viigipuu K, Kallio P. Microinjection of living adherent cells by using a semi-automatic microinjection system. Altern Lab Anim 2004;32:417–23.
[35] Lappalainen RS, Salomäki M, Ylä-Outinen L, Heikkilä TJ, Hyttinen JAK, Pihlajamäki H, et al. Similarly derived and cultured hESC lines show variation in their developmental potential towards neuronal cells in long-term culture. Regen Med 2010;5:749–62.
[36] Park S, Kim KH, Lim TW, Yang D, Lee K. Investigation of three-dimensional pattern collapse owing to surface tension using an imperfection finite element model. Microelectron Eng 2008;85:432–9.
[37] Ovsianikov A, Passinger S, Houbertz R, Chichkov B. Three dimensional material processing with femtosecond lasers. In: Phipps C, editor. Laser ablation and its applications. New York: Springer-Verlag; 2007. p. 121–57.
[38] Ovsianikov A, Shizhou X, Farsari M, Vamvakaki M, Fotakis C, Chichkov BN. Shrinkage of microstructures produced by two-photon polymerization of Zr-based hybrid photosensitive materials. Opt Express 2009;17:2143–8.
[39] Käpylä E, Aydogan DB, Virjula S, Vanhatupa S, Miettinen S, Hyttinen J, et al. Direct laser writing and geometrical analysis of scaffolds with designed pore architecture for three-dimensional cell culturing. J Micromech Microeng 2012;22:115016.
[40] Béduer A, Vieu C, Arnauduc F, Sol J, Loubinoux I, Vaysse L. Engineering of adult human neural stem cells differentiation through surface micropatterning. Biomaterials 2012;33:504–14.

Publication IV

Turunen, S., Joki, T., Hiltunen, M. L., Ihalainen, T. O., Narkilahti, S. & Kellomäki, M.

Direct laser writing of tubular microtowers for 3D culture of human pluripotent stem cell-derived neuronal cells

ACS Applied Materials & Interfaces 9(2017)31, pp. 25717-25730

ACS APPLIED MATERIALS & INTERFACES

Research Article

www.acsami.org

Direct Laser Writing of Tubular Microtowers for 3D Culture of Human Pluripotent Stem Cell-Derived Neuronal Cells

Sanna Turunen,*[,†] Tiina Joki,[‡] Maiju L. Hiltunen,[†] Teemu O. Ihalainen,[‡] Susanna Narkilahti,[‡] and Minna Kellomäki[†,§]

[†]Biomaterials and Tissue Engineering Group, BioMediTech and Faculty of Biomedical Sciences and Engineering, Tampere University of Technology, Korkeakoulunkatu 3, 33720 Tampere, Finland

[‡]NeuroGroup, BioMediTech and Faculty of Medicine and Life Sciences, University of Tampere, Lääkärinkatu 1, 33520 Tampere, Finland

[§]BioMediTech and Faculty of Medicine and Life Sciences, University of Tampere, Lääkärinkatu 1, 33520 Tampere, Finland

Supporting Information

ABSTRACT: As the complex structure of nervous tissue cannot be mimicked in two-dimensional (2D) cultures, the development of three-dimensional (3D) neuronal cell culture platforms is a topical issue in the field of neuroscience and neural tissue engineering. Computer-assisted laser-based fabrication techniques such as direct laser writing by two-photon polymerization (2PP-DLW) offer a versatile tool to fabricate 3D cell culture platforms with highly ordered geometries in the size scale of natural 3D cell environments. In this study, we present the design and 2PP-DLW fabrication process of a novel 3D neuronal cell culture platform based on tubular microtowers. The platform facilitates efficient long-term 3D culturing of human neuronal cells and supports neurite orientation and 3D network formation. Microtower designs both with or without intraluminal guidance cues and/or openings in the tower wall are designed and successfully fabricated from Ormocomp. Three of the microtower designs are chosen for the final culture platform: a design with openings in the wall and intralumial guidance cues (webs and pillars), a design with openings but without intraluminal structures, and a plain cylinder design. The proposed culture platform offers a promising concept for future 3D cultures in the field of neuroscience.

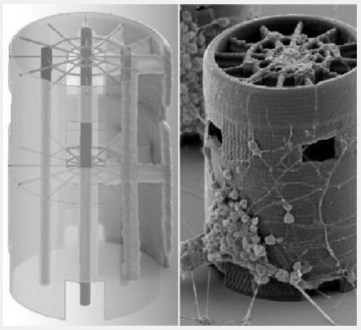

KEYWORDS: *direct laser writing, two-photon polymerization, microstructures, 3D culture platform, neurons, orientation of neurites*

1. INTRODUCTION

In vitro cell culture platforms are invaluable tools for the study of neural functions in health and disease. However, the planar culture of neuronal cells represents an oversimplification of the structure of the *in vivo* neural system. Moreover, two-dimensional (2D) cultures may lead to uncharacteristic cell−cell and cell−matrix interactions and alter cell behavior.[1] Thus, one of the major strategies in the field of neuroscience and neural tissue engineering (TE) is to develop three-dimensional (3D) cell culture models that more closely mimic the *in vivo*-like microenvironment and organization of neural networks into segregated neuronal nuclei connected by discrete axonal tracts.[2] Various approaches can be used to create a 3D environment such as porous solid scaffolds,[3] hydrogel matrices,[4] microscale tubular guidance conduits,[5] polymer microfibers,[6] or arrays of nano- and microscale structures, e.g., pillars[7] or towers.[2] Axonal alignment is an important goal for neural TE in central nervous system (CNS) and peripheral nervous system (PNS) injuries and deficits. Thus, in recent years, several *in vitro* studies of 3D nerve guidance conduit (NGC) geometries using aligned channels and fibers have been conducted.[8,9] Although NGCs have been mainly used for PNS injury studies,[10] microscale tubular guidance channels may also serve as 3D *in vitro* test platforms for the investigation of the different factors (mechanical, chemical, or topographical) that influence CNS neuronal survival and axonal directionality. 3D microconduits can be engineered according to specific need by systematically varying several parameters and thus providing a new approach to study the influences of different guidance cues on axonal path finding *in vitro*.[5] For example, the incorporation of an oriented intraluminal framework into the channel lumen to more accurately mimic the tract-like structure present in both CNS and PNS can result in improved cell attachment, migration, and alignment of regenerating axons in comparison with simple hollow tubular structures.[11] The intraluminal topographical cues or fibers promote the growth of neurons because the larger surface area provided by the introduction of an internal architecture significantly increases cell adherence and growth.[12]

The fabrication of multichannel conduits or channels with a regular filament arrangement or intricate intraluminal details is not an easy task. Conventionally, different natural and synthetic polymers have been fabricated into NGCs via injection

Received: April 20, 2017
Accepted: July 11, 2017
Published: July 11, 2017

DOI: 10.1021/acsami.7b05536
ACS Appl. Mater. Interfaces 2017, 9, 25717−25730

molding,[13] mandrel coating or dip coating,[14] centrifuge casting,[15] film rolling and sealing,[16] extrusion,[17] electrospinning,[18] and microbraiding of filaments.[19] However, these manufacturing techniques cannot reproduce tubes with precise dimensions or complex microscale internal structures.[20] Hence, several rapid prototyping techniques that enable the production of complicated 3D structures automatically according to computer-aided designs (CADs) have been used. These prototyping techniques that include microstereolithography[21] and inkjet microdispensing[22] have been used to fabricate semicircular trenches and tubular nerve conduits. Usually, the sizes of the scaffold features produced by 3D printing and nozzle-based techniques are in the range of 1 to 6 mm with the width of the printed line limited to a minimum of 200 to 300 μm.[23] However, the highest level of flexibility in structural design is achieved by using a rapid prototyping technique called direct laser writing by two-photon polymerization (2PP-DLW). This technique allows the fabrication of complex features including internal walls, overhangs, or tortuous channels with feature sizes in the μm and subμm range.[23] 2PP-DLW is a sequential fabrication technique in which structures are created by translating either the focal spot of a tightly focused laser beam or the target, according to a predefined scanning path.[24] The two-photon absorption (2PA) of photoinitiator molecules initiates radical chain-growth polymerization that converts small, unsaturated monomer molecules from a liquid state to solid macromolecules.[25] The polymerization is localized within the focal volume of the laser beam enabling the fabrication of isolated structures with <100 nm line widths.[26]

2PP-DLW can process various photosensitive, biocompatible materials. The technique has already been harnessed to construct ordered 3D scaffolds with geometrical details on a cellular scale (10 μm) for neuronal cell culture purposes.[27] A nonbiodegradable organically modified ceramic, Ormocomp, has been structured by 2PP-DLW into various geometrical shapes for neural applications such as Lego-like blocks,[28] pillars,[29,30] and microridges[31] and has been successfully used for contact guidance of neuroblastoma cells of rat[28,31] and human[29−31] origin. In addition, Zr−Si hybrid material and methacrylated polylactide (PLA) have been structured into hollow cylinder scaffolds and used for culturing rodent neural cells.[32,33] On the basis of these previously reported results, there seems to be an obvious need for studies conducted with human neuronal cells of nonmalignant origin.

In this paper, we describe the optimization of the fabrication process for a novel, detailed, 3D cell culture platform based on direct laser written tubular microtowers and human neuronal cells. Although 2PP-DLW is not an easily upscalable fabrication method such as electrospinning, it enables the repeatable production of platforms with fine details for *in vitro* applications. These easily tunable platforms can be used for studying the effects of the layout and the design (shapes and dimensions) on cell behavior. Thus, the aim of our study was to polymerize different microtower designs including a design with intraluminal longitudinal micropillars that mimic the axonal tracts *in vivo*. In particular, we investigated the ability of the towers to support the adhesion, growth, and orientation of human pluripotent stem cell (hPSC)-derived neuronal cells.

2. EXPERIMENTAL SECTION

2.1. 2PP-DLW Fabrication Setup. The microtowers were fabricated with a custom-built 2PP-DLW setup, which was an updated version of the system described previously.[34] Briefly, a frequency doubled femtosecond fiber laser (FP-532-0.2-FS-01, Fianium Ltd., United Kingdom), operating at 532 nm with a pulse duration of 200 fs, repetition rate of 40 MHz, and average output power of 200 mW, was used as an irradiation source. The beam was scanned in the *xy*-direction with a fast steering mirror scanner (FSM-300, Newport Corporation, USA) and in the *z*-direction with a piezoelectric objective lens positioning system (Mipos 250 SGEX, Piezosystem Jena GmbH, Germany). The beam was directed into a 50× oil immersion objective (N.A. = 0.90, Meiji Techno, Japan) situated on an upright microscope frame (ECLIPSE ME 600, Nikon, Japan). The objective had an average transmittance of 48%. In order to overfill the back aperture of the objective lens, a combination of two beam expanders, a 10× and an adjustable 1−3×, was used. The average laser power was adjusted to a suitable polymerization level with a motorized attenuator (Watt Pilot, UAB Altechna, Lithuania). The laser power was measured at the back aperture of the objective with a power meter console (PM100USB, Thorlabs Inc., USA) coupled with a S310C thermal sensor.

2.2. Materials and Sample Preparation. A commercial polymer-ceramic hybrid material Ormocomp (Micro Resist Technology GmbH, Germany) was used as a photocurable material in combination with 2 wt % of the photoinitiator Irgacure 127 (Ciba Specialty Chemicals, Switzerland). In order to enhance the adhesion of the microtowers to the glass surface, the coverslips intended for cell culture experiments were pretreated with 3-(trimethoxysilyl) propyl methacrylate (MAPTMS, Sigma-Aldrich Finland Oy, Finland) as described by Käpylä et al.[35] For the polymerization, a drop of Ormocomp was administered on a round coverslip (Ø = 9 mm) that was sandwiched between a microscope slide and a coverslip separated by a 250 μm thick stainless steel spacer. After the polymerization, the unexposed part of the resist was dissolved by immersing the coverslip in Ormodev developer (Micro Resist Technology GmbH, Germany) for 15 min and by rinsing with Ormodev and hexamethyldisilazane (HMDS, Sigma-Aldrich Finland Oy, Finland).

2.3. Determination of Polymerization Window and Feature Size. In order to define the window of practical operation for the fabrication of the microtowers with good quality, the polymerization windows (P_w) were determined for the scanning speeds of 150, 350, and 550 μm s^{-1}. The polymerization window was calculated as the power range between the polymerization (P_{th}) and the damage thresholds (P_D). For the threshold value determination, the laser focus was positioned inside the resist volume to exclude any interaction with the glass surface, and then, the laser power value was gradually increased while polymerizing simple square patterns. The polymerization threshold was defined as the lowest average laser power that yielded a barely visible polymerized pattern and the damage threshold as the power value where the microexplosions first started to emerge. The average threshold values were calculated from the measurements made from four separate samples. To ensure a large enough margin for the damage-free fabrication without the appearance of microexplosions due to the laser power fluctuation or the inhomogeneity of the resin, the microtowers were fabricated with power values corresponding to 70% of the polymerization window according to the formula $P = P_w \times x + P_{th}$, where P_w is the polymerization window, P_{th} is the polymerization threshold, and $x = 0.7$ is the power factor.

In order to determine the optimal slicing distance for the contours, the line width and height were analyzed from suspended lines polymerized between supporting wall structures with scanning speeds of 150, 350, and 550 μm s^{-1}. All the suspended lines were fabricated with the average laser power values corresponding to 70% of the polymerization window determined previously for each scanning speed. Feature dimensions were measured from the top view (0° tilt) and side view (90° tilt) of SEM images with a free software GIMP (version 2.8). The degree of voxel overlap for the chosen contour distances was calculated as the product of voxel displacement in axial and lateral directions according to the following:

$$\delta = \frac{w - \mathrm{dx}}{w} \times \frac{h - \mathrm{dz}}{h} \quad (1)$$

DOI: 10.1021/acsami.7b05536
ACS Appl. Mater. Interfaces 2017, 9, 25717−25730

where δ is the degree of the voxel overlap, w and h are the width and height of the voxel, and dx and dz are the lateral and axial voxel distances, respectively.[36]

2.4. Microtower Design. The tubular microtowers were designed using the Rhinoceros CAD program (version 4.0, Robert McNeel & Associates, USA). The outer shell of the towers was a 150.0 μm high cylinder with an outer diameter of 77.0 μm and an inner diameter of 75.0 μm. The cylinder was designed to have openings at the foot of the tower for the cells to enter and in the upper part of the tower to allow the efficient flow of medium also in the lumen of the tower. Two different shapes for the openings, i.e., elliptical and rectangular, were tested to find the one that best retained its shape and size after polymerization. A set of five longitudinal micropillars inspired by the axonal tracts present *in vivo* was placed inside the tower to offer oriented topography for neurites to migrate along through the channel. The diameter of the pillars was set to 5.0 μm to achieve thin but robust enough structures. Spider web-like platforms were inserted on top and halfway down the tower to further increase the surface area for cells to attach to and for neuronal somas to remain stationary. Two different designs for the spider webs were tested: a dense web comprising three concentric polygons with 5.0 μm line spacing (designs I and III) and a sparse web comprising two concentric polygons with 10.0 μm spacing (designs II and IV). As a comparison, hollow microtowers with and without openings were also designed. In total, six different microtower designs were drawn: designs I and II (Figure S2a,b) had elliptical openings with dense or sparse webs, designs III (Figure S2c) and IV (Figure 1a) had rectangular openings with

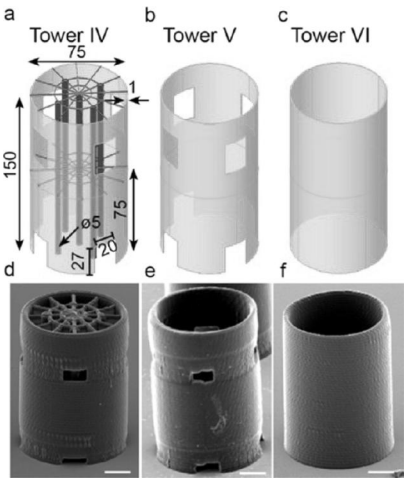

Figure 1. CAD and SEM images of the microtowers: (a, d) design IV with rectangular openings and sparse webs, (b, e) design V with rectangular openings, and (c, f) design VI without openings. The dimensions in CAD images are given in micrometers. SEM images are taken from the 60° tilt angle. The top view and the longitudinal cross-section of the design IV tower are presented in Figure S4. The scale bars represent 20 μm.

dense or sparse webs, design V (Figure 1b) was a hollow cylinder with rectangular openings, and design VI (Figure 1c) was a hollow cylinder without any openings.

2.5. Fabrication of Microtowers. The microtower designs I–IV were polymerized using the 50× objective to find out which version replicated the original CAD model most precisely. The cylinders and pillars were fabricated using the multipath scanning method,[37] in which the cylinder walls were formed by two nested contours separated by a distance of 1 μm, and the micropillars, by three nested contours separated by a distance of 1 μm. Because the spider webs were polymerized as single line scans, a moderate scanning speed of 150 μm s^{-1} had to be used in order to achieve robust and untwisted threads. For the cylinders and pillars, scanning speeds of 350 and 550 μm s^{-1} were tested to optimize the fabrication time versus surface quality of the structures. For each scanning speed, the average laser power corresponding to the predetermined 70% of the polymerization window was used. In order to explore the intraluminal architecture of the microtowers with SEM imaging, longitudinal cross sections of design II and IV towers were also fabricated with the scanning speeds of 350 and 550 μm s^{-1}.

For the cell culture experiment, six parallel samples per time point with an array of nine microtowers comprising three pieces of each design (IV, V, and VI) were fabricated on MAPTMS-coated round glass coverslips (Ø = 9 mm). The distance between individual towers of the same design was ~90 μm and between different tower designs was ~260 μm. The cylinders and pillars were produced with the constant scanning speed of 550 μm s^{-1} and approximately 70% power, and the webs were scanned with the speed of 150 μm s^{-1} and power of 70%.

2.6. Characterization of Microtowers. The dimensions of the fabricated suspended line structures and the microtowers were analyzed by SEM imaging with a Philips XL-30 microscope (Philips Electron Optics, The Netherlands). Prior to imaging, the samples were sputter coated with gold in an argon atmosphere either to a nominal thickness of 113 nm (S 150 Sputter Coater, Edwards Ltd., UK) or 60 nm (SCD 050 Sputter Coater, BAL-TEC AG, Liechtenstein). The feature dimensions were measured from top (0° tilt) and side (90° tilt) view SEM images with GIMP software.

Because the cell adhesion can be affected by surface topography, the surface roughness of the microtower cylinder walls was investigated by noncontact mode AFM (XE-100, Park Systems Inc., USA). For the imaging, the coverslip containing the microtowers was mounted in an upright position on the *xy*-scanning stage in order to access the surface of the walls of the towers with the AFM cantilever. Measurements were performed using silicon probes (ACTa, Applied NanoStructures Inc., USA) with a nominal resonance frequency of 300 kHz, spring constant of 40 N m^{-1}, and a tetrahedral pyramidal shaped tip with a face angle of 18°. Images were acquired with a scan rate of 1.0 Hz. Areas of 10 μm × 10 μm were imaged from the cylindrical walls of each tower design (IV, V, and VI). From the two designs with openings, images were acquired from two different locations of the cylinder: the sections with a smoother surface and the sections located between the openings with a seemingly rougher texture. The roughness of the surface was analyzed from the AFM images with XEI image processing software (version 1.8.0, Park Systems Inc., USA). The curvature resulting from the cylindrical shape of the tower wall was removed from the acquired images by using the flattening tool with second order fitting curve in the *x*-direction. As the microtowers appeared to be tilted to some extent in the *y*-direction, the slope was eliminated by also flattening the images in a vertical direction with a first order fitting curve. The surface roughness was defined as the areal average surface roughness (R_a).

The stiffness of the polymerized structures is mainly expressed by the Young's modulus of the material. Thus, force spectroscopy measurements were performed with AFM to estimate the Young's modulus of Ormocomp. The elastic properties of the sample were investigated with AFM force curves by recording the applied force and the depth of indentation as the tip was pushed against the sample surface.[38] Force–indentation curves were recorded at three points from each tower design by scanning areas of 15 μm × 15 μm from the upper rim of the cylinder with a scan rate of 0.5 Hz. For comparison, similar sized areas were also recorded from the three UV-cured Ormocomp thin films. The fabrication of the thin films is described in the Supporting Information.

One of the most commonly used models for deriving the elastic modulus from force curve data is the Hertz model[39] that gives the force on a spherical tip as a function of the elastic properties of the material, the radius of the tip, and the indentation depth.[40] The following is a modified Hertz model[41] for a four-sided pyramidal indenter:

$$F = \frac{E}{1-\nu^2}\frac{\tan\alpha}{\sqrt{2}}\delta^2 \quad (2)$$

where F is the indentation force applied to the sample, E is the Young's modulus, ν is the Poisson's ratio of the sample (set to 0.35 according to[42]), δ is the indentation depth, and α is the face angle of the pyramidal tip (18° in our case). The cantilever deflection during the indentation was taken into account in XEI by transforming the Force–Z displacement curve to Force–Separation curve via the cantilever's spring constant value (k). The spring constant of the cantilever was not

DOI: 10.1021/acsami.7b05536
ACS Appl. Mater. Interfaces 2017, 9, 25717–25730

calibrated prior to the analysis. Instead, the nominal value of k = 40 N m^{-1} quoted by the manufacturer was used. Stiffness data was calculated automatically with XEI from the slopes of the force curves after fitting with the Hertz model.

2.7. Differentiation of Neuronal Cells and Cell Culture. Human neural cells derived from the hESC line Regea 08/023 (passage 46) were used in cell culture experiments. Stem cell line derivation, culturing, and characterization as well as neuronal differentiation have been previously published.[43,44] The BMT institute has been given ethical permissions to derive hESC lines and to use stem cells for neural research (1426/32/300/05, R05116). The quality control of the used stem cell line was implemented by frequent gene and protein expression analysis for pluripotency in addition to karyotype and mycoplasma assays. Stem cells were predifferentiated for 13 weeks into neural fate before using them for culture experiments. Briefly, undifferentiated colonies were mechanically cut into small cell aggregates and transferred into neural differentiation medium (NDM) on low cell binding culture plates. NDM contains 1:1 DMEM/F12 and Neurobasal supplemented with GlutaMax (2 mM), 1× B27, 1× N2, and penicillin/streptomycin (25 U mL^{-1}), all from Thermo Fisher Scientific Corporation, USA. During differentiation, the medium was supplemented with bFGF (20 ng mL^{-1}, R&D Systems Inc., USA). Cell aggregates formed round freely floating neurospheres, which were kept small (Ø ~ 500 μm) by cutting once a week under a microscope. One third of the medium was changed three times a week.

For cell culture experiments, coverslips containing microtowers were disinfected with 70% (v/v) ethanol for 15 min, immersed in Dulbecco's phosphate buffered saline (DPBS, Lonza Group Ltd., Switzerland) for 2 h at +4 °C, and allowed to air-dry. The PDMS cell restrictors were attached to coverslips, and the samples were placed on 6-well plates. The surfaces were coated using mouse laminin (10 μg mL^{-1}, Sigma-Aldrich). The laminin coating solution was incubated on samples for 72 h at +4 °C.

For the plating of the cells on the microtower samples, neurospheres were enzymatically dissociated into a single cell solution using TrypLE Select 1× (Thermo Fischer Scientific) according to the manufacturer's instructions. The cells were plated as a single cell suspension on top of the laminin-coated samples at a density of ~35 000 cells cm^{-2}. For the first week in culture, NDM without growth factors was used, after which NDM was supplemented with bFGF (4 ng mL^{-1}) and brain-derived neurotrophic factor (BDNF, 5 ng mL^{-1}, ProSpec-Tany TechnoGene Ltd., Israel). During culturing, the cells were monitored and phase contrast images were taken with an inverted microscope (Nikon Eclipse TE 2000-S, Nikon Corporation, Japan) equipped with the Nikon Digital Sight Camera System (DS-5M-L1). Half of the cell culture media was changed three times a week.

2.8. Viability Assay. For viability analysis, the cultures were stained using a LIVE/DEAD viability/cytotoxicity assay (Thermo Fisher Scientific). In brief, the assay comprises two fluorescent dyes: Calcein-AM (0.1 μM, $\lambda_{excitation}$ = 488 nm) that stains intact cells and ethidium homodimer-1 (0.4 μM, $\lambda_{excitation}$ = 568 nm) that stains dead cells. After 30 min of incubation at +37 °C, the cells were imaged with an Olympus IX51 inverted microscope and an Olympus DP30BW digital camera (Olympus Corporation, Japan). Three parallel samples were analyzed per time point (1, 2, and 4 weeks).

2.9. Immunofluorescence and Confocal Imaging. For immunocytochemical staining, cells were fixed for 30 min using 4% paraformaldehyde (Fluka, Italy) after 1, 2, or 4 weeks of culture and stained with neuronal markers. Unspecific staining was blocked for 30 min at room temperature (RT) with 10% normal donkey serum (NDS), 0.1% saponin, and 1% bovine serum albumin (BSA) in DPBS (all from Sigma-Aldrich). The cells were then washed once with 1% NDS, 0.1% saponin, and 1% BSA in DPBS. Primary antibodies, rabbit antimicrotubule associated protein 2 (MAP-2, 1:400, AB5622, Merck Millipore, Germany), and monoclonal mouse anti-β-tubulin III (1:1250, Sigma-Aldrich) were incubated with the cells at +4 °C overnight. Then, the cells were washed three times with 1% BSA in DPBS and incubated with secondary antibodies for 1 h at RT. AlexaFluor-488 or -568 conjugated antirabbit or antimouse secondary antibodies (1:400, Thermo Fischer Scientific) in 1% BSA on DPBS were used. DAPI (0.2 μg mL^{-1}, Sigma-Aldrich) in DPBS was added to the samples and incubated for 15 min. Finally, the cells were washed twice with DPBS. The samples were then mounted according to the manufacturer's instructions with TDE Mounting media (Abberior GmbH, Germany), a 2,2′-thiodiethanol-based embedding media with a refractive index of 1.518 matching perfectly with the refractive index of Ormocomp. The embedding media was used to minimize spherical aberration that causes a scattering of light and a blurring of the images.

Confocal images were acquired with a Zeiss LSM 780 mounted into an inverted Cell Observer microscope (Carl Zeiss, Germany) using 63× (N.A. = 1.40, Zeiss Plan Apochromat, Carl Zeiss) and 25× (N.A. = 0.80, Zeiss LD LCI Plan-Apochromat, Carl Zeiss) objectives. The confocal data was visualized with ZEN Black 2012 SP1 software (version 8.1, Carl Zeiss) and ImageJ (Version 1.39, U.S. National Institutes of Health, USA). For cell number analysis, confocal image stacks were divided into 15 μm thick substacks, and cell nuclei were counted with the Cell Counter ImageJ plugin. The data were further rearranged to represent the proportion of cells attached to smooth and rough surfaces, total cell number in the microtowers, and the proportion and longitudinal distribution of cells inside the towers.

2.10. Confocal Image Analysis of Neurites. For analyzing neurite orientation inside the microtowers, orthogonal projections were created from confocal image stacks. To exclude the cells growing on the outer surface of the towers, cropped slices representing only the center part of the towers were analyzed. These slices were projected into 2D via the maximum intensity projection function in ImageJ. The projection represented 50% of the total microtower volume. Orthogonal projections were analyzed with a spectral analysis software tool, CytoSpectre,[45] to quantify the circular variance and mean orientation of the neurites inside the towers. Circular variance is a measure of the uniformity of the orientation distribution. It varies from 0 to 1. The value of 1 describes a situation where the neurites are spread evenly in all angles lacking a dominant direction, whereas a value of 0 signifies a case of perfect alignment along a single orientation angle. In addition, the orientation angles of all neurite segments with a length of ≥5 μm were traced and measured manually with ImageJ from the same orthogonal projections. In total, ~3200 neurite segments were measured. The angle of each segment was calculated relative to the vertical plane, and all orientation angles across the 0° to 90° spectrum were then binned in 10° sections. This method was adapted from Tuft et al.[46] A lack of neurite alignment would thus be supported by a relatively equal distribution of neurite segment angles across the whole angle spectrum, whereas strong alignment to the longitudinal direction would be evidenced by a high incidence of neurite segments with angles of 20° or less.

2.11. Preparation of Cell Culture Samples for SEM Imaging. The 3D morphology and organization of neuronal cells were assessed by SEM imaging. Prior to imaging, samples were fixed with 5% glutaraldehyde (Sigma-Aldrich) in DPBS (pH 7.4) at RT for 1 h. Afterward, the samples were immersed in ion-exchanged water for 15 min. Next, the samples were dehydrated using an ascending series of ethanol concentrations (10%, 20%, 40%, 60%, 80%, 99.5%, v/v) for 10 min each. Finally, the samples were air-dried and stored under vacuum. After drying, the samples were sputter coated with gold in an argon atmosphere (S 150 Sputter Coater) to a coating thickness of approximately 75 nm. Samples were analyzed by SEM imaging with a Philips XL-30.

2.12. Statistical Analysis. All statistical tests were performed with IBM SPSS-software (version 23, IBM, USA). Statistical analysis was performed using the nonparametric Mann−Whitney U test or Kruskall-Wallis test followed by Dunn-Bonferroni tests. The p-values of <0.05 or <0.01 were considered significant.

3. RESULTS

3.1. Polymerization Windows and Feature Dimensions. In order to fabricate Ormocomp microtowers with good structural quality, i.e., without the emergence of damaging microexplosions, the applicable average laser power range (i.e., the polymerization window) for polymerization was first determined. The measured values are collated in Table 1. The threshold values

DOI: 10.1021/acsami.7b05536
ACS Appl. Mater. Interfaces 2017, 9, 25717−25730

Table 1. Polymerization (P_{th}) and Damage Threshold (P_D) Power Values As Well As the Calculated Polymerization Windows (P_w) and the Power Values Corresponding to 70% of the Polymerization Window for the Tested Scanning Speeds[a]

scanning speed [μm s^{-1}]	P_{th} [mW]	P_D [mW]	P_w [mW]	70% P_w [mW]
150	0.3 ± 0.04	5.4 ± 0.5	5.1 ± 0.5	3.8 ± 0.4
350	0.3 ± 0.04	5.3 ± 0.2	5.0 ± 0.2	3.9 ± 0.2
550	0.3 ± 0.06	5.4 ± 0.2	5.0 ± 0.2	3.9 ± 0.2

[a]The measured data represent mean ± standard deviation (n = 4).

for the examined scanning speeds were almost identical and resulted in very similar polymerization window ranges.

SEM images of suspended line structures polymerized with scanning speeds of 150, 350, and 550 μm s^{-1} are shown in Figure S1. The measured line widths and heights for the three scanning speeds are summarized in Table 2.

Although the voxel dimensions remained nearly constant, the uniformity of the lines decreased and the surface roughness increased with scanning speed. As the fabrication time can be reduced by taking advantage of the axial height of the voxels and setting the layer distance to match the voxel height, the axial voxel distance of the microtower cylinder was set to 3.0 μm and the micropillars to 4.0 μm. In order to achieve relatively smooth surface roughness, the lateral voxel distance was set to 1.0 μm. The lateral, axial, and overall voxel overlap degrees calculated for the cylinder according to eq 1 are presented in Table 2. The voxel overlap ratios were not determined for the scanning speed 150 μm s^{-1} as it was only used for single line scans when polymerizing the spider webs. According to the results of previous studies, the lateral surface roughness tends to saturate when the voxel overlap ratio is over 0.5 due to the self-smoothing effect.[47,48] For the scanning speeds of 350 and 550 μm s^{-1}, the lateral voxel overlap ratios were over 0.5 suggesting that similar surface roughness would be achieved with both scanning speeds.

3.2. Microtower Fabrication by 2PP-DLW. The microtower designs I and II were polymerized with scanning speeds of 350 and 550 μm s^{-1} (Figure S3) to determine the optimal scanning speed for the fabrication and to evaluate whether the elliptically shaped openings would give round openings. However, as the axial contour distance was quite large (i.e., 3.0 μm), the elliptical shape of the openings was not traced properly, especially with the scanning speed of 550 μm s^{-1}. As predicted by the similar voxel overlap degrees, both scanning speeds resulted in comparable surface quality. The rectangular shape of openings (designs III and IV) was reproduced quite accurately with both scanning speeds (Figure S4).

Figures S3 and S4 show that some of the gaps in the spider webs were enclosed by self-polymerized membranes (designs I and III) that formed in-between the web threads as the scanned lines were packed densely enough. These designs were considered too closed to allow efficient cell migration. Thus, microtower design IV (Figure 1a,d) together with the reference structure designs V (Figure 1b,e) and VI (Figure 1c,f) were selected as the most optimal models for the cell culture experiments.

The fabrication of a single design IV tower using scanning speeds of 350 μm s^{-1} (the cylinder and pillars) and 150 μm s^{-1} (the webs) took approximately 7 min 32 s. Increasing the scanning speed from 350 to 550 μm s^{-1} reduced the fabrication time by 22 s to 7 min 10 s. As there was no essential difference in the surface quality of the towers, the samples for the cell culture experiments were fabricated with the scanning speed of 550 μm s^{-1}. In addition, the reference microtowers (designs V and VI) were fabricated with the same scanning speed. The fabrication of design V took only 3 min 49 s and design VI took 4 min 30 s. Design VI towers had a smooth uniform surface morphology with surface roughness R_a = 11.2 ± 0.4 nm (henceforth denoted as "smooth surface") as the cylinder comprised only closed circular contours. The surface roughness (R_a = 30.9 ± 6.6 nm, henceforth denoted as "rough surface") was higher in designs IV and V at the opening layers. The higher surface roughness was caused by the fluctuation of the laser dose due to the acceleration and deceleration of the scanner producing variation in voxel size. Other layers of the design IV and V towers had a smooth surface as in design VI. Figure S5 shows examples of atomic force microscopy (AFM) 3D topography images and the line scan profiles of the smooth and rough parts of the tower walls.

Fabrication accuracy using the 2PP-DLW setup was assessed by measuring the dimensions of the design IV microtowers from SEM images and comparing them with the theoretical dimensions of the CAD model (Table 3). The comparison revealed that the microtowers had shrunk in both xy- and z-directions on average 4% and 21%, respectively. The Young's modulus of Ormocomp processed by 2PP-DLW was estimated via force spectroscopy measurements performed with AFM at the upper rim of the microtower cylinder. For comparison, the Young's

Table 3. Theoretical and Experimental Dimensions of Design IV Microtower[a]

	CAD dimensions [μm]	measured dimensions [μm]	deviation [%]
cylinder height	150.0	119.2 ± 4.5	20.5 ± 3.0
lower opening height	27.0	11.9 ± 4.2	55.9 ± 15.6
lower opening width	20.0	18.6 ± 0.3	7.2 ± 1.3
upper opening height	33.0	10.1 ± 0.4	69.4 ± 1.1
upper opening width	20.0	18.1 ± 0.1	9.3 ± 0.7
cylinder inner diameter	75.0	71.7 ± 0.4	4.3 ± 0.6
pillar diameter	5.0	8.5 ± 0.8	70.6 ± 15.9

[a]The cylinder and pillar diameters were measured from the top view (0° tilt), and height of the cylinder along with the dimensions of the openings, from the side view (90° tilt) of SEM images. The measured data represent the mean ± standard deviation (n = 5).

Table 2. Measured Line Widths and Heights for Scanning Speeds of 150, 350, and 550 μm s^{-1} and Calculated Voxel Overlap Ratios[a]

scanning speed [μm s^{-1}]	line width [μm]	line height [μm]	lateral voxel distance [μm]	lateral voxel overlap	axial voxel distance [μm]	axial voxel overlap	overall voxel overlap degree
150	1.9 ± 0.2	7.5 ± 0.2	n.a.	n.a.	n.a.	n.a.	n.a.
350	2.1 ± 0.1	7.4 ± 0.2	1.0	0.53	3.0	0.59	0.31
550	2.1 ± 0.2	6.8 ± 0.6	1.0	0.51	3.0	0.56	0.29

[a]The data represent mean ± standard deviation (n = 5).

DOI: 10.1021/acsami.7b05536
ACS Appl. Mater. Interfaces 2017, 9, 25717−25730

modulus was also measured from UV-polymerized Ormocomp thin films. According to the Hertz model, the average Young's modulus of the microstructures was $E = 140 \pm 18$ MPa, whereas in the UV-cured Ormocomp thin films it was $E = 2.4 \pm 0.18$ GPa underlining a significant difference between the two differently cured specimens (two-tailed Mann–Whitney U test, $p < 0.001$, $n = 9$). Examples of the force versus indentation depth plots are shown in Figure S6.

3.3. Applicability of the Microtower Structures for Cell Culture Purposes. The applicability of microtowers for cell culture purposes was assessed by cell viability analysis. Cells grew in close vicinity to and inside the towers throughout the four-week experiment (Figure 2a). The viability of the cells was not affected by the microtowers. In addition, cell growth on the outer surface of the towers was studied to further ensure the suitability of the surface texture for cell attachment (Figure 2b,c). The outer surface of the towers at the height of 75 to 90 μm representing either rough (R_a = 31 nm) or smooth (R_a = 11 nm) surface texture was closely examined. Visual inspection showed no differences between the different textures. This was confirmed by also comparing the proportions of cells attached to the analyzed areas. There were no statistically significant differences in cell attachment among surfaces with different roughness. Therefore, microtowers fabricated by 2PP-DLW provided a suitable environment for cells.

3.4. Neuronal Cell Distribution in Microtowers. Cell phenotype was confirmed as neuronal via immunocytochemical staining against the neuronal markers MAP-2 and β-tubulin III (Figure 3a). Cell growth inside and outside the microtowers was studied by counting cell nuclei from confocal image stacks. At the one-week time point, the total cell growth in all the studied tower designs was quite similar (Figure 3b). At the two-week time point, the total cell number increased in designs IV and V, whereas the number remained constant in design VI. By week four, the total cell number decreased in designs IV and V but increased in design VI. Most of the cells, regardless of tower design, were located on the outside walls but there was a high variation in cell number (945 ± 424 cells), whereas the cell number on the inside was lower but interestingly with less variation (440 ± 158 cells). As the inside of the tower provided a more stable microenvironment for the cells, we next calculated the relative proportion of cells inside from the total cell number. Despite the dramatic changes in cell number outside of design IV, the proportion of cells inside increased significantly from week one to week four (Figure 3b,c). In addition, the portion of cells inside tower design IV was significantly higher compared with design VI at the four-week time point.

The cell distribution inside the towers was analyzed on the basis of six layers. Each layer represented different regions of design IV: from 0 to 15 μm lower openings, from 15 to 60 μm pillars, from 60 to 75 μm lower web, from 75 to 90 μm upper openings, from 90 to 120 μm pillars, and from 120 to 135 μm upper web. Figure 4a presents examples of confocal z-projections of samples at the two-week time point. In design IV, the cell distribution at the upper half (from 60 to 135 μm) of the tower remained rather similar throughout the 4 weeks (Figure 4b). Whereas in the lower layers (from 0 to 60 μm), the cell localization was observed to shift from the lowest layer (from 0 to 15 μm) to the next layer (from 15 to 60 μm) over time. However, this movement upward was halted at the layer containing the lower web (from 60 to 75 μm). In design V, most of the cells were located in the lower half of the tower throughout the study (Figure 4c). In design VI, the cells were quite evenly distributed throughout the height of the tower during the first 2 weeks (Figure 4d). By week four, the majority of the cells had migrated to the upper parts of the tower.

3.5. Orientation of Neurites along Microtowers. The orientation of neurites along the microtowers was first analyzed with automated analysis. Then, a more detailed analysis was performed manually to investigate the distribution of neurite

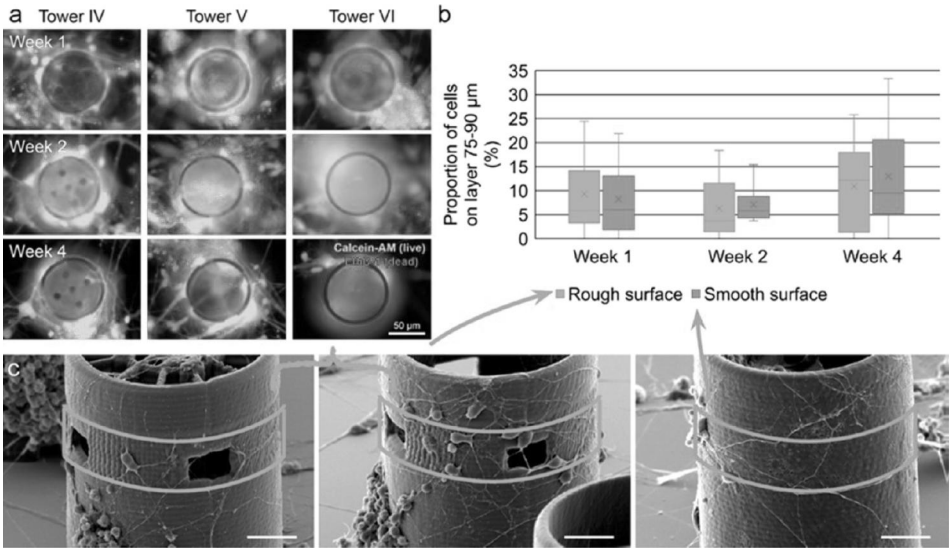

Figure 2. Applicability of the direct laser written microtower structures for cell culture purposes: (a) fluorescence images of live/dead stained cells at different time points; (b) proportion of cells attached to the outer surface layer at height 75 to 90 μm representing either rough or smooth surface texture. The cell numbers on the rough surface have been counted by combining the data of tower designs IV and V. The cell numbers on the smooth surface represent the data of tower design VI. There was no statistically significant difference in cell attachment among surfaces with different roughness ($p > 0.05$, two-tailed Mann–Whitney U test, $n = 8$–18); (c) SEM images of microtower designs IV, V, and VI from one-week time point illustrating the surface area used for analysis of cell attachment on differently textured surfaces. Scale bars represent 20 μm.

DOI: 10.1021/acsami.7b05536
ACS Appl. Mater. Interfaces 2017, 9, 25717–25730

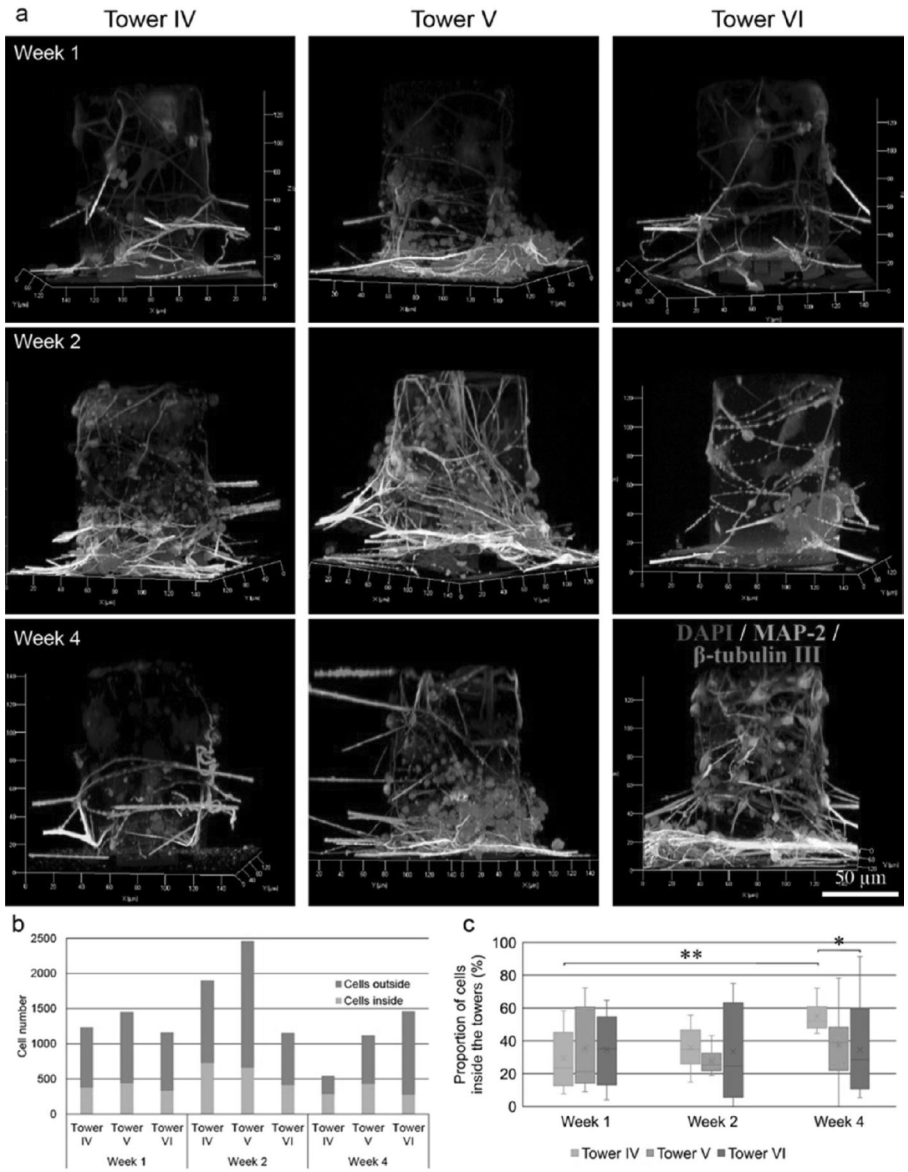

Figure 3. Total cell number in microtowers. (a) Representative 3D renderings of confocal image stacks with immunocytochemical staining against neuronal markers MAP-2 (green), β-tubulin III (red), and DAPI (blue) for nuclei. (b) Total cell number in microtowers and (c) proportions of cells inside the towers ($^*p = 0.041 < 0.05$, $^{**}p = 0.007 < 0.01$, $n = 7–9$, Kruskal-Wallis test followed by posthoc Dunn-Bonferroni tests).

orientation angles. As an example, plots of the neurite orientation distributions from the automated analysis and projections demonstrating manual neurite tracing are shown in Figure 5a–c. According to automated CytoSpectre analysis of circular variances, all tower designs had cases of high orientation (circular variance $\leq$0.6). However, there was a great variation between parallel samples (Figure 5d). The dominant orientation for each tower design is represented as a box plot of mean orientation angles between 0° and 180° in Figure 5e. The longitudinal axis of the tower is at the angle of 90°, and the neurites following this angle were considered to be perfectly oriented. The majority of the measured mean orientation angles represented ±10° deviation from the longitudinal axis throughout the experiment indicating the presence of longitudinally oriented neurites.

In the manual analysis, the lengths of the traced neurite segments were summed and compared with the total cell number (Figure 5f). The main finding was that design IV had the highest neurites to cell number ratio at 1 and 4 weeks. Therefore, design IV provided the most promising environment for neurite growth. Figure 5g–i shows the distribution of the manually measured neurite segment angles. During the first week (Figure 5g), all the tower designs demonstrated similar neurite orientation behavior; the highest neurite occurrence was found in the 10° bin. Throughout the experiment, design IV had the highest incidence of neurite segments (41% to 46%) with an alignment angle of $\leq$20° indicating orientation along the longitudinal direction. At the two-week time point (Figure 5h), design V had a fairly equal distribution of neurite segment angles across the bins demonstrating quite random orientation, whereas in design VI, the highest neurite incidence was detected in bins 10°, 20°, and 40°. All the tower designs had approximately the same number of longitudinally oriented neurites (~40%) at the four-week time

DOI: 10.1021/acsami.7b05536
ACS Appl. Mater. Interfaces 2017, 9, 25717–25730

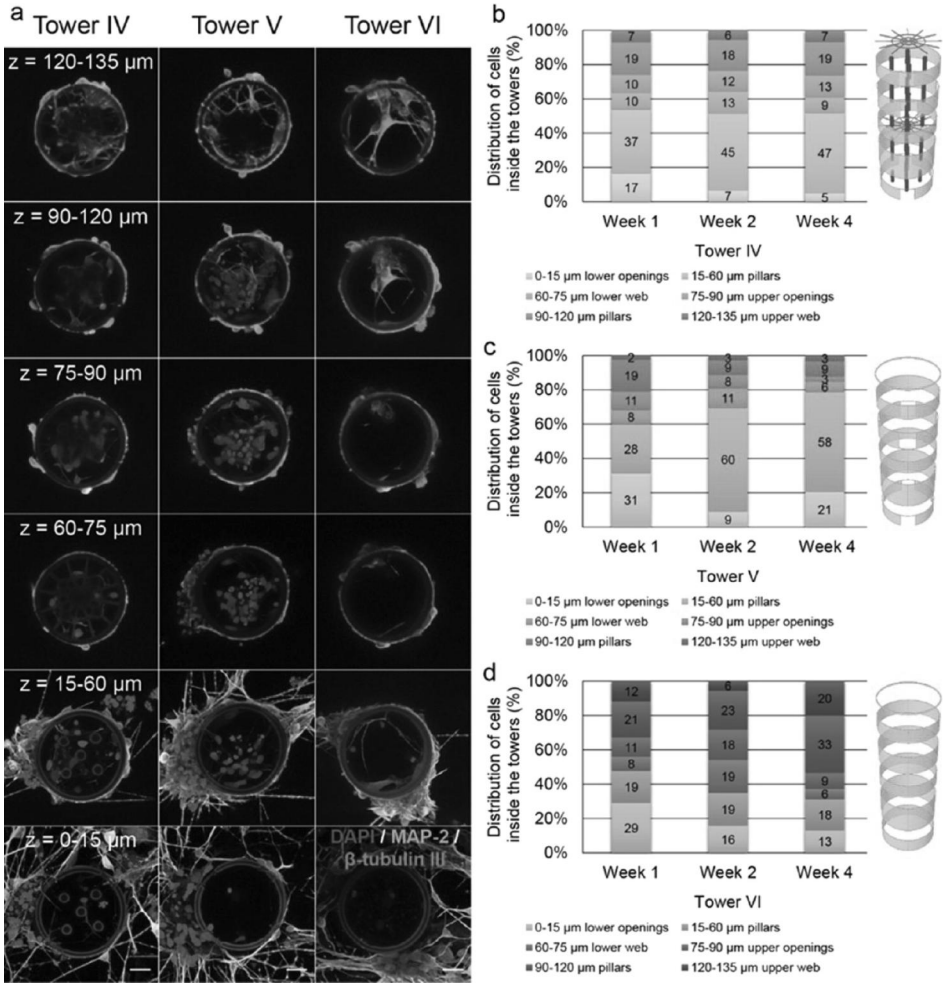

Figure 4. Distribution of cells inside the towers. The counted nuclei data were regrouped into six layers representing different regions of interest present in tower design IV. (a) Illustrative projections of confocal microscopy images from immunocytochemically stained samples representing the six layers of interest. Average cell number per layer inside microtower (b) design IV, (c) design V, and (d) design VI. Immunocytochemical markers MAP-2 (green), β-tubulin III (red), and DAPI (blue). Scale bars represent 20 μm.

point, indicating that the cylindrical shape itself enhanced orientation in long-term culture (Figure 5i). Overall, in all the tower designs throughout the experiment, the highest incidence of neurites was located in the 10° to 20° bins indicating good longitudinal orientation.

3.6. Formation of 3D Networks. The cell morphology and organization of neuronal networks were assessed by SEM imaging. In all microtower designs, neurons grew in close contact with the 2PP-DLW fabricated towers spreading neurites along the inner and outer surfaces, as shown in Figure 6. On the outer surface of the towers, neurons and neurites extended across the total height of the towers. Neurites as well as neurons migrated between the outer and inner surface through the wall openings in designs IV and V. In addition, similar behavior was seen in all designs at the upper rim of the cylinder, where cells formed connections between outer and inner populations by migrating over the edge (Figure 6, Top view). Interestingly, neurons formed 3D networks with suspended bridges between the adjacent microtowers and between tower walls and bottom surfaces (Figures 3a and 6, Last row). These bridges were mostly formed from several neurites intertwined into bundles. On the basis of the known distance between towers, several suspended neurite bridges were estimated to be ~90 μm long and the longest bridges found were ~260 μm.

4. DISCUSSION

Computer-assisted laser-based fabrication techniques such as 2PP-DLW offer powerful tools to produce cell culture platforms with highly ordered geometries that recapitulate the structure and size scale of natural 3D cell environments.[49] Here, we present the design, 2PP-DLW fabrication process, and cell culture results of a novel 3D neuronal cell culture platform based on tubular microtowers. In total, six different microtower designs were successfully fabricated from Ormocomp. To study the relevance of the intraluminal infrastructure (design IV) for cell growth, two designs without internal structures (designs V and VI) were used for comparison. The process was optimized by defining the operational polymerization windows for Ormocomp for the tested scanning speeds of 150, 350, and 550 μm s^{-1}.

Microtower designs with dense spider webs (I and III) were excluded from further study because some web threads were agglutinated due to a self-polymerization phenomenon.[50] On the grounds of the preliminary findings, the microtower designs IV, V, and VI were selected as the most optimal models for the cell

DOI: 10.1021/acsami.7b05536
ACS Appl. Mater. Interfaces 2017, 9, 25717−25730

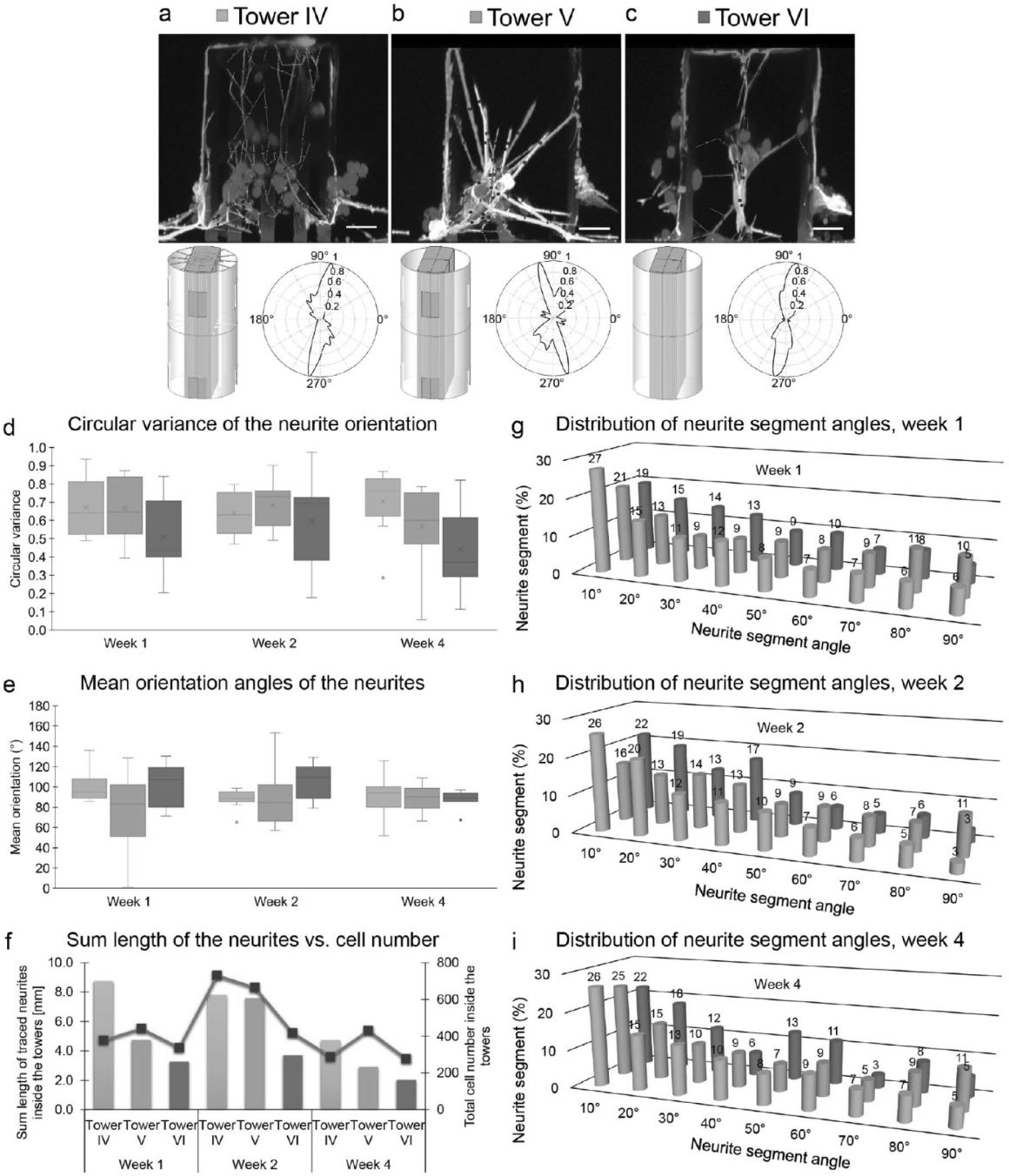

Figure 5. Orientation of neurites inside the towers was determined by measuring the angles of neurite segments from the longitudinal projections taken from the confocal microscopy image stacks of the microtowers. Representative projections of confocal micrographs from the two-week time point with traced neurites marked with yellow lines inside the microtower (a) design IV, (b) design V, and (c) design VI. For each design, the CAD model is presented to illustrate the analyzed volume utilized for the neurite angle measurements (marked with green). In addition, plots of orientation distribution created with CytoSpectre software are shown for each case. The distance from the origin represents the relative frequency of the corresponding angle. Value 1 has been designated to the angle with highest incidence. (d) Box plot of the circular variance of the neurite orientation obtained with CytoSpectre. (e) Box plot of the mean orientation angles of neurites (from 0° to 180°, the longitudinal axis of the tower is at 90°) analyzed with CytoSpectre. (f) Sum length of traced neurites inside each microtower design at different time points and the total cell number (marked with red line). (g–i) Distribution of neurite angles relative to the vertical plane measured from all neurite segments with length 5 μm or more. The longitudinal axis is set to 0°, while horizontal axis is denoted as 90°. Scale bars represent 20 μm.

culture experiments. The fabrication accuracy of the 2PP-DLW setup was evaluated by measuring the dimensions of the towers of design IV. The height of the cylinder had shrunk ~21% because of the low polymerization yield caused by high scanning speed and relatively large axial contour distance. However, this rather high shrinkage rate is in line with the previous results for Ormocomp with ~20% to 24% shrinkage in the z-direction reported.[51,52] The diameters of the micropillars had broadened

DOI: 10.1021/acsami.7b05536
ACS Appl. Mater. Interfaces 2017, 9, 25717−25730

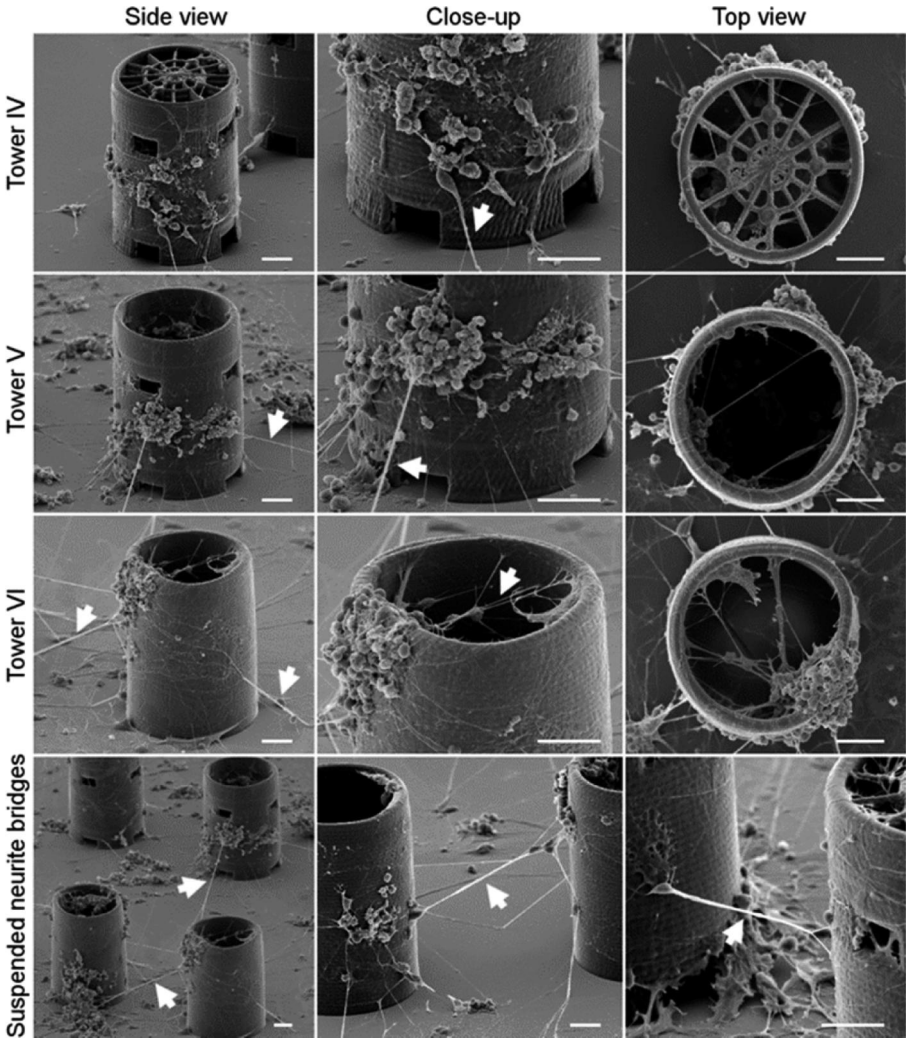

Figure 6. SEM images of neuronal cells inside and outside of different microtower designs at the one-week time point. The images of the three upper rows show the towers from the tilt angles of 60° (first and second column) and 0° (third column). The last row illustrates the close-ups of the suspended neurite bridges extending between adjacent towers. Suspended neurite bridges are marked with arrowheads. Scale bars represent 20 μm.

71% (~3.5 μm), which is more than the width of a voxel (~2 μm). The difference could be explained by the overcuring phenomenon resulting from the multipath scanning with three nested contours separated by a distance of 1.0 μm. Solid voxels are surrounded by subactivated regions, in which the concentration of active radicals is below the polymerization threshold.[53] However, when two subactivated regions overlap as a consequence of closely situated scanning paths as in the case of the multipath scanning method, the laser-generated radical concentration can exceed the threshold value, which leads to self-assembly of oligomers into features sustaining the postexposure development.[50] According to Uppal and Shiakolas,[54] with a diffraction-limited laser spot having a lateral diameter of 1 μm, the radius of the subactivated region is approximately 5 μm. In our case, the lateral diameter of the diffraction-limited laser spot can be estimated as $d = 1.22\lambda/\mathrm{NA} = 720$ nm, where λ is the wavelength of the laser (532 nm) and NA is the numerical aperture of the objective lens (0.90). Thus, in our case, the radius of the subactivated region can be estimated to be ~3.6 μm. The offset between the three nested contours was set to 1.0 μm, so it can be concluded that the overlap of subactivated regions occurred and led to broadening of the diameter of the micropillars. The overcuring could be avoided by taking into account the spot size of the laser beam when preparing the CAD designs and carefully selecting optimal offset between the nested contours. The height of the lower openings deviated from the theoretical height considerably (56%) because the glass-photoresist interface, i.e., the initial focal spot height, had to be manually set for each structure. The experimental width of the lower and upper openings corresponded well with the CAD model when taking into account the overcuring caused by the size of the laser beam. The height of the upper openings shrunk considerably (69%). This finding cannot be solely explained by the height of the voxel (6.8 μm). Presumably, the shrinkage is a consequence of several phenomena such as material shrinkage and overcuring phenomenon occurring at the lower and upper edges of the openings. The inner diameter of the microtower cylinder deviated from the theoretical value by only 4%. One of the acknowledged limiting factors impairing the fabrication accuracy of 2PP-DLW and other photolithographic fabrication methods is that material shrinkage induces deviations from the CAD model.[55,56] However, from the point of view of our test

DOI: 10.1021/acsami.7b05536
ACS Appl. Mater. Interfaces 2017, 9, 25717−25730

arrangement, the shrinkage had no essential effect on the usability for cell culture.

The measured Young's modulus of the UV-cured Ormocomp thin film specimens ($E = 2.4 \pm 0.18$ GPa) was in the same order as that reported earlier by Schizas and Karalekas[57] and Li et al.,[42] 1.27 and 1.58 GPa, respectively. However, the average Young's modulus of the microtowers ($E = 140 \pm 18$ MPa) was considerably smaller when compared with the thin film specimens. This finding is the result of the lower cross-linking degree of polymer chains achieved via 2PP-DLW when compared with the UV-curing process.[57,58] The only reported Young's modulus for Ormocomp microstructures fabricated by 2PP-DLW is $E = 800$ MPa,[59] which is considerably larger than that measured here. The difference can be partially explained by the higher scanning speed (550 μm s^{-1} vs 50 to 250 μm s^{-1}) and the lower laser power values (3.9 mW vs 10 to 17 mW) used in our fabrication process. These factors resulted in a reduction in exposure, a decrease of the cross-linking degree of the polymer, and the lower Young's modulus. Nevertheless, the level of stiffness was adequate for the fabricated microtowers to withstand all the handling and cell culture procedures without major shape distortions.

In 2PP-DLW, the laser exposure dose (i.e., the scanning speed and average laser power) determines the resulting voxel size. Voxel size combined with the chosen contour distance for the CAD model define the final surface topography of the structure.[60] Thus, the surface roughness of the microstructures can be tuned by changing these parameters. Depending on the microtower layer, the surface roughness was either ~11 or ~31 nm due to the fluctuation of the laser dose caused by different contour geometries. The achieved surface roughness is, nevertheless, in line with previous studies; Malinauskas et al. have reported a roughness of ~30 nm ±3 nm for sol–gel photopolymer SZ2080,[61] and Takada et al. found a roughness of 4 to 11 nm for urethane acrylate resin SCR500.[62] It has been suggested that the higher surface roughness resulting in an increase of the surface area can promote the attachment of glioblastoma cells.[63] In our study, there was no significant difference in cell adhesion between the smooth and the rough areas of the tower wall. This is in accordance with previous results stating that the neurons of substantia nigra can adhere to a surface with R_a ranging from 20 to 50 nm, whereas on surfaces with $R_a < 10$ nm or >70 nm adherence is negatively affected.[64] Contrary to the studies mentioned above utilizing uncoated surfaces,[63,64] we studied surface topographies coated with laminin. As reported previously by Käpylä et al.,[65] protein coating levels off differences in the surface roughness of Ormocomp, which in our case resulted in similar cell behavior on both roughnesses. Furthermore, the surface chemistry of Ormocomp appears to have a stronger effect on cell attachment compared with surface roughness. Consequently, although the surface quality of the structures prepared by the 2PP-DLW technique is very susceptible to any variation in fabrication conditions, small changes in the surface roughness were assumingly compensated by the laminin coating.

Interestingly, surface roughness has been shown to dramatically affect cell behavior by Limongi et al.[7] In their study, nanopatterned micropillar ($h = 10$ μm, Ø = 10 μm) arrays supported the formation of 3D networks via suspended neurite bridges, whereas smooth pillars promoted only the formation of a flat sparse neuronal network on the bottom surface as well as at the root of the pillars (surface roughness not reported for either case). In our study, however, the smooth surface appeared to be very attractive for human-derived neuronal cells. Moreover, 3D neuronal networks and suspended bridges were able to form throughout the tower height and along and between the tower walls. To some extent, a similar formation of suspended neurite bridges has also been reported with microfibers[6] and 2PP-DLW fabricated microstructures.[32,33] Thus, it can be concluded that with the 2PP-DLW fabrication method no additional patterning phase is needed to enhance cell growth.

According to the cell behavior, the tower structures seemed to create different microenvironments for the cells: one on the inner and other on the outer surface of the towers. The lumen provided a more stable, enclosed environment, as seen by the relatively constant cell number throughout the experiment. Although the cell number in lumen of all tower designs was similar, the distribution of cells was affected by the microtower design. The openings in the tower wall seemed to have an impact on the extent of cell migration or proliferation inside the towers, whereas the existence of the spider webs did not considerably alter the cell localization. Moreover, cells inside design VI without the openings were more equally distributed throughout the tower height indicating a homogeneous microenvironment.

According to both the automatic and manual analysis of the neurite orientation angles, the microtower structures were able to orient neurites. More detailed manual analysis showed that during the first 2 weeks the longitudinal orientation of the neurites was enhanced by the intraluminal infrastructure, most probably by the micropillars (design IV). By week four, the differences in the degree of orientation leveled off in all tower designs. Overall, the intraluminal structures appeared promising for orientation purposes, but the design clearly needs more optimization. It has been reported that 2PP-DLW fabricated guiding structures (Ø = 10–20 μm) are able to orient rodent neuroblastoma-glioma cells, although quantitative verification has not been conducted.[66] Fibers (Ø = 7–8 μm) have been shown to effectively orient rat neural cells as 63% of the cells had a dominant growth direction of ≤10° compared with the longitudinal direction of the fibers.[6] Our results suggest a similar kind of behavior even though we analyzed the orientation of all neurite segments instead of measuring only the main angles for single neurons. Thus, micropillar structures can be used effectively as components of scaffolds for orientation purposes.

Similar microtower structures without an intraluminal infrastructure ($h = 250$ μm, Ø = 200 μm) embedded in hydrogel have been used to study rodent neural cell interactions and distribution at the tower interface in 3D.[2] In that study, cells accumulated to the towers and formed 3D neural networks around and across the towers. Our study showed surprisingly similar results without the support of the hydrogel matrix. We consider this finding to be important as the use of microstructure-supported cell cultures instead of random 3D cultures in a gel matrix could enhance the reproducibility of the experiments *in vitro*.

5. CONCLUSIONS

Our study introduced a feasible fabrication method for the creation of a microtower-based 3D cell culture platform with intricate and detailed features. The cell culture platform was proven to be efficient for the long-term 3D culturing of human stem cell-derived neuronal cells. The proposed culturing concept may be used as a substitute for the hydrogel matrix commonly used to mechanically support the 3D growth of cells. The platform is especially suitable for studying cell behavior in a 3D environment, for example, the orientation and migration of

DOI: 10.1021/acsami.7b05536
ACS Appl. Mater. Interfaces 2017, 9, 25717–25730

neuronal cells, both of which are important aspects to consider in future studies.

■ ASSOCIATED CONTENT

Supporting Information

The Supporting Information is available free of charge on the ACS Publications website at DOI: 10.1021/acsami.7b05536.

Fabrication of Ormocomp thin films; SEM images of suspended lines polymerized on top of supporting walls with different scanning speeds (Figure S1); CAD images of microtower designs I–III (Figure S2); SEM images of microtower designs I and II fabricated with scanning speeds of 350 μm s^{-1} or 550 μm s^{-1} (Figure S3); SEM images of microtower designs III and IV fabricated with scanning speeds of 350 μm s^{-1} or 550 μm s^{-1} (Figure S4); AFM topography images and line scan profiles of the outer surface of the cylindrical tower walls (Figure S5); representative force versus indentation depth plots from the AFM force spectroscopy measurements performed on microtower and Ormocomp thin film samples (Figure S6) (PDF)

■ AUTHOR INFORMATION

Corresponding Author

*E-mail: sanna.turunen@tut.fi. Phone: +358 50 301 3375.

ORCID

Sanna Turunen: 0000-0002-6823-8811

Tiina Joki: 0000-0001-7397-6694

Maiju L. Hiltunen: 0000-0002-8742-2737

Teemu O. Ihalainen: 0000-0003-4351-8697

Author Contributions

S.T. and T.J. share first authorship. S.N. and M.K. share last authorship. The manuscript was written through contributions of all authors. All authors have given approval to the final version of the manuscript.

Notes

The authors declare no competing financial interest.

■ ACKNOWLEDGMENTS

This research study was supported by the TEKES (the Finnish Funding Agency for Technology and Innovation) Human Spare Parts project, the Finnish Cultural Foundation (Award numbers 00141012, 00140325, and 00150312), Academy of Finland Grant #267471, and the Paulo Foundation. The authors gratefully acknowledge M.S. (Tech.) Taru Karhula for SEM imaging and M.S. Risto-Pekka Pölönen and M.S. Kimmo Kartasalo for guidance with the CytoSpectre software. Hanna Mäkelä and Eija Hannuksela are thanked for technical assistance.

■ REFERENCES

(1) LaPlaca, M. C.; Vernekar, V. N.; Shoemaker, J. T.; Cullen, D. K. Three-Dimensional Neuronal Cultures. In *3D Tissue Engineering*; Berthiaume, F., Morgan, J. R., Eds.; Artech House: Boston, USA, 2010; Chapter 11, pp 187–204.

(2) Cullen, D. K.; Wolf, J. A.; Vernekar, V. N.; Vukasinovic, J.; LaPlaca, M. C. Neural Tissue Engineering and Biohybridized Microsystems for Neurobiological Investigation in Vitro (Part 1). *Crit. Rev. Bioeng.* **2011**, *39*, 201–240.

(3) Lai, Y.; Cheng, K.; Kisaalita, W. Three Dimensional Neuronal Cell Cultures More Accurately Model Voltage Gated Calcium Channel Functionality in Freshly Dissected Nerve Tissue. *PLoS One* **2012**, *7*, e45074.

(4) McKinnon, D. D.; Kloxin, A. M.; Anseth, K. S. Synthetic Hydrogel Platform for Three-Dimensional Culture of Embryonic Stem Cell-Derived Motor Neurons. *Biomater. Sci.* **2013**, *1*, 460–469.

(5) Cullen, D. K.; Tang-Schomer, M. D.; Struzyna, L. A.; Patel, A. R.; Johnson, V. E.; Wolf, J. A.; Smith, D. H. Microtissue Engineered Constructs with Living Axons for Targeted Nervous System Reconstruction. *Tissue Eng., Part A* **2012**, *18*, 2280–2289.

(6) Sharifi, F.; Patel, B. B.; Dzuilko, A. K.; Montazami, R.; Sakaguchi, D. S.; Hashemi, N. Polycaprolactone Microfibrous Scaffolds to Navigate Neural Stem Cells. *Biomacromolecules* **2016**, *17*, 3287–3297.

(7) Limongi, T.; Cesca, F.; Gentile, F.; Marotta, R.; Ruffilli, R.; Barberis, A.; Dal Maschio, M.; Petrini, E. M.; Santoriello, S.; Benfenati, F.; Di Fabrizio, E. Nanostructured Superhydrophobic Substrates Trigger the Development of 3D Neuronal Networks. *Small* **2013**, *9*, 402–412.

(8) He, L.; Zhang, Y.; Zeng, C.; Ngiam, M.; Liao, S.; Quan, D.; Zeng, Y.; Lu, J.; Ramakrishna, S. Manufacture of PLGA Multiple-Channel Conduits with Precise Hierarchical Pore Architectures and in Vitro/Vivo Evaluation for Spinal Cord Injury. *Tissue Eng., Part C* **2009**, *15*, 243–255.

(9) Wen, X.; Tresco, P. A. Effect of Filament Diameter and Extracellular Matrix Molecule Precoating on Neurite Outgrowth and Schwann Cell Behavior on Multifilament Entubulation Bridging Device in Vitro. *J. Biomed. Mater. Res., Part A* **2006**, *76A*, 626–637.

(10) Tian, L.; Prabhakaran, M. P.; Ramakrishna, S. Strategies for Regeneration of Components of Nervous System: Scaffolds, Cells and Biomolecules. *Regener. Biomater.* **2015**, *2*, 31–45.

(11) Huang, Y.; Huang, Y. Biomaterials and Strategies for Nerve Regeneration. *Artif. Organs* **2006**, *30*, 514–522.

(12) Hadlock, T.; Elisseeff, J.; Langer, R.; Vacanti, J.; Cheney, M. A Tissue-Engineered Conduit for Peripheral Nerve Repair. *Arch. Otolaryngol., Head Neck Surg.* **1998**, *124*, 1081–1086.

(13) Wang, S.; Yaszemski, M. J.; Knight, A. M.; Gruetzmacher, J. A.; Windebank, A. J.; Lu, L. Photo-Crosslinked Poly(ε-Caprolactone Fumarate) Networks for Guided Peripheral Nerve Regeneration: Material Properties and Preliminary Biological Evaluations. *Acta Biomater.* **2009**, *5*, 1531–1542.

(14) Bender, M. D.; Bennett, J. M.; Waddell, R. L.; Doctor, J. S.; Marra, K. G. Multi-Channeled Biodegradable Polymer/CultiSpher Composite Nerve Guides. *Biomaterials* **2004**, *25*, 1269–1278.

(15) Dalton, P. D.; Flynn, L.; Shoichet, M. S. Manufacture of Poly(2-Hydroxyethyl Methacrylate-Co-Methyl Methacrylate) Hydrogel Tubes for use as Nerve Guidance Channels. *Biomaterials* **2002**, *23*, 3843–3851.

(16) Yucel, D.; Kose, G. T.; Hasirci, V. Polyester Based Nerve Guidance Conduit Design. *Biomaterials* **2010**, *31*, 1596–1603.

(17) Widmer, M. S.; Gupta, P. K.; Lu, L.; Meszlenyi, R. K.; Evans, G. R.; Brandt, K.; Savel, T.; Gurlek, A.; Patrick, C. W., Jr; Mikos, A. G. Manufacture of Porous Biodegradable Polymer Conduits by an Extrusion Process for Guided Tissue Regeneration. *Biomaterials* **1998**, *19*, 1945–1955.

(18) Kim, Y.; Haftel, V. K.; Kumar, S.; Bellamkonda, R. V. The Role of Aligned Polymer Fiber-Based Constructs in the Bridging of Long Peripheral Nerve Gaps. *Biomaterials* **2008**, *29*, 3117–3127.

(19) Bini, T. B.; Gao, S.; Xu, X.; Wang, S.; Ramakrishna, S.; Leong, K. W. Peripheral Nerve Regeneration by Microbraided Poly(L-Lactide-Co-Glycolide) Biodegradable Polymer Fibers. *J. Biomed. Mater. Res.* **2004**, *68A*, 286–295.

(20) Wang, S.; Cai, L. Polymers for Fabricating Nerve Conduits. *Int. J. Polym. Sci.* **2010**, *2010*, 138686.

(21) Pateman, C. J.; Harding, A. J.; Glen, A.; Taylor, C. S.; Christmas, C. R.; Robinson, P. P.; Rimmer, S.; Boissonade, F. M.; Claeyssens, F.; Haycock, J. W. Nerve Guides Manufactured from Photocurable Polymers to Aid Peripheral Nerve Repair. *Biomaterials* **2015**, *49*, 77–89.

(22) Radulescu, D.; Dhar, S.; Young, C. M.; Taylor, D. W.; Trost, H.; Hayes, D. J.; Evans, G. R. Tissue Engineering Scaffolds for Nerve Regeneration Manufactured by Ink-Jet Technology. *Mater. Sci. Eng., C* **2007**, *27*, 534–539.

(23) Greiner, A. M.; Richter, B.; Bastmeyer, M. Micro-Engineered 3D Scaffolds for Cell Culture Studies. *Macromol. Biosci.* **2012**, *12*, 1301−1314.
(24) Juodkazis, S.; Mizeikis, V.; Misawa, H. Three-Dimensional Structuring of Resists and Resins by Direct Laser Writing and Holographic Recording. In *Photoresponsive Polymers I*; Marder, S., Lee, K., Eds.; Springer Berlin Heidelberg: Berlin, Germany, 2008; pp 157−206.
(25) Sun, H. B.; Kawata, S. Two-Photon Photopolymerization and 3D Lithographic Microfabrication. In *NMR • 3D Analysis • Photopolymerization*; Springer Berlin Heidelberg: Berlin, Germany, 2004; pp 169−273.
(26) Burmeister, F.; Steenhusen, S.; Houbertz, R.; Zeitner, U. D.; Nolte, S.; Tünnermann, A. Materials and Technologies for Fabrication of Three-Dimensional Microstructures with Sub-100 Nm Feature Sizes by Two-Photon Polymerization. *J. Laser Appl.* **2012**, *24*, 042014.
(27) Ovsianikov, A.; Mironov, V.; Stampfl, J.; Liska, R. Engineering 3D Cell-Culture Matrices: Multiphoton Processing Technologies for Biological and Tissue Engineering Applications. *Expert Rev. Med. Devices* **2012**, *9*, 613−633.
(28) Doraiswamy, A.; Jin, C.; Narayan, R. J.; Mageswaran, P.; Mente, P.; Modi, R.; Auyeung, R.; Chrisey, D. B.; Ovsianikov, A.; Chichkov, B. Two Photon Induced Polymerization of Organic-Inorganic Hybrid Biomaterials for Microstructured Medical Devices. *Acta Biomater.* **2006**, *2*, 267−275.
(29) Ovsianikov, A.; Schlie, S.; Ngezahayo, A.; Haverich, A.; Chichkov, B. N. Two-Photon Polymerization Technique for Microfabrication of CAD-Designed 3D Scaffolds from Commercially Available Photosensitive Materials. *J. Tissue Eng. Regener. Med.* **2007**, *1*, 443−449.
(30) Schlie, S.; Ngezahayo, A.; Ovsianikov, A.; Fabian, T.; Kolb, H. A.; Haferkamp, H.; Chichkov, B. N. Three-Dimensional Cell Growth on Structures Fabricated from ORMOCER by Two-Photon Polymerization Technique. *J. Biomater. Appl.* **2007**, *22*, 275−287.
(31) Marino, A.; Ciofani, G.; Filippeschi, C.; Pellegrino, M.; Pellegrini, M.; Orsini, P.; Pasqualetti, M.; Mattoli, V.; Mazzolai, B. Two-Photon Polymerization of Sub-Micrometric Patterned Surfaces: Investigation of Cell-Substrate Interactions and Improved Differentiation of Neuron-Like Cells. *ACS Appl. Mater. Interfaces* **2013**, *5*, 13012−13021.
(32) Timashev, P. S.; Vedunova, M. V.; Guseva, D.; Ponimaskin, E.; Deiwick, A.; Mishchenko, T. A.; Mitroshina, E. V.; Koroleva, A. V.; Pimashkin, A. S.; Mukhina, I. V.; Panchenko, V. Y.; Chichkov, B. N.; Bagratashvili, V. N. 3D in Vitro Platform Produced by Two-Photon Polymerization for the Analysis of Neural Network Formation and Function. *Biomed. Phys. Eng. Express* **2016**, *2*, 035001.
(33) Koroleva, A.; Gill, A. A.; Ortega, I.; Haycock, J. W.; Schlie, S.; Gittard, S. D.; Chichkov, B. N.; Claeyssens, F. Two-Photon Polymerization-Generated and Micromolding-Replicated 3D Scaffolds for Peripheral Neural Tissue Engineering Applications. *Biofabrication* **2012**, *4*, 025005.
(34) Käpylä, E.; Turunen, S.; Pelto, J.; Viitanen, J.; Kellomäki, M. Investigation of the Optimal Processing Parameters for Picosecond Laser-Induced Microfabrication of a Polymer-Ceramic Hybrid Material. *J. Micromech. Microeng.* **2011**, *21*, 065033.
(35) Käpylä, E.; Sedlačík, T.; Aydogan, D. B.; Viitanen, J.; Rypáček, F.; Kellomäki, M. Direct Laser Writing of Synthetic Poly(Amino Acid) Hydrogels and Poly(Ethylene Glycol) Diacrylates by Two-Photon Polymerization. *Mater. Sci. Eng., C* **2014**, *43*, 280−289.
(36) Žukauskas, A.; Malinauskas, M.; Reinhardt, C.; Chichkov, B. N.; Gadonas, R. Closely Packed Hexagonal Conical Microlens Array Fabricated by Direct Laser Photopolymerization. *Appl. Opt.* **2012**, *51*, 4995−5003.
(37) Yang, D.; Park, S. H.; Lim, T. W.; Kong, H.; Yi, S. W.; Yang, H. K.; Lee, K. Ultraprecise Microreproduction of a Three-Dimensional Artistic Sculpture by Multipath Scanning Method in Two-Photon Photopolymerization. *Appl. Phys. Lett.* **2007**, *90*, 013113.
(38) Heinz, W. F.; Hoh, J. H. Spatially Resolved Force Spectroscopy of Biological Surfaces using the Atomic Force Microscope. *Trends Biotechnol.* **1999**, *17*, 143−150.
(39) Hertz, H. Ueber die Berührung fester elastischer Körper. *J. für die reine und angewandte Mathematik* **1882**, *92*, 156−171.
(40) Johnsson, K. L. *Contact Mechanics*; Cambridge University Press: Cambridge, U.K., 1985.
(41) Bilodeau, G. G. Regular Pyramid Punch Problem. *J. Appl. Mech.* **1992**, *59*, 519−523.
(42) Li, Z.; Brand, U.; Ahbe, T. Towards Quantitative Modelling of Surface Deformation of Polymer Micro-Structures Under Tactile Scanning Measurement. *Meas. Sci. Technol.* **2014**, *25*, 044010.
(43) Lappalainen, R. S.; Salomäki, M.; Ylä-Outinen, L.; Heikkilä, T. J.; Hyttinen, J. A.; Pihlajamäki, H.; Suuronen, R.; Skottman, H.; Narkilahti, S. Similarly Derived and Cultured hESC Lines show Variation in their Developmental Potential Towards Neuronal Cells in Long-Term Culture. *Regener. Med.* **2010**, *5*, 749−762.
(44) Skottman, H. Derivation and Characterization of Three New Human Embryonic Stem Cell Lines in Finland. *In Vitro Cell. Dev. Biol.: Anim.* **2010**, *46*, 206−209.
(45) Kartasalo, K.; Pölönen, R.; Ojala, M.; Rasku, J.; Lekkala, J.; Aalto-Setälä, K.; Kallio, P. CytoSpectre: A Tool for Spectral Analysis of Oriented Structures on Cellular and Subcellular Levels. *BMC Bioinf.* **2015**, *16*, 344.
(46) Tuft, B. W.; Xu, L.; White, S. P.; Seline, A. E.; Erwood, A. M.; Hansen, M. R.; Guymon, C. A. Neural Pathfinding on Uni- and Multidirectional Photopolymerized Micropatterns. *ACS Appl. Mater. Interfaces* **2014**, *6*, 11265−11276.
(47) Liao, C. Product Model Creation and Simulation for Two-photon Polymerization Micro-manufacturing. Ph.D. Thesis, Joseph Fourier University/National Taiwan University, 2008.
(48) Wu, D.; Wu, S.; Niu, L.; Chen, Q.; Wang, R.; Song, J.; Fang, H.; Sun, H. High Numerical Aperture Microlens Arrays of Close Packing. *Appl. Phys. Lett.* **2010**, *97*, 031109−1−031109−3.
(49) Greiner, A. M.; Richter, B.; Bastmeyer, M. Micro-Engineered 3D Scaffolds for Cell Culture Studies. *Macromol. Biosci.* **2012**, *12*, 1301−1314.
(50) Malinauskas, M.; Bičkauskaitė, G.; Rutkauskas, M.; Paipulas, D.; Purlys, V.; Gadonas, R. Self-Polymerization of Nano-Fibres and Nano-Membranes Induced by Two-Photon Absorption. *Lith. J. Phys.* **2010**, *50*, 135−140.
(51) Käpylä, E.; Aydogan, D. B.; Virjula, S.; Vanhatupa, S.; Miettinen, S.; Hyttinen, J.; Kellomäki, M. Direct Laser Writing and Geometrical Analysis of Scaffolds with Designed Pore Architecture for Three-Dimensional Cell Culturing. *J. Micromech. Microeng.* **2012**, *22*, 115016.
(52) Turunen, S.; Käpylä, E.; Lähteenmäki, M.; Ylä-Outinen, L.; Narkilahti, S.; Kellomäki, M. Direct Laser Writing of Microstructures for the Growth Guidance of Human Pluripotent Stem Cell Derived Neuronal Cells. *Opt. Laser Eng.* **2014**, *55*, 197−204.
(53) Jariwala, S.; Venkatakrishnan, K.; Tan, B. Single Step Self-Enclosed Fluidic Channels Via Two Photon Absorption (TPA) Polymerization. *Opt. Express* **2010**, *18*, 1630−1636.
(54) Uppal, N.; Shiakolas, P. S. Modeling of Temperature-Dependent Diffusion and Polymerization Kinetics and their Effects on Two-Photon Polymerization Dynamics. *J. Micro/Nanolithogr., MEMS, MOEMS* **2008**, *7*, 043002−1−043002−10.
(55) Koseki, K.; Sakamaki, H.; Jeong, K. M. In Situ Measurement of Shrinkage Behavior of Photopolymers. *J. Photopolym. Sci. Technol.* **2013**, *26*, 567−572.
(56) Ovsianikov, A.; Viertl, J.; Chichkov, B.; Oubaha, M.; MacCraith, B.; Sakellari, I.; Giakoumaki, A.; Gray, D.; Vamvakaki, M.; Farsari, M.; Fotakis, C. Ultra-Low Shrinkage Hybrid Photosensitive Material for Two-Photon Polymerization Microfabrication. *ACS Nano* **2008**, *2*, 2257−2262.
(57) Schizas, C.; Karalekas, D. Mechanical Characteristics of an Ormocomp® Biocompatible Hybrid Photopolymer. *J. Mech. Behav. Biomed. Mater.* **2011**, *4*, 99−106.
(58) Bayindir, Z.; Sun, Y.; Naughton, M. J.; et al. Polymer Microcantilevers Fabricated Via Multiphoton Absorption Polymerization. *Appl. Phys. Lett.* **2005**, *86*, 064105.
(59) Klein, F.; Striebel, T.; Fischer, J.; Jiang, Z.; Franz, C. M.; von Freymann, G.; Wegener, M.; Bastmeyer, M. Elastic Fully Three-

DOI: 10.1021/acsami.7b05536
ACS Appl. Mater. Interfaces 2017, 9, 25717−25730

Dimensional Microstructure Scaffolds for Cell Force Measurements. *Adv. Mater.* **2010**, *22*, 868−871.
(60) Burmeister, F.; Steenhusen, S.; Houbertz, R.; Asche, T. S.; Nickel, J.; Nolte, S.; Tucher, N.; Josten, P.; Obel, K.; Wolter, H.; Fessel, S.; Schneider, A. M.; Gartner, K. H.; Beck, C.; Behrens, P.; Tunnermann, A.; Walles, H. Two-Photon Polymerization of Inorganic-Organic Polymers for Biomedical and Microoptical Applications. In *Optically Induced Nanostructures: Biomedical and Technical Applications*; Konig, K., Ostendorf, A., Eds.; De Gruyter: Berlin, Germany, 2015; pp 239−266.
(61) Malinauskas, M.; Gilbergs, H.; Zukauskas, A.; Belazaras, K.; Purlys, V.; Rutkauskas, M.; Bickauskaite, G.; Momot, A.; Paipulas, D.; Gadonas, R.; Juodkazis, S.; Piskarskas, A. Femtosecond Laser Fabrication of Hybrid Micro-Optical Elements and their Integration on the Fiber Tip. *Proc. SPIE* **2010**, 7716.
(62) Takada, K.; Sun, H. B.; Kawata, S. Improved Spatial Resolution and Surface Roughness in Photopolymerization- Based Laser Nano-writing. *Appl. Phys. Lett.* **2005**, *86*, 071122.
(63) Zamani, F.; Amani-Tehran, M.; Latifi, M.; Shokrgozar, M. A. The Influence of Surface Nanoroughness of Electrospun PLGA Nanofibrous Scaffold on Nerve Cell Adhesion and Proliferation. *J. Mater. Sci.: Mater. Med.* **2013**, *24*, 1551−1560.
(64) Fan, Y. W.; Cui, F. Z.; Hou, S. P.; Xu, Q. Y.; Chen, L. N.; Lee, I. S. Culture of Neural Cells on Silicon Wafers with Nano-Scale Surface Topography. *J. Neurosci. Methods* **2002**, *120*, 17−23.
(65) Käpylä, E.; Sorkio, A.; Teymouri, S.; Lahtonen, K.; Vuori, L.; Valden, M.; Skottman, H.; Kellomäki, M.; Juuti-Uusitalo, K. Ormocomp-Modified Glass Increases Collagen Binding and Promotes the Adherence and Maturation of Human Embryonic Stem Cell-Derived Retinal Pigment Epithelial Cells. *Langmuir* **2014**, *30*, 14555−14565.
(66) Melissinaki, V.; Gill, A. A.; Ortega, I.; Vamvakaki, M.; Ranella, A.; Haycock, J. W.; Fotakis, C.; Farsari, M.; Claeyssens, F. Direct Laser Writing of 3D Scaffolds for Neural Tissue Engineering Applications. *Biofabrication* **2011**, *3*, 045005.

DOI: 10.1021/acsami.7b05536
ACS Appl. Mater. Interfaces 2017, 9, 25717−25730

Supporting Information

Direct Laser Writing of Tubular Microtowers for 3D Culture of Human Pluripotent Stem Cell-Derived Neuronal Cells

Sanna Turunen[+]a, Tiina Joki[+]b, Maiju L. Hiltunen[a], Teemu O. Ihalainen[b], Susanna Narkilahti[++]b, and Minna Kellomäki[++]a,c*

[a]Biomaterials and Tissue Engineering Group, BioMediTech and Faculty of Biomedical Sciences and Engineering, Tampere University of Technology, Korkeakoulunkatu 3, 33720 Tampere, Finland

[b]NeuroGroup, BioMediTech and Faculty of Medicine and Life Sciences, University of Tampere, Lääkärinkatu 1, 33520 Tampere, Finland

[c]BioMediTech and Faculty of Medicine and Life Sciences, University of Tampere, Lääkärinkatu 1, 33520 Tampere, Finland

[+]These authors share first authorship

[++]These authors share last authorship

Corresponding Author:

*E-mail: sanna.turunen@tut.fi, Phone: +358 50 301 3375

Fabrication of Ormocomp® Thin Films

In order to compare the mechanical properties of two-photon polymerized Ormocomp® microstructures with UV-cured Ormocomp® samples, the resist with 2 wt% of the photoinitiator Irgacure® 127 was polymerized into thin films. A drop of prepolymer solution was placed between a microscope slide and a coverslip separated by a 150 μm thick spacer and exposed to UV light for 10 s using a BlueWave® 50 UV curing spot lamp (DYMAX Corporation, USA) having a wavelength from 300 nm to 450 nm and ~540 mW cm^{-2} intensity. Cured films (three pieces) were left attached to the coverslips for easy access with the AFM probe.

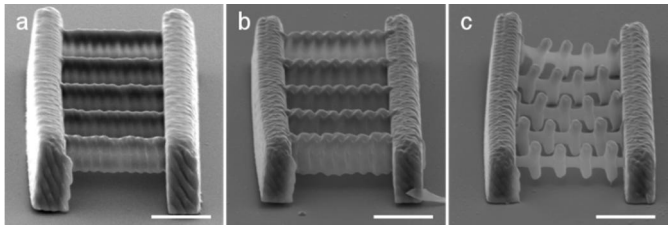

Figure S1. SEM images of suspended lines polymerized on top of supporting walls with scanning speeds of (a) 150 μm s^{-1}, (b) 350 μm s^{-1}, and (c) 550 μm s^{-1}. Images were taken from a 60° tilt. Scale bars represent 10 μm.

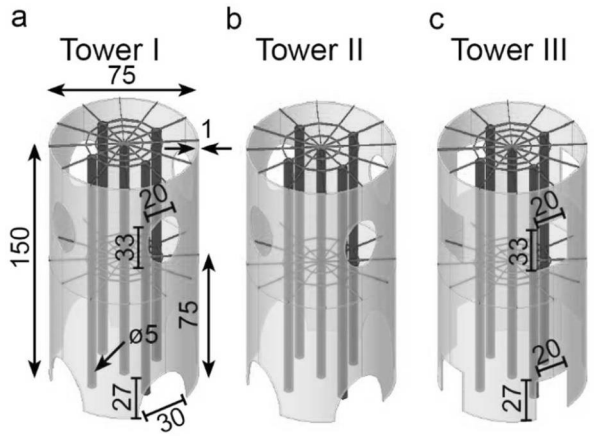

Figure S2. CAD images of the microtowers: (a) design I with elliptical openings and dense webs, (b) design II with elliptical openings and sparse webs, and (c) design III with rectangular openings and dense webs. The dimensions are given in microns.

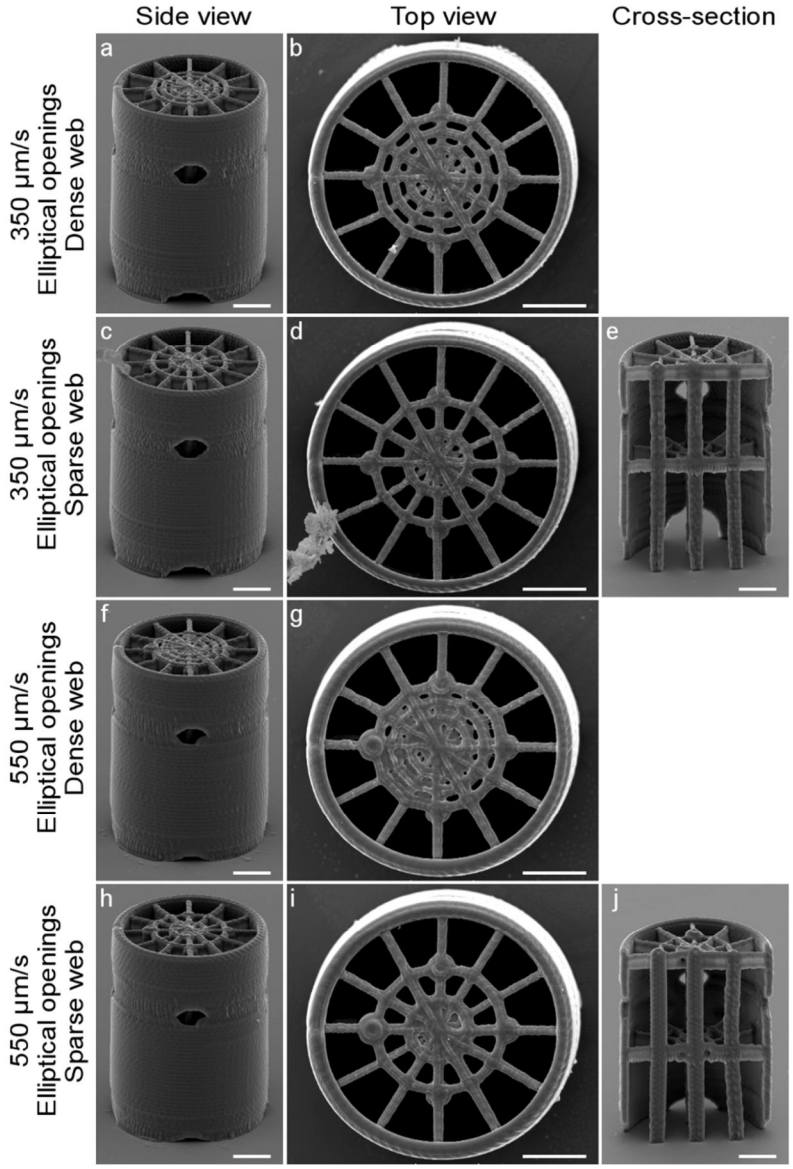

Figure S3. SEM images of microtowers with elliptical openings and with dense (design I) or sparse (design II) webs fabricated with scanning speeds of 350 µm s^{-1} or 550 µm s^{-1}. The images show the towers from the tilt angles of 60° (a,c,f,h) and 0° (b,d,g,i). The third column (e,j) shows the longitudinal cross-sections of the towers from the tilt angle of 60°. Scale bars represent 20 µm.

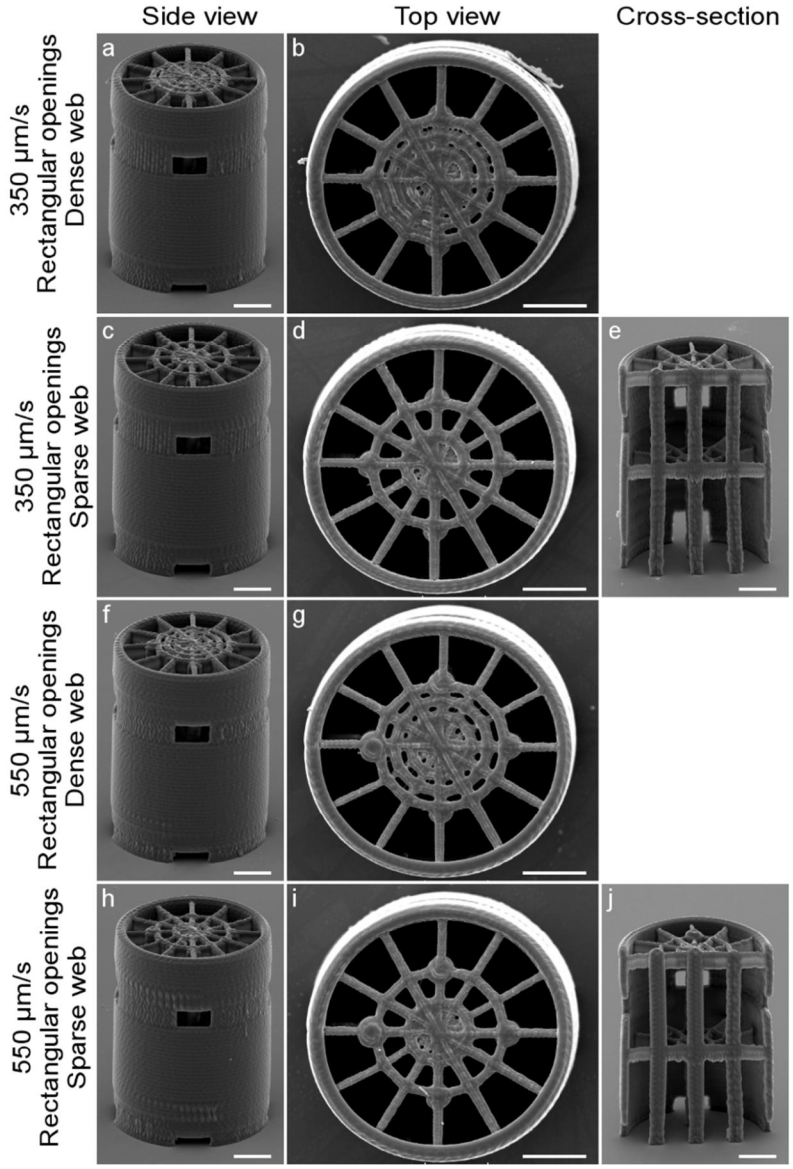

Figure S4. SEM images of microtowers with rectangular openings and with dense (design III) or sparse (design IV) webs fabricated with scanning speeds of 350 µm s^{-1} or 550 µm s^{-1}. The images show the towers from the tilt angles of 60° (a,c,f,h) and 0° (b,d,g,i). The third column (e,j) shows the longitudinal cross-sections of the towers from the tilt angle of 60°. Scale bars represent 20 µm.

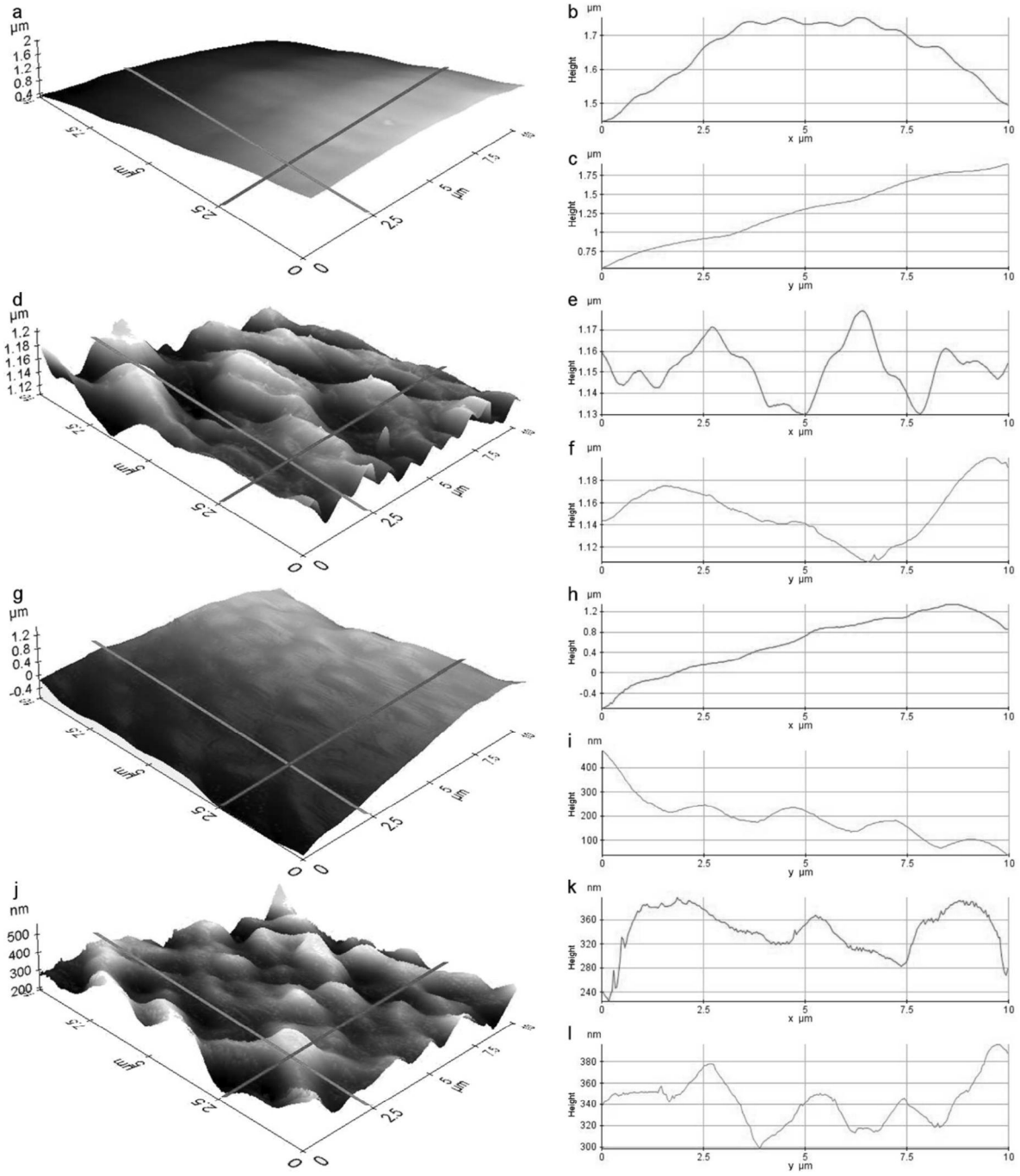

Figure S5. AFM topography images (10 µm × 10 µm) of the outer surface of the cylindrical tower walls. (a) An example 3D image of the wall section with smooth surface before performing the flattening procedure to remove the curvature in the x-direction resulting from the cylindrical shape of the tower wall and the tilt in the y-direction. (b) Line scan profiles of the unprocessed image along the red line in the x-direction and (c) green line in the y-direction. (d) The 3D

topography image of the same area after flattening and (e,f) the corresponding line profiles. (g) Topography image of the wall section located between the openings with rough texture and its line profiles in the (h) x- and (i) y-directions. (j) The rough surface after flattening process and (k,l) the corresponding line profiles.

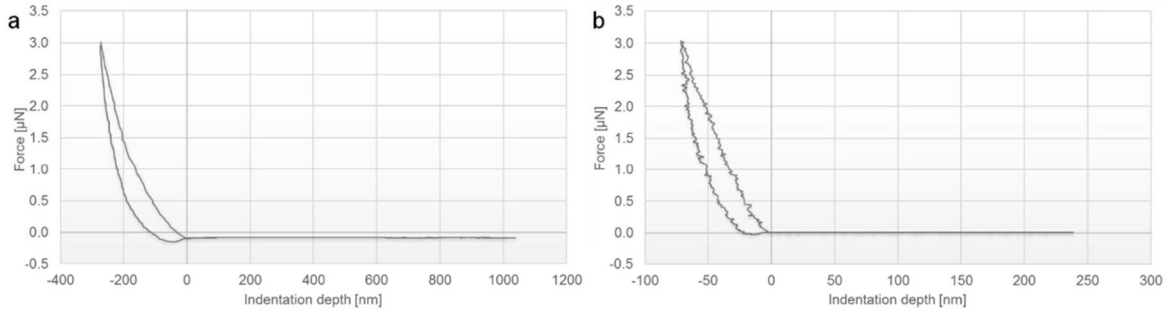

Figure S6. Representative force versus indentation depth plots from the AFM force spectroscopy measurements performed on (a) microtower and (b) Ormocomp® thin film samples. Trace (blue) and retrace (red) curves clearly show hysteresis owing to the plastic behavior of the samples instead of being absolutely elastic as assumed by the Hertz model.

Tampereen teknillinen yliopisto
PL 527
33101 Tampere

Tampere University of Technology
P.O.B. 527
FI-33101 Tampere, Finland

ISBN 978-952-15-3985-5
ISSN 1459-2045